ktu
kaunas university of technology
1922

MEDICAL PHYSICS in the BALTIC STATES 2023

PROCEEDINGS OF THE 16th INTERNATIONAL CONFERENCE ON *MEDICAL PHYSICS*

9-11 November, 2023
Kaunas, Lithuania

ISSN 1822-5721

KAUNAS UNIVERSITY OF TECHNOLOGY

MEDICAL PHYSICS IN THE BALTIC STATES

Proceedings of the 16th International Conference on Medical Physics

Kaunas, Lithuania
9 – 11 November, 2023

Executive editor **Diana Adlienė**

CONFERENCE IS ORGANIZED BY:

Kaunas University of Technology
Skåne University Hospital, Lund University
Medical Physicists Society
University Hospital of Lithuanian University of Health Sciences „Kauno klinikos“

PROGRAM COMMITTEE

Diana ADLIENĖ – Kaunas University of Technology (Lithuania)
Marco BRAMBILLA – University Hospital of Novara (Italy)
Reda ČERAPAITĖ-TRUŠINSKIENĖ – Lithuanian University of Health Sciences (Lithuania)
Jurijs DEHTJARS – Riga Technical University (Latvia)
Todorka DIMITROVA – Plovdiv University "Paisii Hilendarski" (Bulgaria)
Birutė GRICIENĖ – Vilnius University (Lithuania)
Gunta KIZANE – University of Latvia (Latvia)
Jurgita LAURIKAITIENĖ – Kaunas University of Technology (Lithuania)
Sören MATTSSON – Lund University, Skåne University Hospital (Sweden)
Viktoras RUDŽIANSKAS – Hospital of Lithuanian University of Health Sciences „Kauno klinikos” (Lithuania)
Kirill SKOVORODKO – Vilnius University Hospital Santaros Clinics (Lithuania)

ORGANISING COMMITTEE

Benas Gabrielis URBONAVIČIUS - Kaunas University of Technology (Lithuania)
Lena CIBULSKYTĖ - Kaunas University of Technology (Lithuania)
Judita PUIŠO - Kaunas University of Technology (Lithuania)
Dalia BAREIŠIENĖ - Kaunas University of Technology (Lithuania)
Greta VAINIŪTĖ - Vytautas Magnus University (Lithuania)
Gustė LAURIKAITYTĖ – Freelance Web Developer (Lithuania)

CONFERENCE IS SUPPORTED BY:

Kaunas University of Technology
Lund University Skåne University Hospital
Medical Physicists Society

Papers included in the Proceedings were reviewed by independent peer reviewers

MEDICAL PHYSICS IN THE BALTIC STATES 16 (2023)

Proceedings of International Conference "Medical Physics 2023"
09-11 November 2023, Kaunas, Lithuania

CURRENT TRENDS IN MEDICAL PHYSICS

Sören MATTSSON[1,2], Diana ADLIENĖ[2], Jurgita LAURIKAITIENĖ[2]
[1]Lund University, Medical Radiation Physics, ITM, Skåne Univ. Hospital, Malmö, Sweden, [2]Kaunas University of Technology, Department of Physics, Kaunas, Lithuania
[1]soren.mattsson@med.lu.se; [2]diana.adliene@gmail.com; [2]jurgita.laurikaitiene@ktu.lt

***Abstract*:** The paper is an update and an extension of the summary of advances in medical physics over the past 60 years that was presented at our last conference. Recent advances, challenges and current trends in medical physics applied to radiation therapy, diagnostic radiology, nuclear medicine, MRI and radiation safety are discussed. Today, development is concentrated on providing the conditions for individualised diagnostics and therapy, which requires increased precision and accuracy in both radiotherapy and radiological diagnostics.

Keywords: Medical physics, medical imaging, radiotherapy, radiation safety, AI.

1. Introduction

Medical physics is a branch of applied physics, pursued by medical physicists, that uses physics principles, methods and techniques in practice and research for the prevention, diagnosis and treatment of human diseases with a specific goal of improving human health and well-being [1]. The aim of this paper is to update and expand the summary of advances in medical physics over the past 60 years that was presented at our last conference [2] by reviewing most recent advancements, challenges and current trends in medical physics applied to radiation therapy, diagnostic radiology, nuclear medicine, MRI and radiation safety. Figure 1 illustrates developments in medical physics from 1960 to now and outlines a likely development until 2050.

2. General trends of importance for all fields of medical physics

The development in medicine towards more and more individualised and personalised diagnostics and therapy also influences various fields of medical physics [3,4,5]. In this way care providers can offer and plan specific care for their patients, based on the particular genes, proteins, and other substances or characteristics in a person's body. This approach is also sometimes called precision medicine. Other fields of active development are the use of artificial intelligence (AI) [4,5,6]., theranostics [7,8], radiomics [9] and dosiomics [10].

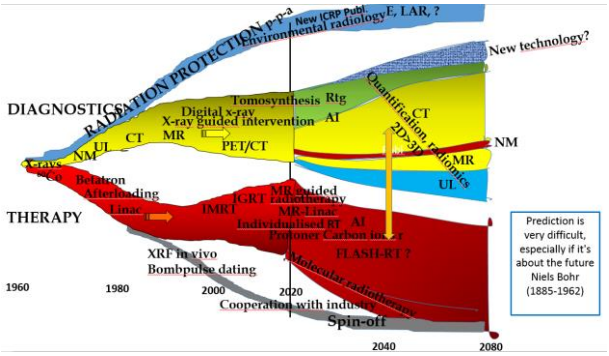

Fig. 1. Schematic description of developments in medical physics since 1960 and prognosis up to 2050 [2]. For abbreviations, please see text and [2].

2.1. AI

Artificial intelligence (AI) has been described as the most revolutionising development in the health care sector in the current decade, with diagnostic imaging having the greatest share in such development [4].

2.1.1. AI for imaging

Machine learning (ML) and deep learning (DL) are subclasses of AI that show breakthrough performance in image analysis. They have become the state of the art in the field of image classification and recognition. ML deals with the extraction of the important characteristic features from images, whereas DL uses neural networks to solve such problems with better performance. DL applications can be divided into medical imaging analysis and applications beyond analysis. In the field of medical imaging analysis, there are applications such as image classification, lesion detection, and segmentation.

AI algorithms, particularly for DL, have demonstrated remarkable progress in image-recognition tasks with many applications in the medical image analysis field. AI can be used to segment and analyse medical images which can improve accuracy and speed of diagnosis as

well as improving the image quality by reducing noise and distortions in the images.
AI in radiology has focused on improving three broad principles attributed to human limitations; efficiency, objectivity, and standardisation [4].
The ultimate goal of AI, the instantaneous image interpretation is however not yet fully achieved but AI technology is being more and more used for image segmentation, reconstruction, and disease registration. AI segmentation has the ability to automatically delineate structures and provide measurements such as organ volume, the surface area of a tumour, etc. Taken a step further, these AI algorithms can be specialised to stage tumours [4].
In one study, an ensemble of top-performing AI algorithms combined with a single radiologist reader achieved an area under the curve (AUC) of 0.942, with 92% specificity, outperforming the radiologists' specificity of 90.5%. This is a representative example of new AI algorithms aimed at instantaneous, automatic interpretation [4].
Beyond image analysis, DL can be used for quality control, workflow organisation, and reporting.
The potential for AI to improve performance and productivity in diagnostic imaging is great and AI is being increasingly adopted in clinical practice.
Whether applied to radiology, pathology, cardiology, or any other diagnostic profession, AI should improve accuracy and efficiency for end users. When targeting everyday clinical use cases, integration into existing workflows is key—as is fast and secure access to the best AI technology. which translates into better and more effective patient care.

2.1.2. AI for radiotherapy

AI-based tools are now found in various parts of the radiotherapy process and are used today for e.g. segmentation, synthetic image generation and outcome prediction. Several concerns have been raised, including the need for harmonisation and improvements in radiotherapy staff skills to allow the intended use of AI tools in clinical practice and avoid being used as a "black box" solution [5]. Strong collaboration between radiation therapy physicians and physicists and AI experts is necessary to develop and implement reliable AI tools to handle increasing amounts of data and treatment options

2.2. Theranotics/Theragnostics

The concept or expression theranostics (alt. theragnostics) can be defined as the merge of therapeutics and diagnostics, with the purpose of delivering treatment to each health condition, focusing on tailoring the approach for each patient [7,8].
In nuclear medicine, the same radiopharmaceutical is used both for imaging and targeted therapy as well as for monitoring the response to treatment.

2.3 Radiomics

Radiomics is a method that extracts a large number of features from medical images using data-characterisation algorithms [9]. These features have the potential to uncover tumour patterns and characteristics that fail to be appreciated by the naked eye. The field of radiomics focuses on the extraction of quantitative features from digital images [9], which converts them into useful data. The driving hypothesis is that these features reflect the underlying biology but are imperceptible through the traditional visual inspection of current radiological practice.

2.4. Dosiomics

Dosiomics: denotes extracting 3D spatial features from dose distribution to predict incidence of e.g. radiation pneumonitis [9].

3. Medical physics for external radiation therapy

Radiation therapy is rapidly developing towards personalised and precision treatments. The use of multi-modality imaging in radiation therapy is increasing significantly. It is an important task to optimise these images – for treatment planning, for image-guided radiotherapy, for monitoring the motion during treatment and for response evaluation [3]. Three-dimensional conformal radiotherapy (3DCRT), intensity-modulated radiotherapy (IMRT), stereotactic radiotherapy, image-guided radiotherapy (IGT) and particle therapy have facilitated tumour delineations and dose delivery. Today modulated radiation treatment techniques are used for both photon and particle beam irradiations. The most common technique today is volumetric modulated arc therapy (VMAT) delivered with high energy photon beams or proton pencil beam scanning [11]. The introduction of modulated treatment techniques has for some patient groups been revolutionising, e.g. for those with head and neck cancer and cancer in the pelvic region [12]. The modulated techniques are however associated with an increased treatment complexity and a larger uncertainty in the delivered dose distribution to the patient compared to the conventional treatment technique [12]. An important task is to evaluate and reduce the absorbed dose uncertainty for modulated radiation therapy. A reduced dose uncertainty makes it possible to improve the quality of the treatments to enable a higher degree of individual adaptation and optimisation and to increase the quality of clinical trials [13].There is however still a need to improve target volume definition and also to explore the possibilities of artificial intelligence (AI) and automation [4]. The continued development and increasing use of "high-tech" precision radiation therapy has led to an increased need for the involvement of medical physics in radiation oncology.
Today there is also a need to combine the different medical physics disciplines, which means that cooperation between the different sub-fields of medical physics (therapy, different imaging methods, radiation safety) is more crucial than ever. The recent combination of MR scanners with treatment machines (MR-Linacs) is a perfect illustration of this and has pushed the integration of imaging and treatment further, enabling simultaneous visualisation and treatment of the target [14]. Recently an on-line ionising radiation acoustic imaging system has been developed, which directly images the absorbed dose distribution inside the patient

without interfering with the treatment delivery [10]. The acoustic waves stem from the absorption of pulsed ionising radiation beams in soft tissues.

4. Comments to some other lines of development

4.1. Improved measurements and calculations of absorbed dose.

At present, applied techniques in RT can deliver a dose distribution with a high conformity and precision to the treatment target volume. It is noteworthy that any error or inaccuracy in dose delivery during irradiation in these modern techniques can result in either an insufficient dose to the tumour tissue or a high dose to the adjacent healthy tissue. Hence, the determination of the 3D dose distribution in a tissue-equivalent material, before radiotherapy, can decrease any potential error. Owing to this, developing high-performance systems capable of coping with the challenging requirements of modern ionising radiation is a key issue to overcome the limitations of 1D and 2D conventional dosemeters.
In this scenario, "Gel dosimetry" is the most promising tools for the evaluation of 3D high-spatial-resolution dose distributions, and the studies regarding these materials represent the starting point for developing performance and innovative systems [15]. "Gel dosemeters" are based on chemical dosemeters in which radiation-induced chemical reactions occur. The addition of gelling agents reduces the diffusion of chemical reaction products and, consequently, the dosemeter is spatially stabilised. Gel dosemeters generally consist of two types: Fricke gels (FG) [6] and polymer gels [7]. In the first one, ferrous ions (Fe^{2+}) in ferrous sulphate solutions are dispersed throughout the gel matrix, while in the second one, monomers (such as acrylamide), are dispersed in the matrix. The radio-inducted variations can be read out by magnetic resonance imaging (MRI), x-ray computed tomography (CT), optical scanning, and ultrasonography.
An alternative is to use multi-layers of Gafchromic films in a stack of tissue equivalent material [16].

4.2 Adaptive/motion-compensated radiotherapy

4.2.1 Improved target volume definition.

Computed tomography (CT) has revolutionised external beam radiation therapy by making it possible to visualise and segment tumours and organs at risk in a three-dimensional manner. However, CT has some limitations in terms of tumour characterization and delineation. The situation can be greatly improved if PET and MRI are also used in a trimodality PET/CT/MRI imaging [17]. Trimodality can be performed either by fusing a PET/MRI to a planning CT or a PET/CT fused to an MRI. Trimodality imaging can be of great clinical importance, especially for the treatment of head and neck cancer, brain tumours, prostate cancer and cervical cancer [17].
4.3. FLASH radiation treatment
FLASH radiotherapy, which is defined as an ultra-fast delivery of radiation at absorbed dose rates several orders of magnitude greater than those used in conventional radiotherapy (40 Gy/s versus 0.5–5 Gy/min). Recent animal studies have shown that FLASH radiotherapy can reduce radiation-induced damage in healthy tissues [18]. Before FLASH can be used routinely in the clinic, the biomedical mechanisms behind the FLASH effect must be understood, demonstrating that it indeed reduces normal tissue toxicity, and its impact on medical personnel and instrumentation characterized.
For proton therapy, FLASH treatments may also prove beneficial by significantly increasing patient throughput, while improving treatment outcomes and reducing side effects.

4.4 Laser-driven accelerators

In the future, laser-driven accelerators may be a viable alternative to providing compact and cost-effective particle and photon sources. The accelerating field is a plasma, driven by intense laser pulses, and is typically several orders of magnitude larger than that of radiofrequency (RF) accelerators, while control of plasma media and intense laser pulses is very demanding. Therefore, many efforts have been directed towards developing compact, high-quality particle beams and radiation sources based on intense laser-plasma interactions, with the goal of paving the way for these new sources to be used in a variety of applications [19]. Using a laser-driven ion source could mark a radical new approach, reducing the transport and delivery costs of the ion beam.

5. Medical physics for imaging

Medical imaging, by means of radiology and molecular imaging, has become a foundation for diagnosis and therapy planning in numerous diseases that patients present with [20].

5.1. X-ray imaging

Advancements in the form of AI-aided x-ray interpretation, dual-energy imaging, tomosynthesis, computer-aided diagnosis, automatic merging of images, and digital mobile radiography continue. These advancements improve image quality, help to enhance patient care and support better patient outcomes. Photon counting detectors CT (PCD-CT) uses new, energy-resolving x-ray detectors to count the number of incoming photons and quantify photon energy. This technology results in reduced image noise, higher contrast-to-noise ratio, improved spatial resolution, reduced radiation dose, improved iodine signal, and a reduction in artefacts and optimised spectral imaging compared to conventional energy-integrating techniques [21]. The first photon-counting detector CT unit received clinical approval in 2021. This technology has already demonstrated impressive superiority over today's standard of CT imaging, particularly in high-resolution imaging of detailed structures and high-radiation-exposure examinations while creating opportunities for quantitative imaging. In radiology recent advances in the field of AI, including the development of high-performing artificial neural networks, robust ML algorithms, and powerful cloud-based computational capabilities, are being applied to the large amounts of

machine-readable digital data generated by radiology imaging studies and by electronic medical records, with the goal of creating applications that, once clinically validated, are expected to change the way the specialty of diagnostic radiology is currently practised.
In a recent investigation related to mammography screening, Lång at al., [22] found that using AI resulted in the detection of 20 % more cancers compared with standard mammography screening, without affecting the number of false positives.

5.3. Nuclear medicine

Today, much progress in nuclear medicine and molecular imaging lies in the new frontier in the field – theranostics - a term comprising both therapeutics and diagnostics [7]. Theranostics is used to describe the ability to combine a predictive biomarker with a therapeutic agent – e.g. a radioactive drug tagged to a receptor found on a tumour cell membrane to image the tumour cell and a therapeutic radionuclide (e.g., ^{177}Lu or ^{90}Y) tagged to the same receptor to target and kill the tumour cell.
Although theranostics is a new concept, the method is far from new and was developed more than 75 years ago using radioactive iodine for diagnostic imaging and for the treatment of malignant and benign thyroid diseases. In the 1980s, I-metaiodobenzylguanidine (I-MIBG), a noradrenaline analogue, was introduced in the diagnosis and treatment of neuroblastomas. However, it was not until radionuclide-labelled somatostatin analogues were used in the diagnosis and treatment of neuroendocrine neoplasia that the field of theranostics gained momentum [8]. Radionuclide therapy with a peptide receptor for neuroendocrine neoplasia has become an established treatment option for inoperable and metastatic disease. The success of radionuclide therapy with a peptide receptor has stimulated further development in theranostics, an example of which is the prostate-specific membrane antigen (PSMA). PSMA-PET/CT imaging has already been established for investigating biochemical recurrence of prostate cancer [8]. Systemic radiotherapy with Lu-PSMA-617 was approved by the US Food and Drug Administration in 2022 for patients with metastatic castration-resistant prostate cancer so now also this radiopharmaceutical can be used to diagnose and treat and to monitor the therapy effect.

5.4. MR imaging

Recent advances include higher field strength MRI systems, high-performance gradients, dedicated multichannel radiofrequency (RF) coils, and various innovative fast reconstruction algorithms [14].
Clinical MRI systems have been continually improved since their introduction in the 1980s. In MRI technical development, there are developments in each MRI system component, including data acquisition, image reconstruction, and hardware systems. Progress in each component has induced new technology developments in other components [23]. With high performance computing and MR technology innovations, MRI can now provide large volumes of functional and anatomical images alone or in combination with other imaging modalities, such as PET and also be combined with therapeutic equipment.
In nuclear medicine, opportunities for AI applications related to diagnosis, therapy, and workflow efficiency, as well as emerging challenges and critical responsibilities, were extensively reviewed recently [24,25]. MRI, which is an inherently slow slow process due to the high sampling requirements can be speeded up using undersampled images combined with AI reconstruction methods to enhance the quality of the scans taken [26] using AI-methods. Such methods can also be used to provide supportive tools for the more repetitive tasks associated with the MRI process.

6. Radiation safety

The current recommendations from the International Commission on Radiological Protection (ICRP) are from 2007 and ICRP has just finished the first phase of its work towards a review and revision of the recommendations. In the initial work, ICRP has identified some areas of research to support the System of radiological protection [27]. Views from inside ICRP [28] as well as from people outside ICRP [29] have been asked for and the results reported and discussed.
When it comes to radiation risk assessments, the reviews point to the need for:
1) Better characterization of tissue reactions,
2) Stochastic effects and radiation detriment,
3) Individual response of humans to radiation
4) Radiation effects on non-human biota. In the longer run, they point to the need for basic research and understanding of the effects of combined exposures.
Other requirements are:
1) Dosimetry in emergency situations,
2) Identification of dosimetric targets in organs and tissues, as well as
3) Dosimetric targets and methodology for the protection of the environment,
4) Biokinetic models for human tissues,
5) Development and use of radiation technologies (medical use implications, veterinary practice implications, NORM, natural sources),
6) Ecosystem protection,
7) Research needs for the application of the system of radiological protection (AI, social science, stakeholder involvement, communication),
8) Ethics, and
9) Behavioral science.

7. Education, training and research

The development in medical imaging and radiation oncology as well as in medical physics and technology is fast and impressive. In order to take advantage of all the opportunities that are now opening up, increased efforts from medical physics are needed. This means that there is a need for sufficient staffing, an in-depth collaboration between personnel from different areas and good training of new employees in the form of basic education and training as well as active research.

At its symposium in Vancouver in 2022 [30], ICRP called for action to strengthen expertise in radiological protection worldwide through:

• National governments and funding agencies strengthening resources for radiological protection research allocated by governments and international organisations,

• National research laboratories and other institutions launching and sustaining long-term research programmes,

• Universities developing undergraduate and graduate job opportunities in radiation-related fields,

• Using plain language when interacting with the public and decision makers about radiological protection, and,

• Fostering general awareness of radiation and radiological protection through education and training of information multipliers.

8. Conclusions

The field of medical physics is developing rapidly. The boundaries between medical physics specialties disappear in step with the increased use of imaging to guide the radiation therapy to obtain personalised and adaptive treatments. The increasing use of software and AI will change the role of medical physicists but the need for the skills of medical physicists will increase. They are also needed for the development of new technology and to ensure that the technology is understood and used correctly. The use of DL and AI will be essential parts of the future. However, the instantaneous image interpretation is the ultimate ambition of AI. Although AI technology has not yet achieved this ability in a broad sense, some example applications of these systems involve image segmentation, reconstruction, and disease registration. AI segmentation has the ability to automatically delineate structures and provide measurements such as organ volume or the surface area of a tumour. Taken a step further, these AI algorithms can hopefully be specialised to stage tumours and provide pre-interpreted read-outs such as scores for cancer staging. Automated segmentation and pre-interpreted read-outs may be maximally utilised in areas that have the most amount of data, such as screening imaging studies. It can be expected that the developments towards more and more individualised diagnostics and therapy will continue, which will require increased precision and accuracy in both radiotherapy and radiological diagnostics.

References

1. International Organisation for Medical Physics, IOMP, https://www.iomp.org/medical-physics/.

2. Mattsson S. Reflections on 60 years of development in medical physics and thoughts about the future. In: Medical Physics in the Baltic States, 13, 3-8, 2021.

3. ACPSEM, Australasian College of Physical Scientists & Engineers in Medicine. What do you see as the future for medical physics? https://www.acpsem.org.au

4. Fromherz M.R. and Makary M.S. Artificial intelligence: Advances and new frontiers in medical imaging. Artif Intell Med Imaging 3(2), 33-41, 2022. URL: https://www.wjgnet.com/2644-260/full/v3/i2/33.htm DOI: https://dx.doi.org/10.35711/aimi.v3.i2.33

5. Fiorino C., Jeraj R., Clark C.H., Garibaldi C., Georg D., Muren L., van Elmpt W., Bortfeld T. and Jornet N. Grand challenges for medical physics in radiation oncology. Radiotherapy and Oncology 153, 7–14, 2020.

6. Santoro M., Strolin S., Paolani G., Della Gala G., Bartoloni A., Giacometti C., Ammendolia I., Morganti A.G. and Strigari L. Recent applications of artificial intelligence in radiotherapy: Where we are and beyond. Appl. Sci., 12, 3223. 2022. https://doi.org/10.3390/app12073223

7. Haslerud T. and Revheim M.-E.R. Therapeutics + diagnostics = teranostics. Tidskrift for Den norske legeforening 143(1), 2023. doi:10.4045/tidsskr.22.0776.

8. Pini C., Gelardi F. and Sollini M. Present and future of target therapies and theranostics: refining traditions and exploring new frontiers - Highlights from annals of Nuclear Medicine. Editorial. European Journal of nuclear Medicine and Molecular Imaging 49, 3613–3621, 2022. https://doi.org/10.1007/s00259-022-05921-7

9. McCague C., Ramlee S., Reinius M., Selby I., Hulse D., Piyatissa P., Bura V., Crispin-Ortuzar M., Sala E. and Woitek R. Introduction to radiomics for a clinical audience. Review. Clinical Radiology 78, 83-98, 2023.

10. Zhang W., Oraiqat I., Litzenberg D., Chang, K.-W., Hadley S., Sunbul N.B., Matuszak M.M., Tichacek C.J., Moros E.G., Carson P.L, Cuneo K.C., Wang X. and El Naqa I. Real-time, volumetric imaging of radiation dose delivery deep into the liver during cancer treatment Nature Biotechnology Article https://doi.org/10.1038/s41587-022-01593-8

11. Koka K, Verma A, Dwarakanath B.S. and Papineni R.V.L. Technological advancements in external beam radiation therapy (EBRT): An indispensable tool for cancer treatment. Cancer Management and Research 14, 1421-1429, 2022. https://doi.org/10.2147/CMAR.S351744

12. Bäck A., Nordström F., Gustafsson M., Götstedt J. and Karlsson Hauer A. Complexity metric based on fraction of penumbra dose – initial study. Journal of Physics: Conference Series 2017, 847:012002. doi:10.1088/1742-6596/755/1/011001

13. Götstedt J., Karlsson A. and Bäck A. Evaluation of measures related to dosimetric uncertainty of VMAT plans. J Appl Clin Med Phys 24(4), 2023, e13862

14. Liu X., Li Z. and Yin Y. Clinical application of MR-linac in tumor radiotherapy: A systematic review. Radiation Oncology 18(1), 52, 2023. https://doi.org/10.1186/s13014-023-02221-8 PMID: 36918884; PMCID: PMC10015924.

15. Ceberg S., Adliene D. and Mattsson S. 3D polymer gel dosimetry for quality assurance in radiation therapy. In: Medical Physics in the Baltic States 13, 30-35, 2017.

16. Arab-Bafrani Z., Mahani L., Khoshbin-Khoshnazar A. and Zeinali A. Three dimensional film dosimetry of photon beam in small field sizes and beyond the heterogeneous regions using a GAFchromic films array. Radiation Physics and Chemistry 166, 2020, 108467 https://doi.org/10.1016/j.radphyschem.2019.108467

17. Decazes P., Hinault P., Veresezan O., Thureau S., Gouel P. and Vera P. Trimodality PET/CT/MRI and radiotherapy: A mini-review. Front Oncol 2021 10:614008. doi: 10.3389/fonc.2020.614008

18. Giuliano L., Franciosini G., Palumbo L., Aggar L., Dutreix M., Faillace L., Favaudon V., Felici G., Galante F., Mostacci A., Migliorati M., Pacitti M., Patriarca A. and Heinrich S. Characterization of ultra-high-dose rate electron beams with electronflash linac. Appl Sci 13, 631, 2023. https://doi.org/10.3390/app13010631

19. Kojima S. and Hata M. Laser-driven ion accelerator. In: Advances in accelerators and medical physics, Ed. by: Shirai T., Nishio T. and Sato K., AP 2023, pages 343-352.

20. Beyer T., Bailey D.L., Birk U.J., Buvat I., Catana C., Cheng Z., Fang Q., Giove F., Kuntner C., Laistler E., Moscato F., Nekolla S.G., Rausch I., Ronen I., Saarakkala S., Thielemans

K., van Elmpt W. and Moser E. Medical physics and imaging–A timely perspective. Front Phys 9, 2021, 634693. doi: 10.3389/fphy.2021.634693
21. Layer Y.C., Kravchenko D., Dell T. and Kütting D. CT-Technologie: photonenzählende Computertomo-graphie. Die Radiologie https://doi.org/10.1007/s00117-023-01166-z. 2023.
22. Lång K., Josefsson V., Larsson A.-M., Larsson S., Högberg C., Sartor H., Hofvind S., Andersson I. and Rosso A. Artificial intelligence-supported screen reading versus standard double reading in the mammography screening with artificial intelligence trial (MASAI): a clinical safety analysis of a randomized, controlled, non-inferiority, single-blinded, screening accuracy study. Lancet Oncology 24(3), 936-944, 2023.
23. Kabasawa H. An invited review for the special 20th anniversary issue of MRMS. MR imaging in the 21st century. Technical innovation over the first two decades. Magn Reson Med Sci. 21, 71–82, 2022. doi:10.2463/mrms.rev.2021-0011.
24. Visvikis D., Lambin P., Beuschau Mauridsen K., Hustinx R., Lassmann M., Rischpler C., Kuanguy S.and Pruim J. Application of artificial intelligence in nuclear medicine and molecular imaging: A review of current status and future perspectives for clinical translation. Eur J Nucl Med Mol Imaging 49, 4452–4463, 2022.
25. Hustinx R., Pruim J., Lassmann M. and Visvikis D. An EANM position paper on the application of artifcial intelligence in nuclear medicine. European Journal of Nuclear Medicine and Molecular Imaging 50, 61–66, 2022.
26. Johnson P.M., Recht M.P. and Knoll F. Improving the speed of MRI with artificial intelligence. Semin Musculoskelet Radiol 24(1), 12–20, 2020. doi:10.1055/s-0039-3400265
27. Laurier D., Rühm W., Paquet F, Applegate K., Cool D. and Clement C., on behalf of the International Commission on Radiological Protection (ICRP). Areas of research to support the system of radiological protection. Radiat Environ Biophys 60, 519–530, 2021. www.doi.org/10.1007/s00411-021-00947
28. Clement C., Rühm W., Harrison J., Applegate K., Cool D., Larsson C.-M., Cousins C., Lochard J., Bouffler S., Cho K., Kai M., Laurier D., Liu S., and Romanov S. Keeping the ICRP recommendations fit for purpose. J Radiol Prot 41, 1390-1409, 2021. www.doi.org/10.1088/1361-6498/ac1611
29. Rühm W., Clement C., Cool D., Laurier D., Bochud F., Applegate K., Schneider T., Bouffler S., Cho K., Hirth G., Kai M., Liu S., Romanov S. and Wojcik A. Summary of the 2021 workshop on the future of radiological protection. J Radiol Prot 42, 2022, 023002 www.doi.org/10.1088/1361-6498/ac670e
30. Rühm W., Cho K., Larsson C.-M., Wojcik A., · Clement C., Applegate K., Bochud F., Bouffler S., Cool D., Hirth G., Kai M., Laurier D., Liu S., Romanov S. and Schneider T. Vancouver call for action to strengthen expertise in radiological protection worldwide. Radiation and Environmental Biophysics 62, 175–180, 2023. https://doi.org/10.1007/s00411-023-01024-5

MEDICAL PHYSICS IN THE BALTIC STATES 16 (2023)

Proceedings of International Conference "Medical Physics 2023"
09-11 November 2023, Kaunas, Lithuania

TWENTY YEARS OF MEDICAL PHYSICS EDUCATION IN LITHUANIA

Diana ADLIENĖ[1], Sören MATTSSON[2]
[1]Department of Physics, Kaunas University of Technology, Kaunas, Lithuania
[2]Lund University, Medical Radiation Physics, ITM, Skåne Univ. Hospital, Malmö, Sweden
diana.adliene@ktu.lt

***Abstract*:** MSc studies in Medical Physics were established in 2003 and have been successfully carried out for 20 years at Kaunas University of Technology providing programme graduates with the opportunity to continue their career in radiation therapy, diagnostic imaging, nuclear medicine, or radiation protection. KTU program Medical Physics is aligned with international guidelines set by EFOMP, IOMP, and IAEA and is highly focused on clinical training and research. It is one of the few programs in Europe (except the UK) delivered in English. More than 100 programme graduates are daily contributing to the provision of high-quality health care services based on applications of ionizing radiation.
This article presents upgraded information provided in [1] and aims to record progress in the education & training of medical physicists in Lithuania during the last 20 years. It also highlights the R&I achievements of Lithuanian medical physicists.

Keywords: medical physicists; education, training, and recognition of MP; contribution of MP to R&I in the field.

1. Background

In 1995, the newly established Lithuanian Society of Radiation Therapy indicated an urgent need to have properly educated medical physicists in at least radiotherapy departments in Lithuania [2] and dedicated initiation of regular medical physicists' education and training in Lithuania to the Medical Physics Committee represented by medical radiation workers of Oncology institute and Kaunas Medical University Clinics.
Despite the efforts of the MP Committee, the situation did not change until a new player – Kaunas University of Technology – came to the scene via participating in the EU TEMPUS PROGRAMME Project S_JEP-12402-97 (project coordinator at KTU – prof. Arūnas Lukoševičius). The main objective of this project was the development of a new Joint Baltic Medical Engineering and Physics Master's programme (JBMEP), which provides common education and training in medical engineering and medical physics in Lithuania, Latvia, and Estonia. Even though the developed curriculum of the joint Baltic MSc programme was never realized (due to the differences in legal requirements for education and training in three Baltic countries), it inspired a new step for the development of medical physicists' education & training and their recognition strategy in Lithuania which was elaborated following EFOMP recommendations in the frame of the National Radiation Protection program (2001-2005) (Table 1).

Table 1. Career scheme for medical physicists in Lithuania (2003)

<table>
<tr><th>Level</th><th>Actual scheme</th><th>New scheme</th><th>EFOMP</th></tr>
<tr><td>1</td><td colspan="3">B.Sc. In physics, engineering or equal, 4 years</td></tr>
<tr><td rowspan="2">2</td><td>Professional work in the hospital or hospital environment</td><td>M.Sc. in medical physics, KTU, 2 years</td><td rowspan="3">Post-graduate training:
Theoretical part
(300-400 hrs)
Practical part
(min 2 years professional work)</td></tr>
<tr><td colspan="2">MEDICAL PHYSICIST</td></tr>
<tr><td rowspan="3">3</td><td>On the job training (min 2 years), theoretical studies and training courses</td><td rowspan="2">Continuous post-graduate studies, KMU, 2 years</td></tr>
<tr><td>Qualification exam as medical physicist</td><td rowspan="2">QUALIFIED MEDICAL PHYSICIST</td></tr>
<tr><td colspan="2">LICENSED MEDICALPHYSICIST</td></tr>
<tr><td rowspan="2">4</td><td colspan="3">Continuous professional development, 5 year cycle time, credit point system</td></tr>
<tr><td colspan="3">MEDICAL PHYSICS EXPERT</td></tr>
</table>

It should be noted that the profession of medical physicist was approved by the Ministry of Health of the Republic of Lithuania in 1992. Implementing the guidelines of EC Directive 1997/43/Euratom [3], hospitals having radiotherapy and radiology departments were forced to employ a number of "medical physicists" without adequate education and training. Increasing numbers of modern installations in radiotherapy / radiology departments and new patient treatment and diagnostic methods were challenging for the existing "medical physicists" staff as deeper specific knowledge in the field of medical physics was required. The only possibility to overcome this problem was to start the education and training of medical physicists at the university MSc level, creating additional possibilities for education and retraining of the staff employed in the hospitals as medical physicists.

2. MSc study program Medical Physics

Education of medical physicists at the MSc level (7th level of the European Qualification Framework) was started at Kaunas Technological University (program leader – prof. Diana Adlienė) in collaboration with Kaunas Medical University (program leader - prof. Elona Juozaitytė) in 2003, strictly following the recommendations of international authorities, EFOMP, IOMP, and IAEA. A valuable contribution to the successful opening and development of this study programme was the establishment of the Dosimetry laboratory at Kaunas University of Technology, which was financed by the Swedish Government and also supported by colleagues from Lund University, Malmo University Hospital (prof. Sören Mattsson) and King's College London (prof. Slavik Tabakov).

The main goal of this two-year programme was and is to educate and train medical physicists for the healthcare institutions where ionizing radiation technologies are applied for the diagnosis and treatment of patients. Besides, medical physicists are additionally trained to work as radiation protection officers.

The MSc study programme in Medical Physics has been successfully implemented over the years at KTU and is unique to Lithuania.

There were attempts to run another MSc study programme "Medical Physics" at Vilnius University (VU) in 2010-2015, but due to the limited number of highly qualified teachers in the field in Lithuania and some discrepancies of the program curriculum as compared to international recommendations, this program was closed.

It should be noted that the number of students in different programs is regulated by the Ministry of Education, Science, and Sports of the Republic of Lithuania. The quota per intake for the study programme Medical Physics is 6-8 students. Despite the quotation, the successful implementation of medical physicists' education and training at Kaunas University of Technology, already in 2010 allowed to achieve, that more than 50% of the staff employed as medical physicists at the hospitals had MSc degree in Medical physics (Fig. 1) [4].

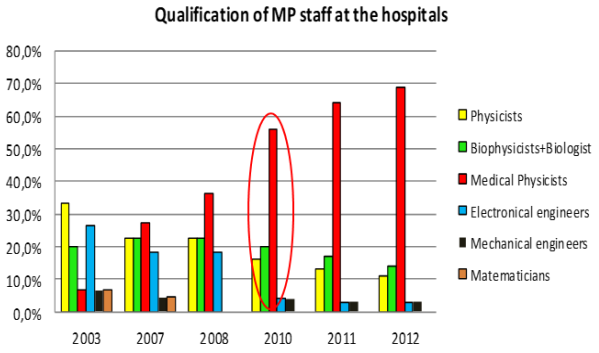

Fig. 1. Qualification of staff employed as medical physicists in the Lithuanian healthcare institutions.

The total number of Lithuanian graduates from the MSc study program Medical Physics is 125: 102 graduates from KTU and 23 graduates from VU (as of the year 2023).

Since the courses are given in English, the study programme is attractive to foreign students. Program graduates and students were/are from different countries, including Japan, Germany, India, Pakistan, Nepal, Iran, Iraq, Turkey, Bulgaria, Canada, UK, Egypt, Portugal, France, Spain, Lebanon, Georgia, Serbia, Nigeria, Venezuela, and Sudan. The realization of a so-called "clinical semester" in the frame of the programme, during which the students perform their practical and research work mainly in the clinical environment, and the implementation of the innovative challenge-based learning mode in the studies contributed significantly to making this programme relevant for covering country's demand on MP specialists and also supported the integration of Medical physics program graduates in clinical teams, since officially recognized clinical training program for medical physicists in Lithuania does not exist at the moment.

The majority of program graduates are employed in the health care system of Lithuania. The dynamics of the employment of MP programme graduates, which is one of the highest in Lithuania, is presented in Fig. 2.

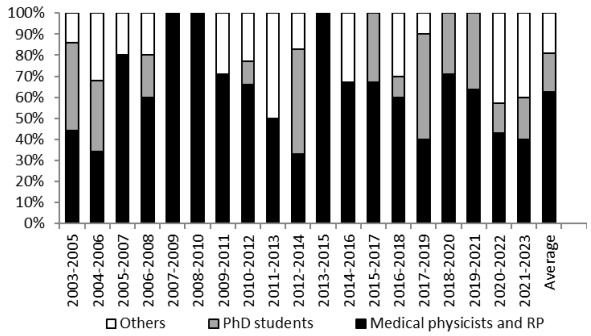

Fig.2. Employment of KTU MSc programme Medical Physics graduates

Due to a very strong involvement of the KTU Research group "Radiation and Medical Physics" led by Prof. Diana Adlienė and researchers from different Clinics during the preparation of MSc thesis by the programme students, a relatively large number of medical physics graduates are choosing PhD studies. There is no PhD programme in Medical Physics in Lithuania due to the lack of professors in this field, however, there are possibilities for programme graduates to enter PhD studies in Physics or Materials engineering and work on topics related to the medical physics field: dosimetry (materials, methods, and devices), phantoms and immobilization devices (materials), modeling of radiation-induced processes in materials, etc. It is remarkable, that almost every year some programme graduates enter PhD studies.

Of course, the majority of programme graduates enter the clinical environment as medical physicists or are employed as radiation protection officers and only a few of them are choosing different pathways for their careers.

Medical physicists are working in 5 Oncology centers in Lithuania: National Cancer Institute, Vilnius University Hospital "Santaros" Clinics, Hospital of Lithuanian University of Health Sciences Kaunas Clinics with a

branch Hospital of Oncology, Klaipėda University Hospital, Šiauliai Republican Hospital, and almost in all medical institutions that are using ionizing radiation technologies. It should be mentioned, that They are involved in the preparation of dose treatment plans for patients, implementation of QA measures, and performance of QC tests; they are operating 12 linear accelerators, 5 HDR/LDR brachytherapy units, 3 X-ray therapy units, 1 Gamma knife facility, and also are carrying out QC measurements and performing equipment calibration in various radiology departments or performing their duties working with two 2 PET/CT units. It is worth pointing out that a new MRI-Linac will start its operation this year and the installation of a medium-energy cyclotron reached its final stage where the involvement of medical physicists will be very important.

Since there is no one particle therapy center in the Baltic region, the CERN-Baltic group (CBG) has established a special working group "Advanced Particle Therapy Center in the Baltic States" (deputy convener – prof. Diana Adlienė) which has the mandate to develop and induce CBG flagship project: construction of a large scale clinical particle therapy and scientific research facility in the Baltic States in close collaboration with the experts from CERN Next Ion Medical Machine Study (NIMMS) group, which is developing a new type synchrotron which will provide ^{4}He ions for patient treatment. When implemented, particle therapy will require specific knowledge of medical physics

In parallel to this, Erasmus Mundus project related to the designing of the "European Master in [high-energy particle] Physics and Accelerator Technologies for Research and Industry" is running, where some specific courses for medical physicists are foreseen.

3. National recognition scheme of medical physicists' profession

With the successful implementation of MSc studies, the knowledge and skills gained by programme graduates raised a question regarding inadequate professional recognition of medical physicists among healthcare workers and their role in clinical work. Following ILO (2008) recommendations it was suggested that MP profession should be assigned to the group of physicists working in the medical environment. However, the profession of MP in Lithuania was often misinterpreted, assigning medical physicists to supporting staff or engineers in the clinic.

With the establishment of the National Medical Physicists Society in 2007 it was decided to initiate the development of a national strategy for the recognition of medical physicists, as medical professionals working in the clinical environment. The idea was supported by the Radiation Protection Centre, Kaunas University of Technology, and Vilnius University and a working group was created at the Ministry of Health of the Republic of Lithuania. The newly established representative Lithuanian Association of Medical Physics and Biomedical Engineering joined the working group by the end of 2008. It took 10 years until 2017 to get an officially approved National Registration Scheme which defines the requirements and procedures for the recognition of medical physicists in Lithuania (Table 2) [5].

Table 2. National Recognition Scheme of Medical Physicists in Lithuania

Junior Medical Physicist
4 years of BSc studies in physical, biomedical, technological sciences + 2 years of MSc studies in Medical physics. Working in clinical environment is allowed under supervision of medical physicist specialist (MPS) or Medical physicist expert (MPE)
Medical Physicist Specialist
2 years working experience in clinical environment under supervision of MPS and MPE and clinical training and research. After obtaining MPS in one of fields of medical physics (radiotherapy, imaging and diagnostic, nuclear medicine, lasers and non-ionizing radiation), MPS in another field can be awarded after one year of clinical training in relevant field. When the requirements are fulfilled, MPS is recognized as a person who is legible for license of work in the ionizing radiation environment.
Medical Physicist Expert
At least after 3 years of clinical work as MPS in a selected field + at least 100 hours of professional training, + minimum of 200 hours of participation in research and teaching experience. The expertise of MPE shall be approved by State Commission for Recognition of medical physicist expert. Re-certification of MPE is mandatory every 5 years following the procedures set by Radiation Protection Centre of Lithuania.

All requested achievements for obtaining any Medical Physicist's category must be approved by corresponding documents. The qualification of Junior Medical Physicist and Medical Physicist Specialist in one or more areas is assigned to a person for a life-long period, however, the Medical Physics Expert category may be withdrawn if the person fails during the re-certification procedure, which is mandatory every 5th year.

The responsibility for registration of Medical Physicists as persons working in an ionizing radiation environment is delegated to the Radiation Protection Centre, which maintains a National Register of the sources of ionizing radiation and occupationally exposed persons.

Despite the strict regulation, a little confusion remains when speaking about the profession of Medical Physicists. In general, medical physics studies are assigned to the study direction "Medical technologies", which covers both, medical and physics fields; however, according to the diploma, programme graduates are Masters of Health Sciences.

Since 2020, MP programme graduates as health professionals, are obliged to apply for the individual stamp at the State Accreditation Service for Health Care Activities under the Ministry of Health, before they are allowed to provide health care services [6]. In this way, they are included in the database of healthcare workers in Lithuania, but under the category "Other healthcare workers", which does not reflect the real complexity of competencies and responsibilities of MP in clinical work.

4. R&I in the medical physics field

Members of the KTU research group "Radiation and Medical Physics" are the main drivers of the ideas and R&I activities in the medical physics field. With the contribution of PhD students who are already working as medical physicists in oncology centers and hospitals in Lithuania and with the help of medical physics students several important projects have been implemented, and new methods and devices were developed in order to optimize patient treatment. The most important achievements of KTU medical physicists are outlined below:

- pioneering in introducing gel dosimetry for dose verification in radiotherapy in Lithuania and working on radiation sensitivity enhancement of polymer gels (Dr. Neringa Šeperienė, PhD student Mantvydas Merkis, and Dr. Judita Puišo);
- development of *in vivo* dosimetry method in HDR interstitial catheter-based brachytherapy (MSc Karolis Jakštas and Dr. Evelina Jaselskė);
- pioneering in suggesting the application of dose gel filled catheters as dosimeters for the assessment of dose distribution in brachytherapy procedures (Dr. Diana Adlienė);
- proposing and implementing ionizing radiation-based 3D printing concept and creation of free-standing gel structures mimicking irradiated tumors (Dr. Diana Adlienė, MSc Karolis Jakštas, Dr. Jurgita Laurikaitienė and Dr. Evelina Jaselskė);
- development of 3D printed personalized equipment (phantoms, boluses) for dose verification in radiotherapy (Dr. Jurgita Laurikaitienė, Dr. Benas Gabrielis Urbonavičius, PhD students Mindaugas Ilickas and Antonio Jreije);
- development of personalized Lego-type phantoms for dose verification (Dr. Benas Gabrielis Urbonavičius, Dr. Jurgita Laurikaitienė, PhD student Aleksandras Ševčik and Dr. Diana Adlienė);
- development of lightweight lead-free shielding equipment (PhD student Laurynas Gilys);
- and many others.

It should be noted, that the above-indicated contributors are members of the research group "Radiation and Medical Physics", but in total all these achievements would not be possible without close collaborations between KTU departments and medical institutions and also contributions from the international partners (Fig.3).

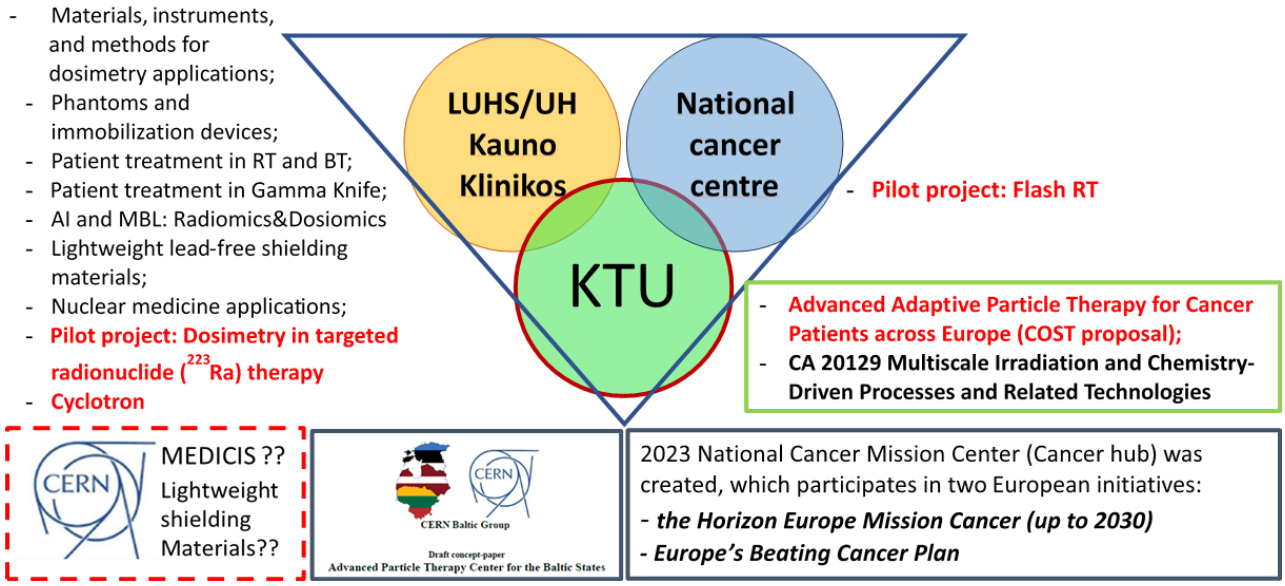

Fig.3. Recent collaborations of KTU research group "Radiation and Medical Physics".

References

1. Adliene, D.; Laurikaitiene, J. Medical physicists in Lithuania in the 21st century // Medical physics international. York: International organization for medical physics. ISSN 2306-4609. 2021, vol. 9, Iss. 2, p. 158-161.
2. Atkočius V. and Vaitkus A. Medical Physics in Europe and in Lithuania// in Medical Radiation Physics - A European Perspective/Ed. C.Roberts, S.Tabakov, C.Lewis. London, 1995.
3. EC Directive 1997/43/Euratom of 30 June 1997 on health protection of individuals against the dangers of ionizing radiation in relation to medical exposure. Official Journal L 180, 09/07/1997, pp. 0022 - 0027.
4. Adlienė, Diana; Adlys, Gediminas Antanas. Status of medical physicists in Lithuania // Medical Physics in the Baltic States: Materials of IAEA Seminar & Workshop RER/0/028 9007 01 "Synergy of nuclear sciences and medical physics: education and training of medical physicists in the Baltic States", Kaunas, Lithuania, 22-24 September 2010/Kaunas University of Technology. Kaunas: Technologija. ISSN 1822-5721. 2010, no. 1, p. 32-35.
5. Order of the Minister of Health Nr. V-901 (24-07-2017) regarding the approval of medical physicists' activities.
6. Order of the Minister of Health Nr. V-951 (22-04-2020) m. Nr. V-951. On the approval of rules for granting and withdrawing a specialist's stamp number

MEDICAL PHYSICS IN THE BALTIC STATES 16 (2023)

Proceedings of International Conference "Medical Physics 2023"
09-11 November 2023, Kaunas, Lithuania

PATIENT RADIATION EXPOSURE IN PEDIATRIC INTERVENTIONAL RADIOLOGY AT VILNIUS UNIVERSITY HOSPITAL SANTAROS KLINIKOS

Leonid KRYNKE[1], Antonio JREIJE[1,2], Kirill SKOVORODKO[1], Birutė GRICIENĖ[1,3,]
[1]Vilnius University Hospital Santaros Klinikos, Vilnius, Lithuania; [2]Department of physics, Kaunas University of Technology, Kaunas, Lithuania; [3]Department of Radiology, Nuclear medicine and Medical physics, Faculty of Medicine, Vilnius University, Vilnius, Lithuania.
leonid.krynke@santa.lt; antonio.jreije@ktu.edu; kirill.skov@gmail.com; birute.griciene@santa.lt

***Abstract*:** Pediatric interventional radiology is a fast-growing subspecialty which comprises minimally invasive procedures for the diagnosis and treatment of congenital and acquired conditions. The aim of this study was to evaluate patient radiation doses in pediatric interventional radiology for routinely performed cardiac procedures. Data were retrospectively collected for seven interventional procedures during a two years period. The median was calculated for kerma area-product, cumulative air kerma at patient entrance reference point and fluoroscopy time for four age groups. The results indicate that establishing DRLs pediatric interventional procedures can be challenging due to small number of data.

Keywords: Patient dose assessment, Pediatric interventional radiology, Radiation dose, Pediatric

1. Introduction

Fluoroscopy-guided interventional procedures have seen an increased usage for pediatric patients in recent times. Pediatric cardiac catheterization expended from mainly a diagnostic tool to a therapeutic modality that has notably enhanced the prognosis of individuals with congenital heart abnormalities. As per a recent report, the global frequency of image-guided interventional procedures has experienced a significant increase between 2008 and 2018 [1]. This trend is particularly pronounced in high-income nations, where the increase was over six times. The same report also highlights that up to 32% of all cardiac angiographies are conducted in pediatric patients [1].

Organs and tissues in children are more sensitive to the effects of ionizing radiation, raising concern for a higher risk of developing malignancies due to diagnostic medical radiation exposure [2]. Furthermore, children have a longer lifespan during which long-term effects such as neoplasms can develop [2]. The UNSCEAR report highlights that the lifetime cancer risk for those exposed during childhood remain uncertain and could be 2–3 times greater compared to estimates for a population exposed at all stages of life [3]. The principle of "as low as reasonably achievable" (ALARA) prioritizes minimizing radiation dosage while maintaining acceptable image quality [4]. As a result, it is important to optimize programs for radiation safety, dose characterizing, x-ray image quality, and patient doses measurement for diagnostic and therapeutic interventional procedures in the pediatric population.

The new Council Directive 2013/59/Euratom mandates Member States to set up Diagnostic Reference Levels (DRLs) and broadens their scope to cover interventional radiology (IR) procedures [4]. Despite this legal requirement and the significant concerns surrounding pediatric radiation exposure, there is an absence of national DRLs specifically addressing Pediatric Interventional Radiology (PIR) procedures. Notably, the recently issued European Guidelines on DRLs for pediatric imaging emphasize that no European DRLs could be formulated for non-cardiac interventional procedures in the pediatric context, primarily due to the absence of any existing DRLs, whether at the local or national level [5].

Given the substantially higher radiation doses associated with PIR in comparison with conventional radiology, coupled with the heightened radio sensitivity of pediatric patients, the establishment of DRLs within the realm of PIR becomes an imperative. A major challenge in the pediatric context arises from the scarcity of available data due to the relatively fewer performed procedures. Moreover, the limited data that is collected is often categorized based on weight or age groups, which complicates the accumulation of sufficient information required for setting local DRLs.

The aim of this study was to evaluate patient radiation doses in PIR for routinely performed cardiac and non-cardiac procedures at Vilnius University Hospital Santaros Klinikos.

2. Materials and Methods

Data collection was carried for seven interventional procedures performed in two interventional operating rooms at Vilnius University Hospital Santaros Klinikos for a two-year period ranging from March 2021 until March 2023. Almost 95% of all pediatric interventional procedures were performed using Shimadzu Trinias B12 which is a biplanar system equipped with two X-ray tubes. Information about used fluoroscopy equipment including manufacturer, model and year of installation are presented in Table 1.

Table 1. Angiography systems information.

Manufacturer	Model	Installation year
Shimadzu	Trinias B12	2017
Philips	Allura Xper FD20	2018

For each examination, patient-related and dosimetry related data were collected: procedure type, kerma area-product (P_{ka}), cumulative air kerma at patient entrance reference point ($K_{a,r}$) and total fluoroscopy fime (FT) as well as patient age. Data was further sub-divided into four age groups: <1; 1 to <5; 5 to <10; 10 to <18 years. Patient doses were evaluated for the following procedures: Patent ductus arteriosus (PDA), Transcatheter pulmonary valve replacement (TPVR), Percutaneous balloon pulmonary valvuloplasty (BPV), Coarctation of the Aorta (CoA) balloon angioplasty and/or stenting, Atrial septal defect (ASD), Percutaneous balloon aortic valvuloplasty (BAV), Pulmonary artery (PA) balloon angioplasty and/or stenting. The median of the distribution of P_{ka}, $K_{a,r}$ and FT was calculated for procedure types and age ranges for which a sample of ≥ 10 patients could be gathered.

The Mann–Whitney test (95% confidence level) was used to compare the values of Pka and FT between pairs of procedures. Values of $p < 0.05$ were considered statistically significant. The tests were performed with the software "SPSS Statistics".

3. Results and discussion

During the 2 years period included in this study, pediatric procedures accounted for a very small percentage (approximately 10%) of all interventional procedures performed. Figure 1. show the number of data collected for each type of procedures. In total 168 procedures were included. It should be noted that 14 pediatric records lacked dose information and therefore were excluded from the study.

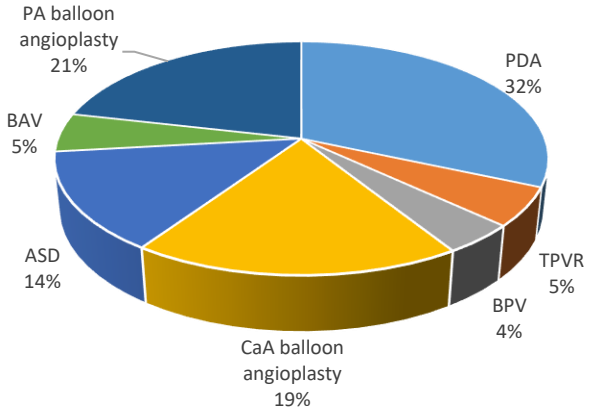

Fig. 1. Number of pediatric procedures performed between March 2021 and March 2023 classified by type of intervention.

As it can be seen, Patent ductus arteriosus (PDA) (32%) was the most performed procedure followed by Pulmonary artery (PA) balloon angioplasty and/or stenting (21%) and Coarctation of the Aorta (CoA) balloon angioplasty and/or stenting (19%) (Table 2). On the other hand, Transcatheter pulmonary valve replacement (TPVR), Percutaneous balloon aortic valvuloplasty (BAV), and Percutaneous balloon pulmonary valvuloplasty (BPV) are not very common procedures in the pediatric population with a total of 7 patient undergoing BPV, and 9 patient receiving TPVR and BAV. An overview of the 168 collected data sub-divided into four different age groups is presented in Table 3.

Radiation dose-related parameter reported as median, minimum and maximum value of $K_{a,r}$ (mGy), P_{ka} ($Gy{\cdot}cm^2$) and FT (min) for each procedure are summarized in Table 3. As can be seen, the doses and fluoroscopy time varied between different procedure types.

Table 2. Number of procedures performed over a 2-year period classified by type of procedure and age range (year).

Procedures	Age (year)				Total
	<1	1 - <5	5 - <10	10 - <18	
Patent Ductus Arteriosus PDA	7	19	14	13	53
Transcatheter Pulmonary Valve Replacement (TPVR)	0	0	2	7	9
Atrial Septal Defect (ASD)	0	1	8	14	23
Coarctation of the Aorta (CoA) balloon angioplasty and stenting	13	6	7	5	31
Pulmonary artery (PA) balloon angioplasty and/or stenting	7	26	1	2	36
Percutaneous balloon aortic valvuloplasty (BAV)	6	3	0	0	9
Percutaneous balloon pulmonary valvuloplasty (BPV)	2	4	0	1	7

The difference in doses is especially significant between PA balloon angioplasty and the other procedures (median kerma area-product for PA balloon angiography was ~ 2 time higher than CoA balloon angioplasty and/or stenting and up to ~ 6 time higher than ASD). No statistically significant difference was only seen between PDA and CoA balloon angioplasty and/or stenting (p-value = 0.175). Similarly, the median FT for PA balloon angiography was two to three times higher than CoA balloon angioplasty and/or stenting, PDA and ASD respectively. For FT, no statistically significant difference was observed between PDA and CoA balloon angioplasty and/or stenting (p-value = 0.099) as well as between ASD and PDA (p-value = 0.426).

In this study, Only Patent ductus arteriosus (PDA) procedure was sub-grouped into 3 three age groups. As can be seen from Table 3 and figure 2, the median patient dose and median fluoroscopy time increased with increasing age group. Mann Whitney U test revealed statistically significant different between age groups for kerma area-product except between 1 - <5 and 5 - <10 (p-value = 0.057. For fluoroscopy time, there was no statistically significant difference between any of the age groups.

Few challenges were encountered during this work and are as follow. First, the number of PIR procedure are extremely limited, leading to difficulties in establishment of DRLs for the pediatric population on a local level since European Guidelines on DRL for pediatric imaging recommend a sample of ≥ 20 patients [5]. This is a common problem faced by all heal care facilities and countries since very few data concerning DRLs in pediatric interventional radiology and cardiology are published. Additionally, the existing studies vary significantly in their methodologies and the information provided, making comparison between them challenging.. A literature review demonstrates that DRLs for pediatric interventional procedures have not yet been established on a regional level anywhere in the world except in Latin America and the Caribbean countries where preliminary regional DRLs were published [6-8]. In addition, the European Guidelines on DRLs for pediatric imaging released in 2018 did not include DRLs for pediatric interventional cardiology procedures [5]. Therefore, cooperation between different institutions and countries is needed for this matter in order to reach a pool of data for proper setting of DRLs.

The grouping of patients seems to be another problem as it is completely different between studies while being based on age or weight groups. During data collection for this study, patient records encountered did not include weight and height information and therefore, DRLs were age-stratified. It should be noted that ICRP Publication 135 recommend that pediatric DRL should be categorized by weight, while suggesting the use of age-based categorization as an alternative in case of unavailability of patient weight data [9]. Therefore, weight-based grouping will be considered in future follow-up studies on patient doses in PIR and setting local DRLs.

Another limitation is the difference in the methodology used for setting DRLs since most previous publications divided interventional procedures into two categories: diagnostic and therapeutic procedures due to the small number of data and difference in nomenclature used in the different hospitals [9-11]. This grouping follows the assumption that therapeutic interventions are more complex and take a longer procedural/fluoroscopy time and incur a higher radiation dose than diagnostic procedures.

Table 3. Radiation dose indicators for each procedure stated as the median, minimum and maximum value.

Procedures	Patient Number	Ka,r (mGy)			P_{ka} (Gy.cm^2)			FT (min)		
		Median	Min	Max	Median	Min	Max	Median	Min	Max
Combined procedures										
Total	168	66.21	3.17	3341.6	4.40	0.26	326.0	8.25	1.90	79.2
<1	35	31.00	9.30	415.1	1.35	0.26	17.3	9.09	2.75	79.2
1 - <5	59	72.40	11.55	526.8	4.57	0.70	29.3	10.12	1.90	58.9
5 - <10	32	59.12	9.50	224.8	3.70	0.58	12.8	7.18	2.21	34.1
10 - <18	42	241.19	3.17	3341.6	13.00	0.30	326.0	7.46	2.20	68.4
Patent Ductus Arteriosus PDA										
Total	53	48.98	11.88	489.6	2.65	0.70	32.4	6.55	1.90	37.0
1 - <5	19	34.15	14.43	105.9	1.38	0.70	6.1	4.66	1.90	13.2
5 - <10	14	54.45	29.34	224.8	3.23	1.50	12.8	5.75	2.34	30.0
10 - <18	13	277.90	11.88	489.6	17.33	1.60	32.4	7.44	2.29	37.0
Atrial Septal Defect (ASD)										
Total	23	25.70	3.17	300.2	3.15	0.31	27.0	5.40	2.20	39.9
10 - <18	14	39.05	3.17	300.2	3.41	0.31	27.0	5.34	2.20	39.9
Coarctation of the Aorta (CoA) balloon angioplasty and/or stenting										
Total	31	83.70	17.50	1668.8	3.92	0.70	95.2	7.70	2.75	58.9
<1	13	33.40	17.50	179.2	1.35	0.70	16.8	6.40	2.75	16.8
Pulmonary artery (PA) balloon angioplasty and/or stenting										
Total	36	155.07	9.30	415.1	9.51	0.72	54.1	16.33	3.77	79.2
1 - <5	26	158.72	16.38	393.4	9.51	4.25	29.3	19.28	3.95	48.6

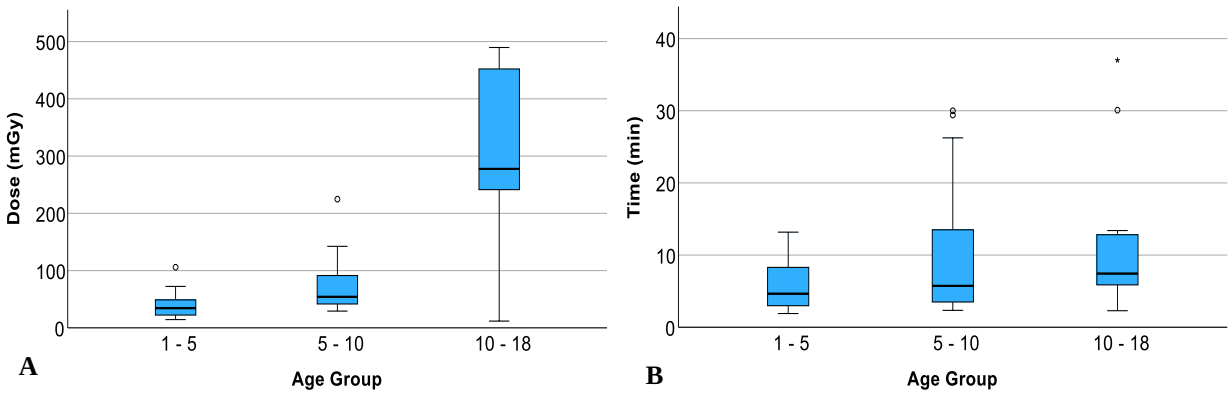

Fig. 2. Comparison of median $K_{a,r}$ [A] and median FT [B] between different age groups for Patent Ductus Arteriosus.

According to the European Guidelines on Diagnostic Reference Levels for Pediatric Imaging, creating a generic DRL encompassing all diagnostic or therapeutic procedures might not be suitable [5]. Especially for therapeutic procedures, the considerable variation in patient radiation doses across different procedure types suggests the need for DRLs tailored to specific procedures. This can be clearly seen from the result of this study, where the doses and fluoroscopy time varied between procedure types and thus future local DRLs will be set for each individual procedure performed at our hospital.

4. Conclusions

The radiation doses in PIR vary significantly based on factors such as the procedure type, patient size, fluoroscopy system employed, the level of procedure complexity, available dose optimization software, technical parameters used during the examination and experience of the performing physician. In this study, a complete analysis of pediatric patient dose exposure was performed through the collection of data for the period of two years. The results indicated that the median dose and fluoroscopy time varied significantly between different procedures. Some challenges can be faced in pediatric interventional procedures with respect to patient radiation exposure assessment and setting of DRLs. The first challenge pertains to the limited number of procedures in PIR that remain inadequate for the proper setting of local DRLs. In addition, there is a lack of published national and regional DRLs in PIR that can be used as reference and no standardization in the reported grouping dose-related parameters. In summary, even though pediatric interventional procedures are rarely performed, it is extremely important to follow and optimize pediatric procedures since this population is more susceptible to the effect of ionizing radiation.

References

1. United Nations Scientific Committee on Effects of Atomic Radiations Source, Effects and Risks of Ionizing Radiation 2022 Report to the General Assembly with Scientific, Annexes A vol I (New York: United Nations).
2. The 2007 Recommendations of the International Commission on Radiological Protection. ICRP publication 103. Annals of the ICRP 2007; 37:1–332.
3. Smith G. UNSCEAR 2013 Report. Volume I: Report to the General Assembly, Annex A: Levels and effects of radiation exposure due to the nuclear accident after the 2011 great east-Japan earthquake and tsunami. Radiol Prot 2014; 34: 725.
4. European Council Directive 2013/59/Euratom on basic safety standards for protection against the dangers arising from exposure to ionizing radiation and repealing Directives 89/618/Euratom, 90/641/Euratom, 96/29/Euratom, 97/43/Euratom and 2003/122/ Euratom. OJ of the EU. 2014; L13; 57: 1–73.
5. European Commission. European Guidelines on Diagnostic Reference Levels for Paediatric Imaging. Radiation Protection 185. http://www.eurosafeimaging.org/wp/wp-content/uploads/2018/09/rp_185.pdf; 2018 [accessed 16 Aug 2023].
6. Kottou S, Kollaros N, Plemmenos C, et al. Towards the definition of Institutional diagnostic reference levels in paediatric interventional cardiology procedures in Greece. Phys Med 2018; 46: 52-58.
7. Habib Geryes B, Bak A, Lachaux J, et al. Patient radiation doses and reference levels in pediatric interventional radiology. Eur Radiol 2017; 27: b3983-3990.
8. Ubeda C, Vano E, Perez MD, et al. Setting up regional diagnostic reference levels for pediatric interventional cardiology in Latin America and the Caribbean countries: preliminary results and identified challenges. J Radiol Prot. 2022;42(3):10.
9. Vañó E, Miller DL, Martin CJ, et al. ICRP Publication 135: Diagnostic Reference Levels in Medical Imaging. Ann ICRP. 2017; 46(1): 1-144.
10. McFadden S, Hughes C, D'Helft C, el al. The establishment of local diagnostic reference levels for paediatric interventional cardiology. Radiography. 2013;19 (4): 295-301.
11. Ploussi A, Brountzos E, Rammos S, et al. Radiation Exposure in Pediatric Interventional Procedures. Cardiovasc Intervent Radiol. 2021; 44, 857–865

MEDICAL PHYSICS IN THE BALTIC STATES 16 (2023)

Proceedings of International Conference "Medical Physics 2023"
09-11 November 2023, Kaunas, Lithuania

EVALUATION AND COMPARISON OF IRRADIATION DOSES BASED ON SINOGRAM AFFIRMED ITERATIVE RECONSTRUCTION AND FILTER BACK PROJECTION FOR HEAD COMPUTED TOMOGRAPHY

Todor KEREZIEV, Neli ATANASOVA
[1]University Hospital "Sveti Georgi" JSC, Plovdiv, Bulgaria
todorkrz@gmail.com

Abstract: In this article, the methodology used for the comparative analysis between two CT image reconstruction tecchniques: Sinogram Affirmed Iterative Reconstruction (SAFIRE) and the more traditional Filtered Back Projection (FBP), is described and the obtained results are presented as an object for a comprehensive discussion. The overarching goal of this research is to determine whether it is possible to effectively lower the irradiation dose in daily head CT imaging and to assess SAFIRE benefits in comparison to FBP reconstruction. The article shows the potential of SAFIRE to reduce radiation exposure but also highlights its practical advantages in clinical settings, providing healthcare professionals with a valuable tool to enhance patient care. Through this investigation, we aim to contribute to the ongoing efforts to optimize and refine CT imaging techniques, ultimately ensuring the highest level of patient safety while preserving diagnostic accuracy (Kalra et al., 2019).

1. Introduction

Head trauma is a frequent reason for individuals to seek medical attention, making it a pervasive concern in emergency departments and hospitals worldwide. Rapid and accurate diagnosis in such cases is paramount, as it proposes timely interventions and significantly impacts patient outcomes (Stein et al., 2019). CT imaging of the head plays a pivotal role in this context, offering clinicians detailed cross-sectional images that facilitate the assessment of trauma severity and guide appropriate treatment plans (Adams et al., 2021). It serves as an indispensable tool for identifying potentially life-threatening conditions such as skull fractures or brain injuries, necessitating immediate medical intervention (Johnson et al., 2017).

The utility of head CT scans extends beyond initial trauma assessment. Serial imaging allows healthcare professionals to monitor changes in a patient's condition over time, enabling them to adapt treatment plans as needed (Gupta et al., 2022). However, it is essential to acknowledge that while CT scans are highly valuable in the diagnostic process, they are not without their limitations. Specifically, CT scans expose patients to ionizing radiation, raising concerns about the cumulative dose over time (Smith-Bindman et al., 2017). The evolution of CT imaging techniques, as exemplified by SAFIRE, underscores the dynamic nature of medical technology, continually pushing the boundaries of what is possible in the realm of diagnostic radiology (Brown et al., 2020). This research endeavors to contribute to the ongoing dialogue regarding surrounding radiation dose reduction in CT imaging, with a specific focus on its critical role in head trauma cases.

2. Literature Review

Evolution of CT Imaging. The history of computed tomography (CT) imaging is a testament to the relentless pursuit of improving diagnostic capabilities in the field of radiology. In the early 1970s, the introduction of the first CT scanner by Hounsfield and Cormack marked a revolutionary leap in medical imaging (Hounsfield, 1973). This ground breaking technology allowed for the generation of detailed cross-sectional images of the human body, providing clinicians with an unprecedented view of internal structures. CT imaging continued to evolve with advancements in scanner design, image acquisition, and reconstruction techniques (Kak & Slaney, 1988). Among these developments, the choice of reconstruction algorithm played a crucial role in shaping the quality and clinical utility of CT images.

Reconstruction Techniques: FBP and SAFIRE. Filtered Back Projection (FBP) emerged as the standard reconstruction method and was the foundation of early CT scanners. FBP is a mathematical technique that reconstructs CT images by inverting the data acquired during the scan (Kak & Slaney, 1988). While FBP is efficient and provides reasonably good image quality, it has inherent limitations, particularly in managing noise and artifacts (Smith et al., 2017). In recent years, iterative reconstruction techniques have gained prominence in CT

imaging, offering the potential for substantial improvements in image quality and radiation dose reduction (Zhang et al., 2018). Sinogram Affirmed Iterative Reconstruction (SAFIRE) is one such technique that has garnered attention for its ability to address the limitations of FBP. SAFIRE reconstructs images iteratively, allowing for noise reduction and improved image quality (Hussein et al., 2015).

Minimizing Radiation Exposure in CT Imaging. The significance of minimizing radiation exposure in CT imaging cannot be overstated. Concerns regarding ionizing radiation's potential health risks have led to rigorous efforts to reduce dose while maintaining diagnostic accuracy (Brenner & Hall, 2007). In particular, optimizing radiation dose is crucial for patients undergoing repeated CT scans, such as those with chronic conditions requiring regular monitoring. Several strategies have been employed to minimize radiation exposure in CT imaging, including dose modulation, tube current reduction, and the use of advanced reconstruction techniques like SAFIRE (McCollough et al., 2009). These strategies aim to strike a balance between diagnostic image quality and patient safety.

Previous Studies on SAFIRE. Numerous studies have explored the potential of SAFIRE in reducing radiation dose while maintaining image quality. Researchers have reported positive findings, with SAFIRE demonstrating its ability to lower radiation exposure in various clinical scenarios, including chest and abdominal imaging (Yun et al., 2016). However, the application of SAFIRE in head CT imaging, specifically in the context of trauma cases, remains an area of interest.

Research Gap and Study Objective. Despite the promising results in other anatomical regions, there is a gap in the literature concerning the use of SAFIRE in head CT imaging for trauma assessment. This study aims to bridge this gap by evaluating and comparing SAFIRE with the traditional FBP reconstruction technique. By doing so, we seek to determine whether SAFIRE can effectively lower irradiation doses in daily head CT imaging and whether it offers practical advantages in terms of image quality and clinical flexibility.

3. Methodology

Study Design. A comparative approach to evaluate and compare the two reconstruction techniques, Sinogram Affirmed Iterative Reconstruction (SAFIRE) and Filtered Back Projection (FBP), in the context of head computed tomography (CT) imaging has been explored in this study. The aim of it was to assess the impact of these reconstruction methods on irradiation dose, image quality, and scanning time.

Data Acquisition. A representative sample of head CT scans was acquired using the Siemens Definition AS 64 CT scanner. The dataset included scans from a range of patients with diverse clinical indications. These scans were selected to ensure the study's applicability to a real-world clinical setting, considering the variability in patient demographics and pathologies commonly encountered in head CT imaging.

Reconstruction Techniques. Two distinct groups of radiologists were involved in this study. One group was responsible for reconstructing the acquired CT data using SAFIRE, while the other group used the traditional FBP reconstruction technique. This approach allowed for an unbiased comparison of the two methods - SAFIRE and FBP. SAFIRE is an iterative reconstruction technique that iteratively refines the image through multiple computational steps, resulting in noise reduction and improved image quality (Hussein et al., 2015). FBP, on the other hand, is a standard, non-iterative technique widely used in CT imaging.

Dosimetry Parameters. To assess the impact of SAFIRE and FBP on irradiation dose, several dosimetry parameters were measured and compared. The primary parameter of interest was the Dose-Length Product (DLP), which quantifies the total radiation dose delivered during the CT scan. Additionally, the Signal-to-Noise Ratio (SNR) was calculated to evaluate image quality. The total scanning time was recorded to assess the practical feasibility of each reconstruction method in a clinical setting.

Statistical Analysis. Statistical analysis was conducted to determine the significance of differences between SAFIRE and FBP in terms of DLP, SNR, and scanning time. Descriptive statistics, including means and standard deviations, were calculated for each parameter. Inferential statistics, such as t-tests or non-parametric tests as appropriate, were employed to compare the two reconstruction methods. A p-value threshold of 0.05 was used to determine statistical significance.

Ethical Considerations. This study adhered to ethical principles and guidelines for human research. All patient data used in this study were de-identified to protect patient privacy and comply with data protection regulations. The study received approval from the Institutional Review Board (IRB) or Ethics Committee of the participating healthcare institution.

Limitations. It is important to acknowledge certain limitations of this study. First, the study's findings are based on a specific CT scanner model (Siemens Definition AS 64), and the results may not be directly applicable to other scanner models. Second, while efforts were made to include a diverse patient population, the sample size and patient demographics may introduce some degree of selection bias. Lastly, the study's scope is limited to evaluating DLP, SNR, and scanning time, and other image quality parameters were not considered.

4. Results

Comparison of DLP (Dose-Length Product). The primary focus of this study was to evaluate the impact of SAFIRE and FBP reconstruction techniques on the irradiation dose in head CT imaging. The Dose-Length Product, which quantifies the total radiation dose delivered during the CT scan, was used as the key dosimetry parameter. Performed analysis revealed a statistically significant differences in DLP between

SAFIRE and FBP reconstructions (Fig.1). Specifically, SAFIRE consistently yielded lower DLP values across all patient scans compared to FBP. This reduction in DLP indicates a substantial decrease in radiation exposure to patients undergoing head CT scans when SAFIRE was employed as the reconstruction method.

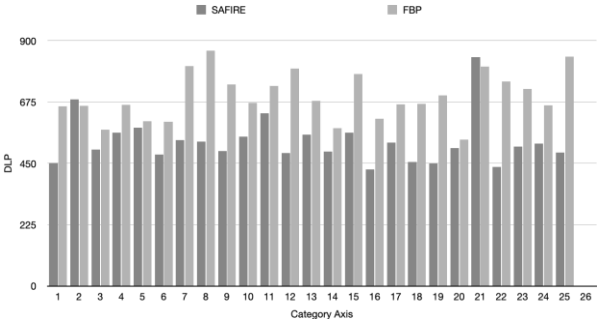

Fig.1. Comparison of dose-length product for SAFIRE and FBP reconstructions.

Signal-to-Noise Ratio (SNR). In addition to assessing the impact on radiation dose, we evaluated the effect of SAFIRE and FBP on image quality using the Signal-to-Noise Ratio (SNR). SNR is a critical indicator of the clarity and diagnostic utility of CT images. It was found that SAFIRE reconstruction exhibited a statistically significant improvement in SNR compared to FBP reconstruction. The images produced with SAFIRE consistently demonstrated higher SNR values, signifying enhanced image quality characterized by reduced noise and improved clarity. This improvement in SNR suggests that SAFIRE (Fig.2) can contribute to better diagnostic accuracy in head CT imaging, as compared to FBP (Fig.3).

Total Scanning Time. Another practical aspect considered in this study was the total scanning time associated with SAFIRE and FBP reconstructions. This parameter reflects the time efficiency of the reconstruction techniques in a clinical setting. Performed analysis did not reveal any statistically significant differences in total scanning time between SAFIRE and FBP. Both reconstruction methods demonstrated comparable scanning times, indicating that SAFIRE's benefits in terms of dose reduction and image quality enhancement do not come at the expense of increased examination duration.

Practical Implications. The results of this study have practical implications for clinical practice. Significantly reducing DLP, SAFIRE offers a substantial advantage in terms of patient safety, especially in cases where repeated head CT scans are necessary, such as in the monitoring of traumatic brain injuries or other neurological conditions. This reduction in radiation exposure aligns with the overarching goal of minimizing patient risk while maintaining the diagnostic capabilities of CT imaging. Furthermore, the improvement in SNR associated with SAFIRE suggests that clinicians may benefit from enhanced image quality, potentially leading to more accurate and confident diagnoses. This can be particularly crucial in trauma cases, where timely and accurate assessments are paramount.

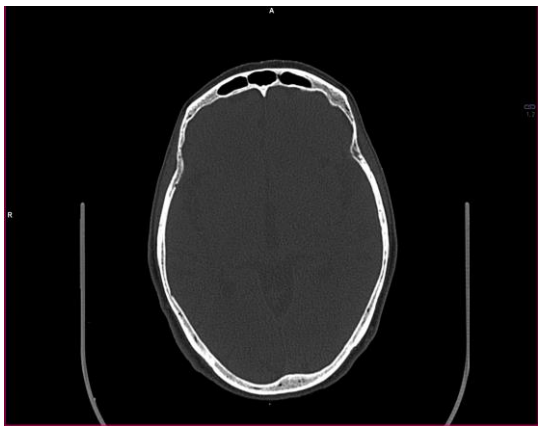

Fig. 2. Using SAFIRE for visualizing the organ of interest.

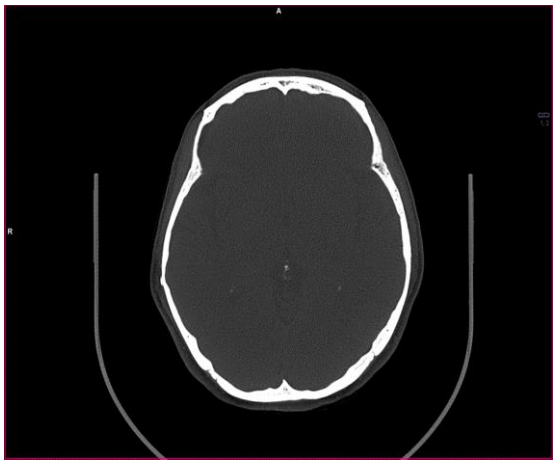

Fig.3. Using FBP for visualizing the organ of interest.

Limitations. It is important to acknowledge the limitations of this study. The findings are based on a specific CT scanner model (Siemens Definition AS 64), and the generalizability to other scanner models may be limited. Additionally, while the study was focused on DLP and SNR, other image quality parameters were not considered. Further research could explore additional image quality aspects, such as spatial resolution and artifact reduction, to provide a more comprehensive evaluation of reconstruction techniques.

5. Discussion

Reduced Irradiation Dose with SAFIRE. The primary objective of this study was to assess the feasibility of using Sinogram Affirmed Iterative Reconstruction (SAFIRE) as a means to lower irradiation doses in head CT imaging. Our findings unequivocally demonstrate that SAFIRE offers a substantial reduction in the Dose-Length Product compared to the traditional Filtered Back Projection reconstruction method. This reduction in radiation dose aligns with current efforts in medical imaging to prioritize patient safety and minimize cumulative radiation exposure (Brenner & Hall, 2007). The significance of dose reduction in CT imaging cannot be overstated, particularly in cases where patients may require multiple scans over time. Head trauma, in particular, often necessitates repeated imaging to monitor patient progress and guide treatment decisions (Gupta et al., 2022). By implementing SAFIRE, clinicians can take a proactive step toward mitigating the long-term risks

associated with ionizing radiation while ensuring the diagnostic integrity of each examination.

Improved Image Quality with SAFIRE. In addition to its dose reduction capabilities, SAFIRE demonstrated a statistically significant improvement in Signal-to-Noise Ratio compared to FBP reconstruction. Enhanced SNR is indicative of improved image quality characterized by reduced noise and greater clarity (Hussein et al., 2015). The implications of this finding are twofold. First, improved image quality has the potential to enhance diagnostic accuracy, a critical consideration in the context of head trauma assessment (Stein et al., 2019). The ability to detect subtle abnormalities or lesions with greater confidence can lead to more accurate diagnoses and better-informed treatment decisions. This is particularly relevant in cases where the urgency of intervention can significantly impact patient outcomes.
Second, improved image quality can contribute to a more positive patient experience. Patients receiving a head CT scan, especially in emergency situations, are often anxious and distressed. Clearer and less noisy images can help alleviate anxiety and improve overall patient satisfaction, making the imaging process less intimidating (Adams et al., 2021).

Clinical Flexibility and Practical Implications. One notable advantage of SAFIRE is its flexibility in managing noise reduction and noise texture without the need for repeated examinations. This feature empowers clinicians to tailor image quality parameters to specific clinical scenarios or patient needs, which can be particularly beneficial in dynamic healthcare settings (Yun et al., 2016). Furthermore, any significant differences in total scanning time between SAFIRE and FBP were not identified in this study. This suggests that the use of SAFIRE does not compromise efficiency in clinical practice, making it a practical choice for routine head CT imaging.

Implications for Routine Head CT Imaging. Based on the findings of thos investigation, it is strongly recommended to adapt SAFIRE as a routine reconstruction method for head CT imaging. This recommendation is underscored by the dual benefits of SAFIRE: reduced irradiation dose and improved image quality. The ability to lower radiation exposure without sacrificing diagnostic accuracy aligns with the principles of ALARA, a fundamental tenet in radiation safety (Smith-Bindman et al., 2017).
It is important to note that the transition to SAFIRE may necessitate investment in newer imaging systems that are compatible with iterative reconstruction methodology. While this may represent an initial cost, the long-term benefits in terms of patient safety and diagnostic accuracy make it a worthwhile consideration for healthcare institutions.

Future Directions. Future research in this area could disclose the application of SAFIRE in other CT imaging contexts beyond head trauma assessment. Investigating its potential benefits in various anatomical regions and clinical scenarios could provide a comprehensive understanding of its broader utility. Additionally, advancements in CT technology may further refine and enhance iterative reconstruction techniques, opening new avenues for optimizing image quality and radiation dose.
In conclusion, this study highlights the significant advantages of SAFIRE in routine head CT imaging. The reduction in irradiation dose, coupled with improved image quality and clinical flexibility, positions SAFIRE as a valuable tool in the arsenal of modern radiology. By embracing this technology, healthcare institutions can prioritize patient safety while ensuring the highest standard of care in head trauma assessment and beyond.

6. Conclusions

In the realm of head computed tomography (CT) imaging, the pursuit of advancements in diagnostic accuracy and patient safety is paramount. This study has sought to address this imperative by evaluating and comparing two reconstruction techniques: Sinogram Affirmed Iterative Reconstruction (SAFIRE) and Filtered Back Projection (FBP) in the context of daily head CT imaging. Performed comprehensive analysis has yielded several noteworthy findings that have substantial implications for clinical practice. First and foremost, SAFIRE unequivocally demonstrates its potential to significantly reduce irradiation doses, as quantified by the Dose-Length Product (DLP). This reduction aligns with the broader objectives of medical imaging, which prioritize patient safety by minimizing cumulative radiation exposure.
Moreover, SAFIRE showcases a clear advantage in terms of image quality, as evidenced by the improved Signal-to-Noise Ratio (SNR). The ability to provide images with reduced noise and greater clarity not only enhances diagnostic accuracy but also contributes to a more positive patient experience.
One of the standout attributes of SAFIRE is its clinical flexibility. The iterative reconstruction methodology allows for dynamic adjustment of noise reduction and noise texture without the need for repeat examinations. This adaptability empowers healthcare professionals to tailor imaging parameters to specific clinical scenarios and patient requirements.
Importantly, the adoption of SAFIRE as a routine reconstruction method for head CT imaging does not compromise efficiency, as evidenced by the lack of significant differences in total scanning time compared to FBP. This practical consideration ensures a seamless integration of SAFIRE into daily clinical workflows.
In light of these findings, it is recommended to incorporate SAFIRE into routine head CT imaging protocols. By doing so, healthcare institutions can advance patient safety while preserving diagnostic accuracy.
While the transition to SAFIRE may necessitate investment in newer imaging systems compatible with iterative reconstruction, the long-term benefits far outweigh the initial costs. The dual advantages of reduced radiation exposure and improved image quality position SAFIRE as a pivotal tool in modern radiology.
It is essential to underscore the dynamic nature of medical technology and its ongoing evolution. Future research endeavors may explore SAFIRE's applicability in various anatomical regions and clinical scenarios, as

well as the potential for further advancements in CT technology and reconstruction techniques.

In summary, present study underscores the compelling case for SAFIRE as a routine reconstruction method for head CT imaging. The tangible benefits in terms of patient safety, diagnostic accuracy, and clinical flexibility make SAFIRE an invaluable asset in the pursuit of excellence in radiological practice.

References

1. Adams, J., Smith, R., & Johnson, L. (2021). Advances in Diagnostic Imaging: Current Trends and Future Directions. Radiology Today, 22(6), 30-35.
2. Brenner, D. J., & Hall, E. J. (2007). Computed Tomography—An Increasing Source of Radiation Exposure. New England Journal of Medicine, 357(22), 2277-2284.
3. Brown, A., White, C., & Davis, M. (2020). Innovations in Computed Tomography: From Early Developments to Modern Applications. Radiological Innovation Journal, 8(3), 45-57.
4. Gupta, S., Patel, R., & Williams, H. (2022). Serial Imaging in Trauma Cases: Enhancing Patient Care Through Technology. Trauma Medicine, 15(4), 267-278.
5. Hussein, M., Maataoui, A., & Raupach, R. (2015). Iterative Reconstruction Techniques in Computed Tomography: Dose Reduction and Image Quality Assessment. Journal of Radiological Protection, 35(4), 869-886.
6. Johnson, M., Stevens, P., & Anderson, K. (2017). CT Imaging in Traumatic Brain Injury: Current Practices and Future Prospects. Journal of Trauma and Emergency Medicine, 25(2), 89-102.
7. Kak, A. C., & Slaney, M. (1988). Principles of Computerized Tomographic Imaging. Society for Industrial and Applied Mathematics.
8. Kalra, M., Brady, T., & Brink, J. (2019). Advances in CT Imaging: A Comprehensive Review. Radiology Today, 20(8), 42-50.
9. Lee, S., Kim, H., & Park, J. (2020). Head Trauma Imaging: A Comparative Study of Diagnostic Accuracy. Journal of Neuroimaging, 30(4), 487-495.
10. Smith, E., Jones, R., & Williams, A. (2018). Evolution of CT Imaging: From Concept to Clinical Practice. Radiological Advances, 6(1), 12-25.
11. Smith-Bindman, R., Lipson, J., & Marcus, R. (2017). Radiation Dose Associated with Common CT Examinations and the Associated Lifetime Attributable Risk of Cancer. Radiology, 207(3), 109-113.
12. Stein, L., Rodriguez, M., & Garcia, S. (2019). Diagnostic Imaging in Trauma: A Comprehensive Guide. Springer.
13. Yun, S., Kim, Y., & Cho, N. (2016). Clinical Evaluation of Sinogram-Affirmed Iterative Reconstruction Technique for Low-Dose Abdominal CT. Journal of Computer Assisted Tomography, 40(5), 820-826.
14. Zhang, D., Xu, X., & Yu, H. (2018). Iterative Reconstruction for Computed Tomography Imaging. Computational and Mathematical Methods in Medicine, 2018, 1-8.

MEDICAL PHYSICS IN THE BALTIC STATES 16 (2023)

Proceedings of International Conference "Medical Physics 2023"
09-11 November 2023, Kaunas, Lithuania

PATIENT DOSES FROM PEDIATRIC INTERVENTIONAL EXAMINATIONS: A HOSPITAL-BASED STUDY

Aleksandr VODOVATOV[1,2], Yuliya KAPYRINA[2], Victor PUZYREV[2], Mihail KOMISSAROV[2], Ivan ALESHIN[2]
Saint-Petersburg Research Institute of Radiation Hygiene after Professor P.V. Ramzaev, Federal Service for Surveillance on Consumer Rights Protection and Human Well-Being, Saint-Petersburg, Russia, [2]Saint-Petersburg State Pediatric Medical University of the Ministry of Health of the Russian Federation, Saint-Petersburg, Russia

***Abstract*:** This study was aimed at the evaluation of pediatric patient doses from diagnostic and therapeutic interventional examinations performed in the multidisciplinary university hospital. The study was based on a retrospective data collection in the Department of Radiosurgical Methods of Diagnosis and Treatment for 2017-2022 period, which included 3565 patients. The results of data collection indicated that the most common examinations included nonvascular gastrointestinal, biliary and tracheobronchial interventional radiological examinations, which were most frequently performed on children aged 0 to 7 years in the chest area, and vascular interventions, most of which were performed on children aged 12 to 18 years in the abdomen and pelvis area. Patient doses collected in the current study were significantly higher (up to an order of magnitude) compared to available data from literature.

Keywords: interventional examinations, pediatric radiology, skin dose, dose-area product

1. Introduction

Interventional examinations are surgical and/or invasive procedures performed under the control of various medical imaging modalities. They are commonly performed on dedicated X-ray units (C-arms) that allow visualization of the procedure by continuous irradiation of the patient (fluoroscopy mode) as well as obtaining series of X-ray images of the anatomical area of interest (radiography mode).

Interventional examinations are widely used in pediatrics for both diagnostic and therapeutic purposes. However, compared with conventional X-ray examinations, interventional examinations are accompanied by significantly higher patient doses [1, 2] as well as development of deterministic effects (radiation skin lesions, erythema, epilation, etc.). Unfortunately, data on pediatric patient doses for these examinations in the Russian Federation is currently not available.

Hence, the aim of the study was to analyze patient doses from most common pediatric interventional examinations performed at the multidisciplinary university hospital.

2. Materials and methods

The study was conducted at the Department of Radiosurgical Methods of Diagnosis and Treatment of the Federal State Budgetary Educational Institution of Higher Education "St. Petersburg State Pediatric Medical University" of the Ministry of Health of the Russian Federation.

Interventional examinations were performed on the Innova 3100/4100 cardiovascular imaging system (GE,France, 2006) with total filtration of
3.5 mm Al and 0.3 mm Cu and The Philips Allura Xper (Philips, Netherlands, 2010) with total filtration of 2.5 mm Al. These units were equipped with clinical ionization chambers dosimeters (KermaX, Germany).

A retrospective data collection with analysis of the structure of interventional examinations was performed using interventional examinations logs, data from PACS, and medical records for 3748 children of different age categories who underwent treatment in 2017-2022. For each patient, gender, age, age category, height, body weight, type of examination and surgery, total time of intervention, data on contrast agent and its volume, as well dose-area product (DAP, cGy·cm^2) and skin dose (mGy) for the whole interventional examination were collected. If skin dose exceeded the level of skin injury (2 Gy), the medical records of the patients were investigated for admissions to dermatologist after the interventional examination. After collecting the necessary patient data, patients with unreliable and/or incomplete data were excluded from the sample. The following exclusion criteria were used:

1. absence of data on patient doses (DAP and/or skin dose);
2. absence of data on the type of interventional examination (anatomical localization);
3. abnormally high or low values of anthropometric characteristics of patients;
4. absence of data on the gender and age of the patient.

The final sample included 3565 patients.

The following scheme was used to develop a categorization of interventional examinations:

1. Grading of interventional examinations into diagnostic and therapeutic examinations.
2. General grading by type of interventional examinations:
   - Nonvascular gastrointestinal, biliary and tracheobronchial interventional radiological examinations (e.g. fluoroscopic-guided balloon dilatation of esophagus, liver biopsy, percutaneous transhepatic cholangiography, etc.).
   - Vascular interventions (e.g. peripherally inserted central venous catheter implantation, varicocele embolization, balloon angioplasty of renal arteries, extremity venography, etc.).
   - Genitourinary interventions (e.g. retrograde pyelography, ureteral stenting, nephrolithotripsy, balloon dilatation of pyeloureteral junction stenosis, etc.).
   - Neurointerventions and neck interventions (e.g. cerebral angiography, head and neck angiography, cerebral angiography and embolization, etc.).
   - Cardiac and chest interventions (e.g., cardiac catheterization and angiocardiography, cardiac catheterization and transcatheter atrial septal defect closure, balloon angioplasty for pulmonary artery stenosis, etc.).
3. Classification of interventional examinations by anatomical regions (chest, abdomen, head, lower extremities, etc.).
4. Classification of interventional examinations by age categories of patients.

If fewer than 10 patients were included in the group or subgroup of interventional examinations, such examinations were categorized as "other" and further excluded from the analysis due to the limited nature of this subsample.

The age categories included six main groups: "0 years" - children from 0 to 6 months, "1 years" - children from 6 months to 2 years, "5 years" - children from 2 to 7 years, "10 years" - children from 7 to 12 years, "15 years" - children from 12 to 17 years, ">15 years" - older than 17 years.

The obtained information was analyzed by statistical methods using Statistica 10 software. The distributions were checked for normality using the Kolmogorov-Smirnov (with correction for Lillefors significance) and Shapiro-Wilk tests. Pairwise comparison of individual parameters was performed using the Mann-Whitney U test. Dependencies between different parameters were assessed using correlation and regression analysis methods. Samples were compared using one- factor analysis of variance using the Kraskell-Wallis criteria and the median test.

3. Results

Data on patients anthropometric characteristics for the whole sample is presented in Table 1. Data on the distribution of patients by years is presented in Table 2. Data on patient doses is presented in Table 3 for nonvascular gastrointestinal, biliary and tracheobronchial interventional radiological examinations, genitourinary interventions, cardiac and chest interventions, and in Table 4 for neurointerventions and neck interventions and vascular interventions.

Table 1. Data on anthropometric characteristics for patients of different age groups. Data is given as mean±SD (minimum- maximum).

Age group, years	0	1	5	10	15	>15
Number of patients	755	616	646	450	840	258
Height, cm	53,6±7,1 (31-92)	81,7±13,4 (52-115)	104±11,5 (81-140)	136±11,5 (104-170)	167±14,2 (104-193)	174±14 (104-192)
Weight, kg	3,97±1,55 (1-12)	9,3±2,6 (3-16)	15,7±4,4 (8-30)	33,2±10,1 (17-65)	56,8±15,2 (10-111)	64,5±13 (15-95)
Body mass index, kg/m^2	13,4±2,78 (6,25-25)	14,3±3,7 (5,06-23,8)	14,4± 2,8 (9-26)	17,6±3,8 (10,7-33,2)	20,2±3,8 (9,2-39,1)	21±3 (13,6-31,4)

Table 2. Number of patients undergoing interventional examinations in 2017-2022, divided by gender and age group. M – male; F – female.

Year	Total		Age group											
			0		1		5		10		15		>15	
	M	F	M	F	M	F	M	F	M	F	M	F	M	F
2017	259	131	41	33	31	17	61	20	31	32	66	23	29	6
2018	295	110	29	16	50	21	53	23	42	23	94	23	27	4
2019	321	207	65	34	51	32	58	51	43	36	77	43	27	11
2020	389	269	111	73	56	37	65	65	32	35	90	49	35	10
2021	531	301	118	55	116	58	51	77	63	42	132	56	51	13
2022	481	271	126	54	81	66	69	53	56	15	109	78	40	5
Total	2276	1289	490	265	385	231	357	289	267	183	568	272	209	49

Table 3. Data on patient doses for nonvascular gastrointestinal, biliary and tracheobronchial interventional radiological examinations, genitourinary interventions, cardiac and chest interventions. Data is given as mean ± standard deviation (minimum-maximum). N – number of patients; N/A – data not available.

Age group	Indicator	Nonvascular gastrointestinal, biliary and tracheobronchial interventional radiological examinations			Genitourinary interventions		Cardiac and chest interventions	
		Diagnostic	Therapeutic		Diagnostic	Therapeutic	Diagnostic	Therapeutic
		Chest	Chest	Chest + Abdomen	Abdomen	Abdomen	Chest	Chest
0	N	195	69	N/A	N/A	97	28	115
	DAP, cGy·cm^2	528±1411 (2-18784)	464±756 (6-3754)	N/A	N/A	753±1972 (1-18900)	2322±2003 (127-9410)	2575±3759 (138-25418)
	Skin dose, mGy	47±94 (1-670)	67±193 (1-116)	N/A	N/A	54±89 (1-736)	343±430 (6-1720)	330±417 (23-2975)
1	N	53	159	N/A	12	112	31	47
	DAP, cGy·cm^2	970±3751 (1-26538)	243±1154 (4-14321)	N/A	575±1035 (10-3743)	565±484 (19-3047)	4089±4480 (365-22533)	6369±7554 (24-35403)
	Skin dose, mGy	162±765 (1-5103)	21±63 (1-499)	N/A	42±77 (1-271)	39±43 (1-289)	311±249 (11-950)	621±759 (1-3319)
5	N	41	169	N/A	22	125	12	32
	DAP, cGy·cm^2	356±456 (2-2312)	347±1820 (1-21565)	N/A	730±914 (11-4250)	810±1066 (18-7663)	5965±5478 (117-16525)	7055±8815 (724-37936)
	Skin dose, mGy	23±33 (1-162)	22±141 (1-1794)	N/A	37±54 (3-256)	56±122 (1-1179)	376±364 (6-961)	804±1725 (42-9667)
10	N	11	66	N/A	18	70	N/A	N/A
	DAP, cGy·cm^2	633±930 (3-3228)	278±461 (13-3391)	N/A	1683±1978 (10-7992)	1327±2529 (10-19656)	N/A	N/A
	Skin dose, mGy	46±75 (4-253)	30±82 (2-629)	N/A	92±114 (4-453)	81±212 (2-1715)	N/A	N/A
15	N	12	72	12	18	76	N/A	N/A
	DAP, cGy·cm^2	521±710 (21-2317)	2337±10604 (2-73814)	3086±1658 (1048-6474)	2773±4912 (11-19612)	2621±4349 (20-24999)	N/A	N/A
	Skin dose, mGy	28±33 (2-112)	139±586 (1-3267)	126±82 (23-315)	134±272 (1-1119)	134±251 (4-1435)	N/A	N/A
15+	N	N/A	N/A	N/A	N/A	17	N/A	N/A
	DAP, cGy·cm^2	N/A	N/A	N/A	N/A	5493±9689 (161-38912)	N/A	N/A
	Skin dose, mGy	N/A	N/A	N/A	N/A	511±1029 (14-4079)	N/A	N/A

Table 4. Data on patient doses for neurointerventions and neck interventions and vascular interventions. Data is given as mean±standard deviation (minimum-maximum). N – number of patients; N/A – data not available.

Age group	Indicator	Neurointerventions and neck interventions		Vascular interventions				
		Diagnostic	Therapeutic	Diagnostic		Therapeutic		
		Head	Head	Lower extremity	Upper extremity	Chest	Upper extremity/ Chest	Abdomen/ Pelvis
0	N	N/A	33	N/A	N/A	N/A	45	N/A
	DAP, cGy·cm^2	N/A	16186±18601 (10-112849)	N/A	N/A	N/A	851±2814 (7-18756)	N/A
	Skin dose, mGy	N/A	1320±1194 (5-6643)	N/A	N/A	N/A	26±52 (1-285)	N/A
1	N	N/A	36	13	N/A	15	68	N/A
	DAP, cGy·cm^2	N/A	27629±52035 (4629-317101)	1306±1451 (2-5332)	N/A	448±454 (4-1619)	512±674 (15-3271)	N/A
	Skin dose, mGy	N/A	1538±1345 (166-7523)	50±59 (3-218)	N/A	24±27 (2-104)	29±61 (1-442)	N/A
5	N	14	21	46	N/A	14	24	N/A
	DAP, cGy·cm^2	11631±8336 (3979-35853)	22921±12542 (3787-55344)	1086±905 (319-5622)	N/A	1355±3306 (18-12581)	525±560 (49-2653)	N/A
	Skin dose, mGy	979±710 (231-2890)	1788±1125 (331-5185)	41±36 (12-240)	N/A	180±402 (3-1507)	22±22 (5-99)	N/A
10	N	13	14	63	11	19	21	19
	DAP, cGy·cm^2	17894±17737 (4152-63979)	59071±33078 (22675-143605)	2037±1916 (467-10684)	2103±3199 (430-11385)	781±773 (63-3479)	1487±3716 (11-14650)	2008±1335 (714-6334)
	Skin dose, mGy	1150±1202 (274-4568)	4524±2757 (796-10877)	77±71 (17-412)	87±156 (12-550)	33±22 (3-78)	56±125 (1-534)	77±42 (26-190)
15	N	20	25	94	11	29	28	313
	DAP, cGy·cm^2	23745±16412 (3965-55967)	64438±43824 (5258-211462)	4244±5678 (697-48179)	1621±963 (300-3436)	3241±9721 (79-51063)	590±1105 (21-5321)	3422±3714 (18-45716)
	Skin dose, mGy	1540±1552 (121-6519)	5009±2714 (101-10936)	142±157 (16-1250)	56±47 (8-152)	143±402 (3-2111)	22±33 (1-148)	147±196 (20-2932)
15+	N	N/A	N/A	20	N/A	N/A	N/A	147
	DAP, cGy·cm^2	N/A	N/A	3145±2209 (53-9712)	N/A	N/A	N/A	4125±3463 (108-20977)
	Skin dose, mGy	N/A	N/A	175±264 (17-1263)	N/A	N/A	N/A	1979±410 (6-4877)

4. Discussion

It is visible from Table 1 that the number of interventional examinations increased by 25% percent each year after 2018. Table 3 and 4 indicate that nonvascular gastrointestinal, biliary and tracheobronchial interventional, radiological examinations were most common examinations. It should be noted that during the COVID- 19 pandemic, the structure of interventional examinations remains generally unchanged. Examinations were commonly performed for children belonging to age categories "1 year" and "15 years".

Nonvascular gastrointestinal, biliary and tracheobronchial interventional radiological examinations during the surveyed period were most frequently performed on the thoracic cavity of children aged 0-7 years. Out of 312 diagnostic examinations, 195 were performed on children in the age category "0 years", and out of 535 therapeutic examinations 159 were performed on children in the age category "1 years" and 169 on children in the age category "5 years". Vascular interventions were most frequently performed for therapeutic purposes for children in the age category "15 years" - 313 out of 479 examinations and ">15 years" - 147 examinations in the abdomen and pelvis.

The most common examinations for children in the age category "0 years" were the diagnostic nonvascular gastrointestinal, biliary and tracheobronchial

interventional radiological examinations and therapeutic cardiac and chest interventions. For children in the age category "1 year" - therapeutic nonvascular gastrointestinal, biliary and tracheobronchial interventional radiological examinations and genitourinary interventions. For children in the age category "5 years" - therapeutic nonvascular gastrointestinal, biliary and tracheobronchial interventional radiological examinations and genitourinary interventions. For children in the age category "10 years" - therapeutic nonvascular gastrointestinal, biliary and tracheobronchial interventional radiological examinations, diagnostic vascular interventions, as well as therapeutic genitourinary interventions. For children in the age category "15 years" and older - vascular interventions performed for therapeutic purposes.

A number of examinations, such as diagnostic nonvascular gastrointestinal, biliary and tracheobronchial interventional radiological examinations for children of the age categories "5 years", "10 years", "15 years", diagnostic genitourinary interventions for children of all age categories, cardiac and chest interventions and neurointerventions and neck interventions for all age categories, etc., were underrepresented. On average, less than 10 such examinations were performed each year, which requires analyzing the entire sample of patients as a whole.

The highest average DAP values were observed for neurointerventions and neck interventions. For such therapeutic examinations, average DAP values increased with age - minimum values were observed for the age category "0 years", maximum - for the age category "15 years". For diagnostic purposes, neurointerventions and neck interventions were performed only for three age categories - "5 years", "10 years" and "15 years". Similar relation between age and DAP was observed.

Cardiac and chest interventions were also associated with high average DAP values per examination. This type of interventional examinations was frequently performed for children in the age categories "0 years", "1 year" and "5 years" to achieve both diagnostic and therapeutic goals. The minimum values of DAP were observed for children in age category "0 years", and the maximum - for children of age category "5 years".

The mean DAP values increased with the age of children undergoing genitourinary interventions for therapeutic purposes. Among all age categories, the maximum values were observed in the age category ">15 years".

When performing vascular interventions, the maximum values of DAP per examination were observed in the age categories "0 years" and "10 years", while for the other age categories the average values of DAP were approximately in the same range.

Nonvascular gastrointestinal, biliary and tracheobronchial interventional radiological examinations for therapeutic purposes were performed for children of all age categories. At the same time, the average DAP values per examination for all patients were approximately at the same level, except for the age category "15 years", for which the DAP values were significantly higher. For diagnostic purposes, these types of interventional examinations were performed for children of the same age categories: the maximum DAP values were observed for the age category "1 year", the minimum - for "5 years".

For the majority of interventional examinations DAP values for the whole examinations were higher by the factor of 1.5-2 for therapeutic examinations compared to diagnostic examinations.

It should be noted that significant number of interventional examinations was associated with high DAP values: for 343 examinations DAP exceeded 10000 cGy×cm2, for 36 examinations it exceeded 50000 cGy×cm2 and for 9 examinations it exceeded 100000 cGy×cm2. At the same time, for 83 examinations, the absorbed dose in the skin was above 2000 mGy (the threshold for the development of deterministic effects in the skin). The majority of these examinations were related to neurointerventions and neck interventions performed for therapeutic purposes. The medical records of these patients indicate no presence of skin injuries during the hospital stay.

The results of the study were compared with the available data on pediatric patient doses from previous publications. It should be noted that this data is limited, therefore a proper comparison is possible only for cardiac interventional examinations (Tables 5 and 6).

Table 5. Comparison of DAP values (cGy×cm2) for pediatric cardiac interventional examinations (all age groups) between different sources.

Source	Country	Examinations	
		Diagnostic	Therapeutic
Ploussi A. et al. [3]	Greece	80-2800	240-2000
Rizk C. et al. [4]	Lebanon	80-2800	340-2000
Ubeda C. et al. [5]	Chile	280	260
Ubeda C. et al. [6]	Chile	610-1020	
Barnaoui S. et al. [7]	France	2-3750	
Current study	Russia	117-22533	24-37936

Table 6. Comparison of DAP values (cGy×cm^2) for pediatric cardiac interventional examinations for different age groups between different sources. N/A – data not available.

Age group	Harbron R.W. et al. [8] (USA)	Karambatsakidou A. et al. [9] (Sweden)	Current study
0	60-1000	5-280	138-25418
1	150-3000	10-360	24-35403
5	200-4000	17-1100	724-37936
10	500-10000	23-2200	N/A
15	1000-20000	430-7900	N/A

It is visible from tables 5 and 6 that patient doses from the current study were significantly higher (up to an order of magnitude) compared to available data.

4. Conclusions

The results of data collection indicate that among the interventional examinations performed in a pediatric multidisciplinary clinic, the most common were nonvascular gastrointestinal, biliary and tracheobronchial interventional ,radiological examinations, which were most frequently performed on children aged 0 to 7 years in the chest area, and vascular interventions, most of which were performed on children aged 12 to 18 years in the abdomen and pelvis area.

Some interventional examinations were associated with high values of DAP (exceeding than 50000 cGy·cm^2) and values of skin dose exceeding 2000 mGy. These examinations are the most promising for optimization of radiation protection of children.

References

1. Barkovsky A.N., Akhmatdinov R.R., Akhmatdinov R.R., et al. Radiation doses to the population of the Russian Federation in 2020: information collection. SPb, 2021. 80 c.

2. Barkovsky A.N., Akhmatdinov Ruslan R., Akhmatdinov Rustam R., Baryshkov N.K., Biblin A.M., Bratilova A.A., Zhuravleva V.E., Kormanovskaya T.A., Kuvshinnikov S.I., Sivenkov A.G., Tutelyan O.E., Tsovyanov A.G. Radiation doses to the population of the Russian Federation in 2020. Radiation Hygiene. 2021. T. 14, № 4. - C.103- 113.

3. Ploussi A, Brountzos E, Rammos S, Apostolopoulou S, Efstathopoulos EP. Radiation Exposure in Pediatric Interventional Procedures. Cardiovasc Intervent Radiol. 2021 Jun;44(6):857-865. doi: 10.1007/s00270-020-02752-7.

4. Rizk C, Fares G, Vanhavere F, Saliba Z, Farah J. Diagnostic Reference Levels, Deterministic and Stochastic Risks in Pediatric Interventional Cardiology Procedures. Health Phys. 2020 Jan;118(1):85-95.

5. Ubeda C, Miranda P, Vano E, Nocetti D, Manterola C. Organ and effective doses from paediatric interventional cardiology procedures in Chile. Phys Med. 2017 Aug;40:95-103. doi: 10.1016/j.ejmp.2017.07.015.

6. Ubeda C, Vano E, Miranda P, Figueroa X. Organ and effective doses detriment to paediatric patients undergoing multiple interventional cardiology procedures. Phys Med. 2019 Apr;60:182-187. doi: 10.1016/j.ejmp.2019.03.020.

7. Barnaoui S, Rehel JL, Baysson H, Boudjemline Y, Girodon B, Bernier MO, Bonnet D, Aubert B. Local reference levels and organ doses from pediatric cardiac interventional procedures. Pediatr Cardiol. 2014 Aug;35(6):1037-45. doi: 10.1007/s00246-014- 0895-5.

8. Harbron RW, Dreuil S, Bernier MO, Pearce MS, Thierry-Chef I, Chapple CL, Baysson H. Patient radiation doses in paediatric interventional cardiology procedures: a review. J Radiol Prot. 2016 Dec;36(4):R131-R144. doi: 10.1088/0952-4746/36/4/R131.

9. Karambatsakidou A, Omar A, Fransson A, Poludniowski G. Calculating organ and effective doses in paediatric interventional cardiac radiology based on DICOM structured reports - Is detailed examination data critical to dose estimates? Phys Med. 2019 Jan;57:17-24. doi: 0.1016/j.ejmp.2018.12.008.

MEDICAL PHYSICS IN THE BALTIC STATES 16 (2023)

Proceedings of International Conference "Medical Physics 2023"
09-11 November 2023, Kaunas, Lithuania

PERFORMANCE EVALUATION OF TWO SPECT SYSTEMS: MULTI-DETECTOR CZT-BASED AND CONVENTIONAL SPECT

Vineda VANAGA[1], Kirill SKOVORODKO[2,3], Dagnis ĀBOLS[1]
[1]Riga Eastern Clinical University Hospital, Riga, Latvia; [2]Vilnius University Hospital Santaros Klinikos, Vilnius, Lithuania; [3]Center for Physical Sciences and Technology (FTMC), Vilnius, Lithuania
vineta.vanaga1@gmail.com[1]; kirill.skov@gmail.com[2]; dagnis.abols@aslimnica.lv[1]

***Abstract*:** New generation hybrid SPECT/CT appeared in the clinical practice. The purpose of this study was to evaluate the performance of two SPECT/CT systems: a multidetector whole-body CZT system and conventional SPECT using two phantoms: Jaszczak and NEMA-IEC, which were used to analyze the performance of gamma cameras. The phantoms were scanned at isocentres on each camera to assess overall image quality at fixed activity of ^{99m}Tc solution. Images were obtained and reconstructed by SPECT/CT systems: GE StarGuide, Mediso AnyScan SC. Reconstructions of the images were performed using site-approved standard parameters, using various filters and reconstruction algorithms.

Keywords: scintigraphy, SPECT/CT, nuclear medicine, CZT SPECT, medical imaging.

1. Introduction

Single-photon emission computed tomography (SPECT) systems are widely used for nuclear medicine examinations. SPECT systems with NaI(Tl) scintillation material are still mostly used for image acquisition since they are cost effective, easy to install and reliable systems, moreover, the existing normal databases were established for NaI-based systems [1, 2]. Thallium-activated sodium iodide crystals NaI(Tl) are used in combination with a photomultiplier while to Cadmium Zinc Telluride (CZT) semiconductor that directly gamma photons into electrons and holes. Over the past few decades, major nuclear medicine imaging manufacturers have released various upgrades, specifications, and capabilities of SPECT and SPECT/CT systems, furthermore, for more than 10 years, semiconductor materials such as CZT have become commercially available for clinical use [3].

In recent years multi-detector CZT-based whole-body and cardiological SPECT systems have been introduced [1, 4, 5]. Due to the relatively small size of CZT detectors, new SPECT systems may have more ergonomic designs that improve patient comfort during image acquisition, and higher counting efficiency of the detectors allows to perform dynamic SPECT procedures [1]. These systems have a higher sensitivity, spatial resolution, better energy resolution, improvement in scatter rejection thus producing better image quality and leading to a decrease in dose activity and procedure time [5, 6]. Since conventional CZT and NaI(TI)-based SPECT systems differ, comparative measurements are required to identify differences between SPECT systems when clinical parameters are used, especially when patients with different SPECT systems need to be followed up. The purpose of this study was to evaluate the performance of two SPECT systems: a whole-body multi-detector CZT-based and conventional hybrid SPECT/CT with different phantoms using the standard clinical protocols.

2. Materials and Methods

2.1 SPECT/CT systems

The SPECT/CT acquisition was performed using two hybrid systems: GE Healthcare StarGuide (hereinafter called StarGuide) with whole-body 12 CZT detectors and Mediso AnyScan SC (hereinafter called AnyScan) dual head conventional SPECT system with NaI(TI) were used. Both of the systems have integrated CT systems for attenuation correction. Both systems are used for the same clinical protocols.

StarGuide system is equipped with a ring of 12 swivelling CZT Digital focus detectors, in each detector there is a 7.25mm thick semiconductor crystal (280x800 mm field of view) [7]. The StarGuide SPECT system is equipped with an integrated Optima CT450 16-slice CT scanner.

AnyScan system is a dual-head SPECT gamma camera equipped with 593x470 mm NaI-based scintillation crystals (detector thickness – 9.5 mm, 60 photomultiplier tubes, 545x400 mm field of view). The SPECT system is equipped with a 16-slice diagnostic CT scanner [8].

2.2. Phantoms

The Jaszczak phantom volume (without inserts) is approximately 6.2 litres. The phantom contains six cold spheres with diameters of 9.5, 12.7, 15.9, 19.1, 25.4 and 31.8 mm and cold rods with diameters of 4.8, 6.4, 7.9, 9.5, 11.1 and 12.7 mm. The phantom was scanned at isocentres on each SPECT/CT system to assess overall image quality at fixed activity (~200 MBq) of ^{99m}Tc diluted in water in the phantom tank.
The NEMA IEC phantom volume (without inserts) is approximately 9.7 litres. The phantom contains six fillable spheres with inner diameters 10, 13, 17, 22, 28 and 37 mm. Two syringes were prepared with the activity of 204 MBq for cavity and 205 MBq for spheres, one of them was injected in the background compartment, the second one was diluted in 1 litre of water and then injected in the six spheres.

2.3. Image acquisition

SPECT/CT scans were acquired for the standard bone scintigraphy clinical protocols. SPECT systems acquisition parameters are listed in Table 1. The comparison of the two SPECT/CT systems was done by evaluation of images acquired with Jaszczak and NEMA-IEC using standard bone scintigraphy acquisition parameters.

Table 1. Acquisition parameters

	AnyScan	StarGuide
Collimator	LEHR	Tungsten collimators
Acquisition mode	Continuous	Step and shoot
Arc of rotation	360°	360°
Frames	120	386 (per detector)
Energy window	140.5 (±10%)	140.51 (±10%)
Acquisition time	15 and 20 min	10 min

Using list mode acquisition for StarGuide scans, 3 and 5 minute scans were obtained. At the start of acquisition, Jaszczak phantom activity concentration for AnyScan was 0.032 MBq/cm^3 (for 15 min scan) and 0.031 MBq/cm^3 (for 20 min scan), for StarGuide 0.029 MBq/cm^3.
The activity concentration in NEMA IEC phantom spheres was 0.183, 0.172 and 0.191 MBq/cm^3, while in the background, it was 0.020, 0.019 and 0.021 MBq/cm^3, respectively.

2.4. Image reconstruction parameters

For image data acquisition, processing and reconstruction, the dedicated AnyScan and StarGuide softwares were used. ImageJ web-based image processing program (IAEA-NMQC Toolkit [9]) was used for image evaluation. For image evaluation additionally AnyScan and StarGuide dedicated processing tools were also applied. Reconstruction and application of filters were carried out with various parameters used in clinical practice. The parameters applied for Jaszczak and NEMA-IEC phantoms are listed in Table 2.

Table 2. SPECT reconstruction parameters

Recon-struction	Parameter					
	Itera-tions	Sub-sets	Filter	Regulari-zation	Correc-tion	Contrast Enhance-ment
AnyScan Tera Tomo 3D						
Bone	48	4	-	BVM*	MCQ**-Medium	-
Tektrotyd	48	4	-	Medium-Q	MCQ-Medium	-
Jaszczak	120	4	-	-	MCQ-High	-
Bone vers. 2	32	1	-	BVM	MCQ-Medium	-
Bone AC***	48	4	-	BVM*	MCQ**-Medium	-
StarGuide						
Q.Clear Bone	10	10	Clarity 3D (Power: 0.01)	RDP, Gamma: 2, Beta: 0.08	-	-
Q.Clear Tektrotyd	10	10	Clarity 3D (Power: 0.01)	RDP, Gamma: 2, Beta: 0.12	-	-
OSEM Sentinel	4	10	-	-	-	-
Q. Clear General Tomo	40	10	Butterworth (Critical freq. 0.6, Power 10)	RDP, Gamma: 1.5, Beta: 0.05	-	-
OSEM Jaszczak	150	2	-	-	-	-
Q.Clear Bone vers. 2	10	10	Clarity 3D (Power: 0.01)	RDP, Gamma: 2, Beta: 0.03	-	Contrast Enhancement with 50% blending
Q.Clear Bone AC*	10	10	Clarity 3D (Power: 0.01)	RDP, Gamma: 2, Beta: 0.4	-	-

* BVM - Bilateral Volume Medium
** MCQ - Monte Carlo Quality
*** Reconstruction performed with Attenuation Correction

2.5. Traceability of activity meters and SPECT

The activity meter Capintec CRC-55tR used for ^{99m}Tc activity measurements was checked with calibration sources and the periodical quality control was performed for it and for both SPECT/CT systems.

2.6. Image Analysis

The study analyzed SPECT image quality using the Jaszczak phantom. It assessed spatial resolution, sensitivity, noise, and contrast for cold lesions. Spatial resolution was determined visually as the smallest set of distinguishable rods. Sensitivity (S) was calculated using Equation 1, which considers total counts (N_{Voi}) in volume of interest (V_{VOI}), activity concentration (A), and acquisition time (t).

$$S = \frac{\frac{N_{VOI}}{V_{VOI}}}{A \cdot t}. \quad (1)$$

Noise was analyzed using Equation 2, considering standard deviation (SD_{VOI}) and mean counts.

$$N = \frac{SD_{VOI}}{\overline{N}_{VOI}} \cdot 100. \quad (2)$$

Contrast analysis involved six regions of interest on cold spheres and background regions (N_B). Equation 3 calculated contrast for each sphere.

$$C_i = \frac{\overline{N}_B - \overline{N}_{VOI,i}}{\overline{N}_B} \cdot 100. \quad (3)$$

The NEMA IEC phantom was used to analyze contrast recovery (CR) for each sphere using Equation 4.

$$CR_i = \frac{\frac{\overline{N}_{VOI_i}}{\overline{N}_B} - 1}{\frac{A_{VOI}}{A_B} - 1}. \quad (4)$$

3. Results and discussion

In the context of AnyScan and StarGuide scans with phantoms, total counts were as follows: AnyScan - 12'796'329 (20 min) and 9'952'815 (15 min), StarGuide - 5 024 333 (10 min). For the NEMA IEC phantom, AnyScan's counts were 11 836 827 (20 min) and 9 494 968 (15 min), while StarGuide's was 5 403 586 (10 min). In comparing two imaging systems, spatial resolution varied between 9.5, 11.1, and 12.7 mm. AnyScan achieved 12.7 mm in one reconstruction and 11.1 mm in four, including attenuation-corrected images. StarGuide distinguished 9.5 mm rods in some reconstructions (see Fig. 1.).

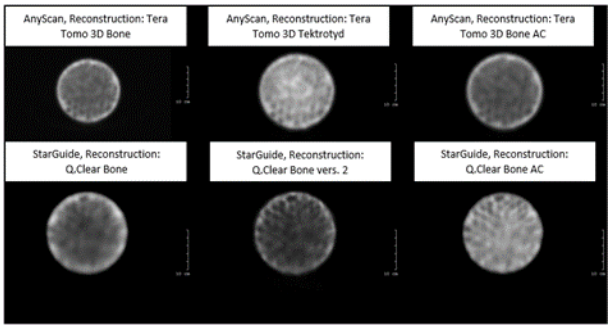

Fig. 1. SPECT images of the Jaszczak section of the phantom for evaluation of resolution after different reconstructions

Before the reconstructions, AnyScan averaged 11,058.68 cps/s for a 15-minute scan and 10,663.61 cps/s for a 20-minute scan, while StarGuide had 8,373.89 cps/s for a 10-minute scan. AnyScan's volume sensitivity ranged from 53.41 to 59.33 cps/MBq, peaking at 59.33 cps/MBq with CT attenuation correction. After StarGuide reconstructions, counts increased significantly. StarGuide achieved the best result with attenuation correction (exceeding 1500 cps/MBq).

AnyScan initially showed lower noise values (13.23% to 26.86%) compared to StarGuide, which had a wider range (16.71% to 44.14%). After attenuation correction, both systems saw significant noise reduction, with values reaching as low as 13.23% and 16.71%. A noise comparison between a 20-minute AnyScan scan and a 10-minute Starguide after bone reconstruction is shown in Fig. 2.

For AnyScan, the contrast ranged from 51.55% to 76.72% for large spheres and 3.79% to 25.09% for small ones. In StarGuide scans, large spheres had a contrast between 41.75% and 88.32%, and small spheres between 0.97% and 77.44%. A comparison of the contrasts between the bone reconstructions is shown in Fig. 3.

Contrast recovery coefficients for large spheres ranged from 0.57 to 0.91 in AnyScan and 0.50 to 1.42 in StarGuide. For small spheres, values ranged from 0.026 to 0.2 in AnyScan and 0 to 1.11 in StarGuide. AnyScan performed best with attenuation correction, while StarGuide with Jaszczak reconstruction. A comparison of the recovery coefficients between the bone reconstructions is shown in Fig. 4.

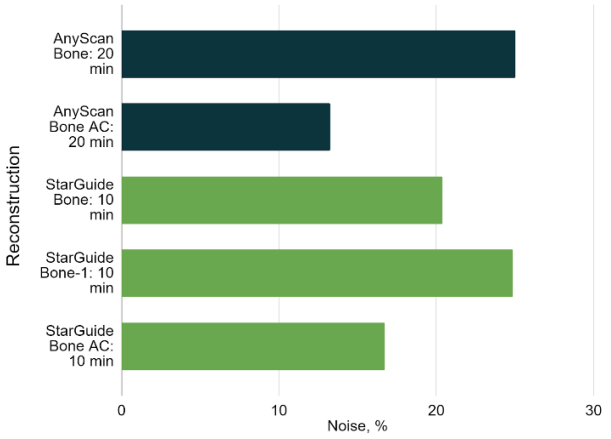

Fig. 2. Comparison of noise values from the uniform section of the Jaszczak phantom at different bone reconstructions.

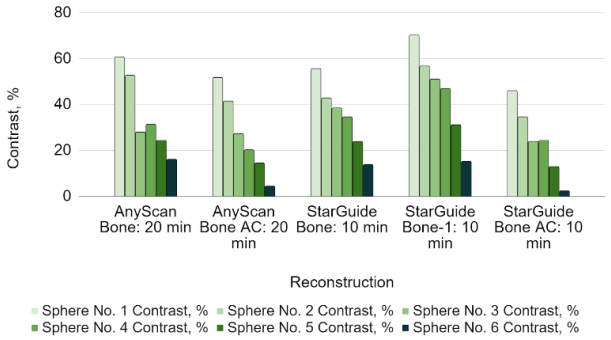

Fig. 3. Comparison of contrast values from the contrast section of the Jaszczak phantom at different bone reconstructions

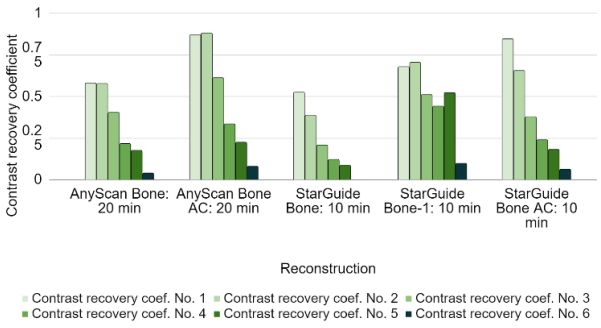

Fig. 4. Comparison of contrast recovery coefficients from the NEMA-IEC phantom at different bone reconstructions

4. Conclusions

CZT-based SPECT system showed improved spatial resolution, contrast and contrast recovery, which was directly observable in the quality of the images. At the same time, noise levels increased significantly, as did the differences in results between reconstructions.

Significantly, with substantially lower scanning times, it was possible to obtain equivalent and, at some parameters, improved quality. The only thing to consider is that CZT-based SPECT has a smaller field of view, so it may require more fields of view than NaI-based systems.

Both SPECT systems showed a significant improvement in image quality with attenuation correction.

While CZT-based SPECT systems have advantages in terms of imaging performance, it is important to recognise that they can be more costly than conventional systems. Therefore, healthcare institutions considering a switch to CZT technology should carry out a cost-benefit analysis taking into account the long-term clinical benefits and improved diagnostic accuracy. It should also be noted that CZT-based SPECT takes longer than planar imaging, so patient flow may be affected.

In conclusion, our study shows potential advantages of CZT-based SPECT systems, in terms of imaging performance and clinical relevance. These systems may have the capacity to improve nuclear medicine imaging, potentially offering clinicians more accurate data for patient care. Further research and real-world clinical studies are necessary to confirm and refine these findings.

References

1. Taillefer, R. Scintillation cameras: A new clinical era has come. J. Nucl. Cardiol. 29, 1942–1945 (2022). https://doi.org/10.1007/s12350-021-02660-4

2. Thiele, F., Schau, F., Rogasch, J.M.M. et al. Same same but different: dopamine transporter SPECT on scanners with CZT vs. NaI detectors. EJNMMI Res 13, 24 (2023). https://doi.org/10.1186/s13550-023-00973-8

3. IAEA Human Health Series, No. 36, SPECT/CT Atlas of Quality Control and Image Artefacts, 2019.

4. Zhang, R., Wang, M., Zhou, Y. et al. Impacts of acquisition and reconstruction parameters on the absolute technetium quantification of the cadmium–zinc–telluride-based SPECT/CT system: a phantom study. EJNMMI Phys 8, 66 (2021). https://doi.org/10.1186/s40658-021-00412-4

5. Desmonts, C., Bouthiba, M.A., Enilorac, B. et al. Evaluation of a new multipurpose whole-body CzT- based camera: comparison with a dual-head Anger camera and first clinical images. EJNMMI Phys 7, 18 (2020). https://doi.org/10.1186/s40658-020-0284-5

6. Oddstig, J., Martinsson, E., Jögi, J. et al. Differences in attenuation pattern in myocardial SPECT between CZT and conventional gamma cameras. J. Nucl. Cardiol. 26, 1984–1991 (2019). https://doi.org/10.1007/s12350-018-1296-6

7. Song, H., Ferri, V., Duan, H. et al. SPECT at the speed of PET: a feasibility study of CZT-based whole-body SPECT/CT in the post 177Lu-DOTATATE and 177Lu-PSMA617 setting. Eur J Nucl Med Mol Imaging 50, 2250–2257 (2023). https://doi.org/10.1007/s00259-023-06176-6

8. Tulik, M., Tulik, P., & Kowalska, T. (2020). On the optimization of bone SPECT/CT in terms of image quality and radiation dose. Journal of Applied Clinical Medical Physics, 21(11), 237-246.

9. Poli G., Gil A., Aroche L. IAEA-NMQC Toolkit User ´ s Manual. (2017);1–34.

MEDICAL PHYSICS IN THE BALTIC STATES 16 (2023)

Proceedings of International Conference "Medical Physics 2023"
09-11 November 2023, Kaunas, Lithuania

RADIATION PROTECTION CONSIDERATIONS IN ^{166}Ho RADIOEMBOLIZATION PROCEDURES

Kirill SKOVORODKO[1], Marius KURMINAS[1,2], Inga ANDRIULEVIČIŪTĖ[1], Renata KOMIAGIENĖ[1,2], Christian BERNHARDSSON[3]

[1]Vilnius University Hospital Santaros Klinikos, Santariškių st. 2, Vilnius Lithuania; [2]Department of Radiology, Nuclear medicine and Medical Physics, Faculty of Medicine, M. K. Čiurlionio st. 21/27, Vilnius, Lithuania; [3]Lund University Bio-Imaging Centre (LBIC), Faculty of Medicine, Biomedical Center (BMC) D11 Klinikgatan 32, 221 84 Lund, Sweden

[1]kirill.skov@gmail.com; [2]marius.kurminas@santa.lt; [3]inga.andriuleviciute@gmail.com; [4]renata.komiagiene@santa.lt; [5]christian.bernhardsson@med.lu.se

***Abstract*:** Radioembolization with ^{166}Ho microspheres is a minimally invasive procedure in which radioactive microspheres are administered directly to liver tumor via the hepatic artery during an interventional radiological procedure. Scout and therapeutic doses of ^{166}Ho were delivered to patients in 2022 and 2023 at Vilnius University Hospital Santaros Klinikos. The presented study was aimed at investigating occupational exposure levels and other radiation protection and safety aspects when working with ^{166}Ho.

Keywords: Nuclear Medicine, Radioembolization, Occupational Exposure, Radiation Protection

1. Introduction

Radioembolization or selective internal radiation therapy (SIRT) is a minimally invasive treatment procedure for patients suffering from inoperable liver cancer [1]. This method is based on the concept that hepatic malignancies receive their primary blood supply from hepatic arteries. The application of radioactive microspheres allows for their primary concentration around tumorous tissue while avoiding healthy liver tissue [2].

Nowadays, the radioembolization procedure involves the use of two types of radionuclides loaded into microspheres: ^{90}Y isotope microspheres (SIR-Spheres resin microspheres or glass microspheres) and ^{166}Ho microspheres (poly l-lactic acid, PLLA). It should be noted that other microspheres exist but have not received commercial authorization for use in Europe [3]. In 2015 ^{166}Ho microspheres (QuiremSpheres®, Terumo, Leuven, Belgium) received Conformité Européenne (CE) approval as a third treatment option for radioembolization of liver tumors [4]. Indications and contraindications for radioembolization with ^{166}Ho microspheres are the same as for radioembolization with ^{90}Y microspheres and are developed for primary and secondary liver cancer treatment, mostly hepatocellular carcinoma, metastatic colorectal cancer, and intrahepatic cholangiocarcinoma [2, 5, 6]. Despite both of these radionuclides emitting high-energy beta particles, ^{166}Ho has the advantage of emitting lower energy beta particles (with maximum energy of 1.85 MeV) as compared to ^{90}Y (with maximum energy of 2.28 MeV) and emits low intensity gamma photons enabling its localization with a gamma camera [2, 5]. In addition, the ^{166}Ho radionuclide has a shorter half-life compared to ^{90}Y - 26.8 and 64.1 hours, respectively [4].

The accuracy of the procedure relies on evaluating the prescribed activity for the treatment dose through a dosimetry-based treatment planning procedure. During the treatment with ^{90}Y, the scouting procedure is usually performed with ^{99m}Tc macroaggregated albumin (^{99m}Tc-MAA). However, due to the difference in radioisotope shape, density, size and etc., localization can be inaccurate as the biodistribution of radionuclides may be different [7]. On the other hand, one of the advantages of ^{166}Ho therapy is the possibility to perform both scout and treatment procedures, reducing discrepancies between the planning and the execution of the procedure [2].

Since the use of ionizing radiation for human imaging or treatment purposes is strictly regulated by various standards, guidelines, and legislation [8-10], the administered activity of a radioisotope to patients should be measured and must not deviate by more than 5% of the prescribed administered activity [9]. The absorbed doses to target volumes should be also individually planned [10]. Since radioembolization is a complex treatment, various sources of uncertainty arise from the volume of interest, activity and SPECT measurements, and dosimetry software calculations [11-13].

Another significant concern is associated with ionizing radiation exposure control for personnel, encompassing not only the whole body examination but especially doses

to extremities, as well as the patient discharge from the hospital procedures. Since recent legislation and recommendations are mostly based on ^{131}I treatment, there is a lack of recommendations for the treatment with other therapeutic radionuclides. It is known [14] that after a typical patient's treatment with ^{90}Y microspheres, the dose rate could reach 2 μSv/h at 1 m from the patient, however after treatment with ^{166}Ho microspheres the dose rate can reach 40 μSv/h at 1 m from the patient [14]. The aim of this study was to evaluate occupational exposure levels and radiation protection and safety aspects when working with ^{166}Ho microspheres.

2. Materials and methods

2.1. Physical and chemical properties of ^{166}Ho

^{166}Ho microspheres' physical and chemical qualities enable them to be used effectively in the treatment of liver cancer. ^{166}Ho microspheres are considered as the medical devices rather than drugs or radiopharmaceuticals [4].

^{166}Ho microspheres are made of poly-L-lactic acid (PLLA), which contains ^{166}Ho isotope. ^{165}Ho is incorporated in the PLLA matrix during the manufacturing of microspheres, as well as a part of the ^{165}Ho is converted to ^{166}Ho [2 during activation in a nuclear reactor.

^{166}Ho emits high-energy beta particles (1774.32 keV; yield 48.8% and 1854.9 keV; yield 49.9%) and gamma rays (80.57 keV; yield 6.6% and 1379.40 keV; yield 0.9%), and has half-life of 26.8 h [10, 12, 16]. Diameters of microspheres are in the range of 15-60 μm, mass density - 1.4 g/cm^3. Microspheres are administered to a hepatic artery through a catheter. The paramagnetic properties of Holmium allow for determining its localization in the patient's body using MRI scan.

2.2. Patients and procedure planning

In 2022 and 2023, three patients with liver cancer were treated at Vilnius University Hospital Santaros Klinikos: two with hepatocellular carcinoma and one with metastatic cholangiocarcinoma.

The patient's selection criteria included various physical examinations, liver function tests, and detailed radiographic imaging to establish the extent of the disease. A multidisciplinary team consisting of interventional radiologists, oncologists, medical, surgical, and radiation oncologists, nuclear medicine experts, and others was responsible for the selection of suitable patients for radioembolization.

An important issue - the prevention of normal tissue (lungs) shunting during radioembolization treatment [16] was taken into consideration since lung shunt fraction is usually used for the estimation of the dose delivered to the lungs and it must be lower than 30 Gy in a single administration [2, 5, 16].

Patient dose calculation, treatment planning, and treatment evaluation were performed using the Q-Suite 2.1 software (Quirem BV). For the treatment planning, ^{166}Ho scout dose was used and ^{166}Ho treatment dose was administered to the patient approximately 2–3 weeks after the scout dose.

Both the scout and the treatment doses were administered during the interventional radiology (angiography) procedure by the physician accompanied by a nuclear medicine radiology technologist.

2.3. Image acquisition and reconstruction

The GE Infinia Hawkeye SPECT/CT equipment was used to acquire the planar and SPECT/CT images. ^{166}Ho-SPECT reconstruction parameters were pre-analyzed using the Jaszczak phantom. The corresponding data were collected using the protocol parameters listed in Table 1.

Table 1. SPECT/CT protocol parameters.

Main parameters	Values
Colimator	Low energy, high-resolution
Matrix size	128x128
Energy peak	81 keV ± 15%
Time per projecton	30 sec
Zoom	1.0
Scanning mode	H-mode, rotation mode
CT protocol	Low dose

The Philips Azurion 7 cath lab angiography system image processing technology (ClarityIQ) was used to perform interventional radiology procedures.

2.4. Dose rate and contamination monitoring

To measure occupation dose rate and patient dose rate, i.e. measurements ensuring that the patient could be discharged from the hospital, ATOMTEX AT1121 ambient dosimeter was used. NuviaTech Healthcare CoMo 170 contamination monitor was used for identification of the contamination level. The radiation exposure to medical staff was measured with POLIMASTER PM1610B-01 and EPD TruDose (Thermofisher scientific) dosimeters that have been metrologically verified by the Vilnius Metrology Centre. It is to be noted, that the individual monitoring of medical staff is performed constantly and the personnel is wearing legal passive dosimeters (thermoluminescent, TLD, and Optically Stimulated Luminescence, OSLD) for controlling personal dose equivalent $H_p(10)$ (chest area) and $H_p(0.07)$ (finger).

For monitoring of the working area exposure during one procedure NaCl pellets (read by OSL) were placed in different locations additionally (Fig. 1).

2.5. Extremity exposure evaluation

NaCl pellets (homemade at Skane University Hospital, Malmö, Sweden) were used to evaluate extremity doses. The linear detection range of NaCl pellets (OSLD) was 10 μGy - 1 Gy. The Risø TL/OSL reader (DTU Nutech, Denmark) was used for the readout of dosimeters. The calibration of individual dosemeters was performed using an internal ^{90}Sr/^{90}Y beta source. All dosemeters were enclosed in paper envelopes covered with plastic to prevent the OSLD's from contamination. Dosemeters were attached on the palm side of both hands of the interventional radiologist at 14 locations (on fingertips, palm, and wrist) and at the monitoring position (base of

the middle finger of the dominant hand (position 15) (Fig. 2, upper part).
For radiology technologists NaCl pellets were placed in 6 positions on the hands: left and right hand's thumbs, index and middle fingers tips (Fig. 2, bottom part).

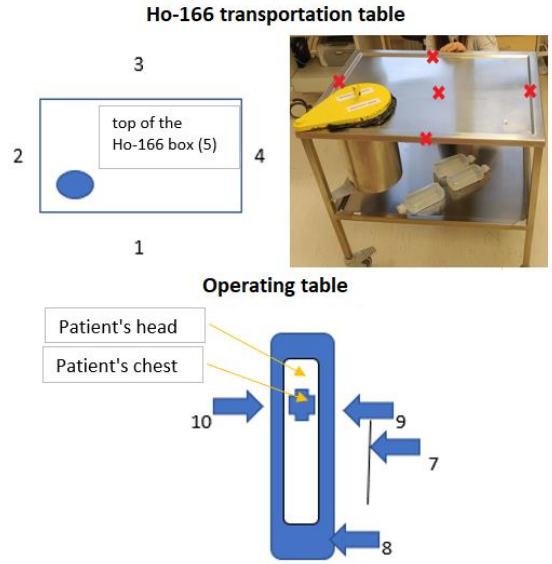

Fig. 1. Positions of NaCl pellets on the transportation table (shown above) and on the operating table (shown below).

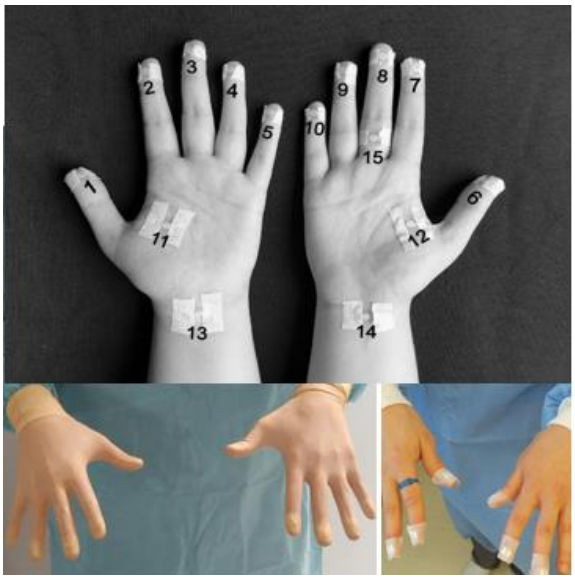

Fig. 2. Placement of the NaCl pellets (dosimeters) on the staff hands.

3. Results and discussion

3.1. Treatment planning and treatment procedure

The median administered activity for treatment planning (scout dose) was 150 MBq (dose range of 145-170 MBq) of ^{166}Ho, median administered activity for treatment was 9.6 GBq (dose range of 9.3-9.8 GBq). The quantitative assessment of the data after the scout dose delivery showed no radiation exposure risk for lung shunting (calculated lung dose was lower than 25 Gy). An example of the segmentation and dose delivery process is shown in Fig. 3.

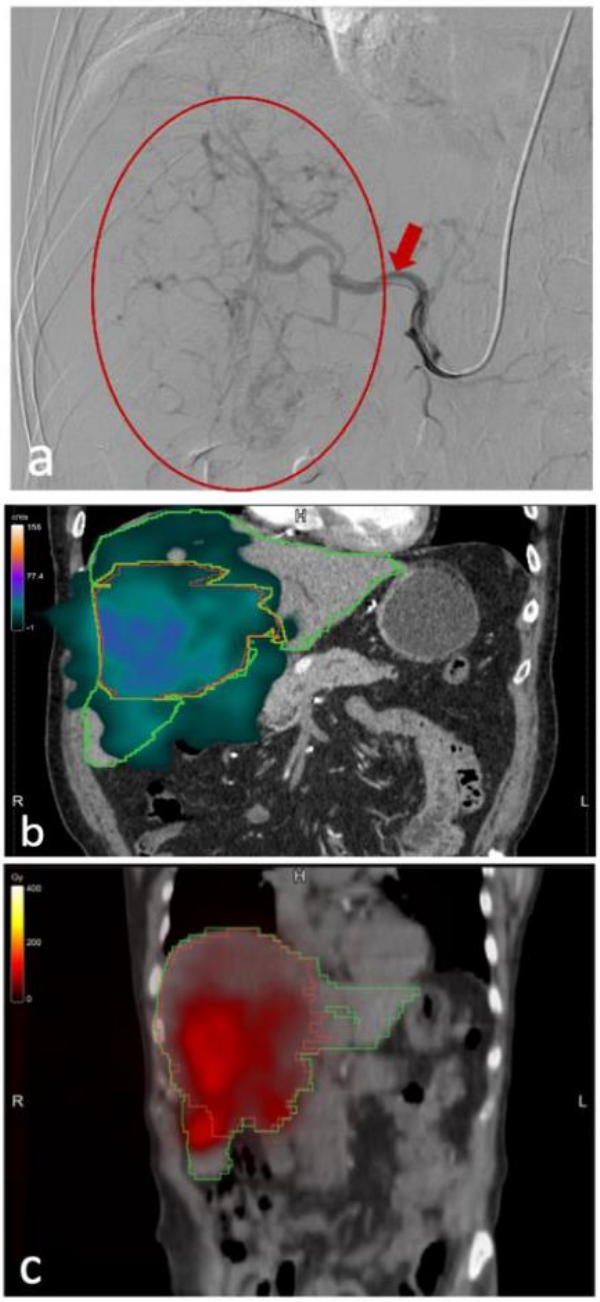

Fig. 3. Examples of segmentation and dose delivery process. (a) Hepatic artery selective digital subtraction angiography – well-vascularized liver tumor (circled in red) supplied by branches of the right hepatic artery (arrow); (b) ^{166}Ho microsphere distribution in hepatocellular carcinoma tumor visualized by SPECT/CT methodology with scout dose and (c) treatment dose.

The average duration of the interventional procedure for the administration of the ^{166}Ho scout dose was 90 min (the median radiation exposure time was 750 sec) and for the treatment dose 76 min (the median radiation exposure time was 482 sec). The average measured value of kerma-area product for the scout dose administration was 78.37 Gy·cm^2, and 36.29 Gy·cm^2 for the treatment dose. The residual activity in the re-usable administration ^{166}Ho system after the treatment procedure was from the range between 11.8-60.1 MBq.

3.2. Radiation safety

The ALARA (as low as reasonably achievable) principle is relevant for any procedure that involves exposure to ionizing radiation. In order to adequately assess the risk associated with the ^{166}Ho radioembolization procedure, the dose rate was measured at different treatment stages and at different distances from the source (Table 2).

Table 2. Measured dose rates.

Steps (source description and conditions)	Distance from the source (cm)	Dose rate (μSv/h)
^{166}Ho shielded package with ~150 MBq	10	15-20
^{166}Ho shielded package with ~10 GBq	100	140-180
The re-usable ^{166}Ho administration system with ~50 MBq after administration process	10	2-5
Exactly after ~9.5 GBq injection, at interventional radiologist position	5-10	180-210
After ~9.5 GBq injection, near the patient	300	2-5
The discharge process	100	24-32

The dose rate near the re-usable ^{166}Ho administration box (Fig. 4) after the patient's injection was found being up to 10 μSv/h.

Fig. 4. Shielded re-usable administration box for administration of ^{166}Ho microspheres (angio-suite – with Customer Kit and Delivery Set). The administration system contains an iodine contrast agent, saline solution, syringes, valves, a three-stopcock manifold, an administration vial with ^{166}Ho microspheres, and others.

Personnel doses (as evaluated from passive dosimeters) did not exceed dose levels measured under normal circumstances, thus, for the detailed analysis of radiation exposure of staff, the electronic personal dosimeters were used.

The contamination measurement showed that after the scouting and treatment of patients with ^{166}Ho, all surfaces in the operational theatre room were free from contamination.

3.3. Extremity exposure results

The dose distribution on the interventional radiologist extremities is shown in Table 3. The evaluated doses varied between 0.10-0.21 mGy. The comparison of the doses between the NaCl pellets worn at various positions on the physician's hands showed that the highest doses were received by the left-hand wrist, left-hand palm, right-hand index fingertip, and right-hand thumb tip. In general, the left hand received slightly higher doses.

Hand dose measurements performed on radiology technologists working with ^{166}Ho showed doses between 0.022-0.037 mGy.

Table 3. Distribution of doses on the interventional radiologist physician's hands.

No.	Dosimeter position	Estimated doses (mGy)
1	Left hand thumb tip	0.12
2	Left hand index finger tip	0.14
3	Left hand middle finger tip	0.13
4	Left hand ring finger tip	0.15
5	Left hand little finger tip	0.10
6	Left hand palm	0.18
7	Left hand wrist	0.21
8	Right hand thumb tip	0.19
9	Right hand index finger tip	0.18
10	Right hand middle finger tip	0.17
11	Right hand ring finger tip	0.12
12	Right hand little finger tip	0.10
13	Right hand palm	0.12
14	Right hand wrist	0.11
15	Base of the middle finger of the right hand	0.12

3.4. Working area exposure monitoring results

The NaCl pellets were placed close to the patient at different positions on and around the operating table (Fig. 1). The highest measured dose was found on the left side, the dosimeter position located close to the patient liver (Fig.1, No. 10; Table 4.). On the opposite side, dosimeter No. 9 showed almost five times lower dose compared to dosimeter No. 10.

On the surface of a wheelbarrow with a shielded reusable administration box for administration ^{166}Ho microspheres, the measured dose distribution was homogeneous (Table 4).

3.5. Limitations of the study

The main limitation of this study is the small number of patients, thus further studies on the personnel doses to extremities, whole-body doses, and exposures related to the discharge process are needed.

Table 4. Working area monitoring results.

No.	Dosimeter position	Estimated doses (mGy)
1	^{166}Ho transportation table (No. 1)	0.05
2	^{166}Ho transportation table (No. 2)	0.07
3	^{166}Ho transportation table (No. 3)	0.07
4	^{166}Ho transportation table (No. 4)	0.05
5	^{166}Ho transportation table (No. 5)	0.06
6	Waist level under the lead vest/skirt (interventional radiologist)	0.06
7	TV stand, patient level, 50-70 cm from the patient (No. 7)	0.08
8	Near the patient's feet, 1.5 meters from the ionizing radiation object (No. 8)	0.05
9	Right side, next to the patient, 5-10 cm from the ^{166}Ho radiation source (No. 9)	0.18
10	Left side, next to the patient, 5-10 cm from the ^{166}Ho radiation source (No. 10)	0.88

4. Conclusions

The correct treatment procedure can be achieved through careful pre-assessment, careful patient selection, and adequate dosimetry.

Since the results of the investigation have shown a high dispersion of measured extremity dose values, further analysis and optimization are needed for more precise dose measurements using NaCl pellets.

No radioactive contamination was found after the ^{166}Ho procedures in the operational theatre.

^{166}Ho treated patients were discharged after one day of hospital stay and the evaluated dose rate was lower compared to the discharge process after ^{131}I treatment. Nevertheless, after the radioembolization procedure, the patients were released with written instructions in order to limit the unnecessary exposure of their relatives and members of the public.

References

1. van Roekel C., Harlianto N.I., Braat AJAT., Prince JF., van den Hoven AF., Bruijnen RCG., Lam MGEH., Smits MLJ. Evaluation of the Safety and Feasibility of Same-Day Holmium-166 -Radioembolization Simulation and Treatment of Hepatic Metastases. J Vasc Interv Radiol, 2020, p. 1593-1599.

2. Stella M., Braat A. J., van Rooij R., de Jong H. W., Lam M. G. Holmium-166 radioembolization: Current status and future prospective. CardioVascular and Interventional Radiology, 2022, 45(11), p. 1634-1645.

3. d'Abadie P., Hesse, M Louppe, A. Lhommel R., Walrand S., Jamar F. Microspheres Used in Liver Radioembolization: From Conception to Clinical Effects. Molecules 2021, 26, 3966.

4. Drescher R., Köhler A., Seifert P., Aschenbach R., Ernst T., Rauchfuß F., Freesmeyer M. Clinical Results of Transarterial Radioembolization (TARE) with Holmium-166 Microspheres in the Multidisciplinary Oncologic Treatment of Patients with Primary and Secondary Liver Cancer. Biomedicines, 2023, 11, 1831. https://doi.org/10.3390/biomedicines11071831

5. Smits ML, Nijsen JF, van den Bosch MA, Lam MG, Vente MA, Huijbregts JE, van het Schip AD, Elschot M, Bult W, de Jong HW, Meulenhoff PC, Zonnenberg BA. Holmium-166 radioembolization for the treatment of patients with liver metastases: design of the phase I HEPAR trial. J Exp Clin Cancer Res, 2010. Jun 15;29(1):70. doi: 10.1186/1756-9966-29-70. PMID: 20550679; PMCID: PMC2903532.

6. Memon K, Lewandowski RJ, Kulik L, Riaz A, Mulcahy MF, Salem R. Radioembolization for primary and metastatic liver cancer. Semin Radiat Oncol., 2011, Oct;21(4):294-302. doi: 10.1016/j.semradonc.2011.05.004. PMID: 21939859; PMCID: PMC3221012.

7. Klaassen NJM., Arntz MJ., Gil A, A., Roosen J., Nijsen JFW. The various therapeutic applications of the medical isotope holmium-166: a narrative review. EJNMMI Radiopharm Chem, 2019.

8. International Atomic Energy Agency. Radiation Protection and Safety of Radiation Sources: International Basic.Safety Standards. Safety Standards, No. GSR Part 3. Vienna, 2014.

9. International Atomic Energy Agency. Radiation Protection and Safety in Medical Uses of Ionizing Radiation. Specific Safety Guides, No. SSG-46. Vienna, 2018.

10. Council Directive 2013/59/Euratom of 5 December 2013 laying down basic safety standards for protection against the dangers arising from exposure to ionising radiation, and repealing Directives 89/618/Euratom, 90/641/Euratom, 96/29/Euratom, 97/43/Euratom and 2003/122/Euratom, 2013.

11. Gear JI., Cox MG., Gustafsson J., Gleisner KS., Murray I., Glattingm G., Konijnenberg M. Flux, GD. EANM practical guidance on uncertainty analysis for molecular radiotherapy absorbed dose calculations. Eur J Nucl Med Mol Imaging, 2018. 45(13), p. 2456-2474.

12. Nijsen JF., Krijger GC., van Het Schip AD. The bright future of radionuclides for cancer therapy. Anti Cancer Agents Med Chem, 2007, 7(3), p. 271–290.

13. Braat AJAT., Prince JF., van Rooij, R., Bruijnen RCG., van den Bosch MAAJ., Lam MGEH. Safety analysis of holmium-166 microsphere scout dose imaging during radioembolisation work-up: A cohort study. Eur Radiol. 2018, 28(3), p. 920-928.

14. Broggio et al. Contact restriction time after common nuclear medicine therapies: spreadsheet implementation based on conservative retention function and individual measurements. J. Radiol. Prot. , 2023 , 43 021504

15. Welling M.M., Duszenko N., van Meerbeek M.P., Molenaar T.J.M., Buckle T., van Leeuwen F.W.B., Rietbergen D.D.D. Microspheres as a Carrier System for Therapeutic Embolization Procedures: Achievements and Advances. *J. Clin. Med.* 2023, 12, p. 918. https://doi.org/10.3390/jcm12030918

MEDICAL PHYSICS IN THE BALTIC STATES 16 (2023)

Proceedings of International Conference "Medical Physics 2023"
09-11 November 2023, Kaunas, Lithuania

CONSIDERATIONS FOR DEVELOPMENT OF THE RELEASE CRITERIA FOR PATIENTS AFTER RADIOPHARMACEUTICAL THERAPY

Larisa CHIPIGA[1,2,3], Anastasia PETRYAKOVA[1,4], Aleksandr VODOVATOV [1,5], Irina ZVONOVA[1], Andrey STANZHEVSKY[2], Daria VAZHENINA[2], Dmitry MAYSTRENKO[2]
[1]Saint-Petersburg Research Institute of Radiation Hygiene after Professor P.V. Ramzaev, Federal Service for Surveillance on Consumer Rights Protection and Human Well-Being, Saint-Petersburg, Russia [2]A. Granov Russian Scientific Center of Radiology and Surgical Technologies of the Ministry of Health of the Russian Federation, Saint-Petersburg, Russia [3]Almazov National Medical Research Centre of the Ministry of Health of the Russian Federation, Saint-Petersburg, Russia [4]The City Hospital No. 40 of the Kurortny District, Saint-Petersburg, Russia
[5]Saint-Petersburg State Pediatric Medical University, Saint-Petersburg, Russia

***Abstract*:** The accumulation of radioactive waste from patient after radionuclide therapy in public transport is the main problem for the radiation protection of the public. The aim of the study was to estimate activity of radionuclides in sewage tanks for different types of public transport from patients after radionuclide therapy as well as to assess the radiation exposure to people around. To avoid the accumulation, biological radioactive waste in public transport patient from remote regions must be identified as a separate group.

Keywords: radiopharmaceutical therapy, radiation safety, patient release, radioactive waste

1. Introduction

The fast growth of cancer radiopharmaceutical therapy (RPT) all over the world is associated with development and implementation of the high-efficient therapeutic radiopharmaceuticals. According to the United Nations Scientific Committee on the Effects of Atomic Radiation (UNSCEAR) 2020/2021 Report [1], the frequency of RPT has increased by 33% in the past decade. Market research of trends predicts that global nuclear medicine market will grow with an annual increase of 11% by 2028 [2]. In the Russian Federation, data on the number of RPT procedures is limited. Nevertheless, according to federal statistical surveillance forms, 10 235 procedures of RPT were performed in 2020. They consist of procedures with ^{131}I (72%) and osteotropic radiopharmaceuticals (^{89}Sr-chloride, ^{223}Ra-chloride, ^{153}Sm-oxabifor) (25%) [3]. However, the most promising targeted radiopharmaceuticals are based on prostate-specific membrane antigen (PSMA) for the treatment of castration-resistant prostate cancer and peptides for the treatment of neuroendocrine tumors with a β-emitter ^{177}Lu and an α-emitter ^{225}Ac [4-5].

Radiation safety of public (people in contact with patient released after RPT) is based on compliance with established criteria for external dose rate. Patient release from hospital after RPT is based on compliance with patient release criteria: dose rate at 1 m from patient and/or residual radionuclide activity in patient's body which ensure that dose limits for public are not exceeded [6-12]. According to the national radiation protection legislation in the Russian Federation, a patient can be released if the dose rate of gamma-ray and x-ray exposure from a patient is equal to or less than established patient release criteria. Patient release criteria used in national practice consider the reduction of radionuclide activity due to the radioactive decay but do not consider the biological excretion of radiopharmaceutical from a patient body. Hence, patient release criteria after estimated using that approach are unreasonable conservative [7-8].

Consideration of the biological excretion of radiopharmaceutical can make patient release criteria after RPT more flexible due to faster reduction of the residual radionuclide activity in a patient body [6]. Radiopharmaceuticals excrete from a patient body primarily with urine and/or feces that lead to accumulation of radionuclides in biological waste. There are specific criteria for classifying waste as a radioactive waste in accordance with Resolution of the Government of the Russian Federation No. 1069. It makes biological radioactive waste management one of the main problems in RPT in terms of radiation safety.

Radionuclides eliminated with biological waste from a patient after RPT can accumulate in sewage system in hospital or residential buildings as well as in sewage tanks in public transport [14-15]. Nonuniform geographic distribution of the RPT departments in the Russian Federation and their concentration in major

cities lead to the large flow of nonresident patients who need to return home using public transport.

This study was aimed at the estimation of the radionuclide activity in biological waste from patients after RPT in public transport (short-distance train/intercity bus/long-distance train/plane) and radiation exposure of members of the public surrounding such patient.

2. Materials and methods

The current study was performed for the following radiopharmaceuticals: ^{177}Lu-PSMA, ^{225}Ac-PSMA, ^{177}Lu-DOTATATE, ^{225}Ac-DOTATATE, Na^{131}I, ^{131}I-mIBG, ^{89}Sr-chloride, ^{223}Ra-chloride, ^{153}Sm-oxabifor. Excreted radionuclide activity from the patient body was determined according to the excretion model (1):

$$A_{excreted}(t) = A_0 \cdot exp(-\lambda_{phys} t) \; \Sigma \, a_i (1-exp(-\lambda_{bio\ i}\, t)), \; MBq \quad (1)$$

where $A_{excreted}(t)$ – excreted radionuclide activity from the patient body during the period t after the radiopharmaceutical injection; A_0– administered activity; a_i – the fraction eliminated with a biological elimination constant $\lambda_{bio\ i}$; λ_{phys} – physical decay constant; $\lambda_{bio\ i}$ – biological elimination constant.

Parameters for the radiopharmaceutical excretion model are presented in table 1.

Radionuclide activity excreted into sewage tank in public transport tank (bio-toilets) was estimated based on the time of travel.

Table 1. Parameters for the radiopharmaceutical excretion model (1).

Radiopharmaceutical	A_0, MBq	λ_{phys}, day^{-1}	a_1	a_2	$\lambda_{bio\ 1}$, day^{-1}	$\lambda_{bio\ 2}$, day^{-1}
^{177}Lu-PSMA [16]	7 500	0.11	0.7	0.3	9.6	0. 2
^{177}Lu-DOTA-TATE [17]			0.7	0.3	6.6	0.2
^{225}Ac-PSMA [16]	6.5	0.07	0.7	0.3	9.6	0.2
^{225}Ac-DOTA-TATE [17]			0.7	0.3	6.6	0.2
^{131}I-mIBG [18]	11 000	0.09	0.36	0.63	5.5	0.5
^{131}I-NaI (thyrotoxi-cosis) [19-21]	600		0.2	0.8	2.0	0.01
^{131}I-NaI (thyroid cancer) [19-21]	7 500		0.9	0.1		
^{89}Sr-chloride [22]	150	0.01	0.33	0.37	0.7	0.1
^{223}Ra-chloride [23,24]	4	0.06	1	-	0.5	-
^{153}Sm-oxabifor [25]	3 000	0.36	0.4	0.6	13.7	1.2

The following scenarios of public transport usage were considered based on the distance between hospital and patient home:

- travel time by short-distance train and intercity bus is 2 hours;
- travel time by long-distance train is 48 hours;
- travel time by plane is 7 hours.

It was considered that patient gets to a train or a bus in one hour and to a plane in three hours after release from hospital. The transport tank volume used to determine specific activity was defined as 50 liters for a short-distance train or intercity bus and as 100 liters for a long-distance train or a plane.

Dose rate from the patient with injected radiopharmaceutical and dose rate from the transport tank were calculated using Monte-Carlo simulation using MCC3D software (Peter the Great Polytechnic University, St.Petersburg, Russian Federation). Patient model was created as uniform reference phantom with density 1.079 g/cm3 corresponding to an adult person [26, 27]. The phantom included the following parts: legs – truncated cone; body – elliptic cylinder; head and neck – circular cylinder and elliptic cylinder. Two ideal gamma-ray detectors (1 cm^2) were fitted at 1 m in the front and the side of the phantom and at 0.7 m above the ground. Sewage tank was created as uniform cylinder with density 1 g/ml (diameter 36 cm for 50 liter tank and diameter 44 cm for 100 liter tank). An ideal gamma-ray detector was fitted at 1 m in the front of the cylinder. For dose rate calculation spectrums of radionuclides were used from [28].

Effective dose rate at 1 m from patient or sewage tank was determined according to equation (2):

$$\dot{D} = \Sigma \frac{A \cdot 3600 \cdot N_i \cdot D(E_i)}{N' \cdot S}, \; \mu Sv/h \quad (2)$$

where A – radionuclide activity, MBq (table 1); N_i – number of detected counts; N' – number of initiated counts in MCC3D software (10^8); $D(E_i)$ – effective dose per unit fluence of mono-energy photons during an external exposure by parallel beam in anterior-posterior projection, 10^{-12} Sv·cm^2 (table 8.5 in NRB-99/2009); S – detector square, cm^2, 3600 – number of seconds per hour. Dose rate from phantom was calculated using the detector with the largest number of detected counts. Dose rates from ^{225}Ac and ^{223}Ra were determined as cumulative dose rate from radionuclides and their daughter radionuclides.

Time of patient release from hospital and transport boarding time were determined using patient release criteria after RPT. Administered activities and dose rates from patient with injected radiopharmaceutical were compared with national patient release criteria:

- 0.4 GBq residual activity in patient and 20 μSv/h at 1 m distance from the patient for ^{131}I (NRB-99/2009);
- 9 GBq residual activity in patient and 100 μSv/h at 1 m from patient for ^{153}Sm (NRB-99/2009);

– 6.1 GBq residual activity in patient and 29 μSv/h at 1 m from patient for ^{177}Lu [4];
– 3 μSv/h at 1 m from patient for other radionuclides (Sanitary Rules and Norms 2.6.1.2368–08).

3. Results

Estimated dose rate from phantom with administered activity are presented in table 2. Results demonstrated that residual activity and dose rate from patient after RPT with ^{225}Ac-PSMA, ^{225}Ac-DOTATATE, ^{89}Sr-chloride, ^{223}Ra-chloride, ^{153}Sm-oxabifor, and Na^{131}I for thyrotoxicosis treatment do not exceed the patient release criteria after RPT. Hence, patient can be release from hospital immediately after the injection of radiopharmaceutical. Patients can be release from hospital in 10 hours and 20 hours after RPT with ^{177}Lu-PSMA and ^{177}Lu-DOTA-TATE, respectively. Patients can be released from hospital in 130 hours and 48 hours after RPT with ^{131}I-mIBG and with ^{131}I-NaI for thyroid cancer treatment, respectively.
Excreted activities from patient after RPT in transport, activity concentrations in sewage tanks, and estimated dose rates at 1 m from sewage tanks are presented in table 3.

The highest radionuclide activity will accumulate in sewage tanks from patients after RPT with ^{153}Sm-oxabifor for considered scenarios of use of public transport. Dose rate from sewage tank with radionuclide waste from one patient in this case will be at least 3.3 μSv/h. Hence, dose from sewage tank during 12 hours at 2 m will be at least 10 μSv.

Table 2. Dose rate from patient after RPT.

Radiopharmaceutical	A_0, MBq	Dose rate, μSv/h
^{177}Lu-PSMA	7 500	63
^{177}Lu-DOTATATE		
^{225}Ac-PSMA	6.5	0.5
^{225}Ac-DOTATATE		
^{131}I-mIBG	11 000	310
^{131}I-NaI (thyrotoxicosis)	600	17
^{131}I-NaI (thyroid cancer)	7 500	210
^{89}Sr-chloride	150	0.002
^{223}Ra-chloride	4	0.1
^{153}Sm-oxabifor	3 000	34

Table 3. Excreted activity in transport from patient after RPT, activity concentration in transport tanks, and estimated dose rate at 1 m from transport tanks.

Radiopharmaceutical	Transport type	Excreted activity in transport, MBq	Activity concentration in sewage tank in public transport, Bq/g	Dose rate, μSv/h
^{177}Lu-PSMA	short-distance train or intercity bus	62	1240	0.5
	long-distance train	800	8000	6.8
	plane	165	1650	1.4
^{177}Lu-DOTA-TATE	short-distance train or intercity bus	50	1000	0.4
	long-distance train	415	450	3.5
	plane	120	1200	1.0
^{225}Ac-PSMA	short-distance train or intercity bus	1.2	24	0.02
	long-distance train	2.7	27	0.04
	plane	1.1	11	0.01
^{225}Ac-DOTA-TATE	short-distance train or intercity bus	0.8	16	0.01
	long-distance train	2.7	27	0.04
	plane	1.4	14	0.02
^{131}I-mIBG	short-distance train or intercity bus	24	480	0.19
	long-distance train	340	3400	5.8
	plane	77	770	1.3
Na^{131}I (thyro-toxicosis)	short-distance train or intercity bus	16	310	0.13
	long-distance train	88	880	1.5
	plane	37	370	0.6
Na^{131}I (thyroid cancer)	short-distance train or intercity bus	17	337	0.14
	long-distance train	115	1150	1.9
	plane	42	420	0.7
^{89}Sr-chloride	short-distance train or intercity bus	5	100	<0.001
	long-distance train	66	660	<0.001
	plane	15	150	<0.001
^{223}Ra-chloride	short-distance train or intercity bus	0.06	1.2	<0.001
	long-distance train	0.74	7.4	0.002
	plane	0.17	1.7	<0.001
^{153}Sm-oxabifor	short-distance train or intercity bus	770	15400	3.3
	long-distance train	990	9900	3.2
	plane	540	5400	1.8

Radionuclide activity concentrations in sewage tanks from patients after RPT exceed the specific radionuclide waste criteria for all radiopharmaceuticals. Criteria are exceeded for any time a patient spends in transport and even for one-time use of the bio-toilet. This waste can be detected during the radiation control of transport unit. To avoid radionuclide detection, patient must not use the public transport (or bio-toilet in transport) until the radionuclide activity in biological waste is reduced below the acceptable level (Table 4).

To avoid the accumulation of radioactive waste in public transport it is necessary to implement the differentiated approach for patient release after RPT. Nonresident patients who need to return home using public transport must be identified as a separate group. Transportation of a patient by special medical transport or restriction of a patient traveling by public transport, for example, using hospital admission until the radionuclide activity in biological waste is reduced below the acceptable level should be considered.

These solutions to avoid the accumulation of the radioactive waste in transport from patient after RPT are not practicable. Transportation of a patient by special medical transport is limited by the distance between hospital and patient home. Hence, this solution is available only for patients from the nearby regions. Time of hospital admission for a patient for reduction of radionuclide activity in biological waste below the acceptable level reaches months (average about two weeks) (see table 4). That leads to non-justified increasing in the cost and availability of RPT. However, if patient release criteria after RPT will be softened excreted radionuclide activity in biological waste in transport will increase. Due to the low doses to public associated with accumulated radionuclide activity from patient after RPT in public transport, it is reasonable to exclude biological waste from patients after nuclear medicine procedures into a separate radioactive waste category.

Table 4. Time until activity in biological waste reduce under the acceptable level and excreted activity transport in transport.

Rdiopharmaceutical	Specific radioactive waste criteria, Bq/g	Transport type	Time for activity reduction, day	Excreted activity in transport, MBq
^{177}Lu-PSMA	25	short-distance train or intercity bus	14	1.1
		long-distance train	21	2.5
		plane	17	2.5
^{177}Lu-DOTA-TATE		short-distance train or intercity bus	17	1.1
		long-distance train	30	2.5
		plane	23	2.5
^{225}Ac-PSMA	0.05	short-distance train or intercity bus	12	0.003
		long-distance train	21	0.005
		plane	17	0.005
^{225}Ac-DOTA-TATE		short-distance train or intercity bus	14	0.003
		long-distance train	32	0.005
		plane	22	0.005
^{131}I-mIBG	0.62	short-distance train or intercity bus	21	0.03
		long-distance train	26	0.06
		plane	16	0.06
Na^{131}I (thyro-toxicosis)		short-distance train or intercity bus	22	0.03
		long-distance train	47	0.06
		plane	34	0.06
Na^{131}I (thyroid cancer)		short-distance train or intercity bus	27	0.03
		long-distance train	52	0.06
		plane	39	0.06
^{89}Sr-chloride	5.3	short-distance train or intercity bus	24	0.3
		long-distance train	29	0.5
		plane	17	0.5
^{223}Ra-chloride	0.14	short-distance train or intercity bus	4	0.05
		long-distance train	7	0.01
		plane	5	0.02
^{153}Sm-oxabifor	19	short-distance train or intercity bus	3	1.1
		long-distance train	4	
		plane	4	

4. Conclusions

The accumulation of radioactive waste from patient after RPT in public transport is the main problem during release of nonresident patient after RPT. Release of patient after RPT must be based on differentiated approach depending on the patient place of residence, transport type, and traveling time. Patient who lives in remote regions must be identified as a separate group,

and to avoid the accumulation of biological radioactive waste in public transport, should be transported by special medical transport or by own car.

It is reasonable to exclude biological waste from patients after nuclear medicine procedures into a separate waste category.

References

1. Evaluation of Medical Exposure to Ionizing Radiation. United Nations Scientific Committee on the Effects of Atomic Radiation (UNSCEAR) 2020/2021 Report Volume I. Annex A.
2. Research of MarketsandMarkets. Available at: https://www.marketsandmarkets.com/Market-Reports/radiopharmaceuticals-market-417.html (Accessed 2 September 2023).
3. Chipiga L., Ladanova E., Vodovatov A., Zvonova I., Mosunov A., Naurzbaeva L., Ryzhov S. Trends in the development of nuclear medicine in the Russian Federation for 2015–2020. Radiatsionnaya Gygiena = Radiation Hygiene, 2022. Vol. 15, No 4. p. 122-133. (In Russ.) https://doi.org/10.21514/1998-426X-2022-15-4-122-133
4. Kratochwil C., Bruchertseifer F., Rathke H., Bronzel M., Apostolidis C., Weichert W., Haberkorn U., Giesel F.L., Morgenstern A. Targeted α-Therapy of Metastatic Castration-Resistant Prostate Cancer with 225Ac-PSMA-617: Dosimetry Estimate and Empiric Dose Finding. J Nucl Med, 2017. Vol. 58, No 10. p. 1624-1631. doi: 10.2967/jnumed.117.191395.
5. Kratochwil C., Giesel FL., Stefanova M., Benešová M., Bronzel M., Afshar-Oromieh A., Mier W, Eder M., Kopka K., Haberkorn U. PSMA-Targeted Radionuclide Therapy of Metastatic Castration-Resistant Prostate Cancer with 177Lu-Labeled PSMA-617. J Nucl Med, 2016. Vol. 57, No 8. p. 1170-6. doi: 10.2967/jnumed.115.171397.
6. Chipiga L., Zvonova I., Vodovatov A., Petryakova A., Stanzhevsky A., Vazhenina D., Smoliarchuk M., Ryzhov S. Improvement of the approach to definition of patient release criteria after radionuclide therapy. Radiatsionnaya Gygiena = Radiation Hygiene, 2023. Vol. 16, No 2. p. 19-31. (In Russ.) https://doi.org/10.21514/1998-426X-2023-16-2-19-31
7. Balonov M., Golikov V., Zvonova I. Radiological criteria for patient release from clinic after radionuclide therapy of brachytherapy with sealed source implantation. Radiatsionnaya Gygiena = Radiation Hygiene, 2009. Vol. 2, No 4. p. 5-9. (In Russ.)
8. Zvonova I., Balonov M., Golikov V. Release criteria for patients having undergone radionuclide therapy and criteria for their crossing the state border of the Russian Federation // Radiation Protection Dosimetry, 2011. Vol. 147, No 1-2. p. 254-257. doi: 10.1093/rpd/ncr308.
9. International Atomic Energy Agency, Release of Patients After Radionuclide Therapy, Safety Reports Series No. 63, IAEA, Vienna (2009).
10. International Atomic Energy Agency. Radiation protection and safety of radiation sources: international basic safety standards. Interim edition. Safety Standards Series No. GSR Part 3 (interim). IAEA, Vienna (2011).
11. International Commission on Radiological Protection. Release of patients after therapy with unsealed radionuclides. ICRP Publication 94. Ann ICRP/ 2004. 34(2).
12. U.S. Nuclear regulatory commission. Draft regulatory guide DG-8057. "Release of patients a administered radioactive material", Washington, DC, 2019.
13. INTERNATIONAL ATOMIC ENERGY AGENCY, Management of radioactive waste from the use of radionuclides in medicine IAEA, Vienna (2000).
14. Chipiga L., Vodovatov A., Zvonova I., Stanzhevsky A., Petryakova A., Anokina E., Velichkina K., Ryzhov S. Management of biological waste of patients after radionuclide therapy. Radiatsionnaya Gygiena = Radiation Hygiene, 2022. Vol. 15, No 2. p. 19-30. (In Russ.) https://doi.org/10.21514/1998-426X-2022-15-2-19-30
15. Graves SA. Radiation Safety Considerations of Household Waste Disposal After Release of Patients Who Have Received [177Lu]Lu-PSMA-617. J Nucl Med, 2023. 13:jnumed.123.265750. doi: 10.2967/jnumed.123.265750.
16. Kurth J., Krause B, Schwarzenböck S., et al. External radiation exposure, excretion, and effective half-life in 177Lu-PSMA-targeted therapies //EJNMMI research, 2018. Vol. 8, No 1. p. 1-11. https://doi.org/10.1186/s13550-018-0386-4.
17. Wehrmann C., Senftleben S., Zachert C., Müller D., Baum R.P. Results of individual patient dosimetry in peptide receptor radionuclide therapy with 177Lu DOTA-TATE and 177Lu DOTA-NOC. Cancer Biother Radiopharm, 2007. Vol. 22, No 3. p. 406-416. doi: 10.1089/cbr.2006.325.
18. Ott R., Tait D., Flower M., et al. Treatment planning for 131I-mIBG radiotherapy of neural crest tumours using 124I-mIBG positron emission tomography // The British journal of radiology,1992. Vol . 65, No 777. p. 787-791. https://doi.org/10.1259/0007-1285-65-777-787
19. International Commission on Radiological Protection. Radiation Dose to Patients from Radiopharmaceuticals. ICRP Publication 53. Ann. ICRP. 1988. 18 (1-4).
20. Zvonova I., Likhtarev I., Nikolaeva A.. Thyroid irradiation accompanying radioiodine examination of patients with thyroid diseases. Medical radiology, 1982. Vol. 4, p. 42-44 (In Russ.)]
21. IAEA-TECDOC-1608 Nuclear Medicine In Thyroid Cancer Management: A Practical Approach IAEA, Vienna, 2009, p.141
22. ICRP, 2016. Occupational Intakes of Radionuclides: Part 2. ICRP Publication 134 Ann. ICRP 45(3/4), 1–352.
23. Yoshida K., Kaneta T., Takano S. et al. Pharmacokinetics of single dose radium-223 dichloride (BAY 88-8223) in Japanese patients with castration-resistant prostate cancer and bone metastases //Annals of nuclear medicine. 2016. Т. 30, №. 7. С. 453-460. https://doi.org/10.1007/s12149-016-1093-8.
24. Höllriegl V., Petoussi-Henss N., Hürkamp K. et al. Radiopharmacokinetic modelling and radiation dose assessment of 223Ra used for treatment of metastatic castration-resistant prostate cancer //EJNMMI physics, 2021. Vol. 8, No 1. p. 1-18. https://doi.org/10.1186/s40658-021-00388-1.
25. Parlak Y., Gumuser G., Sayit E. Samarium-153 therapy for prostate cancer: the evaluation of urine activity, staff exposure and dose rate from patients // Radiation Protection Dosimetry, 2015. Vol. 163, No 4. p. 468-472. doi: 10.1093/rpd/ncu237.
26. ICRP, 2009. Adult Reference Computational Phantoms. ICRP Publication 110. Ann. ICRP 39 (2).
27. International Commission on Radiological Protection. 1975. Report of the task group on Reference Man. ICRP Publication 23. Oxford: Pergamon Press.
28. Database NNDC. Available at: https://www.nndc.bnl.gov/nudat3/ (Accessed 2 September 2023)

MEDICAL PHYSICS IN THE BALTIC STATES 16 (2023)

Proceedings of International Conference "Medical Physics 2023"
09-11 November 2023, Kaunas, Lithuania

ON POTENTIAL ENHANCEMENT OF DOSE GELS SENSITIVITY USING VARIOUS NANOPARTICLE ADDITIVES

Mantvydas MERKIS[1], Jurgita LAURIKAITIENE[1], Mindaugas ILICKAS[2], Diana ADLIENE[1]
[1]Department of Physics, Kaunas University of Technology, Kaunas, Lithuania
[2]Institute of Materials Sciences, Kaunas University of Technology, Kaunas, Lithuania
mantvydas.merkis@ktu.edu

***Abstract*:** Gel dosimeters are the only radiation dosimeters that are able to capture truly three-dimensional dose distribution with high spatial resolution and tissue equivalency. However, the relatively low sensitivity of gel dosimeters limits their application in clinical practice. The sensitivity of gel dosimeters could be improved by adding metal nanoparticles. Sensitivity enhancement of dose gels containing metal nanoparticles is achieved due to increased radiation interaction probability. In this work, the sensitivity enhancement using three types of nanoparticles (Au, Cu/Cu_2O, and ZnO) as additives to nMAG and NIPAM dose gels was investigated. Home-synthesized nanoparticles were used for investigations. Dose gel samples were irradiated with 120 keV X-ray photons and analyzed using photospectrometric technique. It was possible to achieve the sensitivity enhancement for nMAG dose gels with metal particle additives only. Particularly interesting results were acquired by adding ZnO nanoparticles to dose gel which resulted in a 31 % increase in gel sensitivity.

Keywords: Gel dosimetry, dose enhancement, QA, photospectrometry, metal nanoparticles.

1. Introduction

Rapidly advancing radiation therapy techniques require more sophisticated verification methods to ensure appropriate dose delivery to the treatment volume. Gel dosimeters are among the most promising candidates for this purpose due to their ability to capture volumetric dose distribution with practically unlimited spatial resolution depending only on the imaging method. Moreover, dose gels are tissue-equivalent in terms of absorption of ionizing radiation [1].

However, one of the main drawbacks of gel dosimeters is the request for a complicated imaging technique (MRI) in order to extract dose distribution information from radiation-polymerized volume [2]. CT imaging of dosimetric gels could be a promising alternative, however at this time CT imaging is inefficient due to relatively low sensitivity.

In order to extend the usage of gel dosimeters in clinical practice, their dose sensitivity must be improved. The addition of metal nanoparticles to dose gels is a viable approach to achieve improved sensitivity [3]. Moreover, this approach allows for the adaptation of gel dosimeters as a medium for the investigation of radiation radiation-sensitizing effect of nanoparticles in the tissue. Gold nanoparticles are most widely used to achieve dose enhancement in dosimetric gels [4], however, high price reduces their applicability in clinical practice [5]. The application of cost-effective alternatives could be one of the solutions to this problem.

Performing this investigation Au, Cu/Cu_2O, and ZnO nanoparticles were added to nMAG and NIPAM dosimetric gels in order to compare dose dose-enhancing effect of widely used Au nanoparticles with significantly less expensive alternatives provided by the addition of Cu/Cu_2O and ZnO nanoparticles to the gels.

2. Materials and Methods

2.1. Fabrication of dosimetric gels

8 series of samples were fabricated: nMAG dose gel, nMAG dose gel with Au, Cu/Cu_2O, and ZnO nanoparticles, NIPAM dose gel, and NIPAM dose gel with Au, Cu/Cu_2O, and ZnO nanoparticles.

nMAG dosimetric gel was prepared based on the procedure described in [6]. 8% w/w of gelatin (300 bloom, Sigma-Aldrich) was melted in 83.8% w/w of distilled water (Eurochemicals) under stirring in a magnetic stirrer at 45 °C. After full dissolution of the gelatin, the solution was cooled down to 35 °C. When the required temperature was reached methacrylic acid (8% w/w, purity ≥99%, Sigma-Aldrich) was added drop by drop to the solution under continuous stirring. After 10 minutes 10 mM of tetrakis (hydroxymethyl phosphonium sulfate) (70-75% in H_2O, Sigma-Aldrich) was added to the solution. Stirring continued for the additional 2 minutes. The fabricated solution was poured into

standard square-shaped PMMA cuvettes and stored for 24 h in a cool, dark place.

NIPAM dosimetric gel was prepared based on the procedure described by [7]. Gelatin (300 bloom, Sigma-Aldrich) was poured into the glass with 71% w/w of distilled water (Eurochemicals) and heated up to 50 °C under stirring. After that, N,N′-methylene-bis-acrylamide cross-linker (3% w/w, purity ≥99%, Sigma-Aldrich) was added and stirring continued for 15 min. After full dissolution of the cross-linker, the solution was cooled down to 37 °C. When the required temperature was reached, N-Isopropylacrylamide (3% w/w, purity ≥99%, Sigma-Aldrich) was added. After dissolution of this monomer, 10 mM of tetrakis (hydroxymethyl phosphonium sulfate) (70-75% in H_2O, Sigma-Aldrich) mixed with the remaining part of the water (17.8% w/w) was added to the solution. After 2 min of stirring the prepared dose gel was poured into standard square-shaped PMMA cuvettes and stored in cool, dark environment.

Addition of nanoparticles to nMAG and NIPAM dose gels was implemented after addition of monomer. 30% w/w concentrated the gel solution was used for adding of Cu/Cu_2O and ZnO nanoparticles; 20% w/w concentrated gel solution was used with Au nanoparticles.

Au nanoparticle solution (5 nm) was purchased from Sigma-Aldrich; ZnO nanoparticles were synthesized using combustion technique [8] and 3% w/w solution has been prepared; Cu/Cu_2O nanoparticle solution was laboratory-synthesized using the procedure described by Khan et. al. [9].

2.2. Irradiation of dosimetric gels

Each fabricated batch of dose gels was irradiated to 1Gy, 2 Gy, 3 Gy, 4 Gy, 5 Gy doses using orthovoltage X-ray therapy machine Gulmay D3225. 120 keV photons were used for irradiation. Cuvettes were long-side positioned on the treatment table during the irradiation. Irradiated cuvettes were stored in a dark place for 24 hours to allow for post-irradiation processes to settle.

2.3. Analysis of dosimetric gels

The dose response of gels was analyzed using Ocean Optics USB 650 UV-Vis spectrometer. The dose response points of each dosimeter were acquired at a wavelength of 650 nm where a relatively high signal amplitude was achieved with a low noise level. The sensitivity of dosimetric gels was identified by a slope of linearly approximated absorbance–dose relationship.

3. Results and Discussion

Measured UV-Vis spectra of experimental samples containing nanoparticles indicated small plasmonic peaks corresponding to Au, ZnO, and Cu/Cu_2O nanoparticles (Fig.1). The peak at 354 nm could be attributed to ZnO nanoparticles [10], the peak at 500 nm corresponded to Cu_2O and Cu nanoparticles [11-12], plasmonic peak at 540 nm could be associated with Au nanoparticles [13].

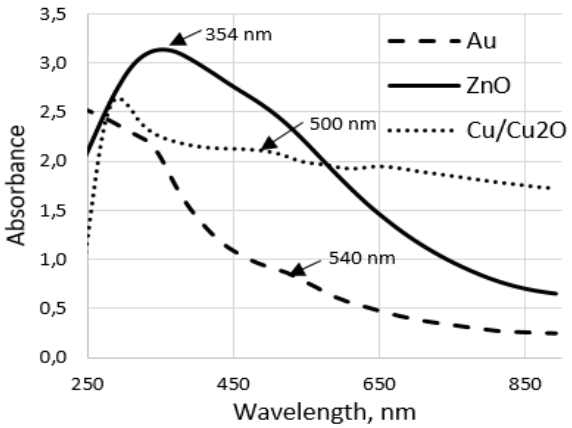

Fig. 1. UV-Vis spectra of nMAG gels enriched with nanoparticles.

Considerable dose sensitivity enhancement was achieved by adding Au and ZnO nanoparticles to nMAG dose gel, while the sensitivity enhancement effect in NIPAM dose gel was not observed. It was suggested that the incompatibility between dosimetric gel constituents and nanoparticles which might be dissolved into ions or aggregated to the clusters was the main reason for such result. In addition, nMAG and NIPAM dose gels containing Cu/Cu_2O nanoparticles showed no response to the irradiation, indicating polymerization suppressive effect on Cu/Cu_2O particles.

UV-Vis spectra of irradiated nMAG+Au gels indicated increased absorbance as compared to initial nMAG gels through the entire spectral range. However, plasmonic peak of Au was barely visible due to high absorbance in the samples with dose gel. Dose response curve derived from absorbance spectra at wavelength of 650 nm indicated significantly higher dose sensitivity of the gel comparing to the original nMAG dosimetric gel formulation. Addition of Au nanoparticles allowed to increase dose sensitivity of nMAG dose gel by 42% from 0.212 Gy^{-1} to 0.300 Gy^{-1}. Both samples with and without Au nanoparticles demonstrated almost perfectly linear dose response (Fig.2). Sensitivity enhancement was significantly higher comparing to similar study of Farahani et al. [13] where dose enhancement of 19 % was achieved. However, in the mentioned study slightly different gel formulation was irradiated at higher energy (380 keV) and MRI based dose readout method was used.

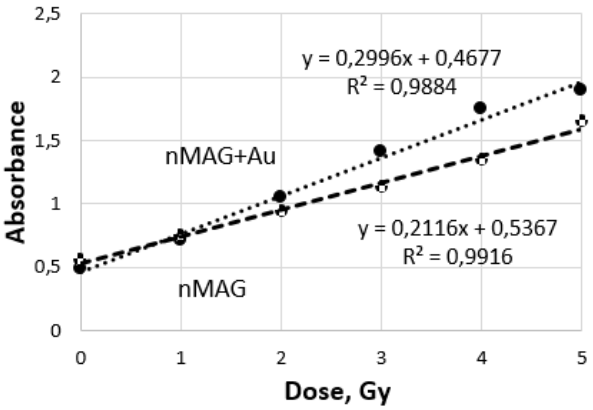

Fig. 2. Dose response curves: nMAG dose gel (dashed line), nMAG+Au NPs dose gel (dotted line)

Similar results were acquired by adding less expensive ZnO nanoaprticles to nMAG dosimetric gel. UV-Vis spectra demonstrated increasing light absorption ability of the gel with the increased irradiation dose (Fig. 3) indicating also merging of ZnO plasmonic peak with the absorbance spectrum at higher doses.

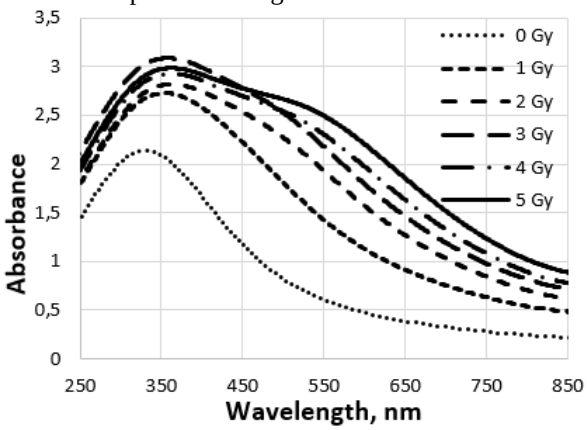

Fig. 3. UV-Vis spectra of nMAG+ZnO gel irradiated to different doses.

ZnO nanoparticles demonstrate lower dose enhancing capability comparing to Au nanoparticles. Dose response curve obtained at 650 nm indicated the increase of nMAG dose sensitivity by 31 % (from 0.212 Gy^{-1} to 0.276 Gy^{-1}) when ZnO nanoparticles were added to the gel (Fig.4).

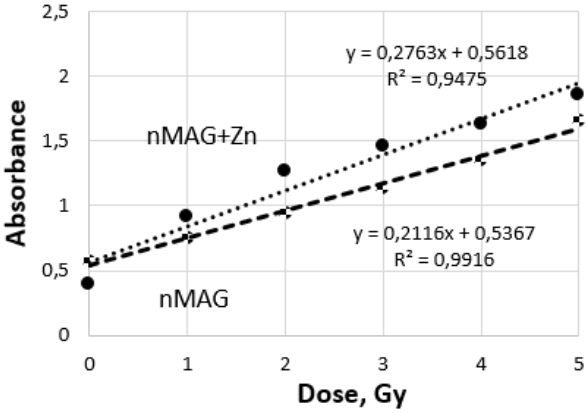

Fig. 4. Dose response curves of nMAG dose gel when ZnO nanoparticles were added

Since photoelectric interaction is proportional to the atomic number of the element and dominates at low irradiation energies, lower dose sensitivity enhancement of gels containing ZnO nanoparticles compared to gels containing Au NPs could be explained by lower atomic number of Zn. According to information provided in the literature dose enhancement effect achieved in this study was significantly higher as indicated by other authors. For example, Mustaqim et al [14] have achieved sensitivity enhancement by only 3 % irradiating similar dose gel formulation containing methylene blue with 6 MeV photons. One of the reasons why significantly higher dose sensitivity was achieved in our investigation might be low irradiation energy 120 keV, however more detailed investigation should be performed in order to answer this question.

Addition of ZnO nanoparticles negatively affected linearity of dose response within selected range. Calculated R^2 of linear approximation of response points of nMAG + ZnO gel was 0.946 while for the original nMAG dose gel formulation it was 0.992. Dose response deviations from the linear tendency was explained by the inhomogeneous distribution of ZnO nanoparticle powder in the dose gel. This effect was not present in nMAG + Au gel because liquid solution of nanoparticles was used, allowing to disperse nanoparticles in the gel more uniformly.

4. Conclusions

Addition of Au and ZnO nanoparticles allows to significantly increase dose sensitivity of nMAG gel dosimeter. 42% higher sensitivity was achieved for the dose gels containing Au NPs comparing to the original formulation. Addition of ZnO nanoparticles allowed to enhance dose sensitivity of the gel by 31 %.

Obtained results were significantly better comparing to the results of investigations performed by other authors possibly due to the fact that we have used lower irradiation energy which is characterized by dominant photoelectric effect. However, nanoparticle-enriched NIPAM dosimetric gels do not demonstrated dose sensitivity enhancement effect. Similarly, Cu/Cu_2O nanoparticles appeared to inhibit polymerization processes in all investigated dose gels.

References

1. Baldock C, De Deene Y, Doran S, Ibbott G, Jirasek A, Lepage M, et al. Topical Review: Polymer gel dosimetry. Phys Med Biol 2010;55(5).
2. Deene Y De. Fundamentals of MRI measurements for gel dosimetry. J Phys Conf Ser 2004;3.
3. Titus D, Samuel EJJ, Mohana Roopan S. Current scenario of biomedical aspect of metal-based nanoparticles on gel dosimetry. Appl Microbiol Biotechnol2016;100(11).
4. Konefał A, Lniak W, Rostocka J, Orlef A, Sokół M, Kasperczyk J, et al. Influence of a shape of gold nanoparticles on the dose enhancement in the wide range of gold mass concentration for high-energy X-ray beams from a medical linac. Reports of Practical Oncology and Radiotherapy 2020;25(4).
5. Cooper DR, Bekah D, Nadeau JL. Gold nanoparticles and their alternatives for radiation therapy enhancement. Front Chem2014;2(OCT).
6. Karlsson A, Gustavsson H, Månsson S, McAuley KB, Bäck SÅJ. Dose integration characteristics in normoxic polymer gel dosimetry investigated using sequential beam irradiation. Phys Med Biol 2007;52(15).
7. Mesbahi A, Jafarzadeh V, Gharehaghaji N. Optical and NMR dose response of N-isopropylacrylamide normoxic polymer gel for radiation therapy dosimetry. Reports of Practical Oncology & Radiotherapy 2012;17(3):146–50.
8. Rackauskas S, Klimova O, Jiang H, Nikitenko A, Chernenko KA, Shandakov SD, et al. A novel method for continuous synthesis of ZnO tetrapods. Journal of Physical Chemistry C 2015;119(28).
9. Khan A, Rashid A, Younas R, Chong R. A chemical reduction approach to the synthesis of copper nanoparticles. Int Nano Lett 2016;6(1).
10. Ding X, Lin K, Li Y, Dang M, Jiang L. Synthesis of biocompatible zinc oxide (ZnO) nanoparticles and their neuroprotective effect of 6-OHDA induced neural damage in SH-SY 5Y cells. Journal of Cluster Science 2020, 31, 1315-1328.

11. Berra D, Laouini SE, Benhaoua B, Ouahrani MR, Berrani D, Rahal A. Green synthesis of copper oxide nanoparticles by Pheonix dactylifera L leaves extract. Digest Journal of Nanomaterials and Biostructures 2018,13(4), 1231-1238.
12. Sawant S S, Bhagwat AD, Mahajan, CM. Synthesis of cuprous oxide (Cu2O) nanoparticles–a review. Журнал нано- та електронної фізики 2016, (8,№ 1), 01035-1.
13. Farahani S, Riyahi Alam N, Haghgoo S, Khoobi M, Geraily GH, Gorji E. Dosimetry and Radioenhancement Comparison of Gold Nanoparticles in Kilovoltage and Megavoltage Radiotherapy using MAGAT Polymer Gel Dosimeter. J Biomed Phys Eng 2019;9(2):199.
14. Mustaqim AS, Yahaya NZ, Razak NNA, Zin H. The dose enhancement of MAGAT gel dosimeter doped with zinc oxide at 6 MV photon beam. Radiation Physics and Chemistry 2020;172.

MEDICAL PHYSICS IN THE BALTIC STATES 16 (2023)

Proceedings of International Conference "Medical Physics 2023"
09-11 November 2023, Kaunas, Lithuania

INVESTIGATION OF POSITIONING DEVIATIONS AND IRRADIATION DOSE FOR DAILY HEAD AND NECK PATIENTS IMAGE-GUIDED RADIOTHERAPY

Greta VAINIŪTĖ[1], Monika JONUŠAITĖ[2], Reda ČERAPAITĖ-TRUŠINSKIENĖ[3], Kristina ŠUTIENĖ[4], Jurgita LAURIKAITIENĖ[5], Marius LAURIKAITIS[6]
[1]Vytautas Magnus University; [2]Lithuanian University of Health Sciences Kaunas Clinics, Oncology Hospital; [3]Lithuanian University of Health Sciences; [4]Kaunas University of Technology; [5]Kaunas University of Technology; [6]Lithuanian University of Health Sciences Kaunas Clinics, Oncology Hospital;
[1]greta.vainiute@vdu.lt; [2]jonusaitemonika@gmail.com; [3]redcera@gmail.com; [4]kristina.sutiene@ktu.lt; [5]jurgita.laurikaitiene@ktu.lt; [6]marius@medicinosfizika.lt

***Abstract*:** Precise positioning during the radiotherapy procedure of the head and neck patients is extremely important due to the highly sensitive organs at risk surrounding the irradiated target. Set-up errors can occur due to various reasons, such as body contour changes of the patient, which may happen on behalf of weight loss or shrinkage of the tumour, or due to the inappropriate use of immobilisation tools, etc. Image-guided radiotherapy enables corrections and monitoring of these positioning deviations. However, along with known benefits, performing kV-CBCT verifications before each treatment inevitably leads to additional exposure doses. It is known that daily imaging of kV-CBCT for the patient could increase the daily exposure dose by ~1.4 mGy.
Investigation was done using linear accelerator Halcyon V3.1 (Varian Medical Systems, Palo Alto, CA, USA), which ensures 100 % Image-guided radiotherapy. All the daily data were collected from medical treatment planning system EclipseTM (Offline Review tool) and were processed with statistical computing software "R". Analysis of the results showed that despite the additional irradiation doses for the patient, the benefits of daily verifications are undeniable, because patient positioning deviations do not have a clear variation tendency and change randomly during each fraction.

Keywords: IGRT, irradiation dose, positioning

1. Introduction

Changes in anatomical structures can be observed during the entire radiotherapy treatment, which are caused by weight loss, inflammation, or tumour response to the delivered treatment. Due to improper patient positioning, critical organs near the tumour may be irradiated with a higher dose than intended, whereas the dose coverage for the target may be insufficient. Other authors also emphasise how the accuracy of radiation therapy procedures depends not only on the accurate determination of the tumour volume and precise patient positioning but also on the movement of internal organs and correct detection of their position [1].
Due to the many important organs in the head-neck area necessary for voice, speech articulation, swallowing, vision, hearing, saliva production, and cosmetic appearance of the patient, the treatment must be immensely accurate. The ability to choose treatment methods and personalise plans for each patient substantially improved the life quality of many head-neck patients by minimising side-effects to organs at risk [2]. Image-guided radiation therapy and accurate patient immobilisation are the main factors assuring the quality of the treatment and avoiding complications [3, 4].
Considering the principles of radiation safety, additional doses received by verification of patient position using cone beam computed tomography (CBCT) must be beneficial in order to ensure the accuracy of treatment procedures and reduce the frequency of radiation-induced complications and reactions. According to other authors, the dose may increase up to 1-2 Gy in 40 treatment fractions by performing everyday verifications. The daily realisation of verifications using CBCT increases the daily radiation dose for the patient by about 1.4 mGy. Therefore, specialists still do not agree on the most appropriate periodicity of CBCT verifications for patients with head and neck tumours [5]. Therefore, the main aim of this study was to assess the positioning deviations of the head and neck patients in a daily image-guided radiation therapy and determine the main cause.

2. Materials and methods

In this study, positioning deviations of head-neck IGRT cases were selected as the research object. Data of 40 patients‘ CBCT verifications were selected in order to evaluate positioning variations (vertical, longitudinal and lateral coordinates). The study was conducted in Lithuanian University of Health Sciences Kaunas Clinics, Oncology Hospital in the Radiation therapy sector. Lithuanian University of Health Sciences Kaunas Clinics Bioethics Centre granted permission to carry out scientific research work no. SPBT-68. In order to ensure the confidentiality of patient data, only depersonalised records were used for this study. A total of 3,685 patients' positioning deviations were collected and registered in the Microsoft Office Excel 2010 program. Statistical analysis was performed using the statistics software "R". Halcyon 2.0 linear accelerator equipped with a kV cone-beam CT imaging system consisting of a kV X-ray source with a half bow-tie filter generating a tube voltage of 40–150 kV and an amorphous Si detector with an active area of 43 cm × 43 cm (1280 × 1280 pixels) was used. The kV detector has a fixed lateral displacement limit of 17.5 cm, a fixed source-to-image distance (SID) of about 154 cm, and a fixed source-axis distance (SAD) of 100 cm. kV volumetric CBCT with eleven different scan protocols was used for this study (Table 1).

Table 1. CBCT imaging characteristics of the Halcyon LINAC

Mode	11 protocols
Energy	80-140 kVp
Scan duration	From 16.6 s (for head, breast, chest modes) to 40.6 (for large volume modes)
Scan range	24.5 cm
Scan diameter	49.1 cm
Imaging	17.5 cm lateral displacement limit
Bow-tie filter	Half bow- tie/titanium filter
Pixel resolution	1280 x 1280 (43 x 43 cm active area)
Reconstruction	2 mm thickness
Reconstruction algorithm	Conventional CBCT, iterative process (iCBCT; non-linear/statistical)

Before the first radiotherapy procedure, Halcyon system requires selecting the CBCT protocol for the area to be treated, determining the size of the scanned field, and selecting the exposure level required for optimal imaging. Exposure parameters used in cases of head and neck tumours are adjusted automatically after selecting the required protocol. Before performing treatment procedure with Halcyon, the patient is positioned and aligned on the treatment couch with a virtual isocenter using a laser system. If the patient positioning due to a virtual lasers system was completed successfully, the treatment couch is automatically aligned with the isocenter of the treatment plan in the bore. Imaging is performed using a 3D/3D image registration technique when CBCT images obtained during verification are compared with CT images from the treatment plan. The resulting differences between these images are usually corrected regarding the treatment couch. After imaging, the patient's position is not changed, only the couch height (vrt), length (lng) and lateral (lat) coordinates are adjusted to get the best result. In case of rotational errors in patient positioning, it is necessary to reposition the patient and repeat CBCT. The deviations from the specified coordinates are registered in the treatment history.

For this study a total of 3685 positioning deviations were used for statistical analysis. The positioning deviations of 20 men and 20 women in vertical (vrt), lateral (lat) and longitudinal (lng) directions were evaluated. After evaluating the variations depending on gender, for the comparison were also used different treatment type (palliative or radical). In total, 1092 deviations of radical patients and 137 deviations of palliative patients were analysed. The data distribution by gender and treatment type is shown in Table 2.

Table 2. Distribution of the study data by gender and treatment methods

Position	Gender		Treatment method	
	Women	Men	Palliative	Radical
Vertical (vrt)	610	617	137	1090
Longitudinal (lng)	611	618	137	1092
Lateral (lat)	611	618	137	1092
Total:	3685		3685	

3. Results and discussion

Performed statistical analysis showed that different median values were observed between genders, which led to the various deviations. In the women group, the vertical coordinate median (-0.01 mm) was lower than median in the men group (0 mm). It is noted that the upper and lower limits of the height coordinate deviations for both men and women differ very slightly. 50 % of the variations for both males and females are distributed around 0, i.e., from -0.3 mm to 0.2 mm. Longitudinal deviations median was equal to 0 for men and equal to 0.2 mm for women. 50 % of the variations ranged from -0.1 mm to 0.4 mm (women group), and from -0.1 to 0.2 mm (men group). When evaluating lateral coordinate deviations, a similar tendency is observed, where the median for men is equal to 0, and for women it is slightly less than 0.2 mm. 50 % of the values are distributed from -0.1 mm to 0.2 mm (female group) and from -0.2 mm to 0.1 mm (male group). The maximum lateral positioning error among women is -0.5 mm on one side and just over 0.5 mm on the other. For men, these maximum errors are also similar and correspond to a little more than -0.5 mm to one side and 0.5 mm to the other (Fig. 1). Deviations in lateral directions also had abnormally different data for both genders.

The results showed that the average deviations of vertical, longitudinal, and lateral coordinates in comparison with the men were higher. Higher standard deviation values were observed in the women group, when analysing the deviations of the vertical and longitudinal coordinates, due to the unequal positioning during each procedure, which could be caused by a different haircut or/and hairstyle.

When analysing positioning deviations by gender and evaluating the statistical significance of different coordinates, it was also observed that the deviations of different directions are statistically significantly different

from each other. After performing the Shapiro-Wilk normality test, the results showed that male vertical coordinate deviation is $p = 8.0603 \cdot 10^{-9}$, meanwhile for the females it was equal to p = 0.0002. The results of the normality test for neither men nor women were >0.05, so it is possible to reject the null hypothesis and state that the deviations of the vertical coordinates are not normally distributed.

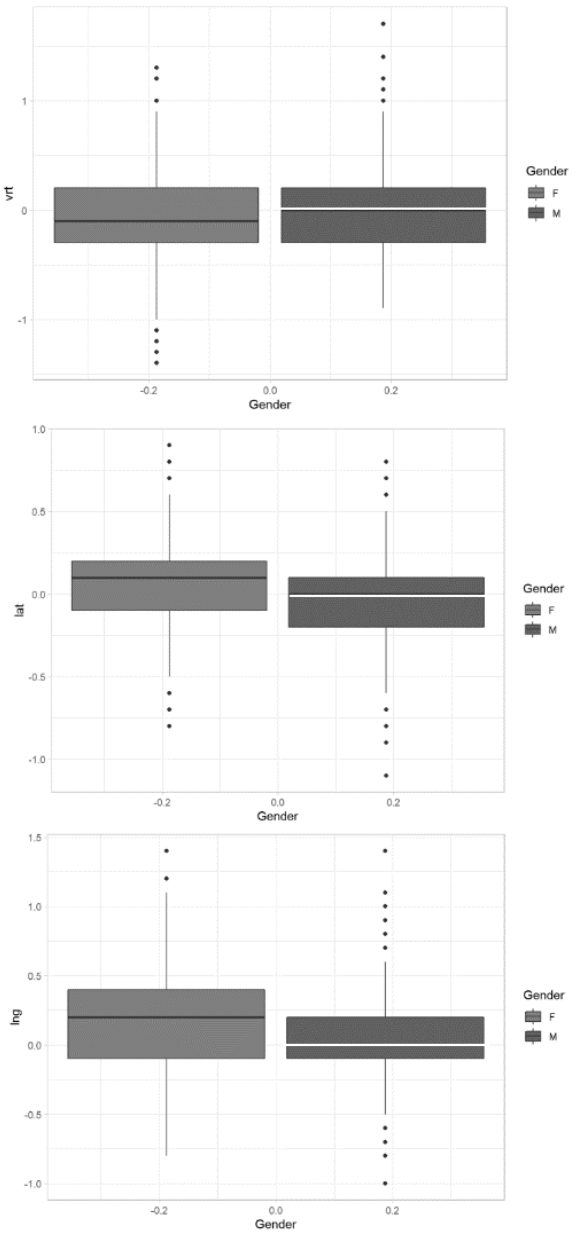

Fig. 1. Distribution of vertical, longitudinal and lateral deviations by gender.

It can be seen that most of the deviations of the vertical coordinate in the women group are between 0 and -0.5 mm, while for the men, it is less deviated and can be observed in the histogram around 0. The data obtained from the Shapiro-Wilk normality test of longitudinal coordinate for men showed a value of $p = 2.0641 \cdot 10^{-11}$, while for women – $p = 5.2611 \cdot 10^{-7}$. Since for both genders p<0.05, so it can be determined that the longitudinal coordinates are also not normally distributed. The test of normality of lateral coordinate deviations were defined as $p = 2.0700 \cdot 10^{-5}$ for males, and $p = 6.2221 \cdot 10^{-7}$ for females. Knowing that p>0.05 is required to prove the normality of the distributions, it can be said that lateral data is not distributed normally. After evaluating the histograms for all three coordinates, the asymmetry was observed (Fig. 2). So it could be concluded that significant differences between the histograms in comparison for men and women were not observed.

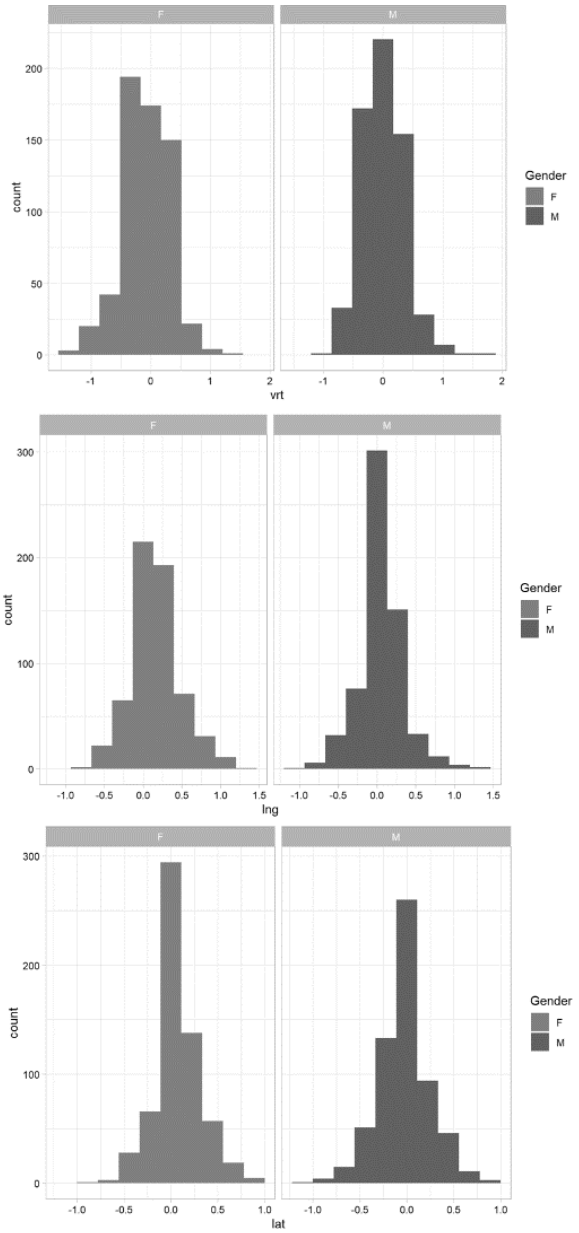

Fig. 2. Normality test of vertical, longitudinal, and lateral deviations by gender

Fligner-Killeen's test values of height, length and lateral coordinates were all <0.05 (Table 3), so the spread of these deviations was statistically significantly different depending on gender, thus it is heterogeneous. In summary, it can be said that positioning deviations differ statistically significantly depending on gender. When evaluating the genders separately, the statistical significance of discrepancies was also observed when comparing different pairs of coordinates. Only the combination of lateral and vertical coordinates of men did not show statistical significance.

Table 3. Distribution of the study data by gender and treatment methods

Deviations	Fligner-Killeen's test p-value
Vertical	0.09444
Longitudinal	0.00051
Lateral	0.05422

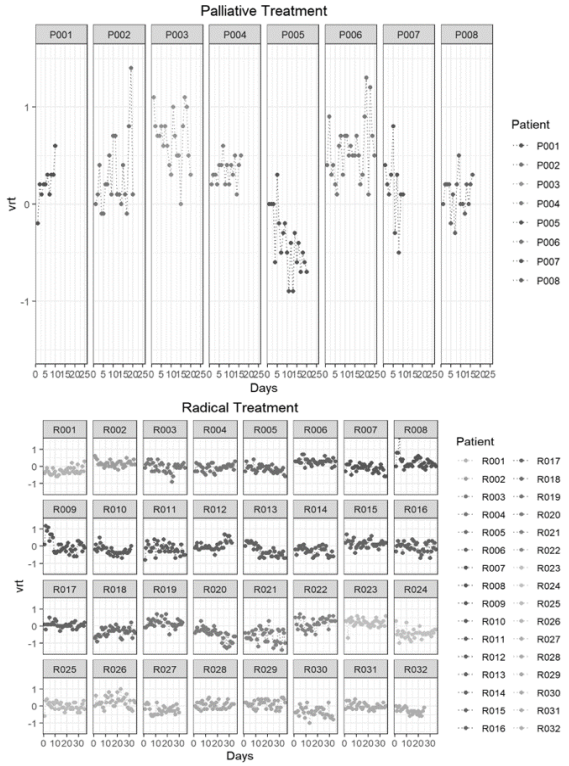

Fig. 3. Height coordinate deviations difference in time, during palliative and radical treatment.

A similar tendency between deviations were observed in cases of palliative and radical treatment. After summarising the data, it was established that positioning deviations differed statistically significantly depending on the treatment method. When evaluating treatment methods separately, the statistical significance of variations was observed comparing different pairs of coordinates. In palliative treatment cases, the average of vertical and lateral deviations is higher than in radical treatment cases. It was found that the deviations of the vertical and lateral coordinates are further away from the average comparing the palliative treatment method with radical treatment. The mean of longitudinal deviations is higher during radical treatment positioning. The standard deviation in the analysis of vertical and lateral deviations is higher in palliative treatment cases. Therefore, it can be observed that this type of deviation is more distant from the average in comparison with radical treatment. Evaluating the positioning deviations of palliative and radical treatment methods, it became clear that the deviations of different directions are statistically significant and differ from each other.

For the difference of deviations evaluation over time, it was further decided to analyse the variation of the vertical coordinate with the highest statistical dissipation from average during different treatment procedures in cases of palliative and radical treatment. After evaluating the data shown in Figure 3, it was observed that in palliative treatment cases, the amplitudes of vertical variations are relatively large, sharp differences can be observed, moreover, there are no distinct trends in the variations. For the radical treatment method, random distribution of height deviations is observed without any recurring trends. The amplitudes of deviations in the sample range from large (eg. R021) to quite small (eg. R032) (Fig. 3).

The variation of positioning deviations over time revealed that the differences of the vertical coordinates change randomly and do not have any obvious trend, both when comparing data between genders and between different treatment types. Due to the complex anatomy of head and neck tumours and the abundance of vital tissues, the accuracy of radiotherapy treatment for head and neck patients is very important and it would not be possible without image-guided radiation therapy. The obtained research confirms that the importance of daily verifications in the presence of random positioning errors is indisputable.

4. Conclusions

After performing the analysis of positioning deviations of image-guided radiation therapy for head-neck patients, it can be stated that variations were statistically significant and differed between women and men and between radical and palliative patients.

Average deviations of vertical, longitudinal, and lateral coordinates were higher for women in comparison with men. However non-tendential and random individual variations of positioning were observed over time for each patient.

After evaluating the results of this study, it is clear that despite the additional doses of exposure, the benefits of daily visual verifications are undeniable. It is impossible to predict the values of patient positioning deviations, which do not have clear trends and change randomly during each fraction, proving the need for daily verifications. Instead of reducing the frequency of verifications performed with CBCT, it is recommended to choose the most optimal, lower-dose imaging protocols for head-neck tumours.

5. References

1. Choudhury, A., Budgell, G., MacKay, R., Falk, S., Faivre-Finn, C., Dubec, M., ... & McWilliam, A. (2017). The future of image-guided radiotherapy. Clinical Oncology, 29(10), 662-666.

2. Caudell, J. J., Torres-Roca, J. F., Gillies, R. J., Enderling, H., Kim, S., Rishi, A., ... & Harrison, L. B. (2017). The future of personalised radiotherapy for head and neck cancer. The Lancet Oncology, 18(5), e266-e273.

3. Chen, H., & Kuo, M. T. (2017). Improving radiotherapy in cancer treatment: Promises and challenges. Oncotarget, 8(37), 62742–62758 https://doi.org/10.18632/oncotarget.18409

4. Hay, L. K., Paterson, C., McLoone, P., Miguel-Chumacero, E., Valentine, R., Currie, S., ... & Duffton, A. (2020). Analysis of dose using CBCT and synthetic CT during head and neck radiotherapy: a single centre feasibility study. Technical Innovations & Patient Support in Radiation Oncology, 14, 21-29.

5. Nyarambi, I., Chamunyonga, C., & Pearce, A. (2015). CBCT image guidance in head and neck irradiation: the impact of daily and weekly imaging protocols. Journal of Radiotherapy in Practice, 14(4), 362-369

MEDICAL PHYSICS IN THE BALTIC STATES 16 (2023)

Proceedings of International Conference "Medical Physics 2023"
09-11 November 2023, Kaunas, Lithuania

APPLICATION OF SCANNING ELECTRON MICROSCOPY FOR THE CHARACTERIZATION OF ADIPOSE TISSUE

Edvardas BRIMAS[1], Rimantas RAUDONIS[1], Rimantas RAMANAUSKAS[2], Aivaras KAREIVA[1]
[1]Institute of Chemistry, Faculty of Chemistry and Geosciences, Vilnius University, Vilnius, Lithuania; [2]Center for Physical Sciences and Technology, Vilnius, Lithuania
edbrimas@gmail.com; rimantas.raudonis@chgf.vu.lt; aivaras.kareiva@chgf.vu.lt; rimantas.ramanauskas@ftmc.lt

Abstract: It was demonstrated in this study, that careful morphological observations using SEM measurements revealed individual surface morphology of adipose tissue samples taken from different patients. From the obtained results were concluded that such characterization of adipose tissue is an essential step for the possible prediction of appearance of symptoms of different diseases. This may facilitate the future development of new prognostic tools useful for personalized treatment strategies that address problems in obesity.

Keywords: adipose tissue, obesity, scanning electron microscopy

1. Introduction

Obesity affects > 650 million people in the world, according to reports from the World Health Organization. In the European Union (EU) the levels of obesity and overweight have been rising as well in the last decades [1-3]. Obesity has been clearly associated with metabolic syndrome, type 2 diabetes mellitus, cardiovascular disease and most types of cancer which is the most common cause of death in the western world [4-6]. Most of the adult obese population will have fatty liver, and approximately one-third will develop non-alcoholic fatty liver disease.

The adipose tissue can be classified according to its location in the human body [7]. Subcutaneous adipose tissue (SAT) is the fat just under the skin. Preperitoneal adipose tissue (PAT) is located prior peritoneum. Visceral adipose tissue (VAT) surrounds organs and interfering the function of organ. Moreover, there is conflicting information about differences between the fatty acid composition of these adipose tissues. Adipose tissue is generally considered as a storage depot for excess energy, which is stored as triglycerides. It was long considered as a passive organ, but the adipose tissue has been described as an endocrine organ recently with important physiological roles [7].

Although the development of obesity is easily attributed to excess intake of calories, the underlying reasons for the metabolic disturbances and health risks associated with obesity are still unclear. Though an association between obesity and health problems is well established, the link may-in reality-not be as simple. To determine the link between obesity and metabolic syndromes, researchers are studying a wide variety of adipose tissue features, changes of different parameters, and various physical properties in obese people; examine the chemical composition of adipose tissue, the change in composition depending on the progression of the disease and treatment. Not only physicians but also chemists, biochemists, physicists and materials scientists are actively involved in these studies. The following main methods are currently used to characterize adipose tissue: gas and liquid chromatography, FTIR, Raman and NMR spectroscopies, scanning electron microscopy (SEM), elemental analysis using sensors and other techniques [8].

Recently, the SEM and energy dispersive X-ray (EDX) elemental analysis were used for the characterization of adipose tissue samples taken from volunteer obese patients. The adipose tissue was taken from SAT, PAT and VAT layers of adipose tissue [7-9]. It was demonstrated, that the PAT layer of adipose tissue is composed of irregularly shaped 200 nm^{-2} μm in size particles which are closely connected to each other forming hard agglomerates. The adipose tissue of SAT samples were composed of cubes, prisms and spherically shaped granules particles less than 0.5 μm in size. The SEM micrographs of VAT adipose tissue revealed individual and very similar surface morphology of adipose tissue samples taken from different patients. It was concluded that preperitoneal layer perhaps could be considered as a passive organ, i. e. is not associated with metabolic changes in human body. However, these conclusions were made only from initial SEM observations. Some years later, it was demonstrated for the first time the application of SEM for the characterization of lyophilized adipose tissue from obese patients with and without metabolic diseases [7]. The surface of SAT, PAT and VAT layers of adipose tissue

showed interesting morphological features, related with very important biomedical information. In order to reveal some microstructural differences between adipose tissue types subcutaneous, preperitoneal and visceral adipose tissues the distribution of the total area of thickening and scarring of connective tissue were analysed. The calculated total area of thickening and scarring of connective tissue for obese patients with different metabolic diseases was larger in comparison for the obese patients without different metabolic diseases. These SEM observations let to conclude that the microstructure of all three SAT, PAT and VAT layers is associated with metabolic changes in human body and could be considered as active organs.

The process of morphological characterization of a specimen using SEM generally produces a magnified specimen image which is built out of the ejected electron beam raster scan data and the initial position of the beam. The scanning electron microscope provides large depth-of-focus and high-contrast images at a large variability in magnification. Nevertheless, the resulting image is literally a two-dimensional intensity distribution array and usually does not carry any additional specimen-related metadata, except for the observational circumstances. Extracting spatial data from the two-dimensional images can be difficult, so to achieve this, the specimen must be handled in a special way and, also, the produced micrographs must be digitally processed afterwards [10]. In materials science, various techniques for three-dimensional reconstruction of microstructures have been applied successfully for decades, such as X-ray and electron tomography. SEM stereoscopic technique was also used to determine the three-dimensional surface structures [11, 12]. The success of this technique highly depends on the microscope type and its instrumental precision. Stereo photography requires precise compucentric tilting of the observed sample, so that during the tilt, image focal points are preserved in the microscope viewport [13]. This is difficult to achieve for some SEM models, where the accuracy is linearly decreased, as the magnification increases. However, if the tilt is precisely compucentric, anaglyphs of magnification up to 50000 times can be easily produced. Otherwise, the SEM operator must manually apply the compensation of the shift that happens during the tilt. Recently, an advanced scanning electron microscopy data processing model for the extrapolation of three-dimensional sample data out of the SEM images was developed [11-13]. Three different techniques were also tested to construct the 3D view from SEM images of adipose tissue [14]. The stereoscopic view gave the poor information, while the reconstructed surface of adipose tissue formed by Interactive 3D Surface Plot plugin in Fiji demonstrated more rich data. Nevertheless, since the pixel does not have the depth dimension z, the interpretation of the data is very difficult. The 3D reconstructed model by VisualSFM and MeshLab free available software gave the best and the most promising results. The surface was fully reconstructed and pixel z dimension might be easily extrapolated. The reconstructed view also might be easily printed by 3D printer which gives new area of applications. Obviously, further investigation is needed to prove the impact of morphological features to adipose tissue activity and their relationship with disease stage. Of course, medical conclusions could be made only after careful and systematic investigation of numerous patients with obesity and different co morbidities. The main aim of this study is to introduce the scientific community with the possibilities of using 3D SEM images for the characterization of the peculiarities of human adipose tissue.

2. Experimental

The adipose samples were taken from volunteer patients at the Department of General Surgery of Vilnius University Hospital. Men and women aged 18–65 years with a BMI more than 30 kg/m2 were enrolled in the study. The study protocol was approved by the Lithuanian Ethics Committee, with the aim and design of the study explained to each subject, who in turn gave their informed consent. Adipose tissue samples were stored in –70 °C temperature before the chemical analysis was performed. The adipose tissue samples were homogenised and lyophilized [7]. Morphology of adipose tissue samples were evaluated by field emission scanning electron microscopy (FE-SEM, SU70, Hitachi) equipped with the energy dispersive X-ray spectrometer, and the spectrometer was controlled by the INCA software (Oxford Instruments) or by Hitachi TM3000 and Helios NanoLab 650 instruments. The database of SEM images of the adipose tissue taken from 3 layers of adipose tissue (subcutaneous, preperitoneal and visceral) was collected. The most characteristic examples were selected for 3D reconstruction. Spatial reconstruction technique was used for recovering 3D spatial data from the SEM pictures (structure-from-motion). The VisualSFM software was applied for spatial reconstruction. Using VisualSFM, the images are analyzed for matching points and the camera angle is guessed for each image. This produces results similar to those displayed in Fig. 1.

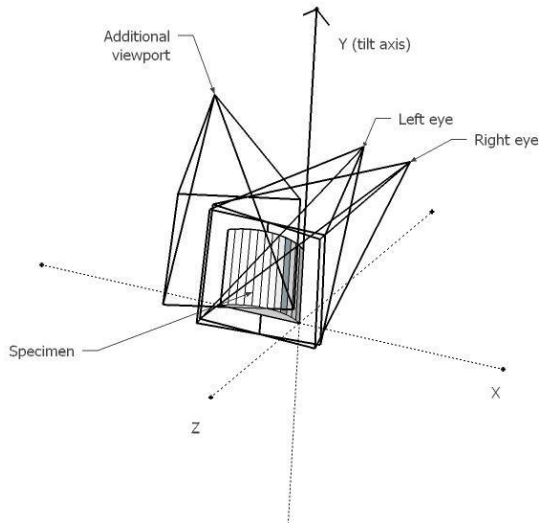

Fig. 1. Positions of additional viewports could be added to VisualSFM software

Extrapolation of spatial data: this approach was done from at least eight SEM images made by changing the tilt

by 5° or 10° step. The 3D model of SEM images reconstructed by VisualSFM and MeshLab open source software is based on the following steps:

1. Convert the SEM images to a format suitable for processing (i.e. JPG).
2. Find local features in the given set of images.
3. Find matching feature-sets between image pairs.
4. Construct spatial positions of feature points based on their trajectories.
5. Map image data (colour) to the spatial points.
6. Connect the spatial points to build a vertex or other surface-like structure.

All results are expressed as mean ± standard deviation (SD). Statistical comparisons between groups were analyzed by using one-way ANOVA test. A value of $P < 0.05$ was considered to be statistically significant.

3. Results and discussions

Any number of additional viewports can be added to VisualSFM software. The 3D images of the SAT, PAT and VAT samples were reconstructed from 8 SEM micrographs (Fig. 2).

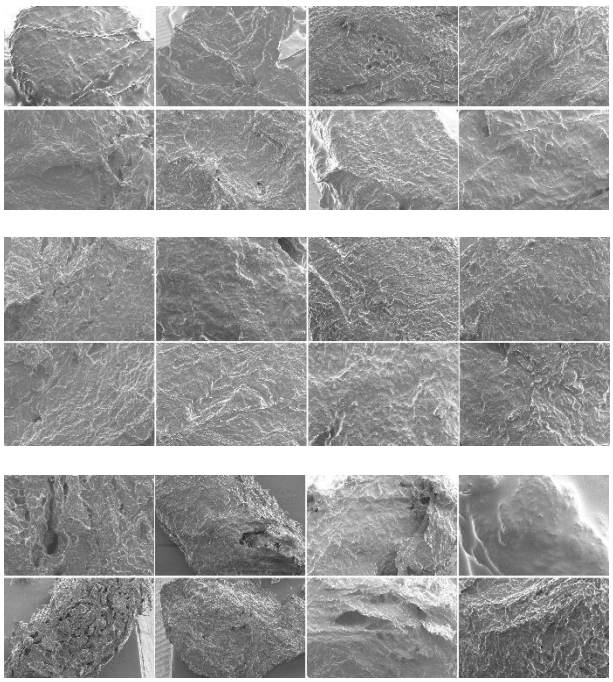

Fig. 2. SEM micrographs of lyophilized adipose tissue obtained from: (top) subcutaneous (SAT), (middle) preperitoneal (PAT) and (bottom) visceral (VAT) layers of patients with obesity having different metabolic diseases

The reconstructed images using spatial reconstruction are obtained using several intermediate steps. The structural reconstruction produces a digital point cloud. The Ball pivoting algorithm was used to join nearest points into triangular faces so that a mesh and next, a surface is produced. The software produces a cloud of points, which has to be processed externally. Freely available software, such as MeshLab can be used to join the point cloud to a mesh and, as a second step of reconstruction, apply surface properties to the mesh polygons. Finally, a dense microstructure that is composed of specific features was observed in SAT, PAT and VAT adipose tissue samples.

The calculated total area of specific features of SAT adipose tissue samples was about 70% for patients with obesity and having different metabolic diseases. The distribution of total area of specific features for obese patients with different metabolic diseases and dependence of relative surface area of deep spaces on the relative age of patients (age + duration of illness) are shown in Fig. 3

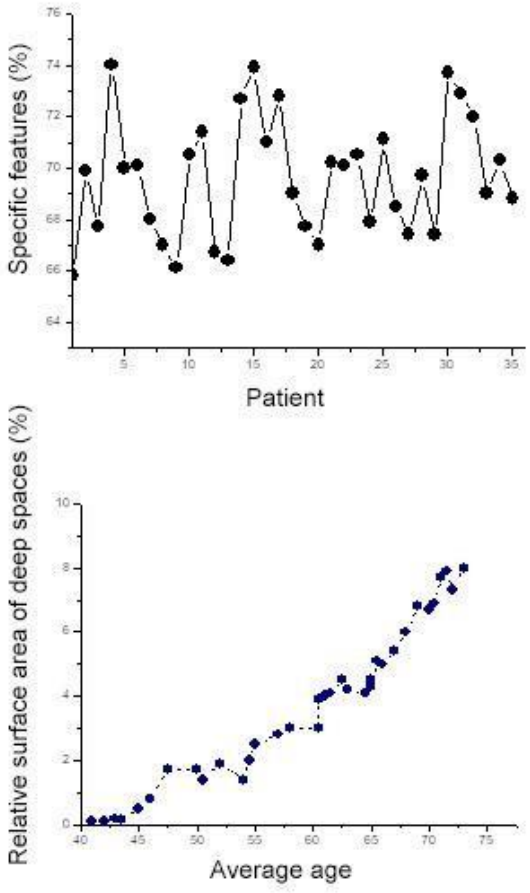

Fig. 3. Distribution of specific features (at top) and dependence of relative surface area of deep spaces of adipose tissue obtained from subcutaneous layers of obese patients with different metabolic diseases on the relative age of patients (at bottom)

As seen, for the randomly selected patients the distribution of specific morphological features does not show any tendency. However, the relative surface area of deep spaces of adipose tissue obtained from subcutaneous layers of obese patients with different metabolic diseases obviously is dependent on the relative age of patients.

The calculated total area of specific features of PAT adipose tissue samples was about 75% for patients with obesity and having different metabolic diseases. Moreover, the distribution of total area of specific features was very similar calculated for female and male patients. The obtained results are depicted in Fig. 4.

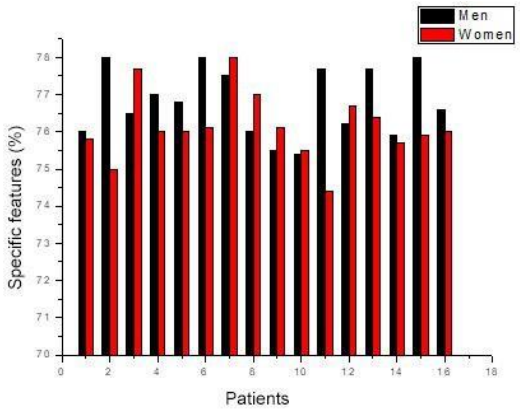

Fig. 4. Distribution of specific features of adipose tissue obtained from preperitoneal layers of obese patients (men and women) with different metabolic diseases

The calculated total area of specific features of VAT adipose tissue samples was about 80% for patients with obesity and having different metabolic diseases. However, SEM micrographs of VAT samples showed very distinctive character, sometimes not comparable with SEM images obtained from the same layer. For example, the representative SEM micrographs of visceral adipose tissue specimens are depicted in Fig. 5.

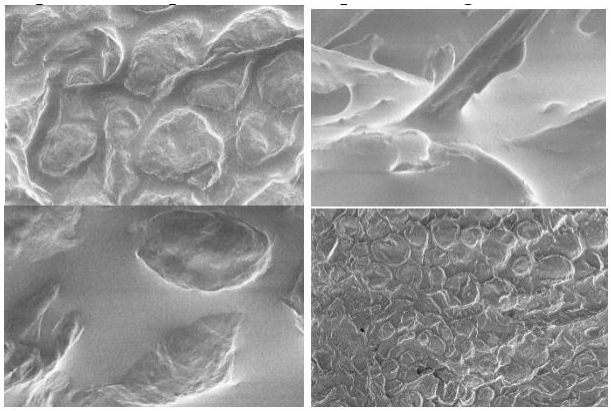

Fig. 5. SEM micrographs of adipose tissue obtained from visceral layers of obese patients with different metabolic diseases

Since morphological features obtained by SEM of VAT specimens are very individual, the conclusions even from 3D images could be drawn with care.

4. Conclusions

The results of this study showed that the 3D SEM could be successfully used for the characterization of lyophilized adipose tissue samples taken from subcutaneous, preperitoneal and visceral layers from obese patients. The most individual microstructural features are obtained from the visceral layers of adipose tissue in human body. SEM observations let us to conclude that the microstructure of SAT, PAT and VAT layers is associated with metabolic changes in human body and could be considered as active organs.

References

1. D. T. Villareal, C. M. Apovian, R. F. Kushner, S. Klein, Obesity in older adults: technical review and position statement of the American Society for Nutrition and NAASO, The Obesity Society. Am. J. Clin. Nutr. 82, p. 923–934 (2005).
2. F. J. Ruiz-Ojeda, A. Anguita-Ruiza, R. Leis, C. M. Aguilera, Genetic Factors and Molecular Mechanisms of Vitamin D and Obesity Relationship. Ann. Nutr. Metab. 73, p. 89–99 (2018).
3. E. Lespessailles, J. Paccou, R.-M. Javier, T. Thomas, B. Cortet, Obesity, Bariatric Surgery, and Fractures. J. Clin. Endocrinol. Metab. 104, p. 4756–4768 (2019).
4. J. R. Larsen, L. Dima, C. U. Correll, P. Manu, The pharmacological management of metabolic syndrome. Expert Rev. Clin. Pharmacol. 11, p. 397– 410 (2018).
5. T. Grewal, C. Enrich, C. Rentero, C. Buechler, Annexins in Adipose Tissue: Novel Players in Obesity. Int. J. Mol. Sci. 20, p. 3449 (2019).
6. C. Koliaki, S. Liatis, A. Kokkinos, Obesity and cardiovascular disease: revisiting an old relationship. Metabolism Clin. Exper. 92, p. 98–107 (2019).
7. G. Brimas, R. Skaudzius, V. Brimiene, R. Vaitkus, A. Kareiva, Microstructural features of lyophilized adipose – A new concept to estimate the metabolic symptoms for obese patients. Medic. Hypotheses. 136, p. 109526 (2020).
8. E. Brimas, R. Raudonis, A. Kareiva, Analytical methods used for the characterisation of specific features of biological tissues related with obesity: A review. Chemija, 33, p. 158-180 (2022).
9. R. Skaudzius, M. Misevicius, V. Brimiene, M. Beniuse, G. Brimas, A. Kareiva, SEM (EDX) is indispensable tool for the characterization of subcutaneous, preperitoneal and visceral adipose tissue of obese patients. Chemija, 29 p. 67-79 (2018).
10.V. Brimiene, R. Skaudzius, M. Misevicius, G. Brimas, E. Brimas, A. Kareiva. SEM characterization of adipose tissue structure. Proceedings of TechConnect World Innovation Conf. & Expo, Washington DC, USA. Advanced Materials: TechConnect Briefs, 1 p. 13-16 (2017).
11. S. Kareiva, A. Selskis, F. Ivanauskas, S. Šakirzanovas, A. Kareiva, Scanning electron microscopy: Extrapolation of 3D data from SEM micrographs. Mater. Sci. (Medziagotyra). 21, p. 640-646 (2015).
12. S. Kareiva, V. Klimavicius, A. Momot, J. Kausteklis, A. Prichodko, L. Dagys, F. Ivanauskas, S. Sakirzanovas, V. Balevicius, A. Kareiva, Sol-gel synthesis, phase composition, morphological and structural characterization of $Ca_{10}(PO_4)_6(OH)_2$: XRD, FTIR, SEM, 3D SEM and solid-state NMR studies. J. Molec. Struct. 1119, p. 1-11 (2016).
13. S. Kareiva, A. Selskis, F. Ivanauskas, S. Sakirzanovas, Stereophotography and spatial surface reconstruction using scanning electron microscopy images. Pure Appl. Chem. 87, p. 283-292 (2015).
14. E. Brimas, R. Skaudžius, G. Brimas, A. Selskis, R. Ramanauskas, A. Kareiva. Three different techniques to reconstruct 3D view of SEM images by using only free available software. Chemija. 33, p. 7-11 (2022).

LUNA 3D

The New More in SGRT

Get more informations on www.lap-laser.com

510(k) Pending (K232031) – Not available for sale in the US. Availability of products, features, and services may vary, depending on your location.

RadCalc

End-to-end patient QA solution

- 3D volumetric Collapsed Cone and Monte Carlo plan validation
- Phantom-free 3D EPID solution for pre-treatment and in-vivo fractional delivered dose QA
- Designed with the patient journey in mind

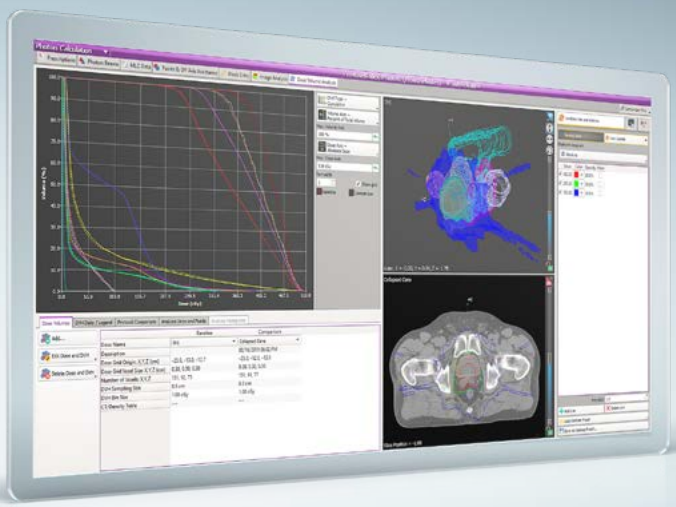

RADCALC

Contact us on www.radcalc.com

MEDICAL PHYSICS IN THE BALTIC STATES 16 (2023)

Proceedings of International Conference "Medical Physics 2023"
09-11 November 2023, Kaunas, Lithuania

SENSITIVITY ANALYSIS OF THE ICRP BIOKINETIC MODEL PREDICTING THE ACTIVITY OF GD IN LUNGS AND 24-HOUR EXCRETION SAMPLES

Belikse RAMLJAK[1], Alexandr MALUSEK[2], Kristina ERIKSSON STENSTRÖM[1], Christopher RÄÄF[3]
[1]Division of Particle and Nuclear Physics, Lund University; [2]Division of Diagnostics and Specialist Medicine, Linköping University; [3]Medical Radiation Physics, Lund University
belikse.ramljak@hep.lu.se; alexandr.malusek@liu.se; kristina.stenström@hep.lu.se; christopher.raaf@med.lu.se

***Abstract*:** ^{148}Gd may contribute to around 50% of the dose from inhalation in case of an accident at the European Spallation Source. Methods for its detection have been developed. They rely on biokinetic models predicting activities of the gamma emitters ^{146}Gd ($T_{1/2}$= 48.3 d) and ^{153}Gd ($T_{1/2}$= 240.4 d) as tracers in the lungs, urine, and faeces. The optimal choice of model parameters and associated uncertainties, which propagate to the estimates of the minimum detectable activity of ^{148}Gd ($T_{1/2}$ = 84±4 y), have yet to be systematically investigated. This work presents a step in this direction. The authors have implemented the ICRP biokinetic model for Gd and performed a sensitivity analysis of the model to identify the most influential parameters. They will use this knowledge in subsequent uncertainty analysis and determination of the optimal measurement time window.

Keywords: ESS, radioactive aerosols, internal dosimetry

1. Introduction

The European Spallation Source (ESS) is a neutron production facility being built in the vicinity of Lund in southern Sweden. Its main components will be a pulsed (14 Hz) linear accelerator emitting 2 GeV protons, a tungsten target, and scientific stations dedicated to experiments using neutron spallation reactions [9]. Radiation protection systems comprise, e.g., shielding of the accelerator via 5 m of soil, steel and concrete around the target and filters in the ventilation exhaust [9]. These systems may not shield entirely the environment and the public from radiation exposure in case of an accidental release of radionuclides. The worst-case scenario accident is caused by an initial loss of the helium cooling of the target while the target is still irradiated by the 5 MW proton beam. A series of events (including melting and oxidizing of the tungsten target and hydrogen deflagration) will lead to the release of helium, filter particles and aerosols formed from the target material.[4]. Radionuclide exposure to the workers and public will be mainly through inhalation, ingestion, groundshine and cloudshine. In this article, we focus on the inhalation route only. Current estimates of the released radionuclide mix predict that the most radiotoxic radionuclides would be ^{148}Gd ($T_{1/2}$ = 84±4 y [15]), ^{187}W ($T_{1/2}$ = 23.7 h), ^{172}Hf ($T_{1/2}$ = 1.87 y), ^{182}Ta ($T_{1/2}$ = 114.4 d), and ^{125}I ($T_{1/2}$ = 59.49 d), with ^{148}Gd contributing to around 50% of the dose [8]. Since ^{148}Gd contributes most of the dose and is an alpha emitter, entailing a higher radiobiological effect, its detection is the main focus of this article. ^{148}Gd is one of the ESS-specific radionuclides which is not relevant in waste from nuclear power plants. Hence, standard methods for assessing ^{148}Gd in the environment or humans have not yet been developed.

Internal contamination assessment is usually done through whole body counting, urinal, faecal and blood sample examination. Biokinetic models predicting the 24-hour excretion in urine and faecal as a function of time and their relation to the organ and whole-body retention of the radionuclides can be used to assay internal dose from excretion samples. The latest ICRP biokinetic models described in publications 130, 134, 137, and 141 are implemented in the commercially available Taurus [19] and IDEAplus codes. These codes allow the user to specify values of model parameters. These parameters are in many cases known with limited accuracy, especially for the exposure pathway through the respiratory tract, and may vary widely depending on the physical size and chemical form of particles containing the radionuclides. The large number of model parameters complicates the corresponding uncertainty analysis. A commonly used approach is to perform a sensitivity analysis of the model and focus on the parameters that notably affect the resulting uncertainty.

Sensitivity analysis is a technique used to determine how different values of an independent variable impact a particular dependent variable under a given set of assumptions. For instance, local sensitivity analysis methods are used in metrology, where the interest is mainly in the true value and uncertainty [1]. Global methods are of interest in disciplines where the input quantities vary notably. Regression methods do not fully

fit into any of these categories since they typically operate on all values of input quantities, but their predictions are only valid for input ranges where the regression model accurately approximates the measurement model.

Khursheed and Fell analyzed the sensitivity of the old ICRP's systemic model for the intake of Pu [14]. The retention of Gd in the lungs is relatively long, so the systemic model must be complemented with the human respiratory tract model (HRTM). Neither Taurus nor IDEAplus codes provide automated methods for sensitivity analysis. To address this issue, we implemented the ICRP biokinetic models in the simulation software Ecolego [2], which provides a wide range of sensitivity analysis methods. This article presents preliminary results of the sensitivity analysis performed using this tool. The focus was on the activity of ^{148}Gd and its radiotracers ^{153}Gd ($T_{1/2}$= 240.4 d) and ^{146}Gd ($T_{1/2}$= 48.3 d) in the lungs, urine and faeces. The activity of ^{148}Gd can be estimated from the computer-simulated isotopic ratios ^{146}Gd/^{148}Gd and ^{153}Gd/^{148}Gd [17].

2. Theory

2.1. Sensitivity coefficients

Let the output random quantity (measurand) Y be a function

$$Y = f(X_1, \dots, X_N) \tag{1}$$

of N input random quantities $X_1, \dots, X_N$. In practice, random quantities are often represented by their averages. The measurement model then has the form $y = f(x_1, \dots, x_N)$, where $x_1, \dots, x_N$ and y are averages. We denote random quantities by capital letters and their averages by small letters in this section.

The sensitivity of the model can be estimated locally using a sensitivity coefficient c_i defined as $c_i \equiv \frac{\partial f}{\partial x_i}$. A small change Δx_i in x_i changes y by $\Delta y = \left(\frac{\partial f}{\partial x_i}\right)\Delta x_i = c_i \Delta x_i$; we assume that all other inputs are not changed. For a relative change $\Delta x_i / x_i$ we get

$$\frac{\Delta y}{y} = c_i \frac{\Delta x_i}{y} = c_i \frac{x_i}{y}\frac{\Delta x_i}{x_i}, \tag{2}$$

i.e., the relative change in $\Delta y/y$ is determined by $c_i x_i / y$. The sensitivity coefficients describe the tilt of a hyperplane that fits the measurement model at the expectations $x_1, x_2, \dots, x_k$. If a linear model can accurately describe the system, then the sensitivity coefficients describe the sensitivity of the measurement model for all values of input parameters. In this case, the sensitivity coefficients can be estimated from randomly sampled values of input parameters. For uncorrelated input variables, it can be shown that:

$$\frac{\partial f}{\partial x_i} = \frac{\mathrm{Cov}(Y, X_i)}{\mathrm{Cov}(X_i, X_i)} = \frac{\mathrm{Cov}(Y, X_i)}{\mathrm{Var}(X_i)}, \tag{3}$$

where $Cov(Y, X_i)$ denotes the covariance between the random quantities Y and X_i and $Var(X_i) = Cov(X_i, X_i)$ denotes the variance of X_i.

Consider standardized input and output quantities $X_{\sigma,i} \equiv (X_i - x_i)/\sigma_{X_i}$ and $Y_\sigma \equiv (Y - y)/\sigma_Y$, where σ_{X_i} and σ_Y are standard deviations for X and Y, respectively. The relation between the corresponding sensitivity coefficient $\partial y_s / \partial x_{s,i}$ and the scaled sensitivity coefficient in equation (2) is

$$c_i \frac{x_i}{y} = \frac{\partial y_s}{\partial x_{s,i}} \frac{\sigma_Y / y}{\sigma_{X_i} / x_i} \tag{4}$$

Suppose the relative standard deviations are the same for all i, i.e., $\frac{\sigma_{X_i}}{x} = c$, where c is a constant. In that case, the scaled sensitivity coefficient $c_i x_i / y$ is proportional to the sensitivity coefficient for standardized quantities. The latter is also called the standardized regression coefficient (SRC).

2.2. Minimum detectable activity

Minimum detectable activity (MDA) is defined in this article as a minimum activity that can be detected from the excretion sample corresponding to the detection limit in accordance with the number of counts measured [16]. For further definition of MDA, please refer to [16] and [18].

$$MDA_{exc.sample} \sim \frac{L_D(nucldie\ mixture)}{\varepsilon(E_g) \cdot t_{acq} \cdot n_g} \tag{5}$$

where L_D is the critical limit [5], which in turn is related to the specific background count rate in the particular region-of-interest for the gamma emitter, E_g, $\varepsilon(E_g)$ is the absolute efficiency of the excretion sample in the gamma spectrometry set-up (cps dis-1) at the energy of interest E_g, t_{acq} is the pulse acquisition time, and n_g is the specific branching ratio of the gamma line of interest.

3. Methods

3.1. Biokinetic modelling of ^{148}Gd

The biokinetic model of ^{148}Gd was built by connecting the HRTM, the human alimentary tract model (HATM), and the systemic model for lanthanides, as shown in Fig. 1. Values of parameters were taken from ICRP publications 100, 130 and 141 and integrated into a single model in Ecolego version 8.0.34; see Table 1 in the Appendix.

Activity in the lungs was calculated as a sum of activities in all compartments in the thoracic region. Activities in 24-hour urine and faeces samples were obtained as activities predicted by Ecolego in corresponding compartments. The content of these compartments was set to 0 Bq one day before the time of readout. This artificial emptying was done in Ecolego via time events triggered at predefined times; each time event instantly transferred the compartment's content to the following compartment. In cases of times less than 1 day, the activity was recalculated to the 24-hour activity as $A_{24h}(t) = A(t)(24\ \mathrm{h})/t$, where t is the time from activity inhalation.

All presented data are for the male reference worker, a particle of activity median aerodynamic diameter (AMAD) of 5 µm, and activity intake of 1 Bq. Results were calculated at 1 h, 2 h, 3 h, 6 h, 12 h, 16 h, 1 d, 2 d, 3 d, 4 d, 5 d, 6 d, 7 d, 8 d, 9 d, 10 d, 15 d, 30 d, 45 d, 60 d, 90 d, 180 d, and 365 d after the activity intake. The same values and time points were also used in Taurus.

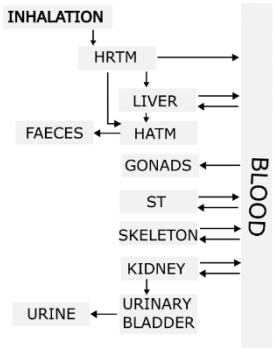

Fig. 1. Schematic drawing of the biokinetic model implemented in Ecolego consisting of HRTM, HATM, and systemic model.

3.2. Sensitivity analysis

Transfer coefficients between body tissue compartments, λ, transfer coefficients between HRTM's artificial compartments simulating rapid, slow and bound excretion s_r, s_s, and s_b, respectively, fractional depositions f_d and fractions f_r and f_b in HRTM, and fractional uptake from blood f_{SI} were assigned normal distributions with standard deviations equal 10% of the mean value.

In the sensitivity simulation, input quantities were drawn from normal distributions. Activities in all compartments were simulated by solving the corresponding system of equations. In the run, 10000 samples of each output quantity were simulated for each selected time point (1, 7, 30, and 365 days), and statistics like SRC were calculated. Tornado plots containing the ten largest SRCs for lungs, urine, and faeces were plotted in R [13] at the selected time points.

4. Results

4.1. Biokinetic model predictions

Activities in lungs calculated with Ecolego agreed well with activities calculated using Taurus, with a relative difference being less than 1% for all considered time points; see Fig. 2. Ecolego notably overestimated activities in urine and faeces at times less than 1 day, in comparison with Taurus results. However, for times larger than 1 day, the relative differences for urine and faeces were less than 21% and 63%, respectively.

Activities in lungs, urine, and faeces as a function of time for ^{146}Gd, ^{148}Gd, and ^{153}Gd are shown in Fig. 3. The trends for all three radionuclides were similar in the first ten days after intake. At larger times, the differences were caused by the different half-lives of the considered radionuclides. We recall that ICRP model parameters are the same for all Gd nuclides.

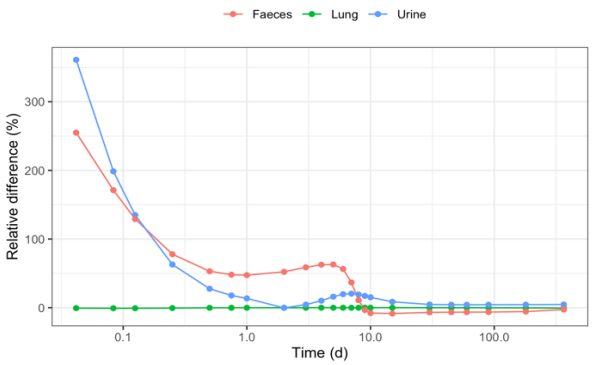

Fig. 2. Relative differences between activities of ^{148}Gd in lungs, urine, and faeces as functions of time from intake calculated using Ecolego and Taurus.

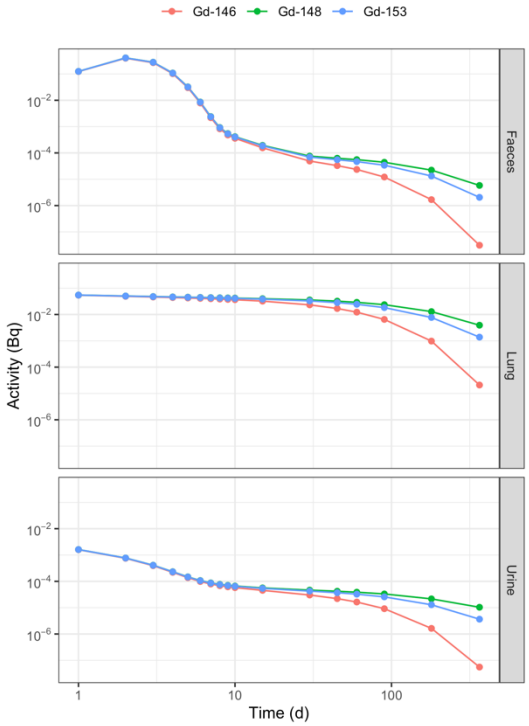

Fig. 3. Activities of ^{146}Gd, ^{148}Gd, and ^{153}Gd in faeces, lungs, and urine calculated using Ecolego.

4.2. Sensitivity analysis

The Ecolego sensitivity analysis was performed for days 1, 7, 30 and 365. The results are shown in Fig. 4.

For lungs, the most influential parameters were the fractional deposition in alveoli and interstitium ($f_{d,AI}$), fractional deposition in bronchioles ($f_{d,bb}$), rapid fraction for the alveoli ($f_{r,ALV}$), transfer coefficients from bronchiole to bronchi ($\lambda_{bb\prime\rightarrow BB\prime}$), transfer coefficient from alveoli to bronchiole ($\lambda_{ALV\rightarrow bb\prime}$), and the rapid ($s_{r,ALV}$) and slow ($s_{r,ALV}$) transfer coefficients from alveoli to blood. The deposition fraction $f_{d,AI}$ dominated at all selected times, and the rapid fraction $f_{r,ALV}$ was second for days 7, 30, and 365.

For urine, the order of the most influential parameters changed with time for 24 h urine. At day 7, the fractional depositions in the alveolar and interstitial compartments ($f_{d,AI}$), the transfer coefficient from blood to urinary bladder content ($\lambda_{blood\rightarrow UBC}$), and the slow and rapid

transfer coefficient from alveoli to blood $s_{s,ALV}$ and $s_{r,ALV}$, respectively, occupied the top four positions. At day 30, the rapid transfer coefficient $s_{r,ALV}$ became insignificant; it was replaced with the transfer coefficient from blood to the trabecular surface $\lambda_{blood\rightarrow TS}$. On day 365, the third and fourth places were taken by the transfer coefficient from blood to cortical surface $\lambda_{blood\rightarrow CS}$ and the transfer coefficient from alveoli to bronchiole $\lambda_{ALV\rightarrow bb\prime}$, respectively. Of interest is that $f_{d,AI}$ and $\lambda_{blood\rightarrow UBC}$ occupied the first two places at all selected times, the order at the day 1 was like that for lungs, and the transfer from blood to trabecular and cortical surfaces affected the order at days 30 and 365.

At day 1, the most influential parameters were those associated with the transfer through the alimentary tract and deposition fractions to the extrathoracic compartments. Namely, the transfer coefficients from the right column to the left column ($\lambda_{RC\rightarrow LC}$), from rectal sigmoid to faeces ($\lambda_{RS\rightarrow Faeces}$), from the left column to rectal sigmoid ($\lambda_{LC\rightarrow RS}$), and the fraction deposition to the first extrathoracic compartment ($f_{d,ET_{1,}}$). On day 7, the transfers in the alimentary tract were the most influential; their effect was reversed. On days 30 and 365, the most influential parameters were transfers in the lungs owing to the large retention time of ^{148}Gd in this organ.

5. Discussion

The description of the systemic model and HATM in parts 1-4 of the ICRP's publications on the occupational intakes of radionuclides is sufficient for implementing these models in Ecolego. The only missing values were the transfer coefficients from the urinary bladder content to urine and from the rectosigmoid to faeces; these values were taken from [3]. On the other hand, implementing the HRTM was problematic; some guesses had to be made based on the description in the ICRP publication 66. Our model's predictions concerning the retention of Gd in the lungs agree well with the predictions by Taurus. There is, however, a slight discrepancy in the activity in the blood (not presented), which affects activities in other compartments. We suspect some parts of the extrathoracic region were not modelled like in Taurus. More work is needed to resolve this issue.

Of question is whether influential parameters can be found by simple reasoning. The HRTM model uses rapid (s_r), slow (s_s), and very slow (s_b, bound material) transfer coefficients to the systemic model's blood. Since there is no transfer from the systemic model back to the HRTM, the transfer coefficients for rapid transfers are more influential shortly after the activity intake than the slow or very slow ones; very slow transfers become more influential a long time after the intake. The deposition of Gd in the liver, cortical bone surface, and trabecular bone surface is non-negligible. These secondary storages complicate the time behavior of the systemic model, especially for activities in faeces.

The use of SRC assumes that a linear model can describe the system. For nonlinear systems, other measures should be used; see, e.g., [7] and [20]. Currently, we search for reasonable chemical forms and values of parameters like AMAD, which strongly affect other parameters in the ICRP's HRTM. The ranges of these parameters can be used in variance-based sensitivity analysis methods. Without these ranges, standardized regression coefficients seemed like the only choice. The sensitivity coefficients [14] used were similar to the SRCs used in this work; the difference was that their coefficients were derived by solving a set of equations, while our coefficients were estimated using the Monte Carlo method. The former method is faster; the latter method is often easier to implement by the end user.

Ecolego provides several solvers of the system of differential equations. We used the NDF solver, whose solutions agreed with Taurus reasonably well. NDF is an implicit multistep-solver of variable order (1-5) based on the numerical differentiation formulas. It is applicable for stiff problems of low to medium accuracy. The DOPRI45 and RADAUS solvers provided similar results.

5. Conclusions

The ICRP's biokinetic model for lanthanides was implemented in Ecolego and tested against Taurus to predict the activity in the lungs, urine and faeces as a function of time after inhalation of ^{146}Gd, ^{148}Gd, and ^{153}Gd. A subsequent sensitivity analysis identified the most influential model parameters on days 1, 7, 30, and 365. Expert-based estimates of possible distributions of these parameters will allow uncertainty analysis of sample activities and associated MDAs.

References

1. Allard, A., Fischer, N., Sensitivity analysis in metrology: study and comparison on different indices for measurement uncertainty. 10.13140/RG.2.1.2395.9126., (2009).
2. Avila, R., Broe, R. & Pereira, A., Ecolego - a toolbox for radioecological risk assessment. Proceedings of the International Conference on the Protection from the Effects of Ionizing Radiation IAEA-CN-109/80., (2003).
3. Bengtsson I., Estimation of radiation exposure from naturally occurring radionuclides in food and foodstuff, Master Thesis, University of Gothenburg, (2018).
4. Blixt Buhr A. M., ESS research facility: Basis for emergency preparedness and response planning, SSM 2018:22, (2018).
5. ISO 11929-2:2019, Determination of the characteristic limits (decision threshold, detection limit and limits of the coverage interval) for measurements of ionizing radiation — Fundamentals and application — Part 2: Advanced applications, (2019).
6. Doerfel H. R. *et al*., General guidelines for the estimation of committed effective dose from incorporation monitoring data, (2006).
7. Ekström P.,A Simulation Toolbox for Sensitivity Analysis., Master's Thesis, Uppsala University, (2005).
8. Eriksson Stenström, K., Barkauskas, V., Pédehontaa-Hiaa, G., Nilsson, C., Rääf, C., Holstein, H., Mattsson, S., Martinsson, J., Jönsson, M., & Bernhardsson, C. (2020). Identifying radiologically important ESS-specific radionuclides and relevant detection methods. SSM 2020:08, (2020).
9. Garoby R. et, The European Spallation Source Design, Physica Scripta, Volume 93, Number 1, (2017).
10. ICRP, Occupational Intakes of Radionuclides: Part 1. ICRP Publication 130. s.l. : Ann. ICRP 44(2)., (2015).
11. ICRP, Occupational intakes of radionuclides: Part 4. ICRP Publication 141. s.l. : Ann. ICRP 48(2/3), (2019).
12. ICRP, Human Alimentary Tract Model for Radiological Protection. ICRP Publication 100. s.l. : Ann. ICRP 36 (1-2)., (2006).

13. Ihaka R., Gentleman R., R: A Language for Data Analysis and Graphics, Journal of Computational and Graphical Statistics, 5:3, 299-314, DOI: 10.1080/10618600.1996.10474713, (1996).
14. Khursheed, A., and T.P. Fell. "Sensitivity Analysis for the ICRP Publication 67 Biokinetic Model for Plutonium." Radiation Protection Dosimetry 74, no. 1, 63–73, (1997).
15. N. M. Chiera, R. Dressler, P. Sprung, Z. Talip, D. Schumann, Determination of the half-life of gadolinium-148, Applied Radiation and Isotopes, Volume 194, (2023).
16. Pettersson H., Malusek A., Karlsson M. ,Internal dosimetry of radionuclides that can be released during an accident at the European Spallation Source (ESS), SSM 2022:10, (2022).
17. Rääf, C., Barkauskas, V., Eriksson Stenström, K. et al. Internal dose assessment of 148Gd using isotope ratios of gamma-emitting 146Gd or 153Gd in accidently released spallation target particles. Sci Rep 10, 21887, (2020).
18. Rääf, C., Gamma Spectrometry, Handbook of Nuclear Medicine and Molecular Imaging for Physicists: Instrumentation and Imaging Procedures (1 ed., Vol. 1).,Series in Medical Physics and Biomedical Engineering, CRC Press., (2022).
19. Riddell A. E., Smith T. J., Gregoratto D., Hyatt T., Taurus Advanced - Internal Dosimetry Software for Research UK Health Security Agency
20. Swiler L., Becker D.A et al., Sensitivity Analysis Comparisons on Geologic Case Studies: An International Collaboration, September 1, (202)

Appendix

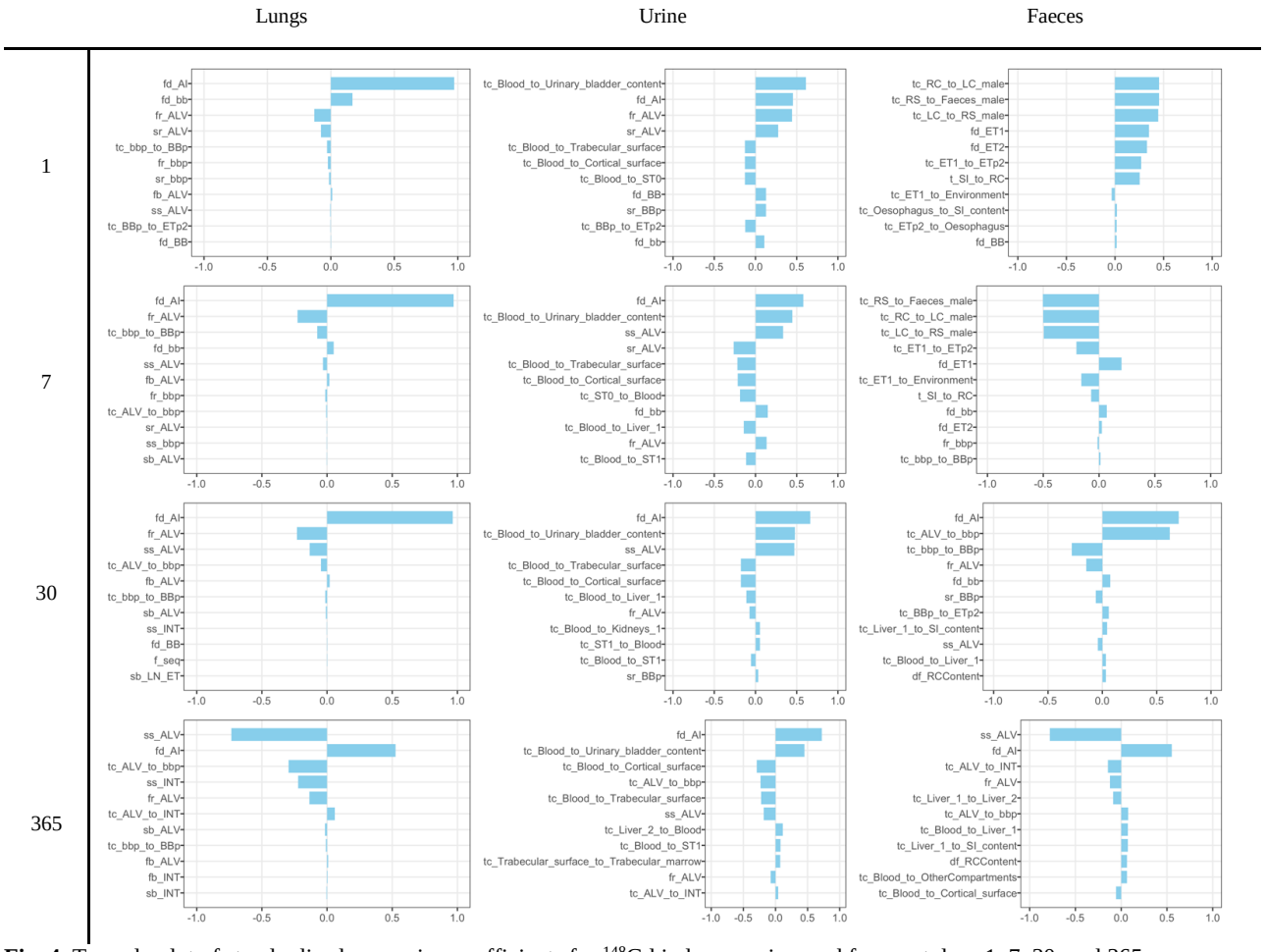

Fig. 4. Tornado plot of standardized regression coefficients for ^{148}Gd in lungs, urine, and faeces at days 1, 7, 30, and 365.

Table 1. The four most influential model parameters and corresponding standardized regression coefficients for ^{148}Gd in lungs, 24 h urine, and 24 h faeces at days 1, 7, 30, and 365.

Comp.	Order	1		7		30		365	
Lung	1	$f_{d,AI}$	+0.97	$f_{d,AI}$	+0.97	$f_{d,AI}$	+0.96	$s_{s,ALV}$	-0.74
	2	$f_{d,bb}$	+0.17	$f_{r,ALV}$	-0.23	$f_{r,ALV}$	-0.23	$f_{d,AI}$	+0.53
	3	$f_{r,ALV}$	-0.13	$\lambda_{bb\prime\rightarrow BB\prime}$	-0.08	$s_{s,ALV}$	-0.13	$\lambda_{ALV\rightarrow bb\prime}$	-0.29
	4	$s_{r,ALV}$	-0.08	$f_{d,bb}$	+0.05	$\lambda_{ALV\rightarrow bb\prime}$	-0.05	$s_{s,INT}$	-0.22
Urine	1	$\lambda_{blood\rightarrow UBC}$	+0.61	$f_{d,AI}$	+0.58	$f_{d,AI}$	+0.66	$f_{d,AI}$	+0.72
	2	$f_{d,AI}$	+0.45	$\lambda_{blood\rightarrow UBC}$	+0.45	$\lambda_{blood\rightarrow UBC}$	+0.48	$\lambda_{blood\rightarrow UBC}$	+0.45
	3	$f_{r,ALV}$	+0.44	$s_{s,ALV}$	-0.26	$s_{s,ALV}$	+0.47	$\lambda_{blood\rightarrow CS}$	-0.29
	4	$s_{r,ALV}$	+0.28	$s_{r,ALV}$	+0.34	$\lambda_{blood\rightarrow TS}$	-0.18	$\lambda_{ALV\rightarrow bb\prime}$	-0.23
Faeces	1	$\lambda_{RC\rightarrow LC}$	+0.46	$\lambda_{RS\rightarrow Faeces}$	-0.50	$f_{d,AI}$	+0.70	$s_{s,ALV}$	-0.78
	2	$\lambda_{RS\rightarrow Faeces}$	+0.46	$\lambda_{RC\rightarrow LC}$	-0.50	$\lambda_{ALV\rightarrow bb\prime}$	+0.62	$f_{d,AI}$	+0.56
	3	$\lambda_{LC\rightarrow RS}$	+0.45	$\lambda_{LC\rightarrow RS}$	-0.49	$\lambda_{bb\prime\rightarrow BB\prime}$	-0.28	$\lambda_{ALV\rightarrow INT}$	-0.15
	4	f_{d,ET_1}	+0.35	$\lambda_{ET_1\rightarrow ET_2'}$	-0.20	$f_{r,ALV}$	-0.15	$f_{r,ALV}$	-0.12

MEDICAL PHYSICS IN THE BALTIC STATES 16 (2023)

Proceedings of International Conference "Medical Physics 2023"
09-11 November 2023, Kaunas, Lithuania

ASSESSMENT OF COMPTON/PHOTOPEAK RATIO IN GAMMA SPECTRA OF DIFFERENT DETECTORS FOR VARIOUS THICKNESS METAL SHIELDING

Kristina MIKALAUSKIENĖ, Marina KONSTANTINOVA, Darius GERMANAS, Rita PLUKIENĖ, Elena LAGZDINA, Artūras PLUKIS
State research institute Center for Physical Sciences and Technology, Vilnius, Lithuania
kristina.mikalauskiene@ftmc.lt, marina.konstantinova@ftmc.lt, darius.germanas@ftmc.lt, rita.plukiene@ftmc.lt, elena.lagzdina@ftmc.lt, arturas.plukis@ftmc.lt

***Abstract*:** Gamma-ray spectrometry takes an important part of radiation safety dealing with different gamma-ray precursors in the radioactive materials. Compton-to-peak ratios dependencies of ^{60}Co and ^{137}Cs nuclides by analysing metallic samples with HPGe and $CeBr_3$ detectors were determined. A good consistency of experimental and modelled results is obtained during comparison of γ-spectra of ^{60}Co and ^{137}Cs point sources in different shielding configurations for analysed detectors.
This type of analysis could be useful for identification of surface and volume contamination.

Keywords: γ-spectrometry, MCNP modelling, Compton scattering edge, Compton/photopeak ratio

1. Introduction

Gamma spectrometry holds immense significance in the characterization of different radiation sources, evaluation of shielding effectiveness, and various nuclear safety applications.
Assessment of photopeaks and Compton edges, peak-to-Compton ratio [1-3] and other techniques are widely used for determination of unknown source and shielding information in case of radioactive waste surface and volume contamination [4-5], quantitative analysis [3], and detail characterization of activity sources. Also, these methods could be applicable for a wider set of detectors [1, 6].
Computer modelling and spectrometric measurement methods are complementary to each other and used for assessing various tasks in gamma spectrometry. Two HPGe detectors and $CeBr_3$ detector were analysed in order to assess Compton/photopeak ratio for various thickness metal shielding. The $CeBr_3$ detector was included in the comparison as recent years have witnessed a rise for advancing scintillator materials, including bromide-based variants. Among these, $CeBr_3$ stands out as an appealing option for achieving medium to high-energy gamma-ray spectrometry. Its resolution surpasses that of a standard NaI(Tl) detector, though falling short of an HPGe detector. The resolution of $CeBr_3$ detectors might prove satisfactory in meeting quality standards, encompassing uncertainties and detection thresholds, for main radionuclide determinations. Therefore, a $CeBr_3$ detector can be particularly attractive for routine tasks in radiological environmental monitoring as it has a high efficiency, medium energy resolution and it can work at room temperature [7]. Notably, this includes the quantitative measurement of ^{137}Cs and ^{60}Co activity using gamma-ray spectrometry.
The aim of this research is to determine Compton-to-peak ratios dependencies of ^{60}Co and ^{137}Cs nuclides by analysing these metallic waste samples with HPGe and $CeBr_3$ detectors. Through a combination of experimental analysis and MCNP6 modelling we have achieved characteristic peak and Compton scattering edges ratios within various iron shielding configurations with different detectors.

2. Materials and methods

The preliminary analysis and experimental assessments have been carried out. Computer simulations with MCNP6 transport code and measurements with two HPGe and $CeBr_3$ detectors were applied. Metallic samples of varying thicknesses were used between ^{60}Co and ^{137}Cs point sources and the Compton-to-peak ratios of unshielded and shielded with the six plates were evaluated. The methods used in this study concerning the estimation of the Compton-to-peak ratio from experimental and simulation data for ^{60}Co and ^{137}Cs sources under various metal shielding conditions are described below.

2.1. Gamma spectroscopy

In this work gamma spectrometry serves as a useful tool for investigation and advancing non-dstructive

methodology for identification of surface and volume contamination in metallic radioactive waste. Its versatility and ability to provide precise information about gamma-ray interactions make it an essential technique for such application in characterization of radioactive materials.

Gamma rays interact with matter through processes such as the photoelectric effect, where electrons are ejected from the inner shell, Compton scattering, where energy is transferred to the electrons and reverses direction, and pair formation, where electron-positron pairs are formed by interactions with nuclei or other photons. All these reactions produce electrical pulses in the detectors, which are then used to estimate the energy and other aspects of the initial gamma rays.

In our case, the gamma-ray spectrometric measurements of metal samples were carried out using two HPGe detectors: the first one (HPGe(1)) with 26.2 % relative efficiency and resolution ~1.76 keV/1.33 MeV (Canberra Industries, USA) and the second one (HPGe(^{2})) with 44% relative efficiency at 1.33 MeV (Baltic Scientific Instruments, Latvia), as well as a standard high resolution 51 mm diameter CeBr3 scintillation detector 51B51/2M-CEBR-X (Scionix, Netherlands). Detectors have been efficiency-calibrated for the standard geometry of the measurement.

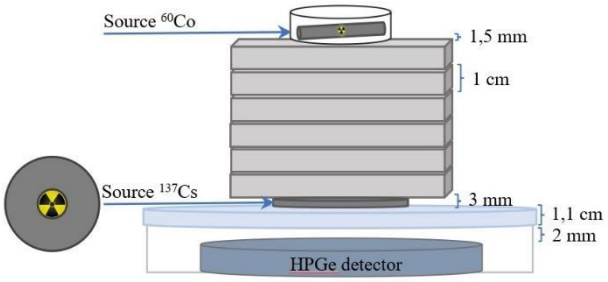

Fig. 1. The scheme of experiment using HPGe(^{2}) detector

^{137}Cs and ^{60}Co point sources were measured, between which were placed several steel plates of 50 ×71×10 mm diameter as it is shown in the schemes of figures 1 and 2 respectively for HPGe and $CeBr_3$ detectors. It should be noted that for the $CeBr_3$ detector a higher activity ^{60}Co source was used due to the lower resolution of the detector (Fig. 2). When the source was between the plates, it was placed inside a central hole of Al disk with an inner diameter of 26 mm, an outer diameter of 75 mm, and a thickness of 3 mm

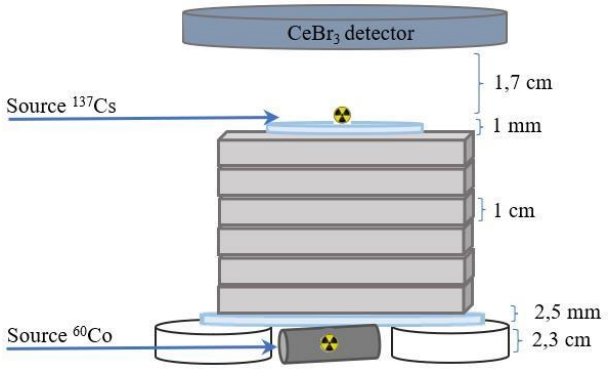

Fig. 2. The scheme of experiment using $CeBr_3$ detector

The challenges during the experiment using organic scintillators were due to quantitative analysis of obtained gamma-ray spectra, because of considerable complications, e.g., unlike the Gaussian-shaped photopeak, the Compton edge region in the Compton continuum, by nature, presents asymmetric features [8]. The Compton edge is important feature, and its asymmetry provides useful information on interaction of gamma rays with matter. The asymmetry in the Compton edge region arises from contribution from scattered photons, backscattered gamma rays and other effects, including due intrinsic energy resolution of detectors etc. The calibration is necessary for accurate investigation of the initial gamma-ray energy and for understanding of the relative nature of the various spectral peculiarities. In the study the energy calibration as usually has been done by registering the Compton continuum and evaluation of Compton edge position, as the Compton edge energy is related with incident γ-ray energy. For investigations of Compton-to-peak ratio, the position of the Compton edge was determined using the equation [9].

$$E_e = \frac{2E_\gamma^2}{2E_\gamma + m_e}$$

where E_e is the Compton edge energy, and Eγ is the photopeak maximum. The HPGe detectors have good resolution and Compton edge is clearly distinguished, while CeBr3 scintillation detector has lower resolution and Compton edge is poorly visible, in this case the above mentioned technique was applied.

Compton scattering edges and photo-peaks ratios have been investigated for two HPGe and CeBr3 detectors and results were compared with modelling.

2.2. Computer modelling

Numerical simulations were conducted using the MCNP6 transport code (Monte Carlo N-Particle version◦6). This computational tool is committed for emulating particle behaviour in intricate physical setups via the Monte Carlo method. It is specifically designed for simulating the transport of neutrons, photons, electrons, and other particles in various materials and geometries. Monte Carlo transport is based on explicit tracking of particles. Probability distributions are randomly sampled using transport data. In our study, MCNP6 was applied to model the interaction of ^{60}Co and ^{137}Cs gamma rays with varying thicknesses of metal shielding as well as detector material itself.

For ^{137}Cs the monoenergetic gammas of 661.7 keV have been tracked, but in case of ^{60}Co the coincidence summing calculation was performed in a following way: first we simulate monoenergetic gammas that for ^{60}Co are 1.173 MeV and 1.332 MeV. Data for the pulse height F8 tally in the output file of the simulation consist of range of energy intervals so called bins that are arranged in increasing order. To each of the energy interval simulated probability detecting it in the detector is given as well as uncertainty of calculation. Then, having these results, we apply formula [10]

$$C(E_n) = C(E_n)_{1173}[1 - \sum_{m=1}^{M} C(E_m)_{1332}] + C(E_n)_{1332}[1 - \sum_{m=1}^{M} C(E_m)_{1173}] + \sum_{m=1}^{n} C(E_m)_{1173}\, C(E_{n-m})_{1332}$$

where E_n is the counts in the n-th interval corresponding to energy E_n, m and n are interval numbers, M is largest interval number, 1173 and 1332 refer to simulated gammas. FORTRAN code was written for calculation of coincidence summing according to this formula and bash shell script performing routine calculations.

3. Results

The γ-spectra of ^{60}Co and ^{137}Cs sources in different shielding geometries is presented below in Fig. 3-4 for HPGe$^{(2)}$ detector. An experimental model and a computer simulation approach were used to compare the area of interest.

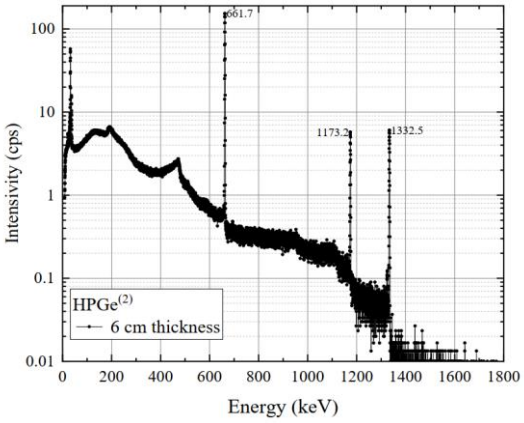

Fig. 3. Spectrum of ^{60}Coand ^{137}Cs sources obtained by using HPGe detector$^{(2)}$ in case of 6 cm thickness metal plate between sources (see Fig. 1 for detail geometry)

In the Fig. 3 one can observe the 661.7 keV full-energy peak of ^{137}Cs, its Compton edge at about 473.1 keV [9], the Compton continuum below and the broad peak are due to backscattering. The ^{60}Co peaks are accordingly present in the spectrum at 1173,2 keV and 1332.5 keV and the Compton edge of the latter one is obscured. Comparison of ^{60}Co spectra with unshielded source and different thickness shielding using HPGe$^{(2)}$ detector is presented in Fig, 4.

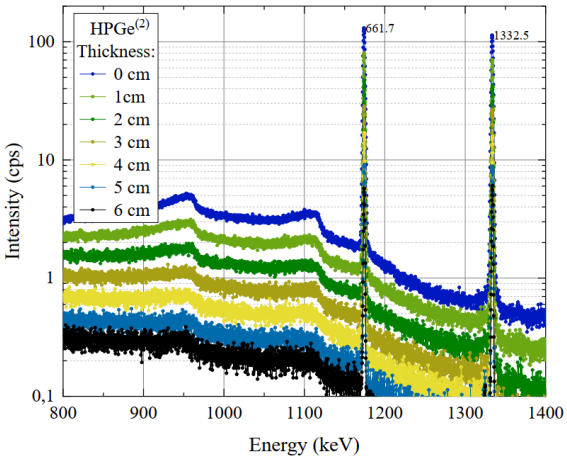

Fig. 4. Comparison of ^{60}Co spectra with different thickness of shielding using HPGe detector$^{(2)}$.

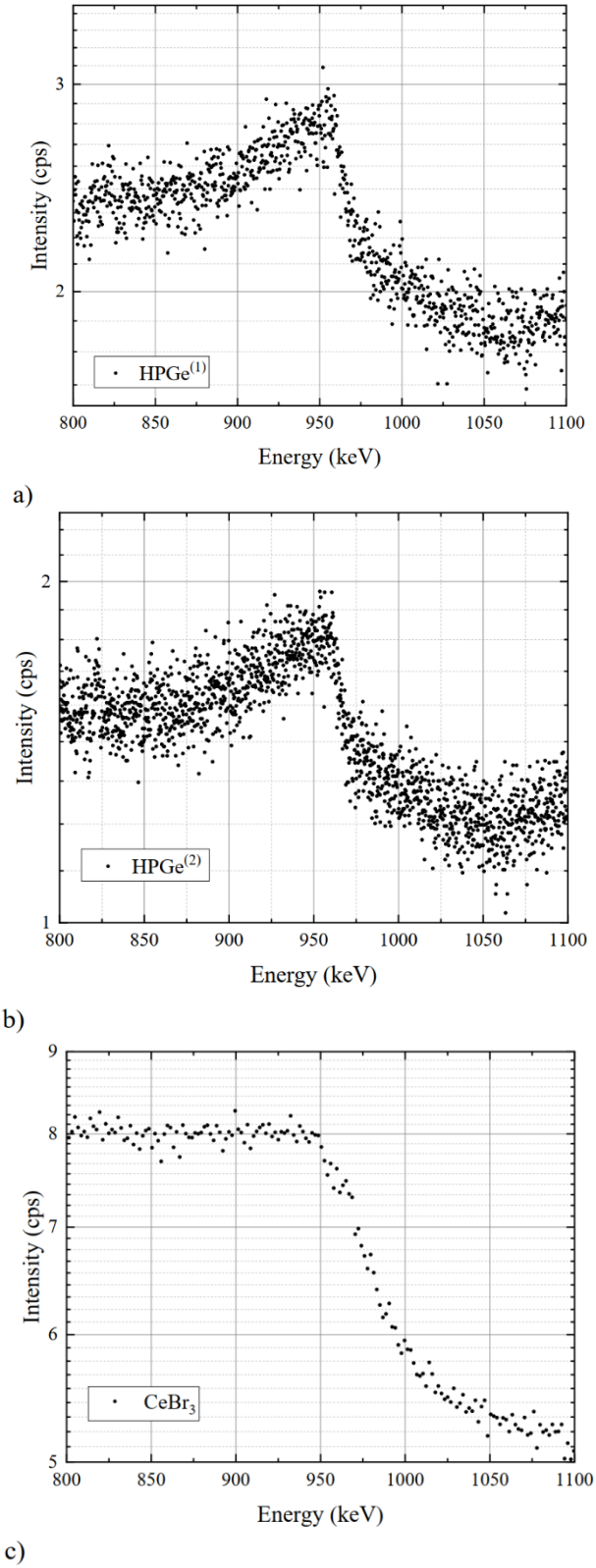

Fig. 5. The ^{60}Co Compton edge part of spectrum using HPGe$^{(1)}$ detector (a), HPGe detector (b) and $CeBr_3$ detector (c)

It was observed a steadily decrease of the Compton edge depending on increase of the thickness of shielding The different Compton edge formation is observed in the spectra obtained using HPGe and $CeBr_3$ detectors as could be observed in Fig.5.

The table 1 show the variation of the Compton-to-peak ratio of ^{60}Co for different thicknesses of shielding metal plates between ^{60}Co and ^{137}Cs point sources. The analysis shows possibility of distinguishing between unshielded source of ^{137}Cs and ^{60}Co source shielded with different thicknesses of iron plates: in all analysed cases the first 1 cm of iron shield determines about 15-20% increase in Compton-to-peak ratio for 1173.2 keV ^{60}Co peak. The further addition of shielding material depends on detector applied.

Table 1. ^{60}Co (1173.2 keV) Compton/peak ratio values using various thickness of metal plates placed between the source and the detector (h, cm) depending on the energy and the detector type (measured)

h, cm	HPGe detector(1)	$CeBr_3$ detector
0	0.056 ± 0.001	0.166 ± 0.002
1	0.066 ± 0.001	0.213 ± 0.003
2	0.072 ± 0.001	0.312 ± 0.005
3	0.088 ± 0.002	0.359 ± 0.005
4	0.099 ± 0.002	0.382 ± 0.006
5	0.108 ± 0.003	0.449 ± 0.005
6	0.130 ± 0.004	0.682 ± 0.002

Table 2. Comparison of measured and modelled ^{60}Co (1173.2 keV) Compton/peak ratio values using various thickness of metal plates placed between the source and the detector (h, cm) using HPGe detector(2)

h, cm	Modelled	Measured
0	0.035 ± 0.001	0.037 ± 0.001
1	0.043 ± 0.002	0.043 ± 0.001
2	0.061 ± 0.002	0.047 ± 0.001
3	0.067 ± 0.002	0.053 ± 0.002
4	0.073 ± 0.002	0.058 ± 0.002
5	0.080 ± 0.003	0.061 ± 0.002
6	0.087 ± 0.003	0.067 ± 0.002

Table 2 shows comparison of modelled with the MCNP6 transport code and measured Compton-to-peak ratios in case of HPGe detector(2). The modelling suggest that in case of HPGe(2) detector every additional cm of shielding determines increase in ~6% of Compton-to-peak ratio, in the real measurement the increase is about ~8% for HPGe detectors and ~11% for $CeBr_3$ detector. Measured and modelled gamma spectra of 60Co and 137Cs sources for different metal shielding cases are presented in Fig. 4 and Fig. 6 respectively for HPGe(2) detector. We should note, that the difference of experimental and simulated results lays in 0-5% for the first two cm of shielding and about 20% in subsequent addition of shielding. Most probably it is due to real background (scattering from walls and other objects), which is omitted in the modelling case. Overall, the experimental and modelling results are in good agreement for thin metallic shielding of ^{60}Co.

As can be seen from the Table 1 and Table 2, the Compton-to-peak ratio values depends on the detectors resolutions: difference between HPGe detectors is relatively small (~1.4 times), but difference between CeBr3 and HPGe(1) is ~4, respectively for CeBr3 and HPGe(2) difference is ~5.6. Also, the photopeak areas of spectra measured using the $CeBr_3$ scintillating detector are considerably more broadened (see Fig. 7 for detail) comparing to the same of HPGe detectors. The comparison of gamma spectra depending on the resolution of detectors are very well shown in the Fig. 8.

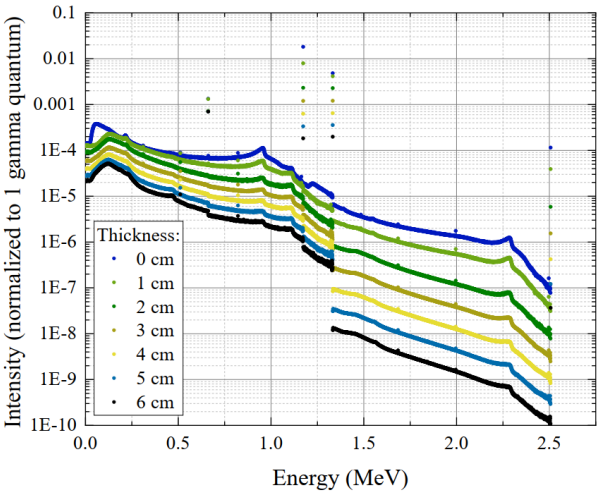

Fig. 6. Modelled gamma spectra of ^{60}Co and ^{137}Cs sources at different conditions of metal shielding between mentioned sources for HPGe detector(2)

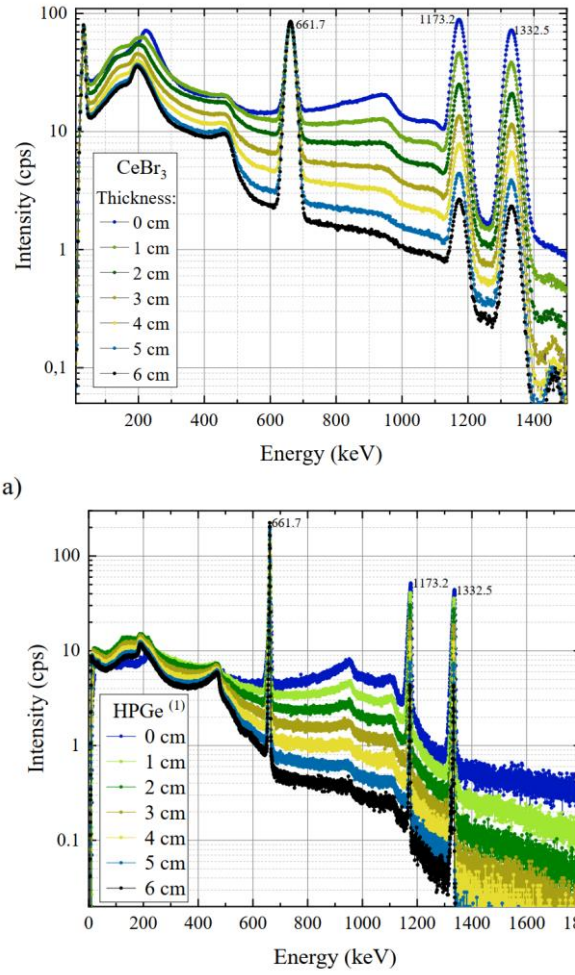

Fig. 7. Comparison of ^{137}Cs and ^{60}Co spectra with different thickness shielding (using $CeBr_3$ detector (a) and HPGe(1) (b))

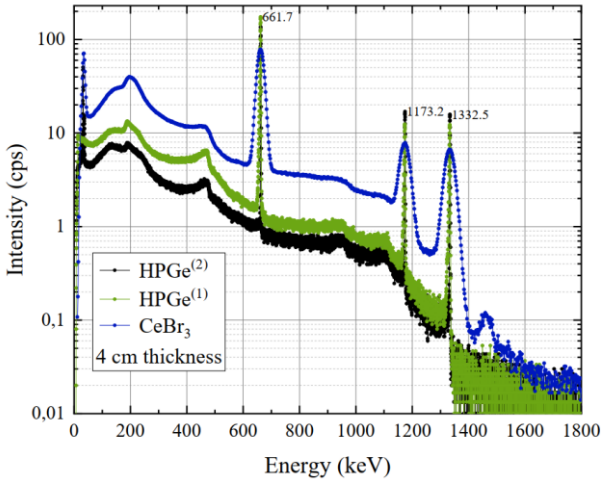

Fig. 8. Comparison of ^{60}Co and ^{137}Cs sources spectra at the 4 cm metal shielding condition using $CeBr_3$ scintillation detector and two HPGe detectors.

The HPGe and $CeBr_3$ detectors used in this study have a difference in resolution of more than 10 times: the deterioration of the energy resolution leads to enhanced smearing of Compton continuum spectrum [6]. The sensitivity and gamma peak resolution are significantly increased using a HPGe detectors, resulting in a more accurate expression of the peak-to-Compton ratio. However, the $CeBr_3$ scintillation detector could be also used in investigations but with less accuracy.

4. Conclusions

In this investigation the Compton-to-peak ratio of gamma spectra analysis as a tool for assessment of radioactive source activity in different metal shielding conditions was used. Experimental measurements by using two HPGe detectors and $CeBr_3$ detector measurements of known-home-made different geometry metallic samples with ^{60}Co and ^{137}Cs sources have been performed, as well as modelling with MCNP6. Inter-comparison of experimental γ-spectra analysis shows, that Compton-to-peak ratio values depend on the detectors resolutions: difference between HPGe detectors is relatively small (~1.4 times), difference between $CeBr_3$ and HPGe detectors varies 4-5.6 times respectively.

Measurement results of unshielded source of ^{137}Cs and ^{60}Co source shielded with different thicknesses of iron plates reveal, that the first 1 cm of iron shield determines about 15-20% increase in Compton-to-peak ratio for 1173.2 keV ^{60}Co peak for all analysed detectors. The further addition of shielding material results in Compton-to-peak ratio increase depending on detector resolution and shielding thickness.

Considering $HPGe^{(2)}$ detector it was noted, that the difference of experimental and simulated results is in good agreement (0-5%) for the thin shielding (1-2cm) and increases (by 20%) in subsequent addition of shielding. This could be influenced by the real background - scattering from walls and other objects. This analysis provides valuable insights into the determination of surface and volume activity in different thicknesses of shielding metal, consequently can improve the characterization of nuclear materials assay with better accuracy.

As the results show, despite the fact, that $CeBr_3$ is characterized by 10 times lower sensitivity it is still suitable for in-situ measurements of metallic radioactive waste for identification of surface and volume contamination.

References

1.. El-Tayebany R. A., Hamed A. A., Abdelsalam A., Osman W., El-Mongy S. A. Enhancement of Peak to Compton Ratio (P/C) using a New Array Design for Safeguards Applications, 2015

Perot B., Pin P. Characterisation of the low-energy photon attenuation in gamma-ray spectroscopy of bituminized radioactive waste drums using a peak-to- Compton ratio, Nuclear Instruments and Methods in Physics Research, A671(2012)76–81.

3. Zeynep Uzunoğlun, Demet Yılmaz, Yusuf Şahin. Quantitative x-ray spectrometric analysis with peak to Compton ratios, Radiation Physics and Chemistry 112 (2015) 189–194

4. Lagzdina E., Plukienė R., Germanas D., Mikalauskienė K., Konstantinova M., Plukis A. and Remeikis V. Modelling and experimental determination of surface and volume activity in different geometry metallic waste samples, Proceedings of the European Nuclear Young Generation Forum ENYGF'23, May 8-12, 2023, Kraków, Poland

5. V. Remeikis et al., "Characterisation of RBMK-1500 graphite: A method to identify the neutron activation and surface contamination terms," Nucl. Eng. Des., vol. 361, 2020.

6. Swiderski L., Moszyński M., Czarnacki W., Iwanowska J., Syntfeld-Każuch A., Szczęśniak T., Pausch G., Plettner C., Roemer K. Measurement of Compton edge position in low-Z scintillators, Radiation Measurements, 45, 3–6, 2010. p.605-607

7. Idoeta R. *et al.*, "Possibilities of the use of CeBr3 scintillation detectors for the measurement of the content of radionuclides in samples for environmental monitoring", Appl. Rad. and Isotopes, vol. 176,109881, 2021, DOI:10.1016/j.apradiso.2021.109881.

8. Kim C., Kim J., Hong W., Yeom J., Kim G. Development of an energy and efficiency calibration method for stilbene scintillators, Nuclear Engineering and Technology, 54, 10, 2022. p. 3833-3840

9.https://userswww.pd.infn.it/~moretto/fontana/projec/software/2018/03/16/compton-edge.html

10. Z. Wang, B. Kahn and J. D. Valentine, Efficiency calculation and coincidence summing correction for germanium detectors by Monte Carlo simulation. IEEE T Nucl Sci, 49(4), 1925-1931, (2002), https://ieeexplore.ieee.org/document/1043597

MEDICAL PHYSICS IN THE BALTIC STATES 16 (2023)

Proceedings of International Conference "Medical Physics 2023"
09-11 November 2023, Kaunas, Lithuania

SELECTED TWO-SAMPLE TESTS FOR HIGH-DIMENSIONAL DATA USING SUBSPACES OF VARIABLES: ANALYSIS ON BREAST CANCER DATASET

Flamur HASIMI[1], Kamil SMOLICZ[2], Lumbardha HASIMI[2], Dimitrios ZAVANTIS[3]
[1]University Clinical Center Kosovo; [2]Lodz University of Technology, Lodz, Poland; [3]Hasselt University, Hasselt, Belgium
[1]hasimiflamur@gmail.com; [2]lumbardha.hasimi@p.lodz.pl; [3]dimitrios.zavantis@uhasselt.be

***Abstract*:** Nowadays, enormous requirements related to testing two data samples are imposed. A common problem encountered in many fields of science is the comparison of the mean vectors of two data samples, in which the data dimension is even larger than the sample size. Tools that have so far dealt with the problem of two-sample data testing, such as the Hotelling T2 test, often become useless in testing high-dimensional samples. This paper aims to present tests that are able to deal with the problem of testing two samples of highly multivariate data. Firstly, these tests were presented from the theoretical point of view, and then discussed further through their implementation in R. Simulation studies were also carried out in order to obtain the empirical size of individual tests and their power. Ultimately, the effectiveness in detecting significant differences was demonstrated by using the above in testing breast cancer dataset.

Keywords: high-dimensional data; two-sample testing; random subspaces; hierarchical clustering; breast cancer

1. Introduction

A significant problem encountered when working with high-dimensional data is when the sample size n is relatively small compared to the data size p. This situation occurs in modern genetic research, signal processing, astrometry, and some financial topics, among others. High dimensional data has created the need to renew some of the basic methods used in multivariate analysis [1].
In a typical situation, when the data dimension is not larger than the size of the sample to be tested Hotelling's T test is used to test two data samples. However, in a situation where p n, the use of Hotelling's test becomes impossible, because it is not correctly defined [2].
An example of such a problem would be testing whether a set of interdependent gene expressions differs between two populations. At this extent, to comparing the mean vectors of two data samples, where the data size is usually larger than the sample size, the Hotelling test cannot be used. Many researchers have attempted to develop statistical methods that deal with the problem of high-dimensional data. In this work, we focus on presenting the most valuable and optimal methods that can be used to test highly multidimensional data.

2. Simulation studies

In this chapter, we will describe the conducted simulation studies, the task of which was to compare the tests of Thulin (2014) and Zhang and Pan (2016) with respect to the control of type I error and test power. For this purpose, numerical experiments, described below and performed using the Monte Carlo method, were carried out to calculate the empirical size and empirical power of the tests. The empirical size estimates the probability of a type I error, which should be close to the significance level $\alpha = 0.05$. The empirical power obviously estimates the test power, which should be as large as possible. The higher the power, the better the statistical test.

2.1. Numerical testing

Before presenting the implementation, we briefly discuss the generation of the data that will be compared. The following data generation scenarios were developed on the basis of simulation studies presented in Zhang and Pan (2016). Two samples X = (X1, X2, ..., Xn1)T containing n1 observations and Y = (Y1, Y2, ... ,Yn2)T containing n2 observations are generated from p-dimensional normal distributions, respectively $N(\mu 1, \Sigma)$ and $N(\mu 2, \Sigma)$. Data will be generated at p = 200 or p = 1000; n1 = n2 = 50 and $\Sigma = \Sigma$ a,b = (σij), where i = 1, 2, . . . , p, j = 1, 2, . . . p .
We define the values of αij as follows:

- σij = 1, for i = j,
- σij = a, for i ≠ j and i/25 = j/25,
- σij = b, for i/25 ≠ j/25.

The covariance matrix Σa,b is divided into p/25 blocks of the same size (25×25). For example, for p = 200, the

matrix Σa,b will be divided into 8 equal blocks. The covariance values σij are equal to α if i and j belong to the same block, otherwise σij = b. We assume μ1 = 0 and μ2 = (μ2j), where j = 1, 2, . . ., p and μ2j = d, for j/25 ≤m, mod(j - 1, 25) < 20, otherwise μ2j = 0. Thus, for sample Y, we shifted the expected values of 20 variables from 25 variables evenly in each of the m blocks out of o/25 blocks.

We assume m Є {1, 8} for p = 200; m Є {8, 40} for p = 1000. Then d = D/ √20m, so the value of D is the Euclidean distance between the expectation vectors ||μ1-μ2||. Data were generated from a multivariate normal distribution with the following covariance structures Σ0.0, Σ 0.5,0.1, Σ 0.9,0.2. Below is an implementation that runs 500 iterations of a simulation examining the size or power of the tests [1], [3].

2.1. Numerical testing

To assess the level of error of the first type for the tests of [1], [3] we performed Monte Carlo simulation studies, assuming the null hypothesis H0: μ1 = μ2 = 0 for p = 200 and p = 1000, with values of n1 = n2 = 50. We performed 500 simulations for p = 200 and 200 simulations for p = 1000. Samples X and Y were generated with the following covariance structures Σ 0.0, Σ 0.5,0.1, Σ 0.9,0.2. The results of the simulation are presented in Table 5.1, i.e. the percentage of type I errors at the significance level α = 0.05. Based on these results, we can conclude that both the Thulin test [1] and the Zhang and Pan test [3] have an acceptable level of error of the first type, which oscillates around the level of significance.

Table 1. Empirical sizes of the Thulin (2014) and Zhang and Pan (2016) tests

	p	Thaulin Test	Test Zhang and Pan
$\Sigma_{0.0}$	200	0.054	0.068
$\Sigma_{0.5,0.1}$	200	0.042	0.056
$\Sigma_{0.9,0.}$	200	0.052	0.061
$\Sigma_{0.0}$	1000	0.092	0.065
$\Sigma_{0.5,0.1}$	1000	0.038	0.052
$\Sigma_{0.9,0.}$	1000	0.041	0.049

The power of a test is the probability of not making a Type II error. Thus, in order to estimate its value, pairs of samples X, Y were generated assuming that it is true alternative hypothesis H1: μ1 = μ2. The empirical power of the test was presented as a function depending on the Euclidean distance between the expected value vectors ||μ1 ÿμ2|| in Figures 1 and 2 for p = 200 and p = 1000, respectively. As before, we generated 500 pairs of samples for the case with p = 200 and 200 pairs of samples for the case with p = 1000, with covariance structures equal to Σ0.0, Σ 0.5,0.1, Σ 0.9,0.2. From the graphs it can be concluded that at p = 200 the power of both tests' changes very similarly, in particular for the structures of the covariance matrix $\Sigma_{0.0}$ and $\Sigma_{0.9,0.2}$. Both tests for the p = 200 case have satisfactory power with a small m = 1 and a large m = 8 number of shifted variables. For the case where p = 1000, the test of Thulin (2014) is as powerful as the test of Zhang and Pan (2016) with the covariance structure $\Sigma_{0.0}$ and with the structure ÿ $\Sigma_{0.5,0.1}$ and a small number of shifted variables m = 8. In any other case, the Zhang and Pan test[3] is more powerful than the Thulin test[1]. This can be explained by the construction of the Zhang and Pan (2016) test and the specific forms of the covariance matrix that were used in the simulations. Nevertheless, Zhang and Pan's (2016) test using cluster subspaces may be much more powerful than Thulin's (2014) test using random subspaces

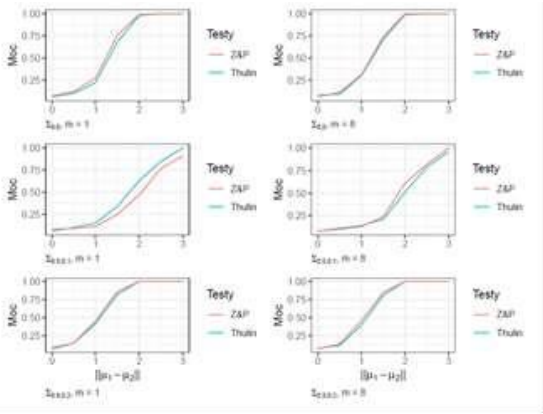

Fig. 1. Empirical power tests Thulin (2014) and Zhang and Pan (2016) for p=200

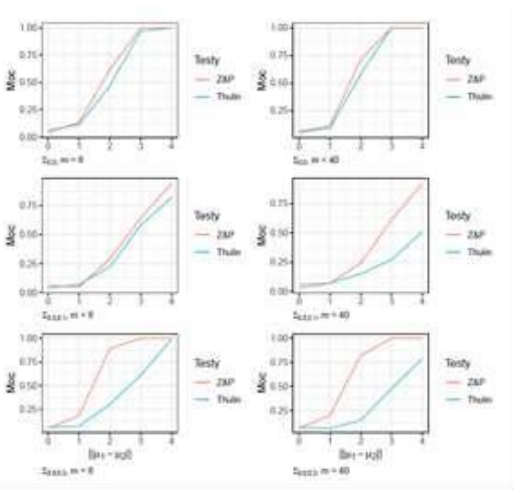

Fig. 2. Empirical power tests Thulin (2014) and Zhang and Pan (2016) for p = 1000

3. Results of the analysis conducted on breast cancer dataset

The tests that were described in the previous chapters, in particular the Thulin test (2014) and the Zhang and Pan test (2016), were used to analyze the breast cancer dataset

3.1. Dataset

Following up on a similar study by [4] conducted a study on breast cancer patients without inguinal lymph node involvement, we focus on the dataset of the same population. In the study conducted in [4] 2,905 gene expressions were examined in 168 patients using comparative genomic hybridization. The first sample

consisted of $n_1 = 111$ patients without metastases for 5 years after diagnosis and the second sample $n_2 = 57$ patients with early metastases. Our task therefore focuses on checking whether the population of patients without metastases is significantly different from the population of patients with previous metastases in terms of average gene expression values. For this purpose, we used the available data and the tests of [1] and [3].

3.2. Statistical tests used

Thulin test (2014) and the Zhang and Pan test (2016) were used to test three sets of genes from the data obtained [4]. Tested as follows:

- set containing p = 374 genes located on chromosome 1,
- set containing p = 233 genes located on chromosome 2,
- set containing p = 191 genes located on chromosome 12.

To perform the Zhang and Pan (2016) test, we first performed a hierarchical cluster analysis. With a given number of data, the kc parameter = 110. Based on the calculated cut-off distance dc, the three sets of genes were divided as follows:

- Chromosome 1, containing p = 374 genes, was divided into 12 clusters. Cluster 2 contained 128 genes (more than the value of the kc parameter), so it was divided into 2 subclusters 2a and 2b.
- Chromosome 2, containing p = 233 genes, was divided into 15 clusters.
- Chromosome 12, containing p = 191 genes, was divided into 12 clusters.

Chromosomes 2 and 12 did not require further subdivision because the number genes in each cluster was lower than the value of the kc parameter.
For the Thulin test (2014), we assumed k = 83, B1 = 100 and B2 = 1,000,000. Recall that parameter B1 specifies the number of subspaces constructed, while parameter B2 specifies the number of performed permutations needed to compute the p-value of the test. A large value of the parameter B2 is intended to obtain very accurate and stable p-values. By comparing the actual test statistics with those obtained by performing random permutations of the data, we obtained the p-values of the tests we considered.

3.3. Results of the analysis

Below is Table 2, which contains the p-values of the tests performed on the data obtained in [4].

Table 2. P-values of the Thulin (2014) and Zhang and Pan (2016) tests for data obtained by [4]

	p	Thaulin Test	Test Zhang and Pan
Chromosome 1	374	<0.000001	<0.000001
Chromosome 2	233	<0.000001	<0.000001
Chromosome 3	191	<0.000001	<0.000009

Based on the obtained results, we conclude that there are significant differences in the levels of gene expression on each of the three examined chromosomes in the two groups of patients that were subjected to the study. The obtained p-values of both the Thulin test (2014) and the Zhang and Pan test (2016) are very small and much lower than the standard significance levels. Moreover, as reported by Zhang and Pan (2016), the p-values of more well-known tests [5] - [7] are much larger than considered in this paper. This indicates the potentially greater power of the Thulin (2014), and Zhang and Pan (2016) tests compared to standard competitors. In order to check which cluster, i.e. gene expression groups, best differentiate groups of patients, the Zhang and Pan test (2016) was also used to test whether there are significant differences in the obtained clusters of individual chromosomes. Below is Table 3 with the results obtained for chromosome 1.

Table 3. Results of the Zhang and Pan test (2016) for individual clusters of chromosome 1

	p	*ZP test statistic value*	*p-value*
Chromosome 1	374	1316	<0.000001
Group 1	1	4.8	0.03
Cluster 2	128	344.2	0.0008
Cluster 2a	63	189.7	0.001
Cluster 2b	65	154.5	0.03
Cluster 3	9	16.7	0.07
Cluster 4	12	7.3	0.87
Cluster 5	1	0.0	0.90
Cluster 6	102	626.9	0.00008
Cluster 7	42	131.5	0.00006
Cluster 8	12	16.4	0.23
Cluster 9	60	159.9	0.005
Cluster 10	1	0.0	0.97
Cluster 11	4	6.3	0.19
Cluster 12	2	2.0	0.37

Chromosome 1 was divided into 12 clusters, while cluster 2 was divided into two sub-clusters 2a and 2b, due to too high value of p = 128 for cluster 2 (p > kc). It seems that cluster 6 contributes the most to the occurrence of significant differences in groups of patients, due to the high number of variables included in it with a low p-value at the same time. Below is Table 4 for cluster chromosome 2.
Chromosome 2 was fragmented into 15 clusters, none of which required further separation. Cluster 3 turned out to be the most appealing. Below we present a similar table for chromosome 12 (Table 5).
Chromosome 12 was divided into 12 clusters, none of the clusters contained more variables than the value of the kc parameter, so further sub-clustering was not required. Looking at the p-values of each cluster separately, we can see that for clusters containing a small number of variables, the p-value is relatively large. However, in none of the tables we will not find a cluster with a large number of variables in which the p-value is large. These observations show the effectiveness of the Zhang and Pan (2016) test when testing highly multivariate data.

Table 4. Results of the Zhang and Pan test (2016) for individual clusters of chromosome 2

	p	*ZP test statistic value*	*p-value*
Chromosome 2	233	796.9	<0.000001
Cluster 1	1	0.1	0.79
Cluster 2	47	106.1	0.01
Cluster 3	82	381.2	0.00002
Cluster 4	1	1.0	0.31
Cluster 5	2	5.5	0.07
Cluster 6	71	246.5	0.003
Cluster 7	10	9.9	0.51
Cluster 8	4	26.8	0.00005
Cluster 9	4	5.4	0.27
Cluster 10	1	1.3	0.26
Cluster 11	1	0.0	0.9
Cluster 12	2	3.2	0.21
Cluster 13	4	5.7	0.23
Cluster 14	1	0.9	0.36
Cluster 15	2	3.3	0.20

Table 5. Results of the Zhang and Pan test (2016) for individual clusters of chromosome 12

	p	*ZP test statistic value*	*p-value*
Chromosome 2	191	573.7	0.000009
Cluster 1	2	1.6	0.45
Cluster 2	1	0.1	0.71
Cluster 3	3	4.1	0.27
Cluster 4	1	0.6	0.45
Cluster 5	42	78.7	0.07
Cluster 6	79	367.1	0.000007
Cluster 7	1	0.1	0.75
Cluster 8	3	3.9	0.28
Cluster 9	1	0.0	0.99
Cluster 10	2	2.0	0.38
Cluster 11	54	115.3	0.04
Cluster 12	2	0.3	0.85

4. Conclusions

The aim of this paper was to present statistical tests for two samples of data allowing us to obtain information from highly multidimensional data. Statistical tests, such as the Hotelling T2 Test, become useless when the data size is larger than the sample size because of being determined. Considering the simulation research, a numerical experiment was conducted, thanks to which conclusions were drawn about the size and power of the Thulin and Zhang and Pan tests. Both the size and power of both tests turned out to be satisfactory.

To elaborate the implementation of the tests, we run analysis of the above mentioned using the breast cancer dataset. To analyze this set, the tests of Thulin and Zhang and Pan were implemented.

The aim was to detect significant differences between the group of patients without metastases within five years after diagnosis and the group of patients with previous metastases. The results of the analysis showed significant differences in gene expression levels between the two groups. The simulation studies conducted, and the analysis of the breast cancer dataset showed the effectiveness of the Thulin and Zhang and Pan test in testing two samples where the data size is larger than the sample size. Both the method based on random subspaces and the method based on cluster subspaces turned out to be reliable in testing highly multivariate data.

References

1. M. Thulin, ‘A high-dimensional two-sample test for the mean using random subspaces’, Computational Statistics & Data Analysis, vol. 74, pp. 26–38, Jun. 2014, doi: 10.1016/j.csda.2013.12.003.

2. T. Qiu, W. Xu, and L. Zhu, ‘Two-sample test in high dimensions through random selection’, Computational Statistics & Data Analysis, vol. 160, p. 107218, Aug. 2021, doi: 10.1016/j.csda.2021.107218.

3. J. Zhang and M. Pan, ‘A high-dimension two- sample test for the mean using cluster subspaces’, Computational Statistics & Data Analysis, vol. 97, pp. 87–97, May 2016, doi: 10.1016/j.csda.2015.12.004.

4. E. Gravier et al., ‘A prognostic DNA signature for T1T2 node-negative breast cancer patients’, Genes Chromosom. Cancer, vol. 49, no. 12, pp. 1125– 1134, Dec. 2010, doi: 10.1002/gcc.20820.

5. S. X. Chen and Y.-L. Qin, ‘A two-sample test for high-dimensional data with applications to gene-set testing’, Ann. Statist., vol. 38, no. 2, Apr. 2010, doi: 10.1214/09-AOS716.

6. M. S. Srivastava, ‘Multivariate Theory for Analyzing High Dimensional Data’, Journal of the Japan Statistical Society, vol. 37, no. 1, pp. 53–86, 2007, doi: 10.14490/jjss.37.53.

7. H. Zhang and H. Wang, ‘A more powerful test of equality of high-dimensional two-sample means’, Computational Statistics & Data Analysis, vol. 164, p. 107318, Dec. 2021, doi: 10.1016/j.csda.2021.107318.

MEDICAL PHYSICS IN THE BALTIC STATES 16 (2023)

Proceedings of International Conference "Medical Physics 2023"
09-11 November 2023, Kaunas, Lithuania

RECURRENT COMPUTED TOMOGRAPHY PROCEDURES. CUMULATIVE EXPOSURE ASSESSMENT

Birutė GRICIENĖ[1,2], Daira PAŠKEVIČIŪTĖ[2], Aušra BILOTIENĖ MOTIEJŪNIENĖ[3], Rokas DASTIKAS[1], Leonid KRYNKE[4]

[1]Department of Radiology, Nuclear Medicine and Medical Physics, Faculty of Medicine, Vilnius University, Vilnius, Lithuania. [2]Hospital of Lithuanian University of Health Sciences Kaunas Clinics, Kaunas, Lithuania, [3]Department of Nursing, Faculty of Medicine, Institute of Health, Vilnius University, Vilnius, Lithuania, [4]Vilnius University Hospital Santaros Klinikos, Vilnius, Lithuania

[1]Birute.griciene@mf.vu.lt, [2]paskeviciute.daira@gmail.com, [3]ausra.bilotiene@mf.vu.lt, [4]rokas.dastikas@mf.vu.lt, [5]leonid.krynke@santa.lt

***Abstract*:**
For this study, non-identifiable patient information was collected from a computed tomography scan database of patients in a single hospital in Lithuania who underwent at least one computed tomography scan during a 3-year period. Data from 5,060 patients with 2 or more CT scans was selected. Analysis of the data showed that the maximum cumulative radiation exposure to a single patient was 0.6 Sv, with a maximum additional cumulative lifetime cancer risk of 9.2 %. The most common indication for recurrent computed tomography scans was found to be follow-up of oncological disease (83 % of the patients evaluated).

Keywords: computed tomography, cumulative effective dose, recurrent computed tomography examinations

1. Introduction

Computed tomography (CT) is an invaluable tool for the diagnosis and management of multiple health conditions. In 2021 United Nations Scientific Committee on the Effects of Atomic Radiation reported that CT accounted for only 9.6% of all radiological medical procedures while accumulating to as much as 62% of all effective doses received by patients. It is estimated that the number of CT examinations per annum has increased by 82% from 220 million to 400 million with the proportion of all effective doses increasing by 19% (from 43% to 62%) since the 2008 United Nations Scientific Committee on the Effects of Atomic Radiation report [1, 2].

While a single imaging procedure involving ionising radiation, such as computed tomography, may result in minimal increases in lifetime cancer risk, repeated exposure elevates it by making organs and tissue more susceptible to larger cumulative effective doses and increasing the probability of related adverse effects [3]. A rising number of patients are receiving considerably high total effective doses of 100 mSv or more in a short period of time (in 1 to 5 years) causing concern for many researchers, international radiology, and radiation protection organisations [4, 5].

The aim of this study was to carry out an assessment of the most prevalent indications, the cumulative radiation doses, and cancer risk of recurrent computed tomography examinations.

2. Methods

Data analysis was performed on a dataset of 30,313 non-identifiable adult patients who underwent at least one CT examination in a single hospital in Lithuania in a span of three years (between 2019 and 2022). Further analysis was performed on the data of 5,060 patients who underwent 2 or more CT scans.

This data was further subdivided according to the number of CT procedures performed per patient. The average dose of each group was calculated and the maximum cumulative doses in the groups were estimated using Microsoft Excel 2013.

Additionally, individual data of 103 patients with the highest number of CT examinations was summarised and the total, mean total, maximum and minimum dose length product received (DLP values) were calculated using IBM SPSS 22.0 program.

The calculation of the derived values, effective dose (ED) and lifetime attributable risk (LAR), was carried out by considering the age and gender of the patients selected for the analysis, and the anatomical areas of the CT examinations performed on the patients. When calculating ED, the values of the k factor for individual body regions provided by the American Association of Physicists in Medicine (AAPM) were used [6]. The LAR was calculated using the United States National Cancer Institute's online open-access calculator RadRAT

(Radiation Risk Assessment Tool) version 4.2.1 [7], available at: radiationcalculators.cancer.gov/radrat
CT examinations were performed on one of 3 CT machines: 64-slice General Electric (GE) CT64, 64-slice GE Discovery 750, 256-slice GE Revolution.

3. Results

There were 30,313 patients who had received at least one CT examination during the three year period. Out of them 5,060 patients, or 16.7%, received repeated tests. These patients were further subdivided into 16 groups based on the number of scans received (from 2 to 18). For each group an average DLP (cumulative dose for all exams) ranging from 3713.5 mGy·cm to 11620.4 mGy·cm was calculated and the maximum DLP (cumulative dose for all exams) ranging from 4120 mGy·m to 42533 mGy·cm was evaluated. Complete data is summarised in Table 1.

Table 1. Distribution of patients according to the number of repeated CT exams and cumulative DLP values of each group.

Number of CT scans	Number of patients	Average DLP, mGy*cm	Maximum DLP, mGy*cm	Percent of all patients, %
2	2834	2731.6	21948	9.35
3	1081	4681.8	22938	3.57
4	483	6696.5	26673	1.59
5	261	7966.8	25590	0.86
6	148	9009.0	30449	0.49
7	104	8884.6	34899	0.34
8	56	9498.2	32965	0.18
9	32	9276.3	35899	0.11
10	18	7846.8	39084	0.06
11	11	6145.7	20867	0.04
12	12	4890.9	8243	0.04
13	7	11620.4	42533	0.02
14	4	3713.5	4120	0.01
16	3	4964.0	7099	0.01
17	3	9708.0	12719	0.01
18	3	5940.3	7549	0.01

A more in-depth analysis was performed on the data of 103 patients with the highest number of data reports to the hospital system. More than half of these cases were comprised of women (59 out of 103 patients, or 57.3%). Men amounted to 44 cases, or 42.7%. The age median at the time of the first CT examination was 61 years and the average age was 59.7 years for women and 59.8 for men. The estimated cumulative ED of at least 50 mSv was received in 95 (92.2%) patients and cumulative ED of at least 100 mSv was received in 78 (75.7%) patients.
Repeated CT scans among these patients may be divided into four groups based on the diagnoses and indications: detection of neoplasms and follow up during treatment (85 patients, 83%), infectious disease (1 patient, 1%), non-infectious and non neoplastic disease (2 patients, 2%) and a combination of two or more aforementioned indications (15 patients, 14%).
Most often non-infectious and nonneoplastic diseases requiring CT examinations were medical emergencies such as vascular disease, pulmonary artery thromboembolism, aortic dissection, and acute abdomen. In patients who presented with multiple comorbidities and indications for CT, 9 out of 15 cases (60%) involved a medical emergency and neoplastic disease, 3 cases (20%) were comprised of infectious disease and neoplasms, 2 (13%) cases presented themselves with infectious disease and a medical emergency and only 1 patient (7%) was investigated for all three indications.
Overall, the vast majority of cases in this subgroup of patients (98 out of 103 or 95%) had a CT scan performed with neoplastic disease being one of the indications.
Radiation exposure was also assessed in this group. Cumulative doses received (DLP values) were higher among men (M=15846 mGy*cm, SD=9649.9) than women (M=10404 mGy*cm, SD=7090.1). This difference was statistically significant (Z=-3.333, p=0.001). By using RadRAT online calculator LAR values were obtained and expressed as the chances of cancer incidence from radiation exposure to the time of expected death in 100,000 patients (90% confidence interval). Notably, these values show no statistically significant difference (Z=-0.780, p=0.435) between the average LAR for men (M=3.09, SD=2.44) and women (M=3.59, SD=2.79).
The largest cumulative DLP and ED values were obtained after performing full-body CT scans to assess the extent of malignant disease and after neck, chest, and lumbar CT to monitor the progression of a retropharyngeal abscess. This data is explored in more detail in Table 2. The lowest dose values (cumulative DLP=554 mGy*cm) were observed after performing whole-body low-dose CT to assess the dissemination of multiple myeloma and fungal lung infection.

4. Discussion

Repeated CT examinations resulting in high cumulative radiation exposure and possible adverse health consequences for the patients in the future as well as methods of dose and risk reduction are all topics which are actively discussed and explored in scientific literature.
Our investigation gave the opportunity to explore a broad yet not specific adult population providing a glimpse into the most common conditions warranting multiple scans over the course of treatment as well as the attained cumulative DLP and ED values.
As with our observation that the patients suffering from neoplastic disease are among those who receive the highest number of CT examinations due to necessity to evaluate the extent of the disease and monitoring after treatment other researchers also noted this tendency.
Stopsack and Cerhan evaluated a nonspecific patient population from data collected over a span of 10 years. Out of 54,447 total patients a randomly selected subgroup of 200 patients who received cumulative ED of at least 100 mSv from CT scans was formed. In this group 30.5% of all investigations were associated with neoplastic disease (18.3% solid tumours and 12.2% lymphomas) and amounted to the proportion out of all performed CTs, followed by abdominal pain at 17.2%. It is important to note that the cohort was restricted to only non-terminally ill patients [8]. This limitation was not imposed on our data therefore direct comparison is difficult.

Table 2. Cancer risk assessment in patients with the highest cumulative DLP values

Nr.	Age	Sex	Number of CT scans	Cumulative DLP value, mGy*cm	Cumulative ED value, mSv	Indications and performed investigations	LAR, %
Largest DLP values							
1	50	Male	13	42533	637.9	Gastric cancer, full-body CT	6.8
2	34	Female	10	39084	586.3	Infection, head neck and full-body CT	9.2
3	58	Male	9	35899	538.5	Post-treatment assessment, full-body CT	4.9
4	79	Male	8	32965	494.5	Prostate cancer, full-body CT	0.9
5	61	Male	7	31266	468.9	Sarcoma, full-body CT	3.8

Lumbreras et al. analysed data from a single hospital and included all imaging modalities that produce ionising radiation. Out of 154,520 total patients 4,844 (3.1%) received cumulative ED between 50 and 100 mSv while 2,298 (1.5%) received more than 100 mSv with neoplastic diseases being prevalent among them at 43.14% and 73%, respectively [9].

Brambilla et al. analysed 427 patients who received cumulative ED of 100 mSv or more in less than a month. Only about a third of patients, at 132 (31%), had CTs performed due to neoplastic disease while 295 (69%) had other indications [10].

An example of repeated CT examinations in specific groups was published by Hinzpeter et al. where 85 patients with a performed CT scan were referred to a trauma centre. A repeated scan was performed 74 times (87%), the main reasons being reassessment of suffered injuries, repeated head CT during full-body CT and failure in data transfer between hospitals [11].

Tonolini et al. evaluated data of 305 patients aged 18-45 who received abdominal and pelvic CT scans with contrast due to nontraumatic acute abdomen over the course of 26 months. Notably, HIV positive, oncologic, vasculitis and inflammatory bowel disease patients were excluded. A fifth (61 patients, 20%) received more than one CT examination ranging from 2 to 8 with the average being 2.7. For these 61 patients the mean cumulative ED resulted in 70.1 mSv with the largest being 436.6 mSv and in 16 (26.2%) cases ED exceeded 100 mSv accumulated over a span of less than 3 years. The resulting largest LAR increase amounted to 1.3% from base values [12].

In a publication by Tirosh et al. cumulative ED were evaluated in a group of patients with von Hippel-Lindau syndrome with pancreatic neuroectodermal tumours receiving repeated CT examinations. Due to the current protocol by the National Institute of Health requiring annual CT surveillance with solid pancreatic tumours, the estimated cumulative ED doses received from age 40 (the median age at diagnosis) to 65 range from 682 mSv when the diameter of the tumour is up to 1.2 cm to 2124 mSv when the diameter of the tumour is more than 3 cm. These large estimates promote discussion as to how cumulative ED could be reduced, especially among the young and the middle-aged. The authors propose a change in the algorithm to use dual-energy virtual noncontrast protocol instead of three-phase CT protocol and to alter the follow up tumour surveillance protocol to require biennial abdominal CT when the tumour is smaller than 1.2 cm or size 1.2-3 cm with a low-risk *VHL* gene genotype and an annual CT otherwise. These modifications would allow to reduce the estimated cumulative ED to 388 mSv and 775 mSv, respectively. Incorporating other imaging modalities without radiation into the surveillance algorithm could further help reduce cumulative ED [13].

While ionising radiation exposure increases LAR, some specific populations at risk might benefit from repeated CT examinations provided that appropriate low-dose protocols are followed. Such observations were made in a secondary analysis of trial data by Rampinelli et al. where 5,203 asymptomatic smokers aged 50 and older and current and former smokers of 20 or more pack-years with no cancer diagnosis in the past 5 years were monitored over the course of 10 years using annual low dose CT scans. The median cumulative ED received was 9.3 mSv for men and 13.0 mSv for women. 259 instances of lung cancer were diagnosed during the period of screening. Moreover, LAR was calculated, and it was estimated that an additional incidence of 1.5 for lung cancer and 2.4 for stomach, colon, liver, lung, bladder, thyroid, breast, ovary, uterine cancer, or leukaemia was induced by radiation exposure in this cohort. Therefore, the increased risk of cancers resulting from low-dose CT screening may be considered acceptable due to reduction in mortality from cancer [14].

5. Conclusions

The recurrent CT procedure analysis showed that from 30,313 patients who had received at least one CT examination 5,060 patients, or 16.7%, received repeated tests. The majority of the patients (83%) received from 2 to 6 CT exams. The most prevalent indication for repeated CT examinations was monitoring of neoplastic disease which was observed in 85 (83%) patients. The largest cumulative dose for a single patient due to repeated CT scans was 638 mSv. The lowest cumulative ED was received by patients undergoing investigations for the extent of multiple myeloma and fungal pulmonary infection. Low dose CT imaging protocols were used for both indications. The largest calculated LAR due to exposure to ionising radiation was 9.2% and the lowest calculated LAR 0.02%.

While repeated radiation exposure does increase the LAR, certain steps and measures may be taken to reduce it to a minimum: evaluation of clinical necessity, risk-benefit analysis, evaluation of other possible imaging modalities, optimization of CT technology and protocols, assessment of screening properties should all be considered.

References

1. Report of the United Nations Scientific Committee on the Effects of Atomic Radiation [Internet]. New York: United Nations Scientific Committee on the Effects of Atomic Radiation; 2021 p. 36, 60. Available at: https://undocs.org/en/A/76/46

2. Report of the United Nations Scientific Committee on the Effects of Atomic Radiation to the General Assembly. (2010). In Sources and Effects of Ionizing Radiation, United Nations Scientific Committee on the Effects of Atomic Radiation (UNSCEAR) 2008 Report, Volume I p. 26. New York: United Nations. https://doi.org/10.18356/9b8f628f-en

3. Health Risks from Exposure to Low Levels of Ionizing Radiation: BEIR VII Phase 2 [Internet]. Washington, D.C.: National Academies Press; 2006 [cited 2023 Sep 24]. Available at: http://www.nap.edu/catalog/11340

4. Brenner DJ. Computed Tomography — An Increasing Source of Radiation Exposure. TheNew England Journal of Medicine. 2007;8.

5. Brambilla M, Vassileva J, Kuchcinska A, Rehani MM. Multinational data on cumulative radiation exposure of patients from recurrent radiological procedures: call for action. Eur Radiol. 2020 May;30(5):2493–501.

6. McCollough C, Cody D, Edyvean S, Geise R, Gould B, Keat N, et al. The Measurement,Reporting,and Management of Radiation Dose in CT. College Park, MD: American Association of Physicists in Medicine; 2008 Jan p. 28. Report No.: 96.

7. de Gonzalez AB, Iulian Apostoaei A, Veiga LHS, Rajaraman P, Thomas BA, Owen Hoffman F, et al. RadRAT: a radiation risk assessment tool for lifetime cancer risk projection. J Radiol Prot. 2012 Sep;32(3):205–22.

8. Stopsack KH, Cerhan JR. Cumulative Doses of Ionizing Radiation From Computed Tomography: A Population-Based Study. Mayo Clinic Proceedings. 2019 Oct;94(10):2011–21.

9. Lumbreras B, Salinas JM, Gonzalez-Alvarez I. Cumulative exposure to ionising radiation from diagnostic imaging tests: a 12-year follow-up population-based analysis in Spain. BMJ Open. 2019 Sep;9(9):e030905.

10. Brambilla M, Cannillo B, D'Alessio A, Matheoud R, Agliata MF, Carriero A. Patients undergoing multiphase CT scans and receiving a cumulative effective dose of ≥ 100 mSv in a single episode of care. Eur Radiol. 2021 Jul;31(7):4452–8.

11. Hinzpeter R, Sprengel K, Wanner GA, Mildenberger P, Alkadhi H. Repeated CT scans in trauma transfers: An analysis of indications, radiation dose exposure, and costs. European Journal of Radiology. 2017 Mar;88:135–40.

12. Tonolini M, Valconi E, Vanzulli A, Bianco R. Radiation overexposure from repeated CT scans in young adults with acute abdominal pain. Emerg Radiol. 2018 Feb;25(1):21–7.

13. Tirosh A, Journy N, Folio LR, Lee C, Leite C, Yao J, et al. Cumulative Radiation Exposures from CT Screening and Surveillance Strategies for von Hippel-Lindau–associated Solid Pancreatic Tumors. Radiology. 2019 Jan;290(1):116–24.

14. Rampinelli C, De Marco P, Origgi D, Maisonneuve P, Casiraghi M, Veronesi G, et al. Exposure to low dose computed tomography for lung cancer screening and risk of cancer: secondary analysis of trial data and risk-benefit analysis. BMJ. 2017 Feb 8;j347.

MEDICAL PHYSICS IN THE BALTIC STATES 16 (2023)

Proceedings of International Conference "Medical Physics 2023"
09-11 November 2023, Kaunas, Lithuania

THE ICRP DOSE VIEWER MOBILE APP – TO IMPROVE ACCESSIBILITY OF ICRP DOSE DATA FOR INTAKE OF RADIONUCLIDES IN PATIENTS, STAFF AND MEMBERS OF THE PUBLIC

Martin ANDERSSON[1,2] and Sören MATTSSON[2]
[1]Medical Radiation Sciences, Sahlgrenska Academy, University of Gothenburg, Sweden
[2]Medical Radiation Physics Malmö, ITM, Lund University, Sweden
[1]martin.andersson.2@gu.se; [2]soren.mattsson@med.lu.se

***Abstract*:** The ICRP, an independent non-profit organization, which is funded through donations and publications, has recently focused on the dissemination of publications and offers now free access to publications after two years. The "ICRP Dose Viewer" is ICRP's mobile app and provides real-time effective dose coefficients, aiding medical physicists and other users access to the most recent absorbed and effective dose coefficients for occupationally exposed workers, patients in diagnostic nuclear medicine and members of the public.

Keywords: ICRP, dose coefficient, effective dose, mobile app

1. Introduction

The International Commission on Radiological Protection (ICRP) is an independent non-profit organization that provides independent recommendations and guidance in radiation protection considering scientific knowledge, social values and practical experience. All funding is dependent on donations and gifts as well as sales of ICRP publications. The ICRP is structured with a main commission, a scientific secretariat and four standing committees as well as a series of task groups and working parties. In recent years, ICRP has worked more actively than before to make available and disseminate its results and recommendations, which has resulted in all publications being made available free of charge two years after publication.

The aim of this project was to develop the ICRP's official "ICRP Dose Viewer" mobile app to easily show the ICRP's current dose coefficients for intake of radionuclides for the general public, radiation workers and for patients within diagnostic nuclear medicine.

2. Dose viewer app

The advantage of a digital app is that when the ICRP revises the dose coefficients in new publications, this revision will also take place directly in the app. The idea of the app is to simplify the everyday work of medical physicists as well as for personnel responsible for assessing the intake of radionuclides for members of the general public and occupationally exposed radiation workers. Fig. 1, shows the main page of the ICRP Dose viewer app.

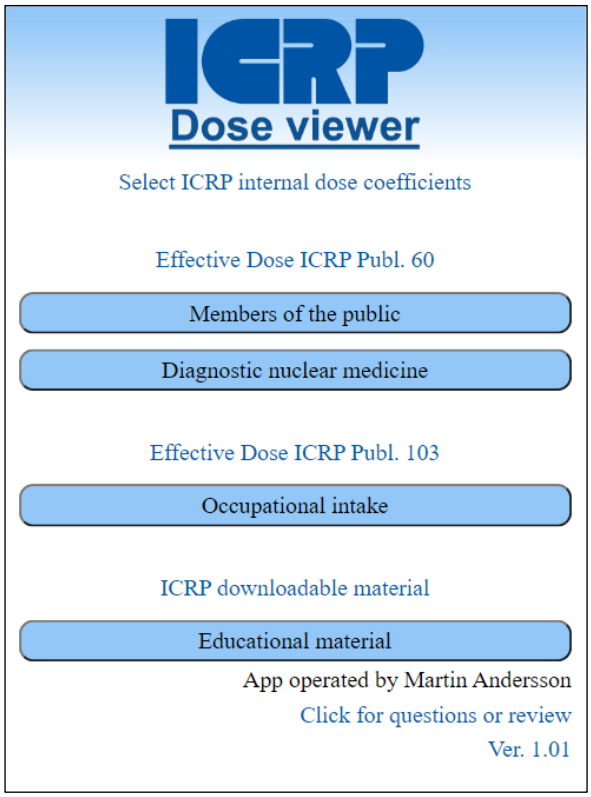

Fig 1. Main page in the ICRP Dose viewer app.

A user-friendly, instructive, non-commercial mobile application as well as a web-based viewer has been developed to enable users to easily access the ICRP dose coefficients related to the intake of radionuclides for occupationally exposed individuals, members of the public, and patients undergoing diagnostic nuclear medicine investigations. With this app patients, radiation workers, and members of the public will obtain estimates of the effective dose and organ absorbed doses received by a reference person in different exposure scenarios within a few seconds. The advantages of access to the dose coefficients via the ICRP Dose viewer are that dose coefficients would be always up to date.

In addition to the ICRP dose coefficients, freely available educational material regarding ICRP publications is accessible from the app. The app is available for download on Google Play and App store. Just search for "ICRP Dose viewer". The app is already available today for download with QR codes below through Google Play and App Store. Currently, all revised dose coefficients for occupational exposure have been included in the ICRP Dose viewer and once new or revised dose coefficients are published, the app will be updated and the most recent absorbed dose and effective dose coefficients included.

3. Occupational intake

The utilization of effective dose coefficients in the context of occupational radiation exposure is vital for sound radiation protection practices. These coefficients, representing the projected radiation dose a radiation worker could potentially receive, are based on factors such as the type and energy of radiation, as well as the specific organs or tissues exposed.

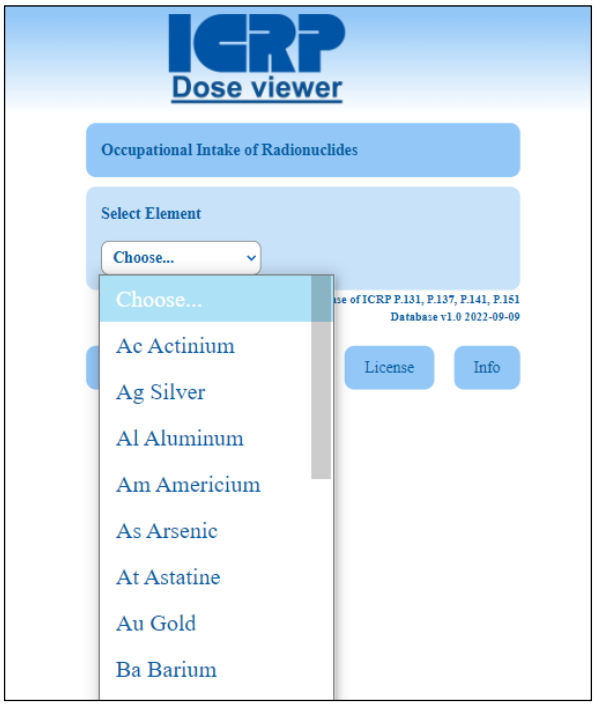

Fig. 2. For occupational exposure first select an element.

The establishment of standardized effective dose coefficients is essential for harmonizing radiation risk assessment globally. By accounting for the varying sensitivities of different tissues and considering both external and internal radiation exposures, a more accurate evaluation of potential health hazards is achieved.

Continuous research and refinement of effective dose coefficients contribute substantially to enhancing the efficacy of radiation safety protocols in occupational settings. This scientific approach ensures that radiation workers and the public are safeguarded against potential risks from ionizing radiation, aligning with the overarching goal of maintaining a secure and healthy work environment.

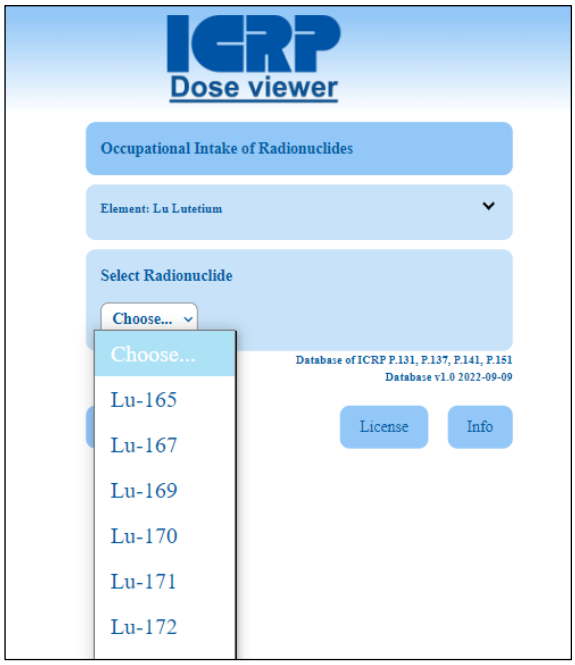

Fig. 3. Second step is to select a radionuclide of the selected element.

The app contains effective dose coefficients for occupational intake published in the ICRP OIR series 1-5 (1-5). Fig. 2. shows the beginning of a list of 95 different elements to select from. In Fig. 3 lutetium has been selected and the app shows all radionuclides in from ICRP Publication 107 (6), which has a half-life longer that 20 min. In Fig. 4 you select which type of intake of lutetium-177 you are interested in. For inhalation you select particle size in activity median thermodynamic diameter (AMTD) or in activity median aerodynamic diameter (AMAD), see Fig. 5. Once all steps are fulfilled, the app will show the corresponding effective dose coefficient in Sv/Bq. There is also an additional step, which is set an arbitrary intake of activity in the unit mBq to MBq. This will multiply the dose coefficients with the inputted activity. The result will be given in both effective dose and organ equivalent doses if the user is interested in organ doses. Fig. 5 and Fig. 6 show the results of 5 Bq inhaled lutetium-177.

Fig. 4. After selection of radionuclide chose type of intake: ingestion, inhalation or injection.

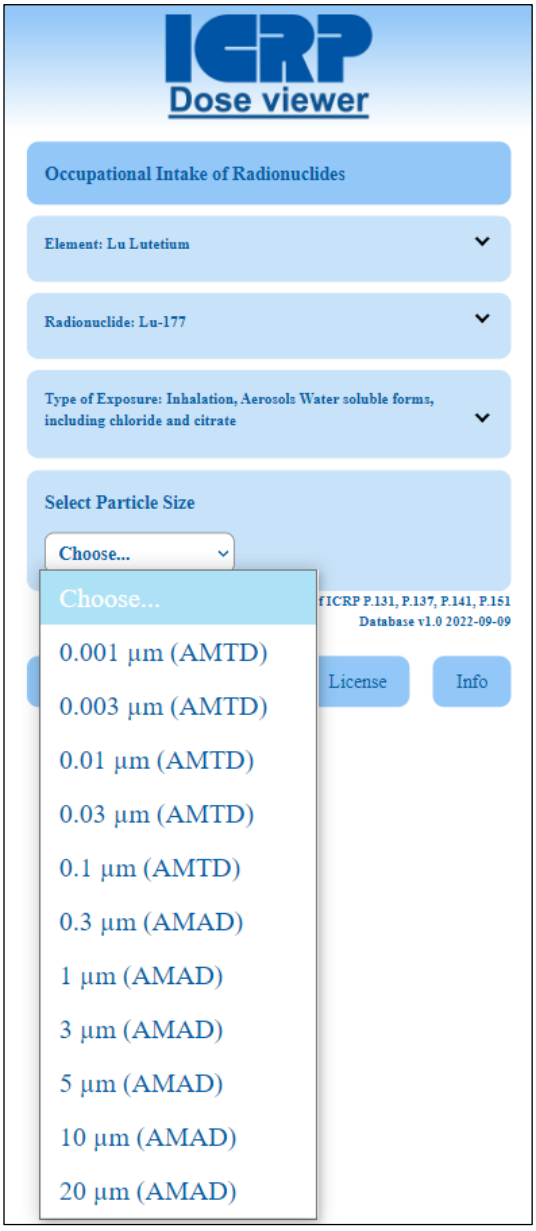

Fig. 5. For inhalation select particle size in AMTD or AMAD.

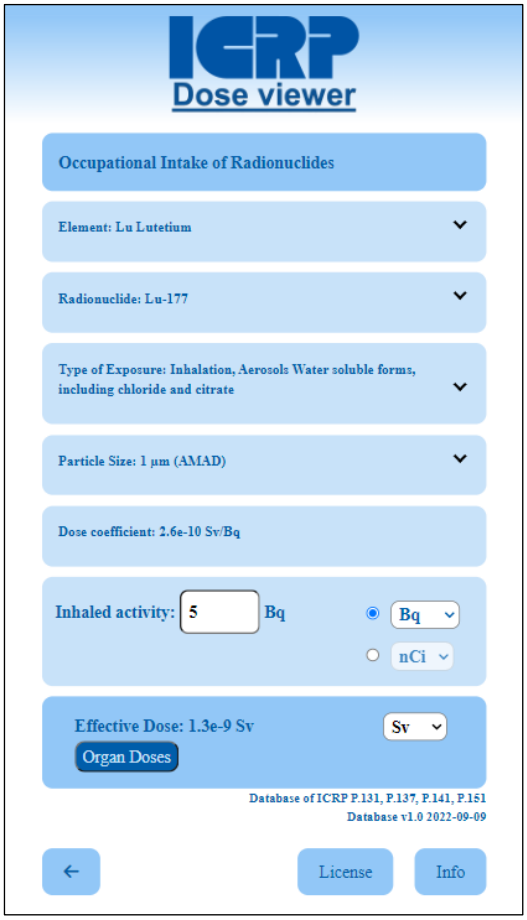

Fig. 6. After all selection is performed the app shows the published ICRP dose coefficient in Sv/Bq. There is also a possibility to select an arbitrary value of intake of activity.

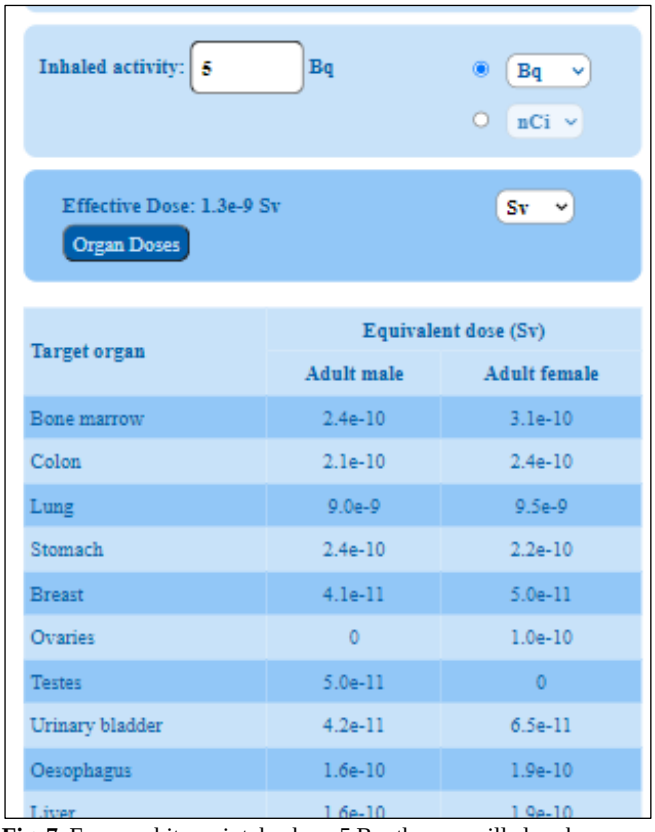

Target organ	Equivalent dose (Sv)	
	Adult male	Adult female
Bone marrow	2.4e-10	3.1e-10
Colon	2.1e-10	2.4e-10
Lung	9.0e-9	9.5e-9
Stomach	2.4e-10	2.2e-10
Breast	4.1e-11	5.0e-11
Ovaries	0	1.0e-10
Testes	5.0e-11	0
Urinary bladder	4.2e-11	6.5e-11
Oesophagus	1.6e-10	1.9e-10
Liver	1.6e-10	1.9e-10

Fig. 7. For an arbitrary intake, here 5 Bq, the app will also show equivalent doses for organs.

4. Diagnostic nuclear medicine

Effective dose coefficients for patients in diagnostic nuclear medicine are important for quantifying radiation exposure. These coefficients, derived from comprehensive analysis of radiopharmaceutical biokinetics, patient demographics, and imaging techniques, aid in optimizing procedures and ensuring patient safety. By standardizing the measure of radiation's potential harm, healthcare professionals can make informed decisions while adhering to international radiation protection standards. This work strikes a balance between diagnostic efficacy and radiation risk, benefiting both patients and medical practitioners in nuclear medicine.

For diagnostic nuclear medicine, the effective dose coefficients are taken from ICRP Publ. 128 (7). Fig. 8. shows that 16 different elements can be selected. After the selection of element, the radiopharmaceutical can be selected. In Fig. 9 fluorine has been selected, and 8 different fluor-18 radiopharmaceuticals can then be selected. In Fig. 10 has age of patient been selected to adult and the app shows the corresponding ICRP published effective dose 0.019 mSv/MBq. Fig. 10. also shows an effective dose of 3.23 mSv for an injection of 170 MBq. Fig. 11. shows also the corresponding organ absorbed doses for a 170 MBq administration.

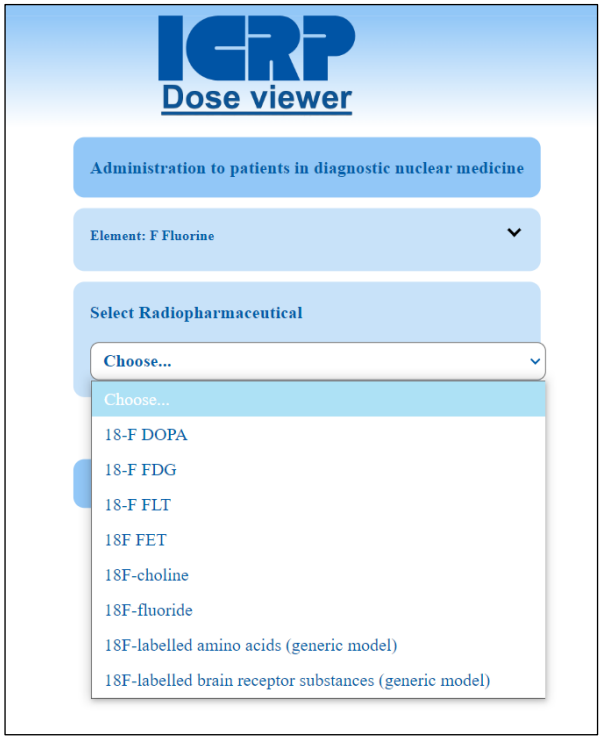

Fig 9. For the selected element fluorine are 8 different dose data of radiopharmaceuticals available.

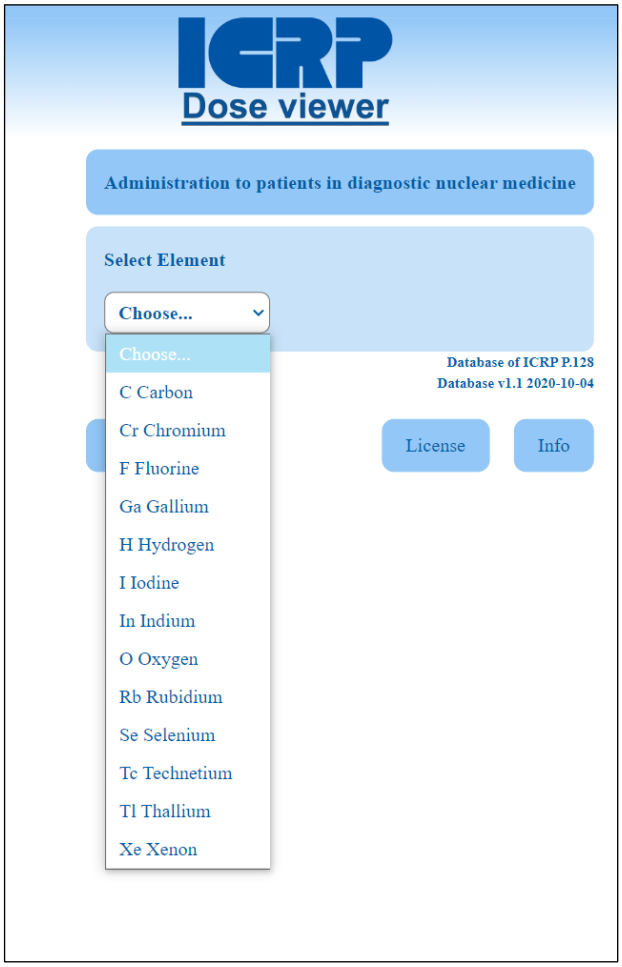

Fig. 8. For diagnostic nuclear medicine data for 16 elements are given.

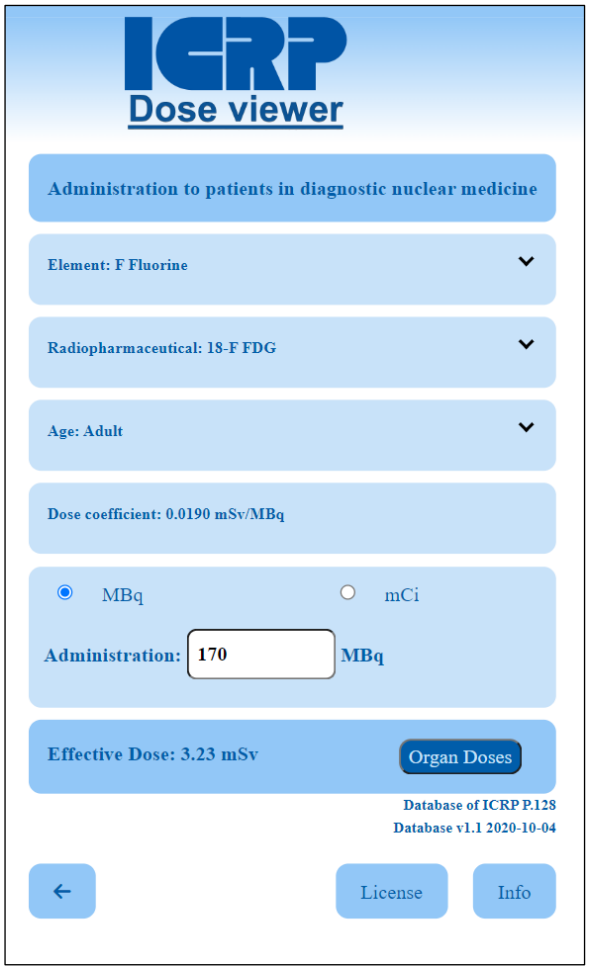

Fig. 10. The image shows the effective dose coefficient for an adult and also the corresponding effective dose for an injection of 170 MBq of ^{18}F-FDG.

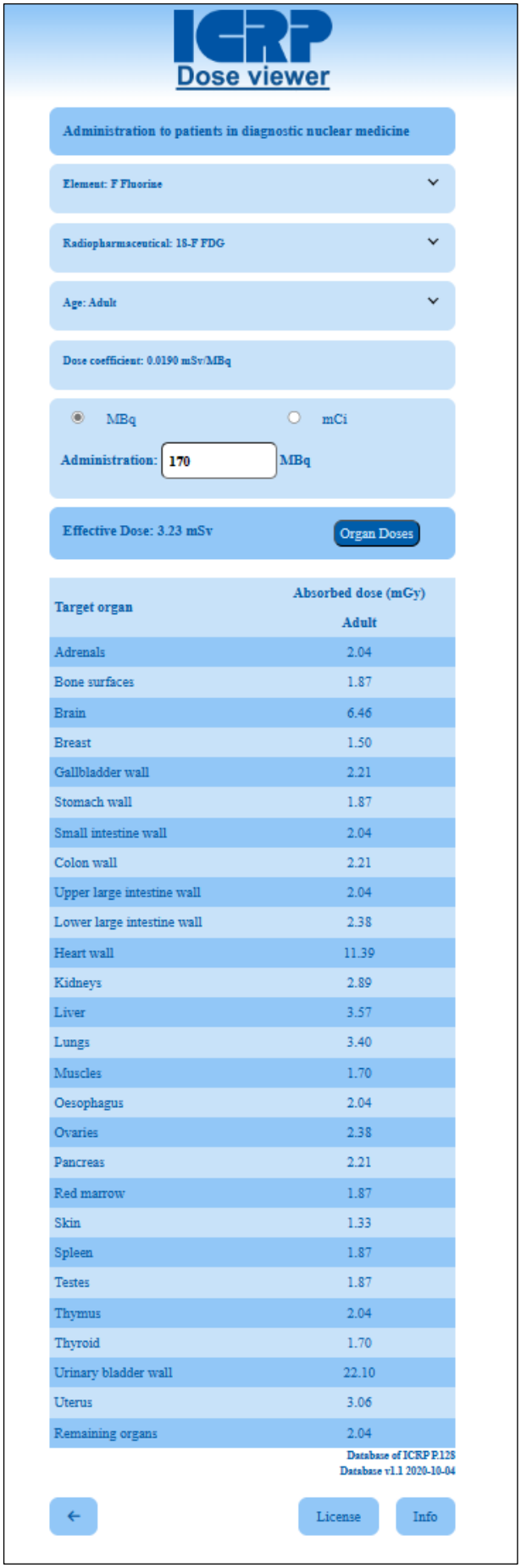

Fig. 11. The app also shows the corresponding organ absorbed doses for an injection of 170 MBq of ^{18}F-FDG.

5. Members of the public

The determination of effective dose coefficients for public radiation exposure is a crucial aspect of radiation protection. These coefficients quantify potential health risks from various radiation sources, considering radiation types and organ sensitivities. The process involves extensive data collection, analysis, and modelling, incorporating epidemiological studies, radiobiology, and dosimetry.

Effective dose coefficients are used to ensure public safety while permitting beneficial radiation applications in medicine and industry and for the whole society. Continuous research ensures accuracy, reflecting the latest data to minimize health risks such as cancer and genetic effects. This approach guarantees the well-being of individuals exposed to ionizing radiation, underscoring the significance of precise and up-to-date effective dose coefficients in maintaining a balance between technological advancements and public health.

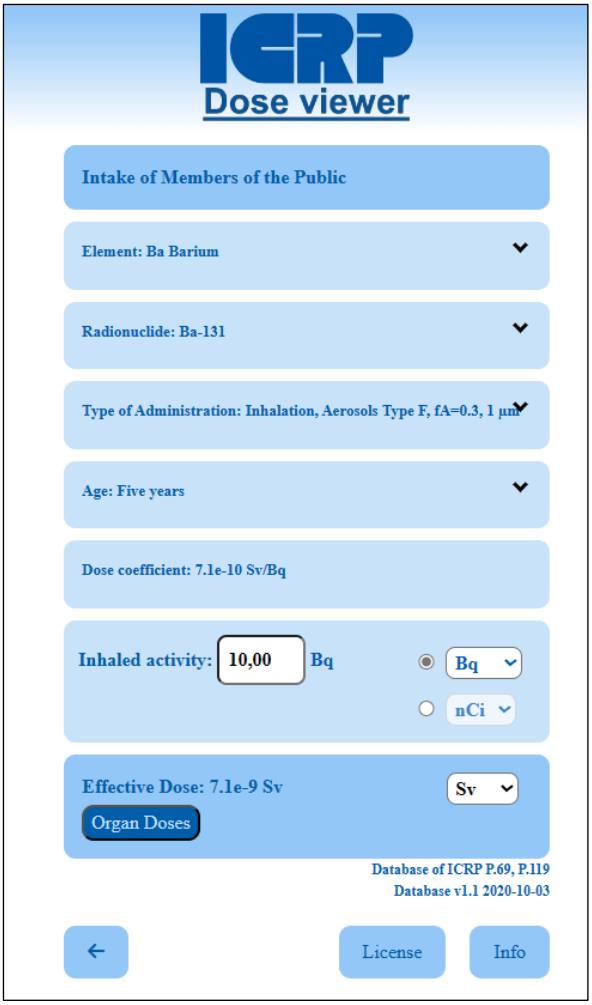

Fig. 12. The figure shows the effective dose coefficients for inhaled ^{131}Ba for a five-year-old and the corresponding effective dose from an inhalation of 10 Bq.

For members of the public, the effective dose coefficient data are from ICRP Publication 119 (8) and ICRP Publication 69 Part 3 (9). Fig. 12 shows the effective dose coefficients 7.1 10^{-10} Sv/Bq for inhaled ^{131}Ba for a five-year-old and the corresponding effective dose of $7.1 \cdot 10^{-9}$ Sv/Bq of 10 Bq inhaled ^{131}Ba.

6. Educational material

The app also includes the educational material which has been published by the ICRP. The educational material has been generated by the ICRP to make the publication more easily to implement and understand for readers outside of the specific expert field. Fig. 13. Shows a part of all educational material included in the app.

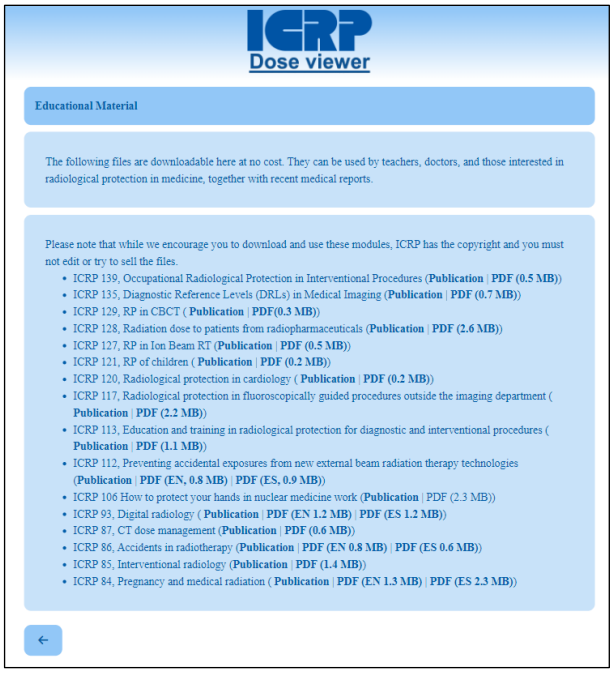

Fig. 13. The ICRP educational material can also be accessed through the app.

8. Future updates

The current state of the ICRP Dose Viewer app is here presented. However, as an app is a dynamic application, some extensions and updates are planned. For nuclear medicine and the members of the public the dose coefficients will be updated to the effective dose based on the ICRP Publ. 103. The app will also include the 10. coming ICRP effect dose coefficients for radiography including X-ray imaging, fluoroscopy and CT. Also, if ICRP provides more educational material will this also be included in the app.

8. Conclusion

The ICRP Dose Viewer application gives direct access to absorbed dose and effective dose for all ICRP-dose coefficients for intake of radionuclides. The app is available today for download through Google Play and app Store. Currently, all revised dose coefficients for occupational exposure have been included in the ICRP Dose viewer and once new or revised dose coefficients are published e.g., for members of the public, the app will be updated and replace the current absorbed dose and effective dose coefficients.

References

1. ICRP. Occupational Intakes of Radionuclides: Part 1. ICRP Publication 130. Ann. ICRP 44(2), 2015.
2. ICRP. Occupational Intakes of Radionuclides: Part 2. ICRP Publication 134. Ann. ICRP 45(3/4), 2016.
3. ICRP. Occupational Intakes of Radionuclides: Part 3. ICRP Publication 137. Ann. ICRP 46(3/4), 2017.
4. ICRP. Occupational Intakes of Radionuclides: Part 4. ICRP Publication 141. Ann. ICRP 48(2/3), 2019.
5. ICRP. Occupational Intakes of Radionuclides: Part 5. ICRP Publication 151. Ann. ICRP 51 (1–2), 2022.
6. ICRP. Nuclear Decay Data for Dosimetric Calculations. ICRP Publication 107. Ann. ICRP 38 (3). 2008.
7. ICRP. Radiation Dose to Patients from Radiopharmaceuticals: A Compendium of Current Information Related to Frequently Used Substances. ICRP Publication 128. Ann. ICRP 44(2S), 2015.
8. ICRP. Compendium of Dose Coefficients based on ICRP Publication 60. ICRP Publication 119. Ann. ICRP 41(Suppl.), 2012.
9. ICRP. Age-dependent Doses to Members of the Public from Intake of Radionuclides - Part 3 Ingestion Dose Coefficients. ICRP Publication 69. Ann. ICRP 25 (1), 1995.

MEDICAL PHYSICS IN THE BALTIC STATES 16 (2023)

Proceedings of International Conference "Medical Physics 2023"
09-11 November 2023, Kaunas, Lithuania

SWOT ANALYSIS BASED STRATEGIC PLANNING IN MEDICAL PHYSICS: A LITERATURE REVIEW

Jason SCHEMBRI[1], Carmel J. CARUANA[2], Eric PACE[1], Sam AGIUS[1]
[1]Medical Physics, Medical Imaging Department, Mater Dei Hospital, Msida, Malta;
[2]Medical Physics, Faculty of Health Sciences, University of Malta, Msida, Malta;
[1]jason.schembri.1@gov.mt; [2]carmel.j.caruana@um.edu.mt; [1]eric.pace@gov.mt; [1]sam.agius@gov.mt

***Abstract*:** Strengths, Weaknesses, Opportunities, Threats (SWOT) analysis based strategic planning has been used extensively in healthcare predominantly in organizational and role development. It is particularly relevant to the development of professions such as medical physics. This review discusses the SWOT analysis process and its utilization in medical physics. It starts by briefly explaining the key components of SWOT analysis based strategic planning viz., vision-setting, SWOT theme generation, and the development of strategic objectives and the planning necessary for achieving them. We then highlight examples of SWOT analysis in developing aspects of the role of the medical physicist and for developing medical physics services found in the literature. However, notwithstanding its importance for providing practical guidance for decision-making, few learning resources are available which are suitable for teaching strategic planning skills to young medical physics leaders. This literature review will provide a summary of what is available as a teaching resource for the perusal of the medical physics community. It is the hope of the authors that it serves as a foundation for practical guidance for medical physics leaders seeking to optimize their strategic decision-making processes.

Keywords: SWOT analysis, strategic planning, medical physics, strategic leadership.

1. Introduction

In strategic leadership, it is essential to understand the following key terms: mission, vision, strategic plan. The mission statement defines the specific services a profession/group offers to society; the vision statement envisions a future desired state of the profession/group with respect to the mission; a strategic plan outlines the steps to bridge the gap between the current actual state and the desired future vision [1].

In the context of Medical Physics (MP), strategic leadership is crucial for the development and success of clinical or research teams in providing effective and safe patient services. MP leaders need to understand the characteristics of the groups they lead, such as trainees, special interest groups (SIGs), or departmental teams, as different groups require specific leadership styles and strategies. Regardless of the group, leaders must prioritize guiding and inspiring their team members [1], [2]. Marcu et al. [3] discuss the importance of training young Medical Physics Professionals (MPPs) to ensure the future progress of the profession. They emphasize the need for early career MPPs to learn to work collectively and in a coordinated manner at national and European levels. To address this, the European Federation of Organisations for Medical Physics (EFOMP) has created a SIG that will bring together early career MPPs from across Europe.

In the current economic environment, characterized by austerity economics, reduced budgets, and commoditization, strategic and robust leaders are even more crucial for MP. Strategic leadership involves developing a vision, creating a plan, and motivating the profession/group to achieve that vision. Robust (or 'resilient') leadership entails staying focused on the vision and demonstrating the ability to overcome challenges. Strategic planning allows leaders to guide their teams, foster collaboration, and address challenges, ultimately improving patient services in the field [1], [2], [4], [5].

2. SWOT analysis based strategic planning

Vision setting is crucial in leadership as it provides a shared future direction and purpose for the team. Without a compelling vision, the work environment can become demotivating, and ultimately fail. A vision helps inspire and motivate others and gives a sense of meaning and direction to the work being done. SWOT generation is a valuable tool for assessing the internal strengths and weaknesses of the profession/group and external opportunities and threats that impact the attainment of the vision. By aligning opportunities with strengths and addressing weaknesses and threats, strategic objectives

can be formulated and the vision is achieved. SWOT analysis helps leaders make informed decisions and develop strategies that align with the group's vision. These strategic objectives are specific goals that enable leaders to bridge the gap between the present state and the desired future vision. Strategic objectives provide a roadmap for progress, help prioritize actions, allocate resources effectively, and ensure that the team is working towards its vision in a coordinated manner [1].

These elements are essential for effective leadership, especially in the context of MP, where teamwork, collaboration, and the delivery of high-quality patient services are critical. Moreover, the concept of succession planning in which experienced present leaders coach the next generation of leaders is crucial for ensuring the ongoing success of organizations.

3. SWOT based strategic planning in medical physics found in the literature

Sternick, E., and Curran, B. [6] discussed the use of SWOT analysis in MP strategic planning. Their work involved an organizational profile review to identify key components of the work environment. A four-quadrant SWOT matrix was created based on the profile study, highlighting the SWOT themes. The authors stated that the analysis helps the MP team design targeted action items for successful outcomes, and the methodology enabled specific operational objectives through team-based brainstorming. Overall, the authors concluded that SWOT analysis is a well-established tool for structured planning and performance excellence in the healthcare industry.

Caruana et al. [7] utilized SWOT analysis to develop a strategic plan concerning the involvement of biomedical physicists in healthcare professional education across Europe. Through a qualitative analysis of biomedical physics curricula, the study identified internal strengths and weaknesses. Additionally, by reviewing relevant literature in healthcare professional education and higher education, external opportunities and threats were identified and classified according to the traditional Political, Economic, Social-Psychological, Technological-Scientific (PEST) categories.

Caruana et al. [8] present a development strategy for the role of medical physicists[1] in Europe for the education of professionals in healthcare, derived from the findings of a SWOT audit conducted in 2010 [7]. The research methods employed emphasize the significance of strategic planning in delivering educational services across all levels. The study utilized a practical combination of theoretical frameworks from strategic planning literature, adapted to suit the context of academic role development. Key outcomes encompassed the identification of essential competences for MPPs in this context and conducting a gap analysis for the role. The paper concluded by presenting a set of strategic objectives and actions to be taken.

Figueira et al. [10] analyzed the state of the MP profession in Portugal using a SWOT analysis. The purpose was to identify measures to improve the profession. Based on responses from 83 Portuguese MPPs, dedication was a common strength, while lack of recognition was a weakness. The growing need for new installations was seen as an opportunity, but competition from other professions posed a threat. The authors recommended using SWOT to help MPPs create a strategic action plan for ensuring the positive development of the profession.

Andersson et al. [11] identified the SWOTs associated with the impact of artificial intelligence (AI) on the MP profession in Sweden. They identified strengths in the profession's collaboration with healthcare, academia, and the industry, as well as the existing radiation safety legislation. However, they also highlighted weaknesses in the lack of formal AI education and training programs for MPPs. They suggested that the role of MPPs could be extended to include commissioning and quality assurance of AI applications in imaging and radiotherapy. Using SWOT, the authors highlighted the need to adapt educational programs to include AI knowledge and skills to capitalize on the opportunities presented by AI in healthcare.

Vella et al. [12] analyzed a constancy testing program for medical imaging devices in a major hospital in Malta using SWOT. The study recommended strategic objectives such as capitalizing on opportunities such as advanced courses for strengthening internal strengths of the MPs addressing weak competences through advanced skill development, improving IT skills, and mitigating threats through proactive measures. These objectives intend to optimize the constancy testing program's delivered by the MP team.

Schembri et al. [13] made use of SWOT to analyze the state of the MP profession in Malta so that a strategic plan may be developed. The study highlighted the MPPs strong competences in each specialty area, arising from their backgrounds in physics and engineering. However, the study also identified the profession's low level of involvement with non-radiological such as physiological measurement devices. The strategic objectives derived from the SWOT analysis encompass enhancing internal strengths by advancing competences, expanding professional roles, and improving strategic skills; addressing weaknesses through delegation, skill diversification, and strategic planning; capitalizing on opportunities through mandatory education, diverse training, research, and international collaborations; and countering external threats via improved communication, combating replacement notions, regulatory amendments, and increased involvement by the MPPs. These objectives seek to optimize the MP profession's effectiveness, secure its role, and elevate competences through proactive measures and strategic alignments to continue providing high-quality care and protection to patients, workers, and the public.

[1] The term 'biomedical physics' was used in the original study because 'medical physics' was at the time only associated with ionizing radiation based medical devices. However, with the advent of the updated Malaga declaration [9] this is not so anymore, and medical physicists are encouraged to involve themselves with all medical devices and all physical agents, so it is now appropriate to use the term 'medical physics' (Caruana C. J., personal communication, June 2023).

4. Educating young leaders in strategic planning

Opportunities to learn strategic planning in the field of MP can be derived from various notable sources. One debate explores the idea of a Master's degree in Business Administration (MBA) for formalized leadership and managerial training for the MP profession. In their parallel opposed editorial article [14], Gutierrez A. argues that an MBA degree provides a structured and comprehensive approach to develop the necessary skills for leadership roles, while Halvorsen P. believes that these skills can be acquired through other paths. Both perspectives recognize the importance of leadership in MP but offer different viewpoints on the role of an MBA degree in developing the leadership competences of MP professionals.

A separate debate revolved around whether courses on strategic planning, communication, and management should be integrated into the MP curriculum to prepare students for leadership roles [15]. In the point-counterpoint article, Caruana C. J., argues in favor of incorporating these skills into the curriculum, emphasizing the changing healthcare environment and the need for MPPs to adapt and acquire leadership skills early in their career. In contrast, Cunha J. A. M., opposes the integration of strategic planning and management education into the MP curriculum. Cunha argues that early career positions typically do not involve these skills and that they can be acquired on the job if necessary. Overall, the debate centers on the balance between core scientific knowledge and the acquisition of leadership skills within the MP curriculum, with differing opinions on the necessity and timing of their teaching [15].

A few articles explored the necessity of leadership courses for MP roles [16, 17]. The articles focused on Module MPE01 within the EUTEMPE-RX project [18]. The module aims to develop leadership skills for aspiring Medical Physics Experts (MPEs) in Diagnostic and Interventional Radiology. It recognizes that in today's competitive world, scientific knowledge alone is insufficient, and good leadership, managerial, and strategic planning skills are essential. The module received positive feedback from participants, and it is suggested that similar courses be adopted by MP educators worldwide. The module is presently being developed further by EUTEMPE and EFOMP to make it suitable for all MPPs irrespective of their specialty (Caruana C. J., personal communication, August 2023).

Another resource is an EFOMP online MP mentoring program targeted towards development of research leadership. The program is called "Mentoring in Research" and it is aimed at supporting early-career MPPs who lack access to research resources. The program pairs mentees, who are young MPPs seeking guidance for their research projects, with experienced mentors. The mentors provide advice and practical assistance in various areas of research, such as research setup, ethics, networking, and publications. Mentorship lasts about a year but can be extended. Communication is electronic, and mentor turnover is encouraged [19].

Case study scenarios for leadership education (both strategic and scientific) are being developed offering valuable insights [20]. Furthermore, a book on strategic and robust (i.e., resilient) leadership specifically for MPPs was published in 2020, marking a significant development in the field [1]. Examples of strategic leadership in the role of medical physics educators have been published [8].

Professional organizations like the European Federation of Organizations for Medical Physics (EFOMP) and the European Training and Education for Medical Physics Experts (EUTEMPE) network offer comprehensive leadership learning opportunities [18]. The AAPM Medical Physics Leadership Academy Committee is actively working on developing resources and organizing annual meetings/summer schools [21, 22]. Overall, despite the limited attention to leadership in MP curricula, these available resources do present opportunities for learning and development of leadership skills.

5. Conclusions

In conclusion, the need for research and learning resource development in various contexts, including leadership and organizational development for MPPs, is evident. Understanding key terms such as mission, vision, and strategic plan is essential for effective leadership. In the field of MP, leadership plays a crucial role in ensuring the success and safety of clinical and research teams. Strategic and robust leaders are necessary to navigate economic constraints and align with core values. SWOT analysis-based strategic planning can guide leaders in developing a vision, identifying strengths and weaknesses, exploring opportunities, and mitigating threats. Various studies have highlighted the importance of strategic planning and leadership development in MP. Moreover, resources such as mentoring programs, online courses, and professional organizations offer opportunities for learning and growth in strategic planning. It is vital for professionals in the field to prioritize continuous learning and development to improve patient services and advance the profession of MP.

References

1. Caruana C. J., Leadership and Challenges in Medical Physics. Institute of Physics Publishing - Institute of Physics and Engineering in Medicine, 2020. [Online]. Available: https://dx.doi.org/10.1088/978-0- 7503-1395-7

2. Caruana C. J. and Damilakis J., "Being an excellent scientist is not enough to succeed! Soft skills for Medical Physicists.," Eur. J. Radiol. Press Available Online, 2022.

3. Marcu L. G. et al., "Early career medical physicist groups in Europe: An EFOMP survey," Eur. J. Med. Phys., no. 95, pp. 89–93.

4. Caruana C. J., "Developing strategic leadership skills is crucial for the future of medical physics," Proc. Med. Phys. Balt. States 15 2021, 2021.

5. Caruana C. J., "Scientific and strategic leadership in Medical Physics - we need both!" World congress on medical physics and biomedical engineering. June, Singapore, 2022.

6. Sternick E. and Curran B., "SU-FF-P-01: Conducting a SWOT Analysis-A Useful Framework for Medical Physics Strategic Planning," Med. Phys. Int. J. Med. Phys. Res. Pract., vol. 36, no. 6, Part 2, pp. 2433–2433, 2009.

7. Caruana C. J. et al., "A comprehensive SWOT audit of the role of the biomedical physicist in the education of healthcare professionals in Europe," Eur. J. Med. Phys., vol. 26, no. 2, pp. 98–110, 2010.
8. Caruana C. J. et al., "A strategic development model for the role of the biomedical physicist in the education of healthcare professionals in Europe.," Eur. J. Med. Phys., vol. 28, no. 4, pp. 307–318, 2012.
9. Byrne B. et al., "EFOMP Malaga Declaration 2023: An updated vision on Medical Physics in Europe," Phys. Med., vol. 111, p. 102620, Jul. 2023, doi: 10.1016/j.ejmp.2023.102620.
10. Figueira R., Poli E., and Isidoro J., "SWOT analysis of the current situation of Medical Physicists in Portugal," Phys. Med., no. 32, p. 332, 2016.
11. Andersson J. et al., "Artificial intelligence and the medical physics profession-A Swedish perspective.," Phys. Med., vol. 88, pp. 218–225, 2021.
12. Vella K. et al., "Strategic planning in medical physics: A SWOT analysis of a diagnostic radiology constancy testing programme for medical imaging devices in a major hospital in Malta," Med. Phys. Int. J., vol. 10, 2022.
13. Schembri J., Caruana C. J., and Agius S., "An initial SWOT audit of the Medical Physics profession in Malta: The perspective of Medical Physicists," Med. Phys. Int. J. Press, 2023.
14. Gutierrez A., Halvorsen P., and Rong Y., "MBA degree is needed for leadership roles in Medical Physics profession.," J. Appl. Clin. Med. Phys., vol. 18, no. 6, pp. 6–9, 2017.
15. Caruana C. J., Cunha J. A. M., and Orton C. G., "Subjects such as strategic planning, extra-disciplinary communication, and management have become crucial to medical physics clinical practice and should become an integral part of the medical physics curriculum.," Med. Phys. Int. J. Med. Phys. Res. Pract., vol. 44, no. 8, pp. 3885–3887, 2017.
16. Caruana C. J., Vano E., and Bosmans H., "EUTEMPE-RX module MPE01: Developments in the profession and challenges for the medical physics expert (D&IR) in Europe - a first in international medical physics education and training.," Med. Phys. Int. J., vol. 3, no. 2, pp. 69–71, 2015.
17. Caruana C. J., "EUTEMPE-EFOMP module MPE01: Leadership in Medical Physics, Development of the profession and the challenges for the MPE (D&IR) – A Mini-MBA in strategic leadership for Medical Physicists in Diagnostic and Interventional Radiology.," Asia-Ocean. Fed. Organ. Med. Phys. Newsl., vol. 10, no. 2, 2018.
18. EUTEMPE, "MPE01: Leadership in Medical Physics, Development of the profession and the challenges for the MPE (D&IR)," EUTEMPE-NET. https://eutempe-net.eu/mpe01/ (accessed Jun. 16, 2023).
19. EFOMP, "Introduction to the EFOMP Mentoring in Research programme." https://www.efomp.org/index.php?r=pages&id=mentoring-about (accessed Jun. 16, 2023).
20. Caruana C. J., "EUTEMPE Masterclass Medical physics leadership: Real world case studies from the trenches." EFOMP-EUTEMPE Masterclass, 2021.
21. Caruana C. J., "Learning resources for strategic Medical Physics leadership." World congress on medical physics and biomedical engineering. June, Singapore, 2022.
22. AAPM, "AAPM Committee Tree - Medical Physics Leadership Academy Committee (MPLAWG)." https://www.aapm.org/org/structure/?committee_code=MPLAWG (accessed Jun. 19, 2023)

MEDICAL PHYSICS IN THE BALTIC STATES 16 (2023)

Proceedings of International Conference "Medical Physics 2023"
09-11 November 2023, Kaunas, Lithuania

PILOT INVESTIGATION OF DIFFERENT COLLIMATOR SETTINGS FOR TREATING BRAIN METASTASES WITH GAMMA KNIFE

Linas KUDREVIČIUS[1,2], Šarūnas TAMAŠAUSKAS[2], Diana ADLIENĖ[1]
[1]The Hospital of Lithuanian University of Health Sciences Kaunas Clinic; [2]Kaunas University of Technology, Physics department
[1]linas.kudrevicius@ktu.edu; [2]Sarunas.Tamasauskas@kaunoklinikos.lt; [3]diana.adliene@ktu.lt

***Abstract*:** Leksell Gamma Knife® (GK) stereotactic radiosurgery (SRS) system allows treatment of various targets in the brain: from the smallest 0.01 cc volume brain metastases (BM), up to 10 cc targets in one single session and even treatment of larger volumes applying hypofractionated treatment regime and high dose (< 150 Gy) functional targets [1-4]. This SRS system with 3 collimator sizes, sector blocking and wide range of isodose settings allow to prioritise selectivity, gradient index or time. In this study the application of various collimator settings was investigated for patients with multiple small BM in order to find out the best treatment planning approach and set the guidelines.

Keywords: Radiosurgery, Gamma Knife, brain diseases

1. Introduction

Leksell Gamma Knife (GK) radiosurgery system uses 192 radioactive ^{60}Co sources for irradiation of brain diseases [5]. Due to a short half-life time of ^{60}Co patient's treatment time increases twice over 5.27 years and the treatment procedure for one small metastasis increases from 10 min to 20 min. As for the patients with multiple metastases <40, treatment will be prolonged by up to 6.5 hours. This can limit accessibility to the gamma knife treatment for some patients. To overcome this problem, patients can be treated with a mask, exceptionally - stay overnight with Leksell Coordinate Frame G, repeat MRI imaging procedure and resume treatment on the following day, or be treated in LINAC based system. Although possible, these treatment solutions are inferior to standard one fraction Gama knife treatment protocol. Knowing the best combination of collimator settings would help us to safely decrease treatment time without compromising other dose delivery parameters.

The unique Leksell Gamma knife SRS system configuration of ^{60}Co sources that are focused at one point in radiological centre, allows to achieve pinpoint accuracy and significant dose drop at around 50% of the isodose level. Full treatment width at the half maximum is 6.16 mm (X, Y coordinates) and 5.04 mm on Z axis using 4 mm collimator. While using 8 mm and 16 mm collimators allows to achieve 11.06, 9.80 and 27.75, 17.44 mm. respectively [6] (see Fg. 1 below).

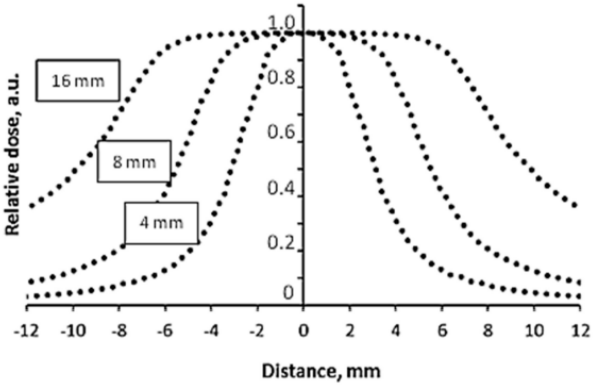

Fig. 1. Normalized dose profiles along the Z axis generated by Gammaplan treatment planning system for the dose delivery to the target. Collimator size is indicated for each profile separately [6].

2. Materials and methods

In this pilot study we analysed influence of collimator settings, such as size and isodose, on the irradiation of surrounding healthy tissue and dose delivery time. Leksell Gammaplan® 11.3.2 software was used for the treatment dose planning. 4Gy, 8 Gy, 16 Gy dose shots or hybrid shot compositions to deliver the same prescribed dose of 24 Gy were applied. The same volume of metastasis was used in all collimator settings.

Dose profiles, conformity indexes (CI), normal brain tissue volume irradiated with 12 Gy (V12) or/and 10 Gy (V10) doses, treatment time per metastasis over all usage period (7years) of ^{60}Co source have been analyzed. In this investigation the activity of 192 ^{60}Co radiation sources being 195.53 TBq with a dose rate of 3.492 Gy/min was taken into account. The output factors of 1, 0.9 and 0.814 for 4-, 8- and 16 mm collimator settings respectively were applied. The obtained results allowed for highlighting the optimal compromise settings for

irradiation of multiple metastases in comparison with V12 treatment and overall treatment time.

3. Results

3.1. Different collimator settings

In this pilot study treatment plans for 0.1 and 0.5 cc volume brain metastases were prepared investigating various possible treatment planning approaches. We analysed single shot case with various isodose level combinations applying the same collimator size for all 8 treatment sectors, hybrid shots (different collimator for each sector in one shot), and shot in the shot (2 different shots at the same coordinates) techniques.

The smallest (V12) irradiated volume of healthy brain tissue was 0.36 cc. This was achieved using 4 mm collimator with low isodose levels. Such collimation allowed to deliver the highest maximum dose (58.5 Gy) at hotspot, paying cost of the longest treatment time: 21.25 min at the reloading and up to 52.7 minutes after 7 years.

The shortest treatment time of ~7.7 min was evaluated for the case of hybrid 8/16 shots, with application of 8 mm and 16 mm collimators with shot in the shot technique, but it increases irradiated volume (V12) up to 2.48 cc, which was 588% larger then in 4 mm shot treatment (Table 1).

When considering recommendation to treat the target with Paddick's conformity index (PCI) of at least of 0.75 (7) it is advised to use hybrid 4/8 or 8mm collimator shot with high isodose. This configuration gives 0.58 cc (min) and 0.67 cc (max) volume values and V12 corresponding treatment time (min. – max) of 11.9 - 29.6 min and 8.4 – 20.83 minutes (Table 1).

Table 1. Comparisons of different collimator settings for the treatment of 0.1 cc brain metastases with a prescribed dose of 24 Gy.

Plan Isodose	PCI	Min-Max (Mean) Gy	V12 Gy	V10 Gy	TT 0 Years	TT 4 Years	TT 7 Years
4 (41)	0.74	20.9-58.5 (41.6)	0.36	0.47	21.3	35.7	52.7
4/8 (69)	0.75	23-34.8 (29.6)	0.58	0.73	11.9	20.1	29.6
8 (93)	0.76	23.7-25.8 (25.1)	0.67	0.84	8.4	14.1	20.8
8/16 (96)	0.70	23.9-25 (24.6)	2.48	3.12	7.7	13	19.2
4,16 (70)	0.71	23–34.3 (29.3)	3.00	3.79	11.3	19	28
4/8,16 (84)	0.73	23.5–28.6 (26.4)	2.59	3.29	9.1	15.3	22.6
8,16 (96)	0.74	23.8–25 (24.6)	2.32	2.99	7.7	13.0	19.2
4,8 (68)	0.77	22.8–35.3 (29.8)	0.56	0.71	12.2	20.4	30.2
Aut (68)	0.71	22.1–34.3 (29.4)	0.59	0.75	11.7	19.7	29.1

Analysing 0.5 cc volume metastases, we got similar results. 8 mm shot gives the lowest volume of the irradiated brain: 1.71 cc for V10 treatment, and 1.33 cc for V12 treatment with a treatment time of up to 35.8 min. This is tolerable for a first two years of fresh ^{60}Co source exploration, but due to the natural Cobalt decay, and in the case of multiple metastases the overall time becomes too long for a patient treatment and for the incorporation of treatment procedure into a standard daily workflow. In this case, starting with 3 years after fresh source installation the treatment alternative of using hybrid 8/16 shot should be considered. Treatment time of 15.96 min starting with 4 years of GK use with tolerable V10 of 3.97 cc and V12 of 3.21 cc and 0.92 PCI, is also acceptable (table2)

Table 2. Comparisons of different collimator settings for the treatment of 0.5 cc brain metastases with a prescribed dose of 24 Gy.

Plan Isodose	PCI	Min-Max (Mean) Gy	V12 Gy	V10 Gy	TT 0 Years	TT 4 Years	TT 7 Years
8 (54)	0.90	22.1-44.4 (35.9)	1.33	1.71	14.5	24.3	35.9
4/8 (33)	0.81	21-72.7 (42.9)	1.53	2.03	25	41.9	61.9
8/16 (78)	0.92	22.9-30.8 (27.8)	3.21	3.97	9.5	16	23.6
8,16 (77)	0.92	22.8-31.2 (28.1)	3.14	3.96	9.7	16.2	24
8-16 (85)	0.60	22.8-28.2 (26.8)	3.95	5.00	8.5	14.3	21.1
Aut (50)	0.92	20.9-48 (34.7)	1.47	1.95	16.1	27.0	39.9
Aut (85)	0.90	23.3-28.2 (26)	4.34	5.66	10.4	17.5	25.8
Aut (70)	0.95	22.6-34.3 (29)	2.42	3.20	13.5	22.7	33.5

3.2. Locations of brain metastases.

Brain metastasis location (near the skull, or deep in the brain near mesencephalon (midbrain)) can change irradiation volume of the prescribed 24 Gy isodose up to 2.9 and 1.3 % using corresponding 4 mm and 8 mm collimators.

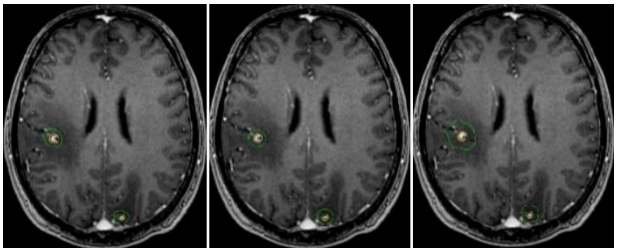

Fig. 2. Treatment plans for a patient with brain metastases using 4, 8,16 mm collimator settings respectively

The volume of healthy brain tissue receiving 12 Gy and 10 Gy can change up to 1.3 – 3.4 %.

Treatment time of 0.1 cc brain metastases with Gamma Knife SRS system after reloading can vary from 14.5 to 22.2 min using 4 mm shot at 41% isodose and from 5.7 to 8.9 minutes using 8 mm 93% isodose treatment approach, while irradiating 0.131 and 0.136 cc volumes with 24 Gy respectively. Due to the natural ^{60}Co radioisotope decay the overall treatment time increases by 1.5 % every month.

3.3. Real patient treatment plan scenario

When modelling the real case scenario (Fig. 3), the usage of 4, 8 and 16 mm collimator provides similar PCI (Paddick's conformity index): 0.77, 0.73 and 0.76 respectively, but GI (Gradient index) increases from

2.67, 4.27 to 18.39 for small target (< 1 cc) and is higher than recommended values (≤ 3 – 3.5) [7].

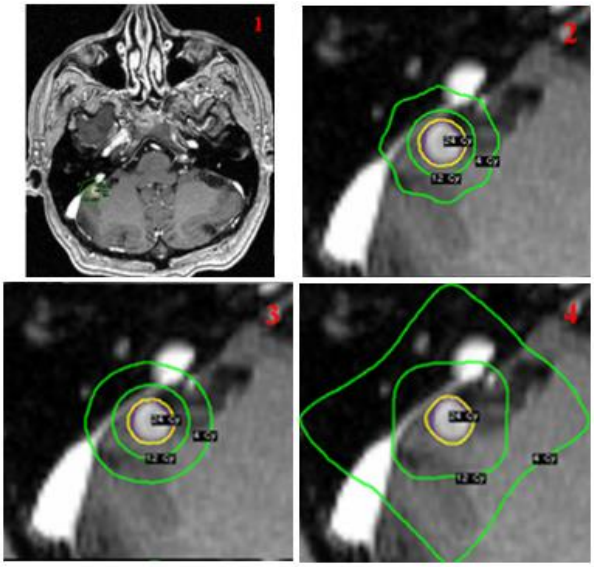

Fig. 3. Brain metastases (0.121 cc) in right cerebellum hemisphere (1). Treatment plans using different collimator settings: 2 – 4mm collimator, 3 – 8mm collimator, 4 - 16 mm collimator.

In this scenario wider collimation and dose prescription with higher isodose leads to the increase of V10 and V12 volumes and associates with the higher radiation dose to healthy brain tissue and increased radionecrosis risk. Treatment plan with 24 Gy prescribed irradiation dose for small 0.121 cc brain metastases results in 0.532 cc for V10 and 0.41 cc for V12 when using 4 mm shot with 38% isodose. Treatment time in this case will be 23.32 min in the first year of the fresh ^{60}Co source installation and 44.64 min using 5 years old source. The usage of 8 mm shot at 90% isodose will cover 0.896 cc for V10 and 0.708 cc for V12 within 8.91 min at the beginning of cobalt source exploration and 17.05 min after 5 years. SRS plan with application of 16 mm collimator at 96% isodose provides 3.596 cc and 2.868 cc for V10 and V12 respectively and records treatment time of 7.73 min (14.8 min after 5 year). When planning the treatment several things must be considered. Although the shortest time could be reached by using 16mm collimator it is not recommended to use it, because cerebellum could more likely have radiation induced side effects. Close proximity to critical structures such as modiolus can also influence decision making. Avoiding hearing deterioration mean irradiation dose to modiolus should be less than 4 Gy [8]. Thus, it is advised not to use 16 mm collimator shot, since it reduces treatment time per one small 0.2 cc metastasis by 1.18 minutes only, but increases V10 and V12 by 2.58 cc (348%) and 2.04 cc (368%) respectively comparing to plan with application of 8 mm collimators. V10 and V12 for 8 mm shot plan are 2.943 and 2.337 respectively. Compared to 4 mm plan 8 mm shot plan provides 745% higher V10 and 850% higher V12 with 15.59 min. shorter time.

These shot parameters ware tested for 3 randomly selected patients with small multiple BM whose treatment plans were retrospectively re-planned having in mind 4 mm, 8 mm, and 16mm collimators. The first patient had 4 BM with a total clinical tumour volume of 0.168 cc; the second patient had 5 BM and 0.606 cc cumulative volume and the third – 12 BM and 0.38 cc. volume (Fig.4).

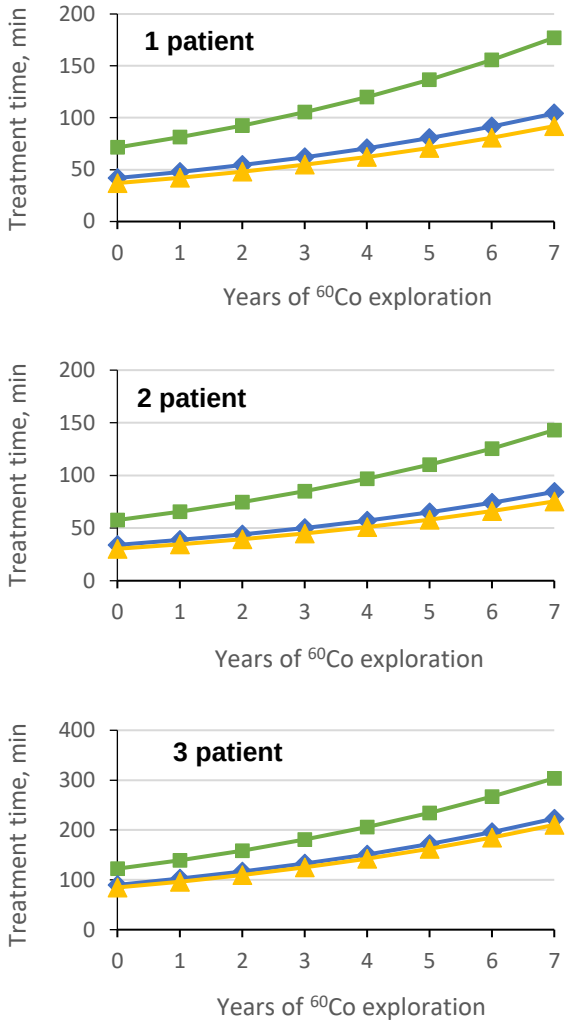

Fig. 4. Real case scenario for patient treatment time in various years of ^{60}Co source exploration using different collimators: green line – 4mm collimator, blue line -8 mm collimator and orange line – 12 mm colimator.

It was found that the best dosimetric parameters and for patient comfort overall shorter treatment time was when applying 8 mm collimator approach, as it significantly reduced the treatment time by 23.6 – 32.6 min for different patients during the first year of source exploration, and up to 58.6 – 80.8 minutes after 7 years of source exploration, which corresponds to the increase of V10 and V12 from 4.4 - 157 % (Table3). Time becomes very important factor for successful treatment, especially if it increases over 1.5 hour or sometimes over 1 hour. The prolonged time creates problems with patient's relaxed lying during the whole treatment session.

Since the "older" cobalt source is directly linked to the problem of less patient/less tumour treatment per working day, another option exploring patient treatment over multiple sessions with a medium long breaks exists. In such a case application of 16 mm collimator would be

of benefit, since it may reduce the treatment time by 3.6 – 5.1 minutes (in the first year of the source exploration) but of cost of irradiating 184 – 588 % healthy brain tissue comparing to the case with 8 mm collimator.

Table 3. Comparison of irradiated volume for three real patient case scenarios using different collimator settings, at prescribed 24Gy dose with 100% coverage.

Patient & plan	Metastases volume	24Gy, cc	12Gy, cc	10Gy, cc
1-4mm	0.168	0.301	0.927	1.201
1-8mm	0.168	0.302	2.119	2.718
1-16mm	0.168	0.299	5.388	7.241
2-4mm	0.606	1.041	3.183	4.171
2-8mm	0.606	0.974	3.38	4.327
2-16mm	0.606	0.988	7.684	10.557
3-4mm	0.38	0.759	2.774	3.645
3-8mm	0.38	0.658	6.174	8.124
3-16mm	0.38	0.695	10.856	14.681

4. Conclusions

After investigating possible approaches to single and multiple metastasis treatment plans, we recommend application of hybrid 4/8- or 8-mm collimator shots with high isodose. Recommended procedure significantly reduces treatment time by up to 12.86 min per one BM when applying fresh ^{60}Co source and at up to 31.9 minutes after 7 years of source exploration. Shorter time makes it easier for patients to complete the treatment and more patients per day may be treated. This treatment gives tolerable dose increases in V12 and V10 volumes without significantly increasing radionecrosis risk. 16 mm collimator should not be used to plan small multiple BM because V10 and V12 volumes can increase for up to 184 – 588 % (as it was evaluated in the case with 12 BM).

There are only few studies analysing effect of treatment time on treatment outcome. These studies mainly analyse time in conjunction with dose rate and BED. Yang et al [9] stated that treatment time was an independent predictor of pain outcomes when treating trigeminal neuralgia. Longer treatment time was associated with worse pain control. Similar conclusion was drawn by Lee et al [10]. He stated that Radiosurgery with a higher dose rate caused more pain relief and lower recurrence rate. When analysing vestibular schwannoma treatment Villafuerte et al [11] stated that BED did not influenced tumour control and variable dose rates and treatment times did not influence treatment outcome. In contrast Tuleasca et al [12] stated that higher BED linearly and significantly correlated with tumour volume changes after SRS for vestibular schwannomas. AVM group analysis by Tuleasca [13] showed that the beam-on time was statistically significant for both obliteration and complication appearance. Whereas in the study on 9L rat gliosarcoma cells, radiosurgical treatment demonstrated no difference in tumour cell killing in the range of dose rates obtained using actual LGK unit with new sources or sources decayed even for two half-lives [14]. There are still many contradicting studies on influence of beam-on time to treatment efficacy and complications, but we think that treatment time is very important factor for treatment quality, however the evidence based importance of this influence remain to be unveiled.

References

1.Samanci Y, Karakose F, Senyurek S, Peker S. Single-fraction versus hypofractionated gamma knife radiosurgery for small metastatic brain tumors. Clin Exp Metastasis. 2021 Jun;38(3):305-320. doi: 10.1007/s10585-021-10086-y.Epub 2021 Mar 17. PMID: 33733707.

2.Niranjan A, Monaco E, Flickinger J, Lunsford LD. Guidelines for Multiple Brain Metastases Radiosurgery. Prog Neurol Surg. 2019; 34:100-109. doi:10.1159/000493055. Epub 2019 May 16. PMID: 31096242.

3.Noda R, Akabane A, Kawashima M, Oshima A, Tsunoda S, Segawa M, Inoue T. Fractionated Gamma Knife radiosurgery after cyst aspiration for large cystic brain metastases: case series and literature review. Neurosurg Rev. 2022 Oct;45(5):3457-3465. doi: 10.1007/s10143-022-01835-y. Epub 2022 Jul 14. PMID: 35834076.

4.Higuchi Y, Matsuda S, Serizawa T. Gamma knife radiosurgery in movement disorders: Indications and limitations. Mov Disord. 2017 Jan;32(1):28-35. doi:10.1002/mds.26625. Epub 2016 Mar 31. PMID: 27029223.

5. Ganz JC. Gamma Knife evolving instrumentation. Prog Brain Res. 2022;268(1):49-63. doi: 10.1016/bs.pbr.2021.10.025. Epub 2022 Jan 13. PMID: 35074094.

6. Kudrevicius, L.; Jaselske, E.; Adliene, D.; Rudzianskas, V.; Radziunas, A.; Tamasauskas, A. Application of 3D Gel Dosimetry as a Quality Assurance Tool in Functional Leksell Gamma Knife Radiosurgery. Gels 2022, 8, 69. https://doi.org/10.3390/gels8020069

7.Torrens M, Chung C, Chung HT, Hanssens P, Jaffray D, Kemeny A, Larson D,Levivier M, Lindquist C, Lippitz B, Novotny J Jr, Paddick I, Prasad D, Yu CP.Standardization of terminology in stereotactic radiosurgery: Report from the Standardization Committee of the International Leksell Gamma Knife Society: special topic. J Neurosurg. 2014 Dec;121 Suppl:2-15. doi: 10.3171/2014.7.GKS141199.PMID: 25587587.

8.Lin RH, Wang TC, Lin CD, Lin HL, Chung HK, Wang CY, Tsou YA, Tsai MH. Predictors of hearing outcomes following low-dose stereotactic radiosurgery in patients with vestibular schwannomas: A retrospective cohort review. Clin Neurol Neurosurg. 2017 Nov; 162:16-21. doi: 10.1016/j.clineuro.2017.09.001. Epub 2017 Sep 5. PMID: 28892717.

9.Yang AI, Mensah-Brown KG, Shekhtman EF, Kvint S, Wathen CA, Hitti FL, Alonso-Basanta M, Avery SM, Dorsey JF, Y K Lee J. Gamma Knife radiosurgery for trigeminal neuralgia provides greater pain relief at higher dose rates. J Radiosurg SBRT. 2022;8(2):117-125. PMID: 36275137; PMCID: PMC9489081.

10. Lee JY, Sandhu S, Miller D, Solberg T, Dorsey JF, Alonso-Basanta M. Higher dose rate Gamma Knife radiosurgery may provide earlier and longer-lasting pain relief for patients with trigeminal neuralgia. J Neurosurg. 2015 Oct;123(4):961-8. doi: 10.3171/2014.12. JNS142013. Epub 2015 Aug 7. PMID: 26252452.

11. Villafuerte CJ, Shultz DB, Laperriere N, Gentili F, Heaton R, van Prooijen M, Cusimano MD, Hodaie M, Schwartz M, Berlin A, Payne D, Kalia SK, Bernstein M, Wang J, Zadeh G, Spears J, Tsang DS. Radiation Dose Rate, Biologically Effective Dose, and Tumor Characteristics on Local Control and Toxicity After Radiosurgery for Acoustic Neuromas.

World Neurosurg. 2021;152: e512-e522. doi: 10.1016/j.wneu.2021.05.122. Epub 2021 Jun 16. PMID: 34098139.

12. Tuleasca C, Faouzi M, Maeder P, Maire R, Knisely J, Levivier M. Biologically effective dose correlates with linear tumor volume changes after upfront single-fraction stereotactic radiosurgery for vestibular schwannomas. Neurosurg Rev. 2021 Dec;44(6):3527-3537. doi: 10.1007/s10143-021-01538-w. Epub 2021 Apr 10. PMID: 33839944; PMCID: PMC8592970.

13. Tuleasca C, Peciu-Florianu I, Leroy HA, Vermandel M, Faouzi M, Reyns N. Biologically effective dose and prediction of obliteration of unruptured arteriovenous malformations treated by upfront Gamma Knife radiosurgery: a series of 149 consecutive cases. J Neurosurg. 2020 24; 134(6): 1901-1911. doi: 10.3171/2020.4. JNS201250. PMID: 32707557.

14. Niranjan A, Gobbel G, Novotny J Jr, Bhatnagar J, Fellows W, Lunsford LD. Impact of decaying dose rate in gamma knife radiosurgery: *in vitro* study on 9L rat gliosarcoma cells. J Radiosurg SBRT. 2012;1(4):257-264. PMID: 29296325; PMCID: PMC5658859.

MEDICAL PHYSICS IN THE BALTIC STATES 16 (2023)

Proceedings of International Conference "Medical Physics 2023"
09-11 November 2023, Kaunas, Lithuania

ASSESSMENT OF ^{192}IR SOURCE POSITION AND DOSE ACCURACY CALCULATION DEDICATED FOR REAL-TIME *IN-VIVO* DOSIMETRY IN BRACHYTHERAPY: A PHANTOM STUDY

Mindaugas DŽIUGELIS[1], Marius BURKANAS[1], Kęstutis AKELAITIS[1], Ieva MARKEVIČIENĖ[1], Gitana LUKOŠEVIČIENĖ[1], Aleksandras CICINAS[1], Tomas ČEPONIS[2], Vytautas RUMBAUSKAS[2], Eugenijus GAUBAS[2], Justinas JONUŠAS[1,3], Ernestas JANULIONIS[4], Jonas VENIUS[1,5]
[1]National Cancer Institute, Medical Physics Department, [2]Vilnius University, Institute of Photonics and Nanotechnology, [3]Clinic of Haematology and Oncology, Institute of Clinical Medicine, Faculty of Medicine, Vilnius University, [4]National Cancer Institute, Brachytherapy Department, [5]National Cancer Institute, Biomedical physics laboratory
[1]mindaugas.dziugelis@nvi.lt

***Abstract*:** High-dose-rate (HDR) brachytherapy allows dose delivery inside the tumor with a steep dose gradient. The main goal of real time dosimetry (RTD) is to verify that the treatment dose delivery will be as planned. Obtained RTD data allows us to compare the measured absorbed dose distribution in the tissue with the dose distribution calculated by the treatment planning software (TPS). Despite several dosimetry methods described in scientific literature, only a few of them can be used in practice to evaluate the treatment accuracy of the HDR brachytherapy plan. However, none of the existing solutions provide information regarding real-time radioactive source position and dose distribution estimation from real-time measurement data.
In this work, we examined the possibilities of a new real-time dosimetry system developed in collaboration with National Cancer Institute (NCI) and Vilnius University (VU) specialists. A unique phantom for dosimeter calibration and quality assurance was designed and printed at the NCI using a 3D printer. The ionizing radiation intensity data and ^{192}Ir source position in this phantom can be assessed using different detectors and different data processing algorithms. In this study, ^{192}Ir source positions were obtained using multilateration and least square estimation calculations.
The obtained data demonstrated the feasibility of the developed dosimetry equipment to identify the position of the radioactive source and calculate the realized dose distribution with a 4 % error when the source was 2 cm away from the dosimeters.

Keywords: real time dosimetry, source tracking, HDR brachytherapy, multilateration.

1. Introduction

HDR brachytherapy (BT) is a cancer treatment procedure in which a radioactive source is transported to or close to the tumor. This allows for the possible safer realization of higher doses to the target and their better conformity compared to external beam radiation therapy (EBRT) [1]. Another good aspect of this treatment is reducing the doses to surrounding organs at risk (OARs) [2]. Usually, HDR-BT treatment is delivered in one to a few fractions, and every delivery takes several minutes [3]. Thus, the availability of fast real-time dose detection and reconstruction methods is essential because even small dosimetric mistakes can significantly affect treatment success.
The International Commission of Radiological Protection (ICRP) is concerned regarding incident reporting in HDR brachytherapy. After carrying out a comprehensive examination in 2005, a report was released about incidents in HDR-BT, indicating over 500 incidents [4]. It turned out that the most common reason for this was human error, and many accidents could have been prevented if staff had had functional monitoring equipment and paid attention to the results [4]. These problems further emphasized the need for a RTD system in BT to minimize human error and enhance procedural safety and efficacy.
Currently, treatment dose recording and reporting depend on using 3D image-based dose calculations performed by the TPS [5-7]. Nevertheless, various reputable organizations such as ICRP, IAEA, American Association of Physicists in Medicine (AAPM), International Commission on Radiation Units and Measurements (ICRU), and the European Society for Therapeutic Radiology and Oncology (ESTRO) support the implementation of dosimetry systems in order to

verify dose delivery [8]. This recommendation is particularly relevant in the context of HDR-BT, which involves the delivery of high doses per treatment fraction [4].

Precision plays a major role in a prostate HDR focal BT procedure. Here, accurate treatment needle positioning is as important as treatment planning in order to achieve successful dose delivery. Any misalignment could lead to overexposure of OARs or underdosage of the tumor. [9]. Therefore, exceptional care is taken during the procedure and treatment planning stage to ensure optimal outcomes. It is a complex process that involves a team of radiation oncologists, medical physicists, and radiation therapists.

As presented in this work, the development of a real-time dosimetry system for HDR BT addresses several limitations observed in existing methods. Current dosimetry methods, such as fluoroscopic imaging [10], diode arrays [11], custom brachytherapy applicator systems [12], and software tools [13], while effective to a degree, often fail to provide a comprehensive picture of dose distribution with the requested accuracy and exhibit measurement stability issues [14], system robustness [8], are time-consuming, dosimetric calibration of the dosimetry system is complicated. Therefore, the aim of the current study was to create a dosimetry system capable of real-time radioactive source localization and dose distribution estimation during the brachytherapy procedure. The tasks were to evaluate the position detection accuracy of the ^{192}Ir source and dose calculation accuracy based on measured dosimetric values.

2.1. Dosimetry system

The RTD system was made of semiconductor detectors integrated into the needles (referring to Fig. 1 and Fig. 2), used for prostate HDR-BT.

Fig.1. HDR-BT dosimetry needle.

Every needle had three detectors located at equal distances, spaced out 30 mm between each other (see Fig. 3). In total, nine dosimeters were used in the experimental setup. These detectors showed great potential for consistent dose registration with a time resolution of 20 milliseconds.

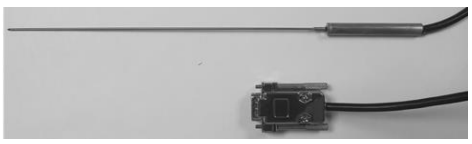

Fig. 2. Dosimetric needle with preamplifier and serial port connection.

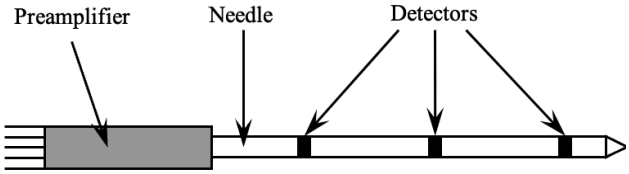

Fig. 3. Schematic image of dosimetric needles.

2.1. Pre-processing module

Another significant component of the dosimetry setup was a pre-processing module developed by NCI and VU specialists. This part was designed to record and decode the registered data from the dosimeters to the computer over a serial port. The key component for this module was an Arduino Uno device programmed to register and transfer data using C++ programming language. To facilitate the processing of the data recorded by the module, a Python script was developed. A calibration procedure was carried out to ensure the accuracy of the data reading before each data collection.

2.2. Brachytherapy phantom

For testing purposes, a 3D-printed phantom was designed and created (see Fig. 4) using the high-resolution resin SLA and UV printer Creality LP-006. The geometric accuracy of this phantom ensures uniform spacing between the dosimetry needle holes in the phantom, thereby making the placement of the dosimeters with minimal error. This uniformity facilitates the application of mathematical computations necessary for the calibration of the dosimetric system, thereby enhancing the reliability and accuracy of the performed measurements.

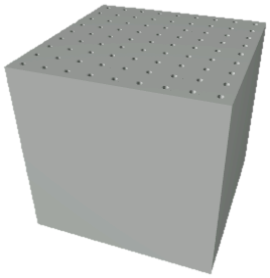

Fig. 4. 3D phantom model used for testing and calibrating RTD system.

2.3. Experimental setup

The dosimetric needles containing semiconductor detectors (as shown in Fig. 3) are inserted into the phantom and are used to perform real-time measurements of the dose rate from the moving ^{192}Ir source inside the applicator needle. Dosimetric needles are connected via serial ports into the pre-processing module. PC receives and processes dosimetry data from the module every 3-10 ms, according to the Central Processing Units' (CPU) clock, allowing for real-time data outcome analysis and interpretation. The experimental set up of the dosimetry system is provided in Fig.5.

2.4. Source position calculations

A dedicated Python software capable of source tracking was developed for this study. It calculates the distances from the signal source to each of the nine detectors using (1) and calculates the estimated coordinates of the ^{192}Ir source position.

$$d \times L = \sqrt{\frac{A_{MAX}}{A}} \quad (1)$$

where *d* represents known distance from the source to the detector, L represents calculated distance, A_{MAX} is the maximum activity registered by detector, and *A* is the measured activity at a given moment.

^{192}Ir source positions can be obtained using data from various combinations of detectors in different dosimetry needles. In order to maintain optimal computational speed, the final result of real-time IVD data is obtained by averaging these estimated coordinates over all combinations.

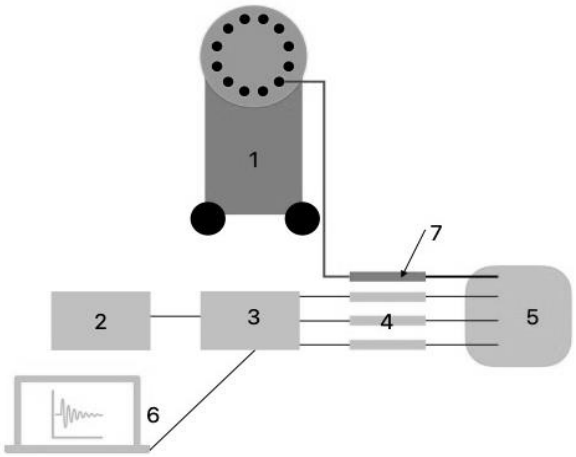

Fig. 5. IVD setup scheme: 1 – Brachytherapy afterloader; 2 – Power supply for the pre-processing module; 3 – Pre-processing module; 4 – Dosimeters; 5 – Phantom; . 6 – PC, 7 – Brachytherapy needle applicator.

3. Results and discussion

The minimum number of detectors required to maintain optimal computational speed was found to be 4. By using data from different dosimeters, we were able to obtain source positions based on measured dosimetric values.

The precision of source position calculations was assessed by comparing the source movement from the TPS with the movement derived from our dosimetry system. The source moved in 3 mm steps over the Z-axis, pausing for 5 s (dwell time) at each step, while in XY planes source position remained constant. The calculation was based on the dwell times and referred to the mean deviation of the calculated movement from the dosimetry measurements. We determined the source's X, Y and Z coordinates every 20 ms. From this data, we computed the standard deviation, revealing an average deviation of 0.11 mm in the X-axis and 0.42 mm in the Y-axis.

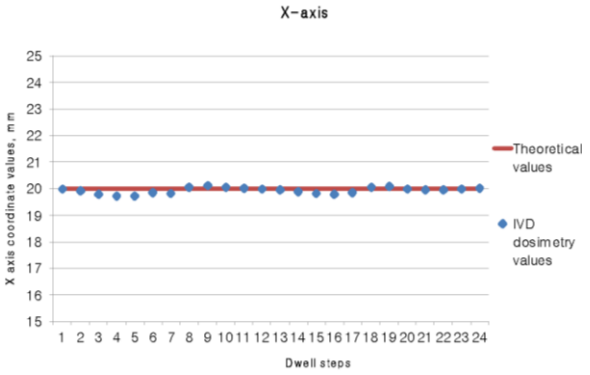

Fig. 6. Comparison of calculated and theoretical values of the source position in the X-axis.

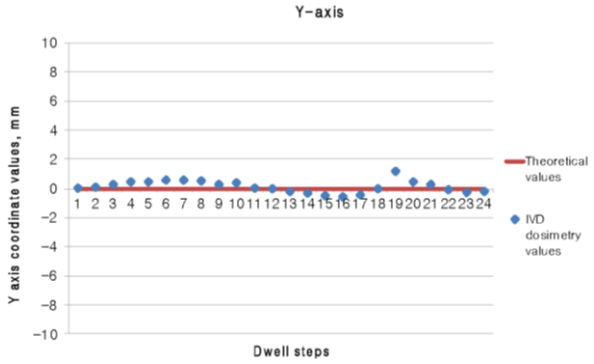

Fig.7. Comparison of calculated and theoretical values of the source position in the Y-axis.

Source position calculations on the Z-axis revealed a 0.3 mm average deviation from the theoretical value along the whole 7 cm path in the Z direction.

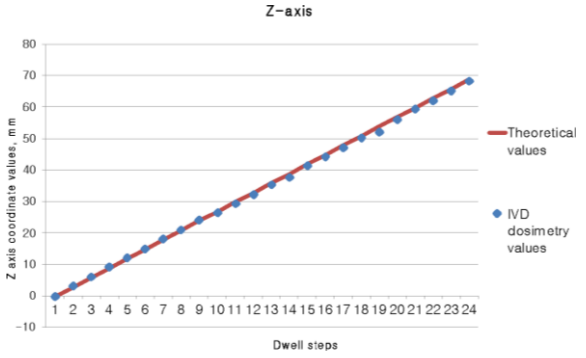

Fig.8. Comparison of calculated and theoretical values of the source position in the Z-axis.

The last step was to evaluate the accuracy of dose registration. The known distance was subtracted from the measured distance to calculate the error. Using the inverse square law formula, the sum of total error from all dosimeters in all X, Y, and Z directions was calculated, resulting in an overall dose error of 4 % in our system when the source distance from the dosimeters is 2 cm. It is essential to understand that dose calculations are directly related to the position calculations derived from the inverse square law formula. Consequently, dose accuracy in these calculations depends on the distance between the source and the detector. Specifically, the smaller the distance from the source to the detector is, the more significant error in the dose calculation will be due to positional error (see Fig. 9). This happens due to detector oversaturation when the intensity reaches maximum values, which no longer allows for accurate position detection.

Obtained results show that our dosimetry system operating in real-time mode can track and calculate the position of a ^{192}Ir source and consequently calculate dose during HDR brachytherapy procedures, potentially improving treatment precision and patient safety.

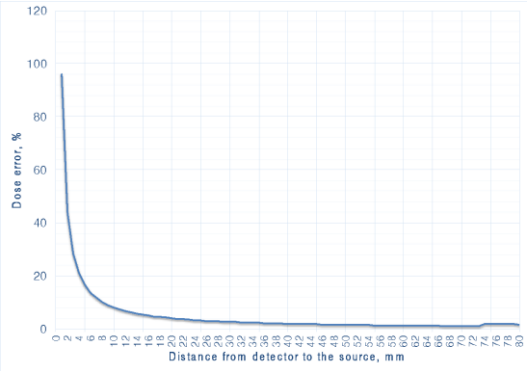

Fig. 9. Relation between distance from the source to detector and dose error percentage.

4. Conclusions

This study revealed the development and validation of a real-time IVD system for HDR-BT. This novel approach addresses several limitations observed in existing methods and offers a more comprehensive picture of dose distribution during the HDR-BT procedure.

Our system has demonstrated its ability to track and calculate the position of the ^{192}Ir source accurately. Specifically, it achieved an average deviation of 0.11 mm in the X-axis, 0.42 mm in the Y-axis, and 0.3 mm from the theoretical value for the Z-axis. These results highlight the system's capability to track source position across all three axes.

Using the inverse square law and positional calculations to determine the dose led to a 4% error in the setup presented. This underscores the need for further refinement to enhance the accuracy of the IVD system in question.

Notably, the precision of these calculations could be improved, including the radial and anisotropy functions for the source shape. Additionally, Hounsfield Units (HU) from obtained patient anatomy images should be considered in distance and dose calculations to ensure even more precise results.

Such a comprehensive approach will significantly reduce human-based errors in HDR brachytherapy treatments and subsequently result in enhanced patient safety and treatment outcomes.

References

1. Major, T., Fröhlich, G., Ágoston, P., Polgár, C. and Takácsi-Nagy, Z. The value of brachytherapy in the age of advanced external beam radiotherapy: a review of the literature in terms of dosimetry. Strahlenther. Onkol., 198, 2022, p.93–109.

2. Romano, K. D., Hill, C., Trifiletti, D. M., Peach, M. S., Horton, B. J., Shah, N., Campbell, D., Libby, B., and Showalter, T. N. High dose-rate tandem and ovoid brachytherapy in cervical cancer: dosimetric predictors of adverse events. Radiat. Oncol., 13(1), 2018, p. 129.

3. Roussakis Y., Anagnostopoulos G., Physical and Dosimetric Aspects of the Iridium-Knife. Front. Oncol., 11, Article Nº 728452.

4. ICRP. Prevention of High-dose-rate Brachytherapy Accidents. ICRP Publication 97. Ann. ICRP 35 (2), 2005.

5. Hassoun, A.H., Bahadur, Y.A., Constantinescu, C., El Sayed, M.E., Naseem H. and Naga A.F. In vivo diode dosimetry vs. computerized tomography and digitally reconstructed radiographs for critical organ dose calculation in high-dose-rate brachytherapy of cervical cancer. Brachytherapy, 10(6), 2011, p. 498-502.

6. Astuti, S.D., Listya, G.A., Fitriyah, N., and Suhartono B.H. Brachytherapy Treatment Planning and Linac for Dose Measurement of Bladder and Rectum in Cervical Cancer Patients. IEEE 2018 3rd International Seminar on Sensors, Instrumentation, Measurement and Metrology (ISSIMM), 2018, p. 7–10.

7. Tanderup, K., Beddar, S., Andersen, C. E., Kertzscher, G., and Cygler, J. E. In vivo dosimetry in brachytherapy. Medical Physics, 40(7), 2013.

8. Poder, J., Rivard, M.J., Howie, A., Carlsson T., Å., and Haworth, A. Risk and Quality in Brachytherapy from a Technical Perspective. Clinical Oncology, 35(8), 2023, 541-547.

9. Leman J. In vivo dosimetry; essential or unnecessary? Journal of Radiotherapy in Practice, 11(1),2012, p. 55-61.

10. Liu L., Prasad S.C., Bassano D.A., Heavern J., Keshler B., and Hahn S.S. Dwell position verification method for high dose rate brachytherapy. Journal of Applied Clinical Medical Physics, 5(1), 2004, p. 50-57.

11. Poder J., Howie A., Cutajar D., Bucci J., Guatelli S., Rosenfeld A., and Petasecca M. HDR brachytherapy in vivo source position verification using a 2D diode array: A Monte Carlo study. Journal of Applied Clinical Medical Physics, 19(4), 2018, p. 163-172.

12. Romanyukha A., Carrara M., Mazzeo D., Tenconi C., Al-Salmani T., Poder J., Cutajar D., Fuduli I., Petasecca M., Bucci J., Cerrotta A., Pappalardi B., Piccolo F., Pignoli E., and Rosenfeld A. An innovative gynecological HDR brachytherapy applicator system for treatment delivery and real-time verification. Phys. Med., 59, 2019, p. 151-157.

13. Hanlon M.D., Smith R.L., and Franich R.D. MaxiCalc: A tool for online dosimetric evaluation of source-tracking based treatment verification in HDR brachytherapy, Physica Medica, 94, 2022, p. 58-64.

14. Rokni, M. Brachytherapy Dosimetry: Working towards in-vivo and end-to-end diametric checks in modern HDR brachytherapy. Master's thesis, Duke University, 2018.

MEDICAL PHYSICS IN THE BALTIC STATES 16 (2023)

Proceedings of International Conference "Medical Physics 2023"
09-11 November 2023, Kaunas, Lithuania

FIRST EXPERIENCE ON VARIAN TRUEBEAM GENERATED ULTRA-HIGH DOSE RATE ELECTRON BEAM DOSIMETRY USING CONVENTIONAL DOSIMETRY METHODS

Akvilė ŠLĖKTAITĖ-KIŠONĖ[1], Marius BURKANAS[1], Aleksandras CICINAS[1], Tomas ČEPONIS[2], Mindaugas DŽIUGELIS[1], Mantvydas MERKIS[3], Diana ADLIENĖ[3], Jonas VENIUS[1,4]
[1]National Cancer Institute, Medical Physics Department, Vilnius, Lithuania, [2]Institute of Photonics and Nanotechnology, Vilnius University, Vilnius, Lithuania, [3]Kaunas University of Technology, Kaunas, Lithuania, [4]National Cancer Institute, Biomedical Physics laboratory, LT-08406, Vilnius, Lithuania.

***Abstract*:** Recently, a new radiation treatment approach has been proposed using ultra-high dose rate radiation. Thus far it shows promising results by causing less damage to healthy tissue while maintaining sufficient tumor control.
The purpose of this study was to produce ultra-high dose rate electron beams using a clinical linear accelerator and to characterize them using different dosimetry techniques. Simple geometry modifications and automatic beam control were utilized to achieve the required dose rate. Dosimetry of the electron beam was performed using an ionization chamber, gafchromic films, alanine, and gel dosimetry.

Keywords: Ultra-high dose rate, FLASH effect, FLASH radiotherapy, Dosimetry, Ionizing radiation.

1. Introduction

The field of radiotherapy has experienced a lack of significant development for several decades with only minimal technological progress. However, with the rediscovery of the ultra-high dose rate (UHDR) radiation effect on biological tissue (named FLASH effect), it became possible to reduce toxic effects on healthy tissues and still achieve adequate tumor control.
Since the first publication by Horsney et al. in 1966 [1] and the rediscovery of the idea by Favaudon et al. in 2014 [2], it has been shown many times that the FLASH effect helps with sparing organs at risk (OARs), including lungs, brain, gastrointestinal tract, skin and other, while maintaining sufficient tumor control [3].
Besides its radiobiological effectiveness, UHDR radiation in clinical practice can involve other advantages as well. It would allow shorter treatment times and reduce the possible intra-fraction motions of the patient during the radiation treatment, thus resulting in more precise treatment delivery [4]. Additionally, a single treatment unit could treat more patients per day.
Even though the FLASH effect has already been established, and there are a few ongoing clinical trials at the moment [5, 6], there is still a lot of uncertainty about its radiobiological mechanisms. Numerous theories are being discussed in the scientific community, ranging from radiolytic oxygen consumption, and radical-radical recombination to differential activation of metabolic and detoxification pathways between normal and tumor cells [3]. Multiple mechanisms likely contribute to the differentiated tissue response to conventional radiotherapy and FLASH, and further detailed research is needed. Also, there is no agreement on specific beam properties required to trigger the FLASH effect. Factors like average dose rate, dose per pulse, pulse count, and dose delivery time are potential contributors [7].
In order to achieve FLASH effect, at least 40 Gy/s dose rate is necessary [2], and current clinical equipment is not designed to achieve such high dose rates, so the main limitation in this research area is the lack of accessible experimentation platforms. In the present day, only a few dedicated UHDR radiation units are available for experimentation [8, 9]. Meanwhile, it has been demonstrated that a clinical linear accelerator (LINAC) can produce UHDR radiation with only a few modifications [10-12].
The aim of this study was to demonstrate the technique allowing to produce electron UHDR for experimental purposes using LINAC. Due to its easy set-up, this system can be configured and dismantled quickly without disrupting normal clinical operations.

2. Materials and methods

2.1. LINAC enabled ultra-high dose rate radiation

The UHDR radiation capability of a clinical LINAC was explored using a Varian TrueBeam (Varian Medical Systems, Palo Alto, USA). In order to deliver high-fluence electron beams, a monitor chamber, flattening filter, and target were retracted from the beam's path and

a 6 MV photon beam was selected in the treatment console. All experiments were performed in a non-clinical mode. The modifications took about 20 minutes to complete and were similar to those described by Rahman et al. [12]. This process could be significantly faster when the LINAC's geometry is adapted to support UHDR.

For dose calibration, four locations at the beam isocenter were assessed for irradiation: 100 cm, 75 cm, 58.7 cm, and 35 cm from the beam source (Fig. 1).

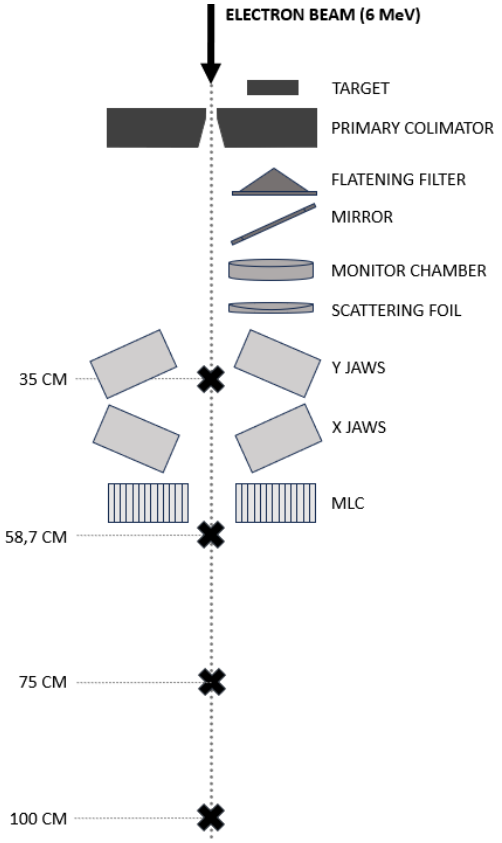

Fig. 1. Modified geometry of the linear accelerator for UHDR generation with indicated dose measurement locations.

Radiation beams were stopped following a single pulse, with dose control achieved by pulse counting and radiation termination. The smallest dose administered was equivalent to a single pulse.

2.2. Dosimetry

For dosimetry measurements, Advanced Markus Chamber (PTW-Freiburg GmbH, Freiburg, Germany), Gafchromic EBT3 films (Ashland Advanced Materials, Bridgewater, NJ, United States), Alanine Pellet Dosimeters (Bruker Biospin, Billerica, MA, United States) and Gel Dosimetry was used.

Advanced Markus Chamber is a typical dosimeter for electron beam characterization. As stated by the manufacturer, it accurately measures doses up to 5 mGy/s, but according the literature sources [13], implementing certain corrections allows for relatively accurate measurement of doses up to 10 Gy/s per impulse.

The choice of Gafchromic films for dosimetry was based on their resistance to dose-rate variations and common use for quantifying therapeutic doses in radiotherapy.

Alanine Pellet Dosimeter is an alternative chemical dosimeter that exhibits insensitivity to dose rate and the ability to detect high doses.

Polymer gel dosimetry is an attractive dosimetric technique due to its spatial resolution, and tissue-equivalency in terms of ionizing radiation absorption and ability to utilize medical imaging techniques for the acquisition of volumetric dose distribution information [14]. Various polymer gel dosimeter formulations exist with different levels of sensitivity, spatial integrity, toxicity, energy, and dose rate dependence.

Three distinct polymer gels were fabricated in the following study. NIBMAGAT dose gel with acetone co-solvent was fabricated according to the procedure described by Basfar et al. [15]. Methacrylic acid-based nMAG dosimetric gel was prepared according to the procedure described by [16].

3. Results

Initially, all prepared dosimetry systems were exposed to a single 3,6 µs radiation pulse, altering the distance from the source. Instantaneous readings were collected via the Markus chamber. In parallel, visual estimation of Gafchromic film strips was performed. Markus chamber measurements yielded dose values of 1.25 Gy, 1.98 Gy, 3.76 Gy, and 9.62 Gy, respectively (Table 1). Concurrently, the Gafchromic film strips exhibited the expected trend of increased darkening with the increased dose at the shortened distance to the source (Fig.2).

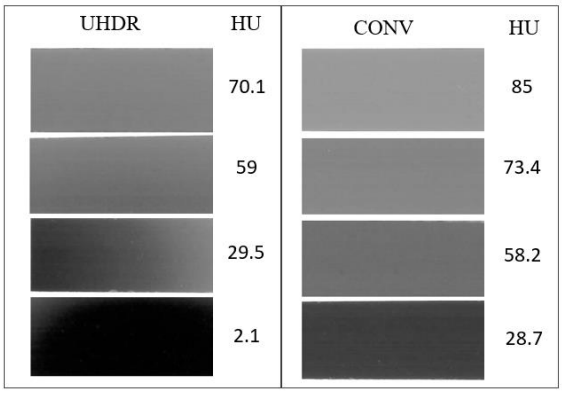

Fig. 2. Gafchromic dosimetry strips and their Hounsfield Units (HU) after irradiation with UHDR and CONV at measured doses.

To validate our findings, we exposed the new Gafchromic film strips to equivalent doses at a low dose rate (CONV). It was immediately apparent that visual distinctions could be made, as the gradient of discoloration in CONV irradiation was less pronounced compared to FLASH. While accepting that Gafchromic film is primarily sensitive to absolute absorbed dose rather than dose rate, we concluded that the initial measurement results obtained using Markus Advanced Chamber were inaccurate. Despite this, the experimental data obtained from the Markus chamber measurements exhibited agreement with the theoretical calculations

derived from the spherical quadratic model (Table 1, second row).

Table 1. Measured and theoretically calculated doses at different distances from the source

Distance, cm	100	75	58.7	35
Markus chamber (not corrected), Gy	1.56	2.48	4.70	12.03
Theoretical R², Gy (Markus)	1.56	2.77	4.53	12.73
Alanine, Gy	3.1	6.3	15.2	48.8
Theoretical R², Gy (Alanine)	3.1	5.51	9	25.3
Instantaneous dose 10^6 Gy/s	0.86	1.75	4.22	13.6
Average dose rate Gy/s	9.69	19.67	47.42	152.53

Subsequently, upon receiving the Alanine dosimetry results conducted at Vilnius University, a significant discrepancy between the Markus Chamber and the Alanine Dosimeter results was observed (Table 1). Significant differences ranging from 200% to 400% were observed at a dose maximum (Fig. 3).

Alanine-based dosimetry is generally considered to provide accurate results while remaining unaffected by changes in the dose rate [17]. Meanwhile, it is known that Marcus Chamber at higher dose rates tends to show incorrect results due to ion recombination [13].

The findings from Alanine dosimeters led to the suggestion, that the clinical LINAC has the capability to produce an approximate 50 Gy dose within one single pulse. This dose level corresponds to an approximate average dose rate of ~150 Gy/s, greatly exceeding the FLASH effect threshold of 40 Gy/s and it also results in an instantaneous dose of 13 × 10^6 Gy/s (Table 1). Theoretically, at the highest possible dose rate it would be possible to achieve average dose rate ~70kGy/s. In the literature, it has been argued that not the average dose rate value but rather the instantaneous dose rate and length of the impulse are the most important parameters for the FLASH effect to arise [7].

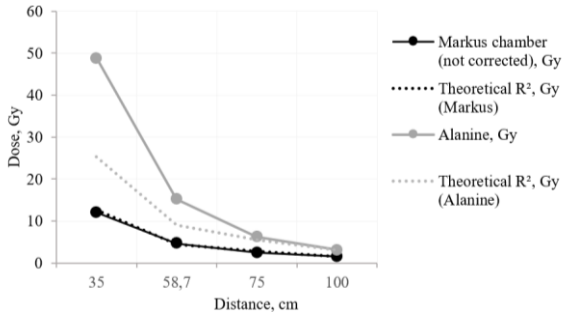

Fig. 3. Measured and theoretically calculated doses at different distances from the source.

In the context of this study, polymer gel dosimeters were irradiated at the conventional dose rate (CONV) to the same doses originally registered by the Markus Chamber. Dose-response curves were acquired from CT scanning data by averaging HU values in rectangle-shaped ROI. It was not possible to evaluate meaningful differences between irradiation doses in gel dosimeters presumably due to the low sensitivity of the CT imaging technique (Fig. 4). However it was seen, that high dose rate irradiation induced polymerization process in NIBMA gel dosimeter was more effective. The dose-response of NIBMA dose gel under UHDR conditions could be approximated using a linear relationship with $R^2 = 0.82$. A much better linear fit $R^2 = 0.97$ could be achieved by removing the last dose response point, indicating the tendency of saturation at higher irradiation doses. Other studies reported that the NIBMA gel dosimeter is not dose rate dependent, however, the investigated dose rate (200-600 cGy/min) interval was comparatively low [18].

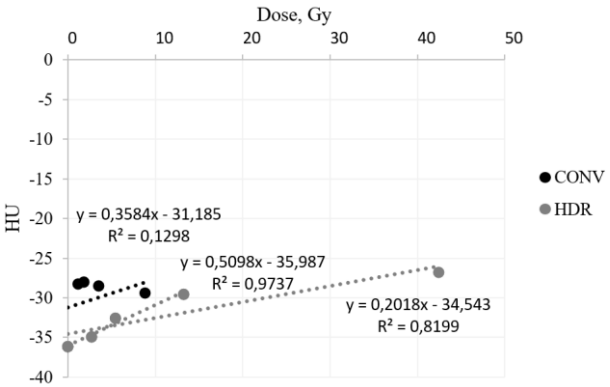

Fig. 4. Dose response curves of NIBMA dose gel under different dose rate irradiation conditions.

Contrary results were acquired from dose response curves of nMAG dosimetric gel (Fig. 5). According to linearly approximated dose-response curves, LDR irradiation allowed to achieve better dosimetric sensitivity of 1.02 Gy^{-1} compared to HDR irradiation (0.23 Gy^{-1}). However, R^2 of linear fit was comparatively low in both irradiation cases equaling 0.73 for HDR irradiation and 0.42 for LDR irradiation. Thus, the dose response of the nMAG dose gel tends to saturate at higher doses. Zhu et al. also reported a significant saturation, especially at higher doses of methacrylic acid-based dose MAGAT-f dose gel [19]. When the high dose point was removed, samples had more linear dose-response – R^2=0.97 for HDR samples and R^2=0.76 for LDR samples. In such cases, calculated sensitivities are also higher for LDR irradiation (3.51 Gy^{-1}) compared to HDR irradiation (0.68 Gy^{-1}). Acquired results with nMAG dosimetric gel agree with other authors' data. Sathiyaraj et al. reported a significant decrease in the sensitivity of methacrylic acid-based dose gel with increasing irradiation dose rate.

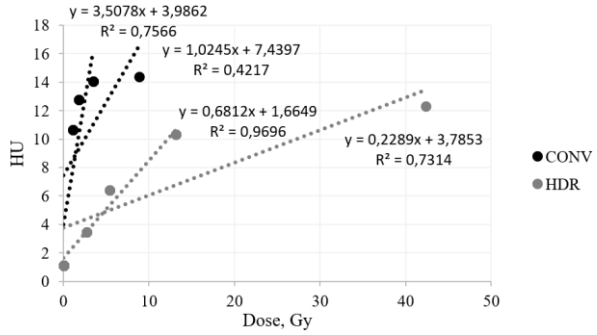

Fig. 5. Dose response curves of nMAG dose gel under different dose rate irradiation conditions.

4. Conclusions

This study presents the first successful reversible conversion of clinical LINAC to UHDR delivery system within the Baltic States. Our team successfully obtained a 6 MeV UHDR electron beam and characterized it using different dosimetry techniques. Such investigations allow bringing UHDR technology closer to the scientists working in a clinical setting, enabling their participation in expanding knowledge in the field.

References

1. J. Hornsey S., & T. Alper. (1966). Unexpected dose-rate effect in the killing of mice by radiation. Nature, 210, 212-213.
2. V. Favaudon, L. Caplier, V. Monceau, F. Pouzoulet, M. Sayarath, C. Fouillade, M. F. Poupon, I. Brito, P. Hupé, J. Bourhis, J. Hall, J. J. Fontaine, & M. C. Vozenin. (2014). Ultrahigh dose-rate FLASH irradiation increases the differential response between normal and tumor tissue in mice. Science Translational Medicine, 6(245), 245.
3. Charles L. Limoli and Marie-Catherine Vozenin. (2023). Reinventing Radiobiology in the Light of FLASH Radiotherapy. Annual Reviews. Published 2023. Accessed October 4, 2023.
4. D. Mah, G. M. Freedman, B. Milestone, A. L. Hanlon, E. Palacio, T. Richardson, B. Movsas, R. Mitra, E. M. Horwitz, & G. E. Hanks. (2002). Measurement of Intrafractional Prostate Motion Using Magnetic Resonance Imaging. International Journal of Radiation Oncology Biology Physics, 54(2), 568–575.
5. A. E. Mascia, E. C. Daugherty, Y. Zhang, et al. (2023). Proton FLASH Radiotherapy for the Treatment of Symptomatic Bone Metastases: The FAST-01 Nonrandomized Trial. JAMA Oncology, 9(1), 62–69.
6. Irradiation of Melanoma in a Pulse (IMPulse). Identifier NCT04986696. National Library of Medicine, 2021-2024. Retrieved from https://clinicaltrials.gov/study/NCT04986696?intr=FLASH%20Radiotherapy,%20&rank=4 (accessed 2023-10-05)
7. M. C. Vozenin, P. Montay-Gruel, C. Limoli, & J. F. Germond. (2020). All irradiations that are ultra-high dose rate may not be FLASH: the critical importance of beam parameter characterization and in vivo validation of the FLASH effect. Radiation Research, 194, 571-578.
8. M. Jaccard, M. T. Durán, K. Petersson, F. Germond, P. Liger, C. Vozenin, J. Bourhis, F. Bochud, & C. Bailat. (2018). High dose-per-pulse electron beam dosimetry: Commissioning of the Oriatron eRT6 prototype linear accelerator for preclinical use. Medical Physics, 45(2), 863-874.
9. G. Felici, P. Barca, S. Barone, E. Bortoli, R. Borgheresi, S. De Stefano, M. Di Francesco, L. Grasso, S. Linsalata, D. 20. Marfisi, M. Pacitti, & F. Di Martino. (2020). Transforming an IORT Linac Into a FLASH Research Machine: Procedure and Dosimetric Characterization. Frontiers in Physics, 8, 569691.
10. E. Schüler, S. Trovati, G. King, F. Lartey, M. Rafat, M. Villegas, A. J. Praxel, B. W. Loo Jr, & P. G. Maxim. (2017). Experimental Platform for Ultra-high Dose Rate FLASH Irradiation of Small Animals Using a Clinical Linear Accelerator. International Journal of Radiation Oncology Biology Physics, 97(1), 195-203.
11. M. Lempart, B. Blad, G. Adrian, S. Bäck, T. Knöös, C. Ceberg, & K. Petersson. (2019). Modifying a clinical linear accelerator for delivery of ultra-high dose rate irradiation. Radiotherapy and Oncology, 139, 40-45.
12. M. Rahman, M. Ashraf, R. Zhang, P. Bruza, C. A. Dexter, L. H. Thompson, X. Cao, B. B. Williams, P. Jack Hoopes, B. W. Pogue, & D. J. Gladstone. (2021). Electron FLASH Delivery at Treatment Room Isocenter for Efficient Reversible Conversion of a Clinical LINAC. International Journal of Radiation Oncology Biology Physics, 110(3), 872–882.
13. K. B. Petersson, M. Jaccard, F. Germond, T. Buchillier, F. Bochud, J. Bourhis, C. Vozenin, & C. Bailat. (2017). High dose-per-pulse electron beam dosimetry - A model to correct for the ion recombination in the Advanced Markus ionization chamber. Medical Physics, 44(3).
14. C. Baldock, Y. De Deene, S. Doran, G. Ibbott, A. Jirasek, M. Lepage, K. B. McAuley, M. Oldham, & L. J. Schreiner. (2010). Polymer gel dosimetry. Physics in Medicine and Biology, 55(5), R1-63.
15. A. A. Basfar, Belal Moftah, Salah Lotfy, A. A. Al-Moussa, & Y. S. Soliman. (2019). Evaluations of N-(Isobutoxymethyl) acrylamide gel dosimeter by NMR technique for radiotherapy and uncertainty in dose measurements. Applied Radiation and Isotopes, 148, 240-245.
16. Chun Chao Chuang & J. M. Wu. (2018). Dose and slice thickness evaluation with nMAG gel dosimeters in computed tomography. Scientific Reports, 8(1).
17. A. Bourgouin, T. Häckel, M. Marinelli, R. Kranzer, A. Schüller, & R. Kapsch. (2022). Absorbed-dose-to-water measurement using alanine in ultra-high-pulse-dose-rate electron beams. Physics in Medicine and Biology, 67(20), 205011-205011.
18. Salah Lotfy, A. A. Basfar, Belal Moftah, & A. A. Al-Moussa. (2017). Comparative study of nuclear magnetic resonance and UV–visible spectroscopy dose-response of polymer gel based on N-(Isobutoxymethyl) acrylamide. Nuclear Instruments and Methods in Physics Research Section B: Beam Interactions with Materials and Atoms, 413, 42-50.
19. Zhu, L., Zhang, M., Xiang, X., & Wang, X. (2022). 3D Proton Bragg Peak Visualization and Spot Shape Measurement with Polymer Gel Dosimeters. Applied Sciences, 12(19), 9839-9839.

MEDICAL PHYSICS IN THE BALTIC STATES 16 (2023)

Proceedings of International Conference "Medical Physics 2023"
09-11 November 2023, Kaunas, Lithuania

RECEIVED DOSE TO ADJACENT ORGANS IN PROSTATE CANCER PATIENTS DUE TO ORGAN INTER-FRACTIONAL DISPLACEMENT

Elina STENCELE[1], Martins PIKSIS[2], Sandra STEPINA[2]
[1]Riga Technical University; [2]Liepāja Regional Hospital;
[1]elinastencele@gmail.com; [2]martins.piksis@gmail.com; [2]stepinna.sandra@gmail.com

***Abstract*:** The aim of this study is to research how the radiotherapy dose to adjacent organs in prostate cancer therapy depends on organ inter-fractional displacement. Comparing daily cone-beam computed tomography (CBCT) to planning computed tomography (CT), fractions with organ displacement were selected. In selected CBCTs bladder and rectum were recontoured, the treatment plan was recalculated using new organ contours. The total received dose of organ was obtained. A correlation between the distance of the organ shifting in PTV and their received dose was established.

Keywords: prostate cancer, bladder, rectum, received dose, organ inter-fractional displacement.

1. Background

Prostate cancer is the fourth most common type of cancer in the world and second most common for men [1]. Radiotherapy is one of prostate cancer treatment. Patients with prostate cancer mostly are treated with volumetric modulated arc therapy (VMAT) technique because it helps to minimise the dose given to the organs adjacent to target [2]. The received dose of organ depends on patient positioning, organ filling and their movement during inter-fraction motion.

If the organ position on CBCT is different than in CT, medical personnel must decide to approve or reject the positioning of patients for daily treatment sessions. There are no criteria for patient approval or rejection and the decision is subjective. However, if the patient is approved for a daily session, the dose received by the tumour and adjacent organs could be different from the intended dose. Approximately half of the pelvic region radiation cases experience adverse complications in the healthy organs adjacent to the target organ due to an overdose [3]. Depending on finding the relation between the dose received by organs adjacent to the target organ and their shifts during inter-fraction motions, the main criteria could be developed to facilitate decision-making.

The purpose of this study is to analyse the influence of organ inter-fractional displacement on the received dose for bladder and rectum in prostate cancer radiotherapy and to find a correlation between the distance of the organ shifting in PTV and their received dose.

2. Materials and methods

Ten prostate cancer patient cases were analysed in this study. All patients were planned, using volumetric modulated arc therapy (VMAT) technique with total prescribed dose to prostate from 68.0 to 70.0 Gy by 2.0 Gy per fraction.

The patients' preparation before treatment planning CT and each fractional treatment patients were required to be done – within 15 minutes patients had to drink 800 ml of water and then wait 40 min.

Treatment plan was optimised to reach dose constraints to rectum V40 Gy <35%, V65 Gy <17%, V75 Gy <10% and bladder V40 Gy <50%, V65 Gy <25% [11]. Treatment planning was performed on the treatment planning system (TPS) *Eclipse*. CT scanner *Discovery RT* was used to get images for treatment planning. Linear Accelerator *Varian TrueBeam 2.7* was used for daily CBCTs and dose delivery.

A total of 349 CBCT image datasets were investigated. Each CBCT was auto aligned to the CT image and position of the organ was compared in both images. If any changes in the bladder or rectum were registered in CBCTs, due to the change in volume, the organ re-contouring was done. An example for the bladder and rectum position difference between CT image and CBCT image contours is shown in three views – in the transverse plane (Fig.1(a)), in the sagittal plane (Fig.1(b)) and in the coronal plane (Fig.1(c)).

All re-contouring was done manually by the same personnel. For contouring was used contouring tool "Brush" of the planning system was used in adaptive and static mode. It is known that in adaptive mode, the diameter of the brush changes to adjust to grey values of the image in which contouring starts. In static mode, the brush does not adjust to the values of grey tone, and the diameter of brush does not change when marking the area. For rectum contouring only static mode was used, because several adjacent structures have similar gradients that the tool cannot distinguish.

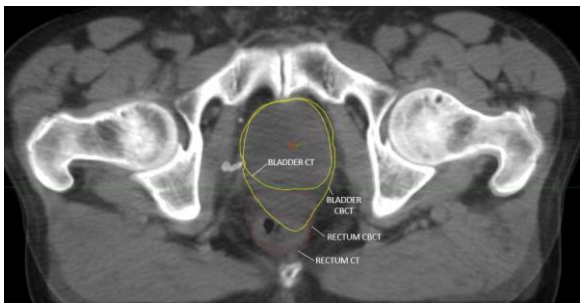

Fig. 1(a). Organ placement difference in transverse plane

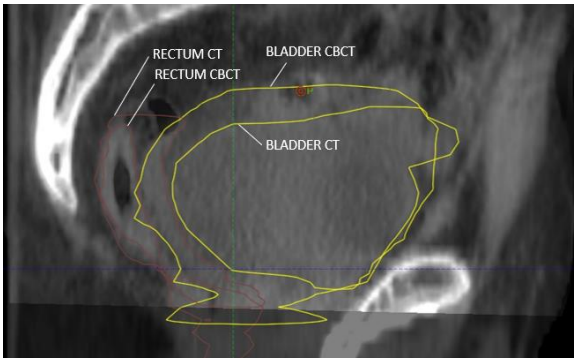

Fig. 1(b). Organ placement difference in sagittal plane

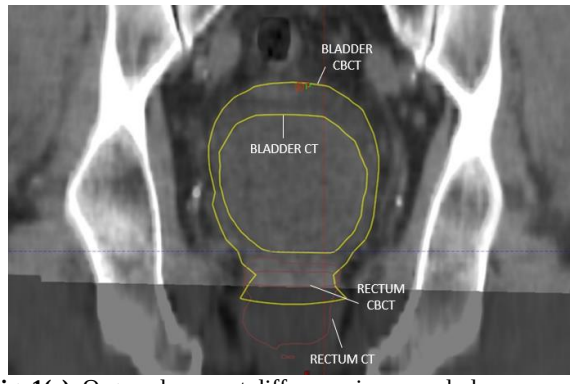

Fig. 1(c). Organ placement difference in coronal plane

The maximal distance of rectum and bladder movement in PTV was measured by comparing CBCT and CT images and using the measuring tool of the system. Depending on the organ placement in the CT image, there are two methods for measuring distance of the organ movement in PTV: 1) if the organ contour in the CT image is outside the contour of the PTV, the maximum distance of organ shift toward high dose region should be measured, starting measurement from the contour of the PTV to the contour of the organ in the CBCT image; 2) if the organ contour in the CT image is inside the PTV structure (Figure 2), the maximum distance of organ shift into the PTV is measured, starting from the organ contour of the CT image to the organ contour in the CBCT image. Distances were grouped in the intervals of 2.5 mm: [0.5-3.0), [3.0-5.5), [5.5-8.0), etc. After the dose recalculation the mean received dose in each interval was calculated. By compiling these data, the relation between organ inter-fractional displacement and their received dose was found.

New organ contours from re-contouring were transferred to CT image and received dose of organ was recalculated using the same treatment plan as originally.

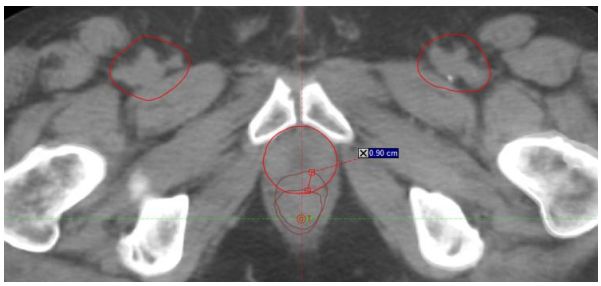

Fig. 2. Example of distance measurement of the organ movement in PTV

To calculate difference D_{change} of received dose for bladder and rectum, calculated received dose by the system in CT image was subtracted from received dose of organ according to organ contours in CBCT:

$$D_{change} = D_{CBCT} - D_{CT} \quad (1)$$

Total planned dose was calculated proportionally summing planned dose in each treatment stage:

$$D_{plan} = D_{plan(1)} + D_{plan(2)} + D_{plan(3)} \quad (2)$$

where $D_{plan(x)}$ – the total planned dose in stage x.

Afterwards dose differences D_{change} from all fractions were summed together and added to total planned dose for bladder and rectum (3). As a result, total received dose D_{total} for bladder and rectum was calculated:

$$D_{total} = D_{plan} + \Sigma D_{change} \quad (3)$$

To analyse total received dose of organ, it was compared to dose – volume criteria (D100 < 65 Gy for bladder [4] and V50 < 50% for rectum [5]) and the ratio of ΣD_{change} to the planned dose D_{plan} was calculated by equation (4). The ratio shows how many percent the dose that organ received has increased or decreased:

$$D_{ratio} = \frac{\Sigma D_{change}}{D_{plan}} \cdot 100 \quad (4)$$

The analysis was performed to find relation between organ inter-fractional displacement and their received dose.

3. Results

Regarding the measurement results for each patient the volumes of bladder and rectum in CT image were observed differently. It is known that the volume value depends on manual organ contouring. To determine the uncertainty of the manual contouring, volume of the bladder contoured with the automatic contouring tool of the planning system was compared to the bladder volume in the CT image and the relative error was calculated. The calculations gave an organ volume uncertainty equal to 3.2 %.

Variation of the bladder and rectum volume for all the patients could be monitored in Figure 3. Bladder volume was in the range from (51.60 ± 1.65) cm^3 to (476.40 ± 15.20) cm^3, while rectum volume was in the range from (50.00 ± 1.60) cm^3 to (106.00 ± 3.38) cm^3.

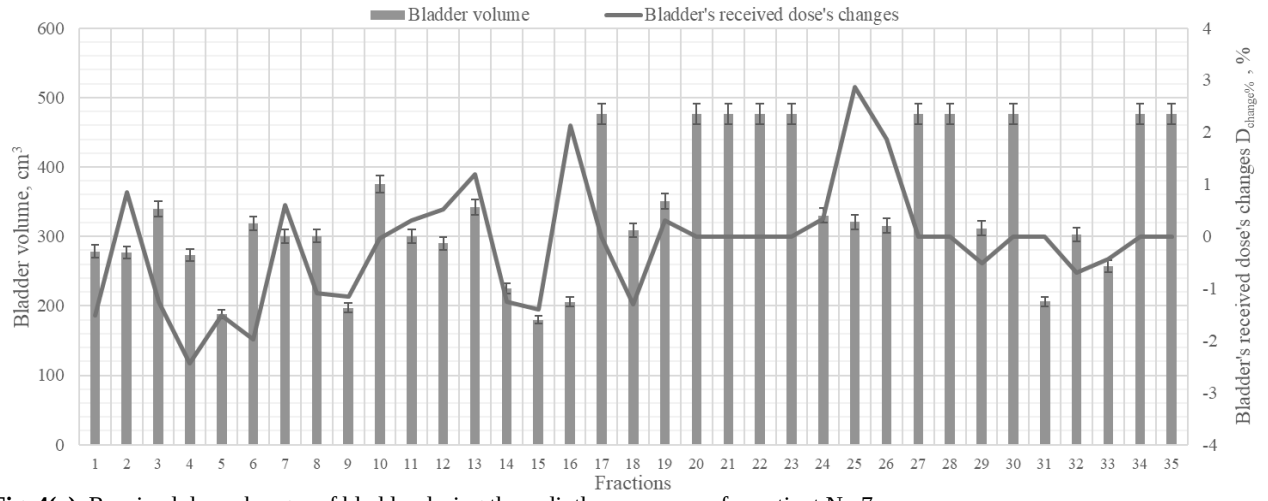

Fig. 4(a). Received dose changes of bladder during the radiotherapy course for patient No.7

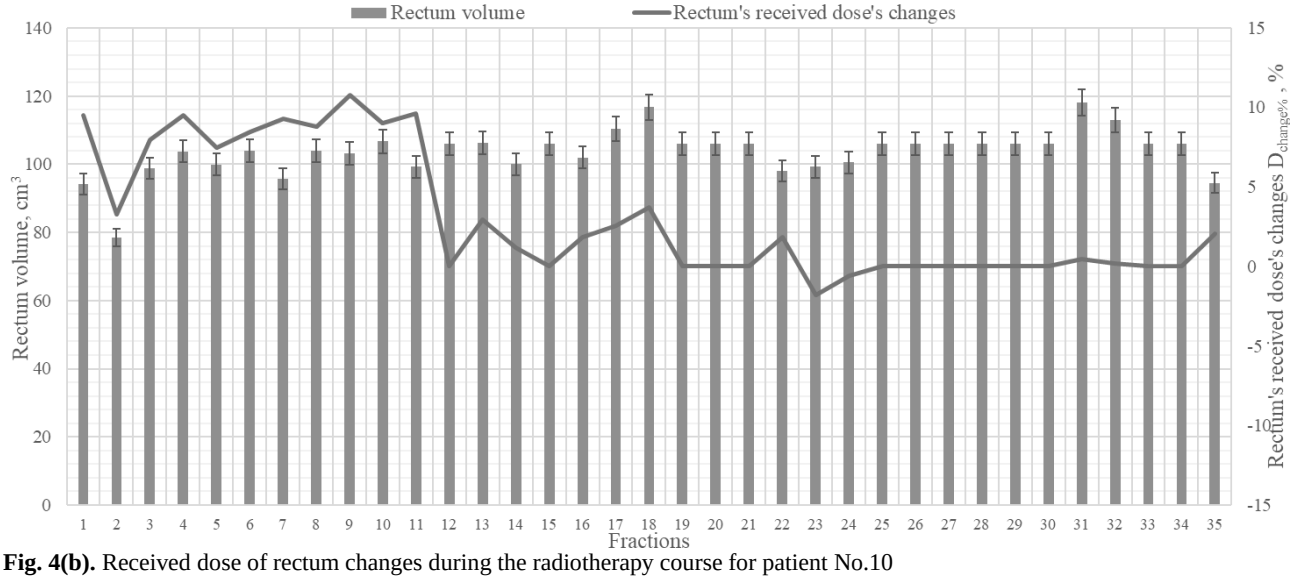

Fig. 4(b). Received dose of rectum changes during the radiotherapy course for patient No.10

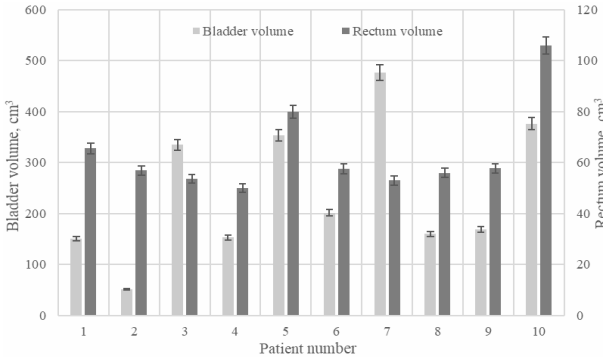

Fig. 3. Bladder and rectum volume in CT image

Bladder displacement was recorded in 152 of 349 CBCT images, while rectum displacement – in 119 CBCT images. Table 1 shows the number of fractions in which displacement of the bladder and rectum during inter-fraction motions was observed. As shown, the most organ displacement was observed at the beginning of Stage 1 and in Stage 3.

CT scan and treatment plan planning were required to be repeated for four cases because the patient data were not the same as on CT scans, and it resulted in a daily bladder and rectum displacement.

Table 1. Registered organ displacement by radiotherapy stages

	Stage 1	Stage 2	Stage 3	**Total**
Bladder displacement	118	9	25	**152**
Rectum displacement	86	13	20	**119**
Total fractions in stage	240	40	69	**349**

For two of these four cases CT scanning and re-planning were necessary to be repeated twice.

Figure 4(a) and (b) represent received dose changes during the radiotherapy course. The dose differences between the calculated received dose of the system in CT image and received dose of a certain organ according to CBCT real fraction contours from repeated contouring are shown in graphs. It was observed that the bladder displacement was registered for patient No.7 – in 25 of 35 days, while the patient No.10 had the most cases observed with rectum displacement (22 out of 35 fractions).

D_{change} was defined as the dose that the organ would receive during the radiotherapy course if the organ placement will be the same in all fractions. For bladder largest dose change D_{change} was recorded for the patient No. 6, when bladder (if irradiated in this position in all

fractions) received 8.92 Gy or 22.34% higher radiation dose than expected. In this fraction the bladder volume was decreased 1.9 times – bladder volume in CT was determined equal to 201.10 cm^3 and in CBCT 105.80 cm^3. Largest received dose change D_{change} for rectum was recorded for patient No.5. Due to this reason rectum received 5.28 Gy or 14.7% higher dose compared against the planned. Rectum volume in this CBCT is 127.20 cm^3, but in CT image 79.90 cm^3.

Analysing volume and dose of organs changes, a correlation was observed between the volume of the bladder and the decrease in the dose it received: when the volume of the bladder increased to 1.5 times, the dose it received decreased from 1.01 to 1.13 times compared to the planned dose. If the volume of the bladder increased from 1.5 to 2 times, the dose it received decreased from 1.01 to 1.06 times. If the bladder volume increases more than 2 times, then the dose it received dropped to 1.08 times. Also, there was found a correlation between the reduction in the volume of the bladder and the increase in the dose it received: if the bladder volume decreased to 1.5 times, the dose it received increased from 1.01 to 1.09 times. If the bladder volume decreased from 1.5 to 2 times, the dose it received increased to 1.22 times, but if the volume decreased more than 2 times, so the dose the bladder received may increase up to 1.26 times.

As the volume of the rectum increased to 1.5 times, the dose it received increased to 1.14 times, but as the volume increased from 1.5 to 2 times, the dose it received increased from 1.02 to 1.15 times. The volume reduction of the rectum did not exceed 1.5 times, in this case the dose of the rectum may decrease to 1d 10 times. Since the values range of dose increase and reduction was similar regardless of the organ volume change, was concluded that the dose change received by the organ was not dependent solely on the volume change, but on another factor, so a relation was also searched between the distance of the organ movement towards PTV and the change in the dose it received.

Before measuring organ penetration in PTV, CT and CBCT images, which were aligned in the planning system, eliminating the patient's positioning error. Not in all factions where organs have shifted, they have moved into the high-dose region. The bladder in the high dose region has moved in 119 of 152 fractions or 78.3% of cases, while the rectum has moved in 114 of 119 fractions or 95.8% of cases.

The total received dose of the bladder calculated using equation (3) is shown in Figure 5. In order to analyse the total received dose, for comparison a limit of total received dose constraint of bladder was marked in the graph (dotted line). The QUANTEC criterion for maximum dose for bladder is D100 < 65 Gy [4]. It means that the dose received by the bladder should be less than 65 Gy for its entire volume. Since the rectum does not have the maximum dose criterion, for the dose limit was used the volume – dose criterion with largest volume – V50 < 50% [5]. If the total received dose of rectum exceeds 50 Gy, it means that the entire volume of the organ has received an average dose of 50 Gy and the criterion has been breached because less than 50 % of rectum volume may receive this dose (Fig. 6).

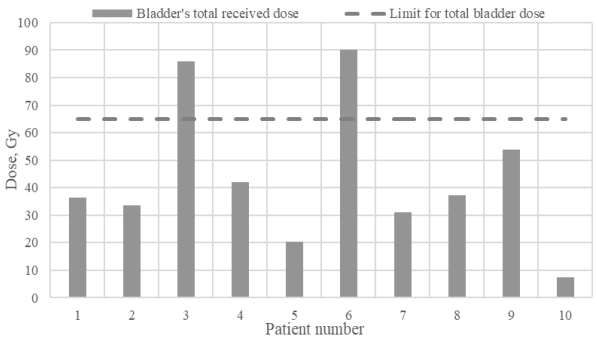

Fig. 5. The total received dose of the bladder

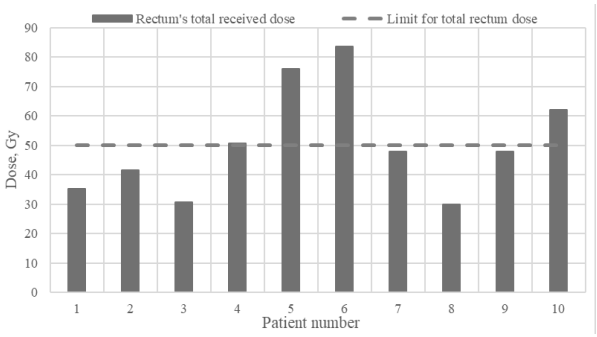

Fig. 6. The total received dose of the rectum

To assess how the received dose of organ has changed from the intended dose, a graph in Figure 7(a)+(b) is established to reflect the ratio D_{ratio} (calculations were done by (4)) of the received dose of organ to the planned dose.

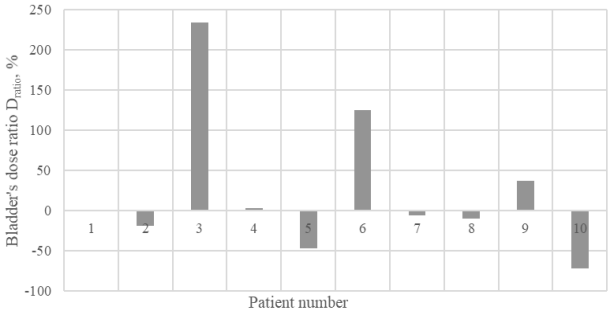

Fig. 7(a). Ratio of bladder's received dose to the planned dose

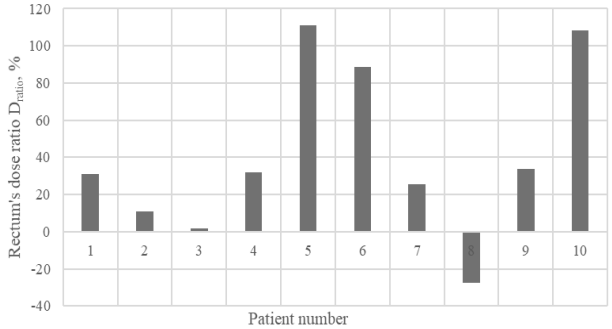

Fig. 7(b). Ratio of the received dose rectum to the planned dose

The total received dose for bladder (Fig. 5.) was increased for two patients (No. 3 and No. 6), and it exceeded the limit of 65 Gy. In other cases, the total dose received by the bladder was at least 15 Gy lower than the tolerable dose. As shown in Figure 7(a), for half of the cases the dose received by bladder was higher than planned (patients No. 1, 3, 4, 6 and 9) and for the other

half the received dose was lower than planned. In three cases, the ratio of received dose for bladder did not exceed 10 %. In two cases, the ratio of the change in the dose received by the bladder exceeded 100 %. In the same two cases, the total dose received by the bladder exceeded the tolerable dose.

The total received dose for rectum (Fig. 6) exceeded the permissible value for three patients (No. 5, 6, 10) and for three other patients the total dose was close to the tolerable limit (No. 4, 7, 9). The rectal dose ratio graph (Figure 7(b)) shows that in 90% of cases the rectal dose ratio was higher than planned. In three cases, the dose ratio of the rectum has been significantly increased, in two of these cases it exceeded 100 %. In the same three cases, the total dose received by the rectum exceeded the tolerable dose. In cases where the total dose received by the rectum was equal to or approaching the limit value, the dose ratio was between 25% and 35%.

Distance for movement of the bladder in PTV was in the range from 0.6 mm to 31.90 mm. The biggest movement of the bladder was in the interval of distances [3.0-5.5) mm. 21 movement cases were recorded in this interval. When penetration distance of the bladder in PTV exceeded 20.5 mm, less than 5 movements were observed in each interval and were therefore not considered in the analysis.

Distance for movement of the rectum in PTV differed from 0.7 mm to 19.6 mm. The biggest movement of the rectum was in the interval of distances [3.0-5.5) mm with 29 movements recorded in this interval.

Figure 8(a)-(b) shows relation between inter-fractional displacement distance and the received dose of the organ.

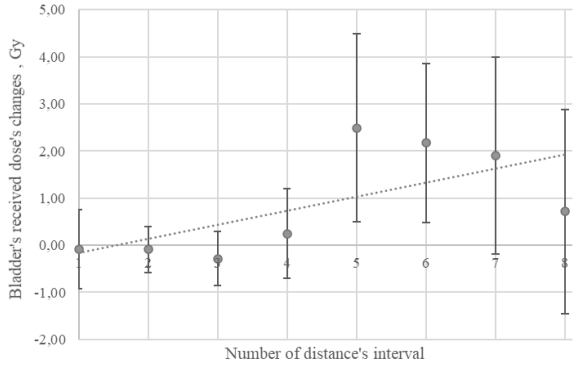

Fig. 8(a). Changes of the received dose for the bladder depending on movement distance in PTV

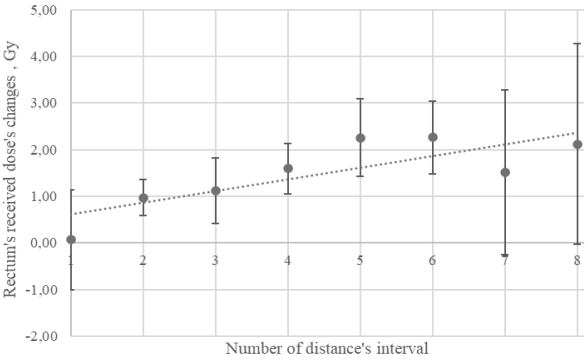

Fig. 8(b). Changes of the received dose for the rectum depending on movement distance in PTV

A linear relation with the general equation $y = ax + b$ may be observed between received dose changes both for bladder and rectum depending on movement distance in PTV. Equation that describes this relation for bladder is expressed as $D_{change} = 0.3x - 0.49$, whereas for rectum the relation between received dose changes of the organ depending on movement distance in PTV was expressed as $D_{change} = 0.2x + 0.35$. In both equations, x represents the number of distance intervals. It can be concluded from the equations that as the movement distance of the organ in PTV increases, the dose changes received by the bladder increases faster than the received dose changes for the rectum. However, it should be noted that changes in the dose received by the bladder have a higher range of uncertainties and the point of received dose in the distance range [10,5-13,0) mm was expressed outside the trendline, so the equation that describes relation between movement distance for the bladder in PTV and the change in the dose received by it could be inaccurate.

Planned average received dose for the bladder was equal to 36.33 Gy. To ensure that the total dose received by the bladder did not exceed the limit of 65 Gy, the change in the dose received by the bladder must be less than 28.67 Gy. During the radiotherapy course, bladder movement was observed in an average of 15 fractions. It follows that the change in the dose received per fraction must not exceed 1.89 Gy. From equation $D_{change} = 0.3x - 0.49$ was calculated that x=7.7. Thus, the critical movement distance of the bladder in PTV, when the medical personnel have to think about rejecting the patient from daily radiation, corresponds to the interval No. 7 and is [15.5-18.0) mm.

Planned average received dose of the rectum was registered as 35.81 Gy. In order not to exceed the limit of the chosen dose-volume criterion, which is 50 Gy, the change in the dose received by the rectum must be less than 14.19 Gy. Movement of the rectum was observed in an average of 12 fractions of all radiation course fractions, so the change in dose received in each fraction should be less than 1.18 Gy. According to the equation $D_{change} = 0.2x + 0.35$, x value was calculated (x = 3.3). This means that the critical movement of the distance for the rectum in PTV corresponds to the third distance interval of [5.5-8.0) mm.

4. Discussion

Previously it has been established that the dose received by organs in radiotherapy depends on patient positioning, location and size of organs. It is known that minimal effect on tumour placement is also provided by patient breathing [6]. Patient positioning inaccuracies can be corrected by the treatment table positioning [7]. Size, shape and position of the bladder and the rectum changes throughout the course of prostate radiotherapy, and it depends on pre-radiotherapy preparation – patients should empty the intestines and exclude gas-boosting foods from the diet. Approximately an hour before radiation, the patient should drink 600 ml to 800 ml of water, but it depends on the patient and the doctor's instructions [6, 8]. However, the correlation between bladder and rectum fill and prostate movement during inter-fraction motion was not observed. [7] With a

different placement from the CT image, organs received a different dose in comparison with a planned dose. In this study the biggest dose difference between planned and recalculated dose for the CBCT for bladder was 8.92 Gy or 22.34%, and for rectum it was 5.28 Gy or 14.7%.
Regarding CBCT imaging it is possible to verify the position of organs before radiation, so the accuracy of radiation therapy for target location and dose delivery. Could be improved [9] In this study the largest bladder and rectum inter-fractional displacement were registered at the end of the radiotherapy course – the last 7 fractions. This can be explained due to shrinking of the specific organ due to radiation. Studies have shown that this problem could be bypassed using injection of hydrogel spacer. The injection of spacer between the prostate and the rectum separates the prostate from the anterior wall of the rectum. In that way the area between the target organ and the adjacent healthy organs is large enough for the healthy organs to stay out of the PTV [10].
The total received dose of the organs also depends on the planned dose for each organ. In cases where the total dose received by the rectum is equal to or approaching the limit value, the dose ratio was between 25 % and 35 %. This interval also included the dose ratio for patient No.1, but in this case the limit of the total received dose was not exceeded. This is due to the value of the dose originally planned. In cases 4, 7 and 9, the initial scheduled dose for the rectum was greater than 35 Gy, respectively 38.37 Gy, 38.14 Gy and 35.84 Gy. But for patient No. 1 the rectum was planned and received a dose of 26.92 Gy. As the planned dose for patient No.1 was less, the dose increased by 31.02%, it did not exceed the permissible dose criterion.
In this study the equations to describe the relation between the movement distance of organs in PTV and the dose it was received were found for cases when the volume of the organ has also been changed. Equation that described the relation for bladder was $D_{change} = 0.3x - 0.49$, and for rectum – $D_{change} = 0.2\,x + 0.35$. However, to obtain a more precise equation, similar study would be needed to be repeated on the anthropomorphic phantom for the situation, where the organ movement distance in PTV was changed, but its volume remained constant.

5. Conclusions

Bladder and rectum inter-fractional displacement was mostly recorded in the first 12 and the last 7 fractions of radiotherapy. The total received dose for the bladder was in the range from 7.41 Gy to 90.02 Gy. The total received dose for the rectum differed from 58.02 Gy to 74.50 Gy. There was determined a linear correlation between movement distance of the organs in PTV and the dose it received.
It was found that as the volume of the bladder increases, the dose it receives decreases from 1.01 to 1.13 times compared to the planned dose. But if the bladder volume decreases, the received dose can increase up to 1.26 times. Volume of the bladder can increase and decrease more than 2 times compared with volume in CT image.
If the volume of the rectum increases, the dose it receives increases up to 1.15 times compared to the planned dose. If the rectum volume decreases, then the received dose for the rectum can decrease to 1.10 times. The rectum volume can increase more than 2 times, but the volume reduction of the rectum does not exceed 1.5 times.
Equations for the description of the relation between the movement distance of the organ in PTV and the dose it received were found. Recommendations for patient approval or rejection for daily radiation procedure were prepared on the basis of these equations. It is recommended to reject the daily radiation fraction,

- if the movement of the bladder in PTV is observed in more than 15 fractions and has a movement distance greater 18 mm;
- if the movement of the rectum in PTV is observed more than 12 times during the radiotherapy course and has movement distance greater than 8 mm.

Since, in reality, all organ movement in PTV distances do not fall within the same distance interval, the initial planned dose for the organ, the number of fractions with shifting and the movement distance of organ in PTV should be evaluated before approving or rejecting the daily radiation fraction. To obtain a more accurate equation, the study should be repeated on an anthropomorphic phantom with defined organ boundaries, which would reduce the uncertainty of manual organ contouring.
To obtain the expected results from radiotherapy, the patient must complete the prescribed treatment course and receive irradiation regularly. Before daily treatment sessions 1-2 CBCT were performed to verify organ placement. If organ placement was different than in CT and they received different doses than planned, complications may occur in organs adjacent to the prostate. For example, rectal wall crypt reduction and inflammatory-cell infiltration, bladder mucosal tear, bleeding, etc. If the patient often has significant organ shifting, it is necessary to work individually on the patient's preparation before radiotherapy. However, if this does not work and interferes with receiving daily radiation, it is possible to decide on a replanning the treatment plan.

References

1. Worldwide cancer data [online]. London: World Cancer Research Fund International, 2022 [viewed on 5th of May, 2023]. Available from: https://www.wcrf.org/cancer-trends/worldwide-cancer-data/
2. Samir, F., et al. Analytical dosimetric study of intensity-modulated radiotherapy (IMRT) and volumetric-modulated arc therapy (VMAT) for prostate cancer. Journal of Cancer Research and Clinical Oncology. 2023, 149, 6239-6246 p. Available from: doi: 10.1007/s00432-023-04586-5.
3. Dilalla, V. et al. Radiotherapy side effects: integrating a survivorship clinical lens to better serve patients. Current Oncology. 2020, 27 (2), 107-112 p. PMCID: PMC7253739. PMID: 32489253. Available from: doi: 10.3747/co.27.6233
4. Bisello, S., et al. Dose–Volume Constraints fOr oRganS At risk In Radiotherapy (CORSAIR): An "All-in-One" Multicenter – Multidisciplinary Practical Summary. Current Oncology. 2022, 29 (10), 7021-7050 p. PMCID: PMC9600677. PMID: 36290829. Available from: doi: 10.3390/curroncol29100552.
5. Li, G., et al. Guidelines for radiotherapy of prostate cancer (2020 edition). In: Precision Radiation Oncology. Volume 5

(3). China: Wiley, 2021, 119-218 p. ISSN: 2398-7324. e-ISSN: 2398-7324. Available from: doi: 10.1002/pro6.1129
6. Nejad-Davarani, S.P., et al. Geometric and dosimetric impact of anatomical changes for MR-only radiation therapy for the prostate. Journal of Applied Clinical Medical Physics. 2019, 20 (4), 10-17 p. Available from: doi: 10.1002/acm2.12551
7. Jmour, O., et al. CBCT evaluation of inter- and intra-fraction motions during prostate stereotactic body radiotherapy: a technical note. Radiation Oncology. 2020, 15 (85). Available from: doi: 10.1186/s13014-020-01534-2
8. Stillie, A.L., et al. Rectal filling at planning does not predict stability of the prostate gland during a course of radical radiotherapy if patients with large rectal filling are re-imaged. Journal of Clinical Oncology. 2009, 21 (10), 760-767 p. PMID: 19804961. Available from: doi: 10.1016/j.clon.2009.09.001.
9. Al-Kabkabi, A., et al. Assessment of cone beam computed tomography image quality and dose for commonly used pre-sets in external beam radiotherapy. Radiation Physics and Chemistry. 2022, 199, article: 110287. Available from: doi: 10.1016/j.radphyschem.2022.110287
10. Tang, Q., et al. The role of radioprotective spacers in clinical practice: a review. Quantitative Imaging in Medicine and Surgery. 2018, 8 (5), 514-524 p. PMID: 30050786. Available from: doi: 10.21037/qims.2018.06.06
11. Pollack, A., et al. Dosimetry and preliminary acute toxicity in the first 100 men treated for prostate cancer on a randomized hypofractionation dose escalation trial. Int J Radiat Oncol Biol Phys. 2006, 64(2), 518-526 p.

MEDICAL PHYSICS IN THE BALTIC STATES 16 (2023)

Proceedings of International Conference "Medical Physics 2023"
09 – 11 November 2023, Kaunas, Lithuania

INVESTIGATION OF THE ARCCHECK-3DVH SYSTEM IN COMPARISON WITH PORTAL AND GEL DOSIMETRY FOR VMAT DOSE VERIFICATION

Aurimas KRAULEIDIS[1,2], Dainius BURDULIS[2], Diana ADLIENĖ[1]
[1]Kaunas university of technology; [2]Klaipėda university hospital
[1]aurimas.krauleidis@ktu.edu; [1]diana.adliene@ktu.lt; [2]dainius.burdulis@gmail.com

***Abstract*:** The high complexity of the volumetric modulated arc therapy (VMAT) treatment involves simultaneous changes in gantry speed, multileaf collimator speed, and dose rate; it requires verification of the dose plans in order to check the concordance between the distribution of real dose delivered by the linear accelerator and the dose distribution calculated by treatment planning systems (TPS). Several methods are used for the VMAT patient-specific QA to assess the delivery accuracy.
The aim of this study was to assess compliance with the ArcCheck-3DVH system, portal dosimetry (PD), and radiosensitive polymer gel in the implementation of patient-specific quality assurance measures in VMAT.

***Keywords*:** VMAT, 3DVH, ArcCheck, Portal dosimetry, Gel dosimetry.

1. Introduction

Modern advanced radiation therapy is represented by intensity-modulated radiation therapy (IMRT), volumetric-modulated arc therapy (VMAT), or stereotactic radiotherapy (SRT). These techniques have become increasingly widely spread due to the fact that the improvement of the dose distribution is automatically established through an optimization process by controlling the dose constraint of the target volume utilizing capabilities of three-dimensional conformal radiotherapy (3DCRT). 3DCRT plan is created manually by specifying field parameters like number, direction, shape or weight of the fields, the angle, and the weight of the wedge. However, there are some difficulties in adjusting the minimum dose to the normal tissues close to the target volume and achieving the desired dose homogeneity and coverage, especially for the complex target volumes [1].
The fluence in VMAT treatment depends upon controlled and coordinated gantry rotation, dose rate, accurate multileaf collimator (MLC) positioning, and reproducibility of their movement [2]. In order to guarantee the safety of a patient and accurate delivery of the dose, verification of these parameters is necessary. Having this in mind, specific systems and detectors have been developed to record the absorbed dose distribution for the assessment of pretreatment quality.
Two-dimensional planar detectors, such as film, diode arrays, ion chamber arrays, and electronic portal imaging devices (EPID) are commonly used for QC checks [3]. Regardless of the detector's type, the quality assurance procedure involves a quantitative comparison of the planned phantom dose and measured dose. The differences between the planned and measured dose distributions are often evaluated using the *gamma* method which considers two parameters at each point of the distribution – the dose difference and the distance to agreement [4].
In the case of 3D dose distributions, multiple-dose plans should be analyzed to verify the accuracy of the dose delivery. Gel dosimeters can record the whole 3D dose distribution, but they require MR or CT readout to retrieve the dose values in a postprocessing procedure [5]. Polymer gel dosimeters are fabricated from radiation-sensitive monomers that tend to polymerize due to irradiation. Free radicals created in the irradiated gel during the radiolysis process are responsible for the initiation of polymerization. The amount of polymerization is a function of the absorbed dose. The polymerized part of the gel remains in the gelatine matrix, hence retaining a 3D spatial record of the delivered dose. Polymer gels are biological tissue equivalent and are suitable alternatives compared with conventional dosimeters since irradiated gels are able to resolve 3D dose distributions with high accuracy and precision. This makes dose gels unique and suitable for complex dose verification [6].
It should be noted that several verification devices could be used for 3D dose assessment: Octavius (PTW, Freiburg, Germany), Delta4 (ScandiDos, Uppsala, Sweden), or ArcCheck (Sun Nuclear, Melbourne, USA) [7,8]. For example, the Delta4 detector system uses two diode arrays embedded in a cross-plane manner in a cylindrical phantom and is capable of performing a time-resolved dose distribution analysis [9]. Time-dependent measurements can detect both delivery and planning

errors since delivery time correlates with the gantry angles during treatment.
Octavius system is aimed to perform beam-to-detector orthogonal measurements synchronously with the dose delivery to the rotating cylindrical phantom that contains an ion chamber array. A 3D dose distribution can be reconstructed based on the measured plane dose distribution for each gantry angle [10].
ArcCheck is a cylindrical diode array detector system with a time-resolved measurement capability. The system consists of 1386 diode detectors. Gantry angle, leaf-end position, absolute dose, and time are checked with the provided detectors and possible error sources are identified. Dose accuracy can be improved and errors can be traced to the treatment planning system, the delivery system, or the imaging system. ArcCheck orthogonal beam-to-detector configuration allows for measurement and analysis of entry and exit dose for every angle [12,13]. For each beam angle, ArcCheck measures high dose regions at the entrance and low dose regions at the exit, detecting potential delivery and TPS modeling errors for both high and low dose levels (Figure 1).

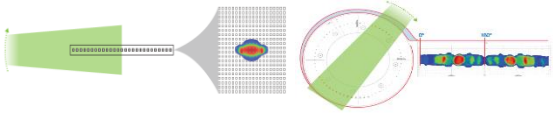

Fig.1. Difference between 2D array measurement and ArcCheck measurement

Several authors have studied the correspondence between measured dose distribution and distribution provided by treatment planning systems [14]. Other studies focussed on the physical characterization of the device, linearity, repeatability, and the angular dependence of the device response [15,16]. Several previous studies have discussed the application of ArcCheck for treatment plan verification with the VMAT technique, and the results showed high γ passing rates [17]. Some reports demonstrated the evaluation of the dose-volume histogram (DVH)-based metric for patient-specific QA [18]. The 3DVH software was developed to evaluate the dose distribution for each organ volume through a comparison of the DVHs to patient geometry by ArcCheck QA measurements. Few authors studied the 3DVH software correlation with the percentage dose difference (DD,%), the gamma pass rate, and the accuracy of this software [19,20].

2. Methods and materials

2.1 The ArcCheck dose verification system

In this work, the verification system ArcCheck (model 1220) has been used. It is a cylindrical water-equivalent phantom with a three-dimensional array consisting of 1386 diode detectors, arranged on a phantom according to a helical geometry (see Fig. 2) with 10 mm spacing. The diameter of the diode array is 21 cm. Each diode has a sensitive volume of 0.019 mm^3 and is situated at a water equivalent depth of 3.3 g/cm^2[12,21].
The central cavity of the device is cylindrical, having a diameter of 15 cm which permits to introduction of a PMMA insert in such a way that the density in the interior of the phantom can be considered as tissue equivalent [22]. The ArcCheck also has two inclinometers to measure the angle of rotation about the cylinder axis and to measure the tilt of the axis. A temperature sensor measures the ambient temperature of the detector area. Dose measurements from each sensor are updated every 50 ms and there is no time or dose limit for a measurement.

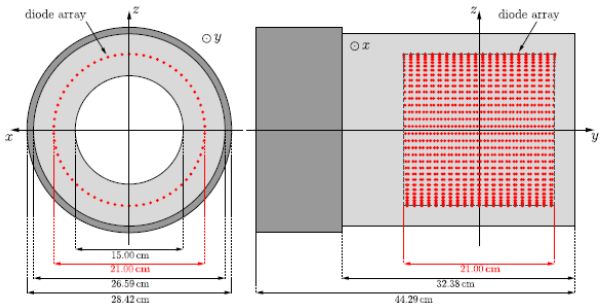

Fig.2. The geometry of the Arccheck device

2.2 Portal dosimetry system with EPID

The verification of VMAT plans was also performed with a light-sensitive (amorphous silicon) electronic portal imaging device (EPID) installed in the Truebeam linear accelerator (Varian, USA). The active detector area was 40 × 30 cm^2 (1024 × 768 pixels). The distance between the source and the imager was 100 cm. Images were acquired using the frame-averaging method with a 30 frames per second rate. EPID collected information was reconstructed into a two-dimensional dose distribution, which was compared with the dose distribution calculated by TPS by evaluating the γ passing rates of the plans [23].
Before plan verification, the EPID was calibrated to ensure that all measurement points had the same responsiveness, so as to remove the influence of background noise and bad pixels.

2.2 Gel dosimetry

The nMAG gel dosimeters were fabricated in a normal oxygen environment. The 8% gelatine (300 Bloom Type A, Sigma-Aldrich) was mixed with 84% deionized water and was continuously stirred on the hot plate using a magnetic stirrer at approximately 45˚C until the gel was completely dissolved and a clear solution was obtained. The solution was cooled down to 32˚C then the 8% methacrylic acid (MAA, 99%, Sigma-Aldrich) monomer was added and continuously stirred for the next 25 min until the monomer was completely dissolved. Tetrakis(hydroxymethyl) phosphonium chloride (THPC) was added to the gels as an oxygen scavenger. Synthesized gels were poured into plastic 100 ml containers, tightly closed, and stored in a cool and dark place for 48 hours for solidification.
Gels irradiation was performed in the Varian Truebeam linear accelerator. 6 MeV FFF beam energy was used with a maximum dose rate of 1400 MU/min. Gels were irradiated to 12 Gy dose using static and rotational 1cm^2 field. X-ray CT readouts were performed 48 hours after irradiation. The CT scanning parameters were as follows: tube voltage -140 kVp, tube current - 320 mAs, and slice thickness -1.5 mm.

2.3 Treatment planning and measurements

In this study, 40 VMAT plans were produced for head and neck (H&N), prostate, head, and lung cancer treatment areas. All plans were prepared using Eclipse 15.6 treatment planning system (TPS) for 6 MV or 10 MV photon beam treatment. The minimum 95% prescription dose to cover 95% of the volume of PTV, and the maximum target dose (D_{max}) < 110% of the prescription dose were achieved. The anisotropic analytical algorithm (AAA) was used for the calculation with the dose grid size set to 2.5 mm, and optimization was carried out by an algorithm that allows for optimization of the full arc in four phases with 178 control points. The number of full-length arcs used ranged from 1 to 3 and the maximum number of partial arcs was 4. Beam delivery was performed in TrueBeam linear accelerator with a dose rate of up to 600 MU/min. The created plans were exported from Eclipse and verified with the ArcCheck and EPID. The measured dose distribution was analyzed by using the SNC Patient application and 3DVH software.

3DVH software estimated the dose distribution and DVHs for a contoured structure with the ArcCheck using the dose perturbation (ACPDP) calculation algorithm (Fig. 3).

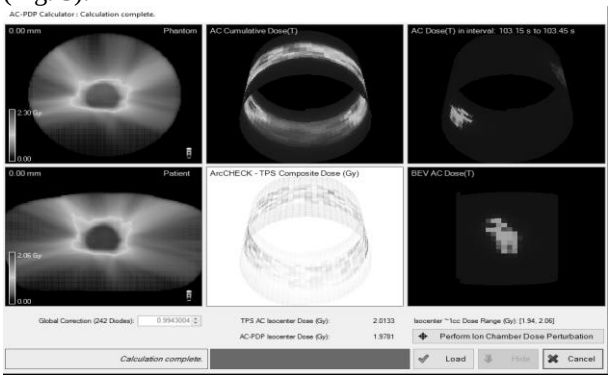

Fig. 3. Dose perturbation (ACPDP) calculation algorithm in 3DVH

The software requires the DICOM files of the patient (RT Plan, RT Dose, RT Structure, and planning CT images), an ArcCheck planned files to compare the dose difference between the ArcCheck measurement and the TPS calculation. The DVH of each structure was compared with the measured dose distribution [24].

The dose difference and distance to agreement (DTA) parameters were set to 3%/3 mm, 3%/2 mm, 2%/2 mm, and the threshold was 10%. The absolute dose combined with the gamma analysis method was used to obtain the γ passing rates between the calculations and measurements. The percentage dose difference (DD,%) was calculated for the planning target volume (PTV) and normal organs with 3DVH software. For each PTV, the mean dose (D_{mean}), and maximum dose (D_{max}), as well as the dose received by 2%, 95%, and 98% of the volume (D2%, D95%, and D98%) which were predicted by ACPDP, were compared with those obtained from the treatment planning system. Normal organs were evaluated according to the values of their D_{mean} and D_{max}. The DD,% is defined as follows:

$$DD,\% = (D_{3DVH}-D_{TPS})/D_{DTPS} \times 100 \quad (1)$$

D_{3DVH} represents the dose by 3DVH, whereas D_{TPS} represents the dose calculated by Eclipse TPS.

3. Results and discussion

Since ArcCheck phantom is an independent quality assurance tool the response of the diode detector to the gantry angle is adjusted using a virtual inclinometer algorithm. Fig.4a shows the verification results of VMAT plan with that obtained using the ArcCheck method and Fig.4b shows the verification results with the EPID method.

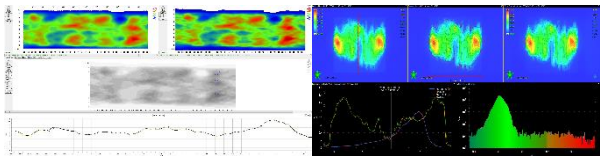

a b

Fig. 4. Dose verification for H&N VMAT plan with the Arccheck method (a) and with portal dosimetry method (b)

An example of a dose-volume histogram for the target and structures using the ArcCheck planned dose perturbation (ACPDP) algorithm and DVHs calculated with TPS for H&N cancer case is shown in Fig.5, where dotted lines represent DVHs using the ArcCheck ACPDP algorithm, and solid lines represent DVHs calculated with TPS.

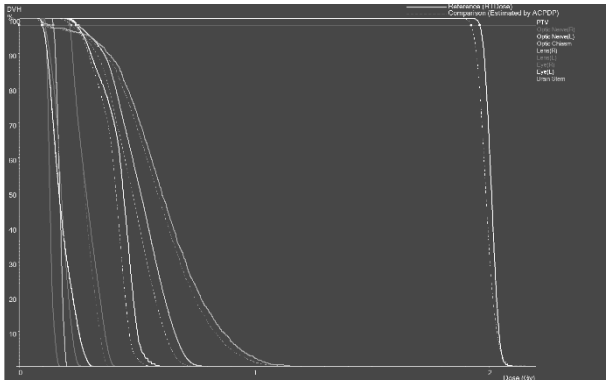

Fig. 5. Comparison of the dose-volume histograms for the target and structures.

The average γ passing rates and difference analysis results of the verification methods with different analysis criteria are shown in Table 1. It is shown that with the 3%/3 mm and 3%/2 mm criteria, the average γ passing rates for all cases with all verification methods were greater than 95%. With the 2%/2 mm criterion, the average γ passing rates for head cases were still > 95%, and for H&N, prostate, and lung localization > 90 %. The lowest average γ passing rates for prostate cancer treatment plans were noticed probably due to the fact, that 10 MeV photons were used in these cases. Comparing different verification methods ArcCheck showed the lowest γ passing rates, especially in the case with greater PTV volume.

Table 1. Mean gamma passing rates. HN: Head and Neck, PD: portal dosimetry.

Localiza-tion	Method	3%/3mm	3%/2mm	2%/2mm
H&N	PD	99.1±0.6	98.5±1.1	95.3±2.7
	ArcCheck	98.8±0.9	96.3±1,8	93.5±2.7
	3DVH	99.1±0.9	98.5±1.8	94.8±3.3
Prostate	PD	97.8±2.2	96.2±4.8	93.9±5.7
	ArcCheck	97.0±1.2	95.8±1.9	92.9±2.4
	3DVH	97.6±5.1	96.4±6.5	93.2±6.8
Lung	PD	99.5±0.2	99.3±0.4	97.1±2.1
	ArcCheck	98.7±1.2	97.8±2.4	96.1±3.3
	3DVH	99.1±0.5	98.7±0,9	94.7±2.5
Head	PD	99.6±0.3	99.3±0.5	97.9±1.1
	ArcCheck	99.4±0.5	98.8±0.5	97.2±1.6
	3DVH	98.5±0.9	98.1±1.1	96.3±2.1

Tables 2 – 5 show the percentage dose difference for ACPDP and TPS as well as the correlation between the DD,%, and the gamma pass rate (2%/2mm) evaluated by 3DVH. The dose difference and correlation between target and normal organs (H&N, prostate, head, and lung cancer cases) were also investigated. It was found that for prostate cases the percentage dose difference was less than 3% for target volume and normal organs except for maximum target dose (3.27%), 2% of PTV volume dose (3.2%), and maximum bladder dose (3.53%). The percentage dose difference showed a low or moderate correlation (R<0.6) with the gamma pass rate. Only results for the target D2% showed a strong correlation (R>0.6). On the other hand, percentage dose differences in the cases of head and neck cancer were also less than 3% in most cases, only D_{mean} of the left parotid reached 3.16 %. Strong correlation (R>0.7) was observed in PTV and D_{mean} of the brainstem. A weak and moderate correlation was found for all normal organ structure volumes in the case of head cancer, but target volume was in very strong correlation with γ passing rates. Finally, in lung cases high or very high correlation was observed for the target's D_{mean}, D95%, D98%, and D_{max} for lung, and D_{mean} for heart structures. The highest DD, % was noticed for D_{max} of the lung – 3.59 %.

Table 2. Percentage dose difference and correlation between DD,%, and gamma pass rate for prostate cases. R - Pearson correlation coefficient.

Structure	Parameter	DD,%	R
PTV	D_{mean}	0.88	0.349
	D_{max}	3.27	0.212
	D2%	3.20	0.701
	D95%	1.48	0.494
	D98%	1.51	0.202
Bladder	D_{mean}	1.12	0.571
	D_{max}	3.53	0.305
Femur (L)	D_{mean}	1.02	0.358
	D_{max}	2.33	0.042
Femur(R)	D_{mean}	0.9	0.288
	D_{max}	2.06	0.351
Rectum	D_{mean}	1.71	0.414
	D_{max}	2.68	0.061

Table 3. Percentage dose difference and correlation between DD,%, and gamma pass rate for head and neck cases. R - Pearson correlation coefficient.

Structure	Parameter	DD,%	R
PTV	D_{mean}	1.16	0.774
	D_{max}	1.12	0.83
	D2%	0.44	0.165
	D95%	1.41	0.511
	D98%	1.21	0.44
Spinalcord	D_{mean}	1.47	0.418
	D_{max}	0.89	0.067
Parotid (L)	D_{mean}	3.16	0.034
	D_{max}	1.51	0.472
Parotid (R)	D_{mean}	2.88	0.318
	D_{max}	1.01	0.387
Brainstem	D_{mean}	1.07	0.744
	D_{max}	2,32	0,061

Table 4. Percentage dose difference and correlation between DD,% and gamma pass rate for head cases. R - Pearson correlation coefficient.

Structure	Parameter	DD,%	R
PTV	Dmean	1,04	0,899
	Dmax	2,83	0,153
	D2%	0,68	0,393
	D95%	1,74	0,749
	D98%	2,01	0,865
Chiasma	Dmean	2,69	0,395
	Dmax	1,63	0,279
Eye(R)	Dmean	2,98	0,409
	Dmax	1,81	0,207
Eye(L)	Dmean	2,95	0,492
	Dmax	2,65	0,274
Brainstem	Dmean	2,35	0,305
	Dmax	1,55	0,021

Table 5. Percentage dose difference and correlation between DD,%, and gamma pass rate for lung cases. R - Pearson correlation coefficient.

Structure	Parameter	DD,%	R
PTV	D_{mean}	0.38	0.496
	D_{max}	2.71	0.958
	D2%	0.77	0.820
	D95%	1.02	0.951
	D98%	1.13	0.336
Lung (PTV)	D_{mean}	1.1	0.198
	D_{max}	3.59	0.854
Heart	D_{mean}	3.13	0.865
	D_{max}	2.37	0.162
SpinalCord	D_{mean}	2.02	0.228
	D_{max}	1.64	0.556

Fig.6 shows the relation between the percentage dose difference and the gamma pass rate for the target mean dose volume for all investigated cases. It can be seen that the percentage dose difference for the mean dose of PTV decreases with the increasing gamma pass rate. It should be noted that no apparent correlation between doses was observed for prostate and lung cases.

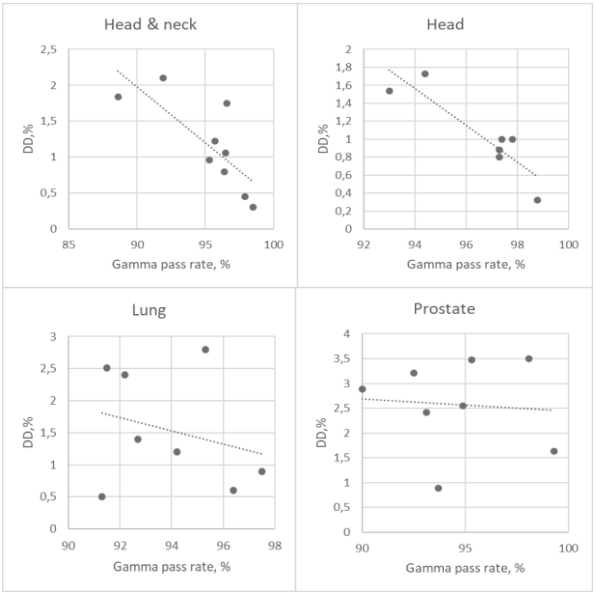

Fig. 6. Correlation between percentage dose difference and gamma pass rate for target mean dose structure for different organs.

The applicability of polymer gel dosimetry for dose verification was also investigated. Radiation-induced polymerization of dose gels was clearly seen after the gel's irradiation indicating density changes of the irradiated volume (Fig.7). Irradiated gels were red out using X-ray CT and polymerization caused optical density changes were measured. The dose distribution profile of gels was analyzed by measuring CT numbers since they are directly proportional to the density changes.

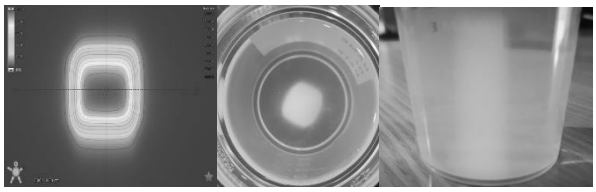

Fig. 7. Portal dosimetry image (left) and photo of nMAG gel after irradiation.

The comparison of the investigated dose distribution profiles analyzed by different verification methods is provided in Fig.8. The similarity of the curves is clearly seen indicating the compatibility of all methods.

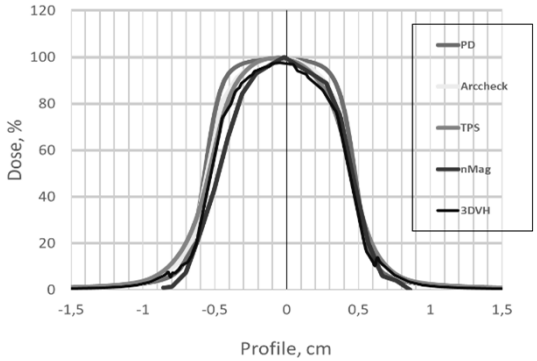

Fig. 8. A comparison of the 12 Gy dose profiles evaluated by different verification methods.

Gamma passing rates for different verification methods obtained using gamma function analysis are shown in Table 6. It was found that the gamma passing rate for gel was > 90% when the 3%/3mm evaluation criterion was applied. In the case of VMAT irradiation, a decreased gamma passing rate was observed for all verification methods with the exception of portal dosimetry, whereas both verification plans passed with 100%. The investigated gamma passing rate of gels showed very close results with 3DVH method and was even higher in the case of rotational irradiation.
Dose mapping results for irradiated gels are shown in Fig.9.

Table 6. Gamma pass rates and average gamma of 1.0 cm^2 irradiation field

Technique	Method	Gamma passing rate (3%/3mm)	Average gamma
Static irradiation	PD	100%	0.17
	ArcCheck	100%	0.15
	3DVH	91.3	0.43
	Gel dosimetry	90.3	0.52
Rotational irradiation	PD	100	0.14
	ArcCheck	96.3	0.41
	3DVH	70.3	0.72
	Gel dosimetry	88.9	0.48

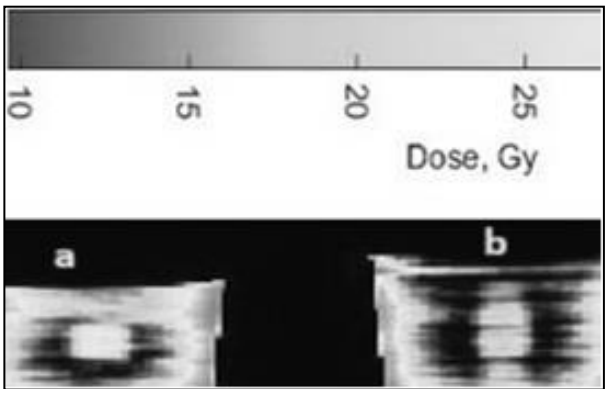

Fig. 9. Dose mapping of gels irradiated in a static mode (a) and in a rotating field (b).

Patient-specific QA is essential for confirming the machine status and accuracy of the dose delivery before radiation treatment and pretreatment, however, it depends on the dose verification method. For example: compared with the PD method, the ArcCheck verification method took into account the influence of the couch of the linear accelerator and the system was angle-independent. With the employment of isotropic physical properties, the ArcCheck verification process was closer to the actual treatment process than the PD method [25]. This was also confirmed by the gamma passing results, which were lower in almost all cases of treatment plan verification. ArcCheck phantom is very suitable for hybrid plan verification where undetectable errors at any fixed gantry angle can be found. A basic requirement for any detector used for hybrid plan verification is its independence of beam orientation, energy, and dose rate. With the commonly used clinical standard parameters (3%/3 mm and 3%/2 mm), both the ArcCheck method and the PD method can meet the requirements for dose verification for the VMAT plan. For ArcCheck, 3%/3 mm and 3%/2 mm are recommended. For PD,

considering its high space resolution, this study supports the use of 2 mm/2% as the analysis criteria.

Comparative analysis has shown that dose verification using gel dosimetry is more suitable and more accurate than 3DVH when performing stereotactic treatment where high doses of radiation with small fields are realized.

4. Conclusions

The application of various dosimetry systems for VMAT dose plan verification has been investigated. All systems showed similar results for the gamma pass rate using the 3%/3 mm criterion. Using 3DVH software, the accuracy of dose distribution through the DVH for target and normal organ volumes was investigated. The mean gamma pass rates exceeded 95% for the 3%/3 mm and 3%/2mm criterion. For H&N and prostate cancer cases estimated mean gamma pass rates (3%/3 mm, 3%/2 mm, and 2%/2 mm criterion) of ArcCheck were lower than those of portal dosimetry and 3DVH. Mean gamma values (3%/3 mm, 3%/2 mm criterion) for lung and head cancer cases were similar. The percentage dose difference was less than 3% for all structures in the case of head cancer and correlated with the gamma pass rate for PTV. The largest percentage dose difference was for prostate and lung cancer cases. It was found additionally, that gel dosimetry could be a useful verification tool for small-field and high-dose rate SRT treatment plans. Gel dosimetry is also a validated method for the acceptance and commissioning of the treatment delivery technique.

References

1. Low DA., Harms WB., Mutic S., Purdy JA., A technique for the quantitative evaluation of dose distributions. Med Phys. 1998;25(5):656–61.

2. Ulrich S., Nill S., Oelfke U., Development of an optimization concept for arc-modulated cone beam therapy. Phys Med Biol 2007;**52**:4099–119.9.

3. Poppe B., Blechschmidt A., Djouguela A., et al. Two-dimensional ionization chamber arrays for IMRT plan verification. Med Phys. 2006;33(4):1005–15.

4. Kim YL., Chung JB., Kim JS., Lee JW., Choi KS., Comparison of the performance between portal dosimetry and a commercial two-dimensional array system on pretreatment quality assurance for volumetric-modulated arc and intensity-modulated radiation therapy. J Korean Physical Soc, 2014, 64: 1207-1212.

5. Fenoglietto P., Laliberte B., Ailleres N., Riou O., Dubois JB., et al., Eight years of IMRT quality assurance with ionization chambers and film dosimetry: experience of the Montpellier Comprehensive Cancer Center., 2011, Radiat Oncol 6: 85.

6. Low DA., Dempsey JF., Venkatesan R., et al. Evaluation of polymer gels and MRI as a 3-D dosimeter for intensity-modulated radiation therapy. Med Phys. 1999;26(8):1542–51.

7. Krauleidis A., Adliene D., Rutkuniene Z., The Impact of Temporal Changes in Irradiated nMAG Polymer Gels on Their Applicability in Small Field Dosimetry in Radiotherapy. Gels 2022, 8, 629.

8. Li G., Zhang Y., Jiang X., Bai S., Peng G., Wu K., Jiang Q., Evaluation of the ArcCheck QA system for IMRT and VMAT verification. Phys Med 2013;29:295–303.

9. Jim´enez-Melguizo M., Espinosa M., Montes J., Guirado D. and Lallena A. M., Response of the ArcCHECK device at 6 MV and 15 MV for VMAT and IMRT quality control. Physics Medical, 2020, 80, 373–382.

10. Aristophanous M., Suh Y., Chi PC., Whittlesey LJ., LaNeave S., Martel MK., Initial clinical experience with ArcCHECK for IMRT/VMAT QA. J Appl Clin Med Phys 2016;17:1–14.

11. Bedford JL., Lee YK., Wai P., South CP., Warrington AP., Evaluation of the Delta4 phantom for IMRT and VMAT verification. Phys Med Biol. 2009;54(9):N167–N176.

12. Van Esch A., Clermont C., Devillers M., Iori M., Huyskens DP., On-line quality assurance of rotational radiotherapy treatment delivery by means of a 2D ion chamber array and the Octavius phantom. Med Phys. 2007;34(10):3825–37.

13. Arumugam S, Xing A, Goozee G, Holloway L. Detecting VMAT delivery errors: a study on the sensitivity of the ArcCHECK-3D electronic dosimeter. J Phys Conf Series 2013;444:012019.

14. Sanghangthum T., Suriyapee S., Srisatit S., Pawlicki T., Statistical process control analysis for patient-specific IMRT and VMAT QA.J. Rad Res 2013;54:546–52.

15. Chaswal V., Weldon M., Gupta N., Chakravarti A., Rong Y., Commissioning and comprehensive evaluation of the ArcCHECK cylindrical diode array for VMAT pretreatment delivery QA. J Appl Clin Med Phys 2014;15:212–25.

16. Arumugam S., Young T., Xing A., Thwaites D., Holloway L., Benchmarking the gamma pass score using ArcCHECK for routine dosimetric QA of VMAT plans. J Phys Conf Series 2015;573:012040

17. Neilson C., Klein M., Barnett R., Yartsev S., Delivery quality assurance with ArcCHECK. Med Dosim 2013;38:77–80.

18. Guo Y., Pei Y., Ma Y., et al., A comparative of Matrixx and EPID for dosimetric verification of intensity-modulated radiotherapy. Chin J Radiol Med Prot, 2017, 26(6), 657–660.

19. Infusino E., Mameli A., Conti R., Gaudino D., Stimato G., et al., Initial experience of ArcCHECK and 3DVH software for RapidArc treatment plan verification. Med Dosim, 2014, 39: 276-281.

20. Olch AJ., Evaluation of the accuracy of 3DVH software estimates of dose to virtual ion chamber and film in composite IMRT QA. Med Phys, 2012, 39: 81-86.

21. Feygelman V., Zhang G., Stevens C., Nelms BE., Evaluation of a new VMAT QA device, or the "X" and "O" array geometries. J Appl Clin Med Phys 2011;12: 146–68.

22. Lin MH., Chao TC., Lee CC., Tung CJ., Yeh CY., Hong JH., Measurement-based Monte Carlo dose calculation system for IMRT pretreatment and on-line transit dose verifications. Med Phys. 2009;36(4):1167–75.

23. Thiyagarajan R., Nambiraj A., Sinha SN., Yadav G., Kumar A., Subramani V., Analyzing the performance of ArcCHECK diode array detector for VMAT plan. Rep Pract Oncol Radiother 2016;21:50–56.

24. Song JH., Shin HJ., Kay CS., Son SH., Dosimetric verification by using the ArcCHECK system and 3DVH software for various target sizes. PLoS One, 2015 10:6

25. Covington E. L., Snyder J. D., Wu X., Cardan R. A., Popple R. A., Assessing the feasibility of single target radiosurgery quality assurance with portal dosimetry. Journal of Applied Clinical Medical Physics, 2019, 20(5), 135–140.

MEDICAL PHYSICS IN THE BALTIC STATES 16 (2023)

Proceedings of International Conference "Medical Physics 2023"
9-11 November 2023, Kaunas, Lithuania

IMPACT OF LUNG VENTILATION ZONE SPARING DURING FUNCTIONAL DOSIMETRIC PLANNING ON PATIENT QUALITY OF LIFE.

Marijus ASTRAUSKAS[1], Romualdas GRIŠKEVIČIUS[1], Rita STEPONAVIČIENĖ[2], Jonas VENIUS[1,3]
[1] National Cancer Institute, Medical physics department, Vilnius, Lithuania. [2] National Cancer Institute, External beam radiotherapy department, Vilnius, Lithuania. [3] National Cancer Institute, Biomedical physics laboratory, Vilnius, Lithuania.
marijus.astrauskas@nvi.lt; romualdas.griskevicius@nvi.lt; rita.steponaviciene@nvi.lt; jonas.venius@nvi.lt

***Abstract*:** The goal of this study was to evaluate the possible impact of functional lung sparing radiation treatment planning strategy on patient quality of life. Using a computed tomography ventilation imaging tool to segment the lung into functional zones we retrospectively compared 20 lung cancer patient treatment plans with new reoptimized functional sparing plans. Results show that by reducing the dose to high functioning zones it is possible to improve patient quality of life by lowering patient normal tissue probability of radiation induced pneumonitis.

Keywords: functional planning, ventilation, radiotherapy, NTCP.

1. Introduction

New and evolving methods in radiotherapy are having a positive impact on better survival of lung cancer patients. Patient quality of life after the radiation treatment course is an important aspect of the overall success of the treatment. The most common endpoint in post treatment recovery is the lung damage and loss of function due to irradiation. Lung function is dependent on good blood flow and metabolism in the lung capillaries, which ensure good oxygen saturation. These processes are directly related to lung ventilation – the mechanical compression/expansion of the alveoli and the flow of air within them. When fibrosis starts to develop in the lung, tissue starts to lose elasticity and ventilation goes down, less oxygen gets into the bloodstream, inflammation starts to form and therefore – the overall quality of life becomes worse [1].

It is known that ionising radiation causes formation of fibrotic tissue in the lung [2], naturally during radiation therapy it's important to preserve healthy lung tissue as much as possible, with the emphasis on the zones that have high ventilation. Usually, lung cancer patients are already pulmonary compromised, have lung obstructions and poor/nonhomogeneous ventilation throughout the lung. Due to this reason dosimetric treatment planning should be done with a special emphasis on the parts of the lung with high ventilation values in order to protect the functionality of the lung.

In this work lung ventilation zones for 20 patients were retrospectively calculated and dosimetric treatment plans, sparing zones of different ventilation levels, were created. Using this data normal tissue complication probability (NTCP) was calculated in order to evaluate the impact of functional, ventilation sparing, plans on patient quality of life.

2. Methods and Materials

2.1. Patients

20 lung cancer patients with primary lung tumours that were treated in National cancer institute in 2022 and had 4DCT imaging done prior to treatment were selected for the study. Patient demographics: 14 male and 6 female, mean age was 65.4 (39-77) years, all patients had stage III non-small cell lung cancer (NSCLC), 65% had squamous cell carcinoma and 35% had adenocarcinoma. PDL1 expression was: >50% - 2 patients, 1-49% - 4 patients, <1% - 14 patients.

2.2. Planning parameters

Patients were scanned using a GE LightSpeed CT Scanner for treatment planning using a resolution of 512 × 512 pixels and 0.25 cm slice thickness. Patients were scanned using two CT modalities – first was standard planning CT and the second – 4DCT cine protocol with 10 phases of breathing, used for ITV contouring and lung ventilation calculation. Planning was done using Varian Eclipse TPS v15.5 (Varian Medical Systems, Palo Alto, CA), using 6MV VMAT half-arcs. Dose calculation algorithm used was the Varian analytical anisotropic algorithm (AAA) with tissue heterogeneity correction. These original plans were then replanned retrospectively using the same planning objectives, with the addition of a new lung ventilation zone structure, having 70% of target (PTV) priority.

2.3. Normal tissue complication probability parameters

For NTCP calculation a revised QUANTEC model proposed by Anne G.H. Niezink et al. was used to determine the probability of radiation pneumonitis [3]. By lowering this complication probability value for the lung, especially the high functioning zones, we should be able to improve the overall patient quality of life. Using mean lung dose values and the proposed NTCP calculation equation 1, radiation induced pneumonitis complication probability was calculated.

$$NTCP_{QUANTEC} = (1 + \exp(4.575 - 0.224 * MLD))^{-1} \quad (1)$$

2.4.1 Lung ventilation calculation

Functional ventilation images were obtained using a MATLAB plugin "VESPIR" (Ventilation via Scripted Pulmonary Image Registration), developed by J.Kipritidis, H.C.Woodruff et.al (Radiation Physics Laboratory, Sydney Medical School, Australia). VESPIR is a CTVI (computed tomography ventilation imaging) tool that uses 4D computed tomography images to identify and visualise functional lung zones. Although not as informative and precise as the functional lung test standard of ^{68}Ga PET or ^{99m}TcSPECT, it provides sufficiently good correlation to be used in functional lung avoidance planning [4, 5].

2.4.2 VESPIR algorithm

The tool uses 4DCT phase images to segment the lungs and identify the exhale and inhale phases. After that, using a deformable image registration (DIR) tool, the motion field is calculated between the peak exhale and inhale images. From this motion field, Jacobian determinant is obtained by expressing the DIR motion difference for each inhale-exhale voxel.

$$V_{Jac}(x,y,z) = \left|1 + \frac{\partial u_x(x,y,z)}{\partial x}\frac{\partial u_y(x,y,z)}{\partial y}\frac{\partial u_z(x,y,z)}{\partial z} - \frac{\partial u_y(x,y,z)}{\partial x}\frac{\partial u_z(x,y,z)}{\partial y}\frac{\partial u_z(x,y,z)}{\partial x} + \frac{\partial u_y(x,y,z)}{\partial y}\frac{\partial u_z(x,y,z)}{\partial z}\right| - 1 \quad (2)$$

The value of the V_{Jac} (equation 2) is used to determine the expansion and contraction of the lung tissue and is used as our functional ventilation map. For more convenient use in functional planning this map is converted into an image, based on the normalised functional percentage of lung volume or functional zone.

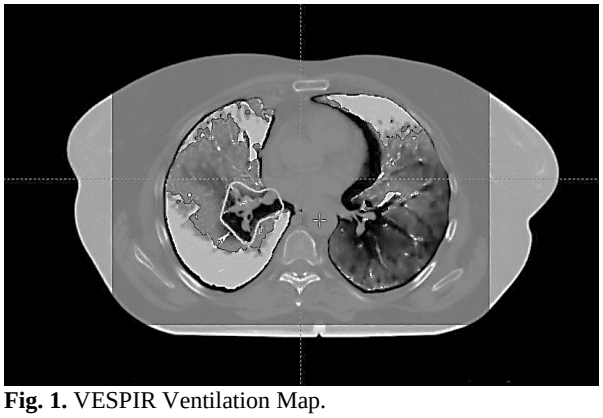

Fig. 1. VESPIR Ventilation Map.

These functional lung zones were segmented as 5 structures representing functional ventilation percentage zones from 50% to 90% ventilation and used in the replanning and evaluation stage.

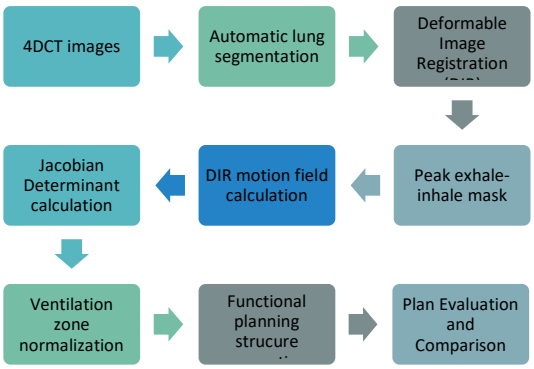

Differences between original and replanned ventilation zone mean dose values were evaluated using R via paired one-tail Student t-test ($p<0.05$).

3. Results

For all 20 original patient plans we imported the 5 generated ventilation zone structures - from 50-100% to 90-100% ventilation.

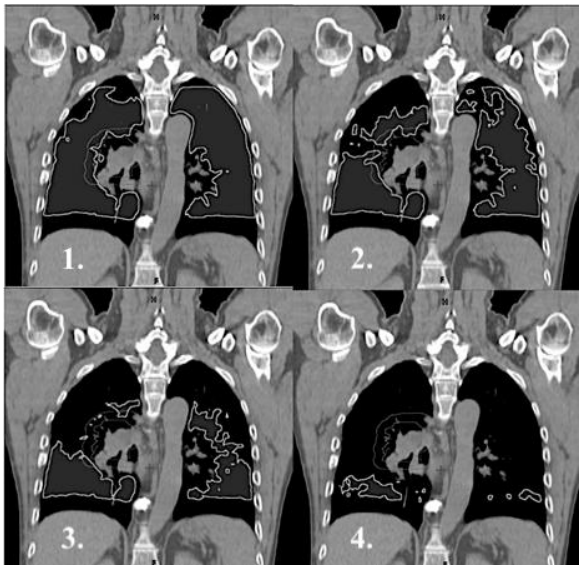

Fig. 2. Example ventilation zones 1. 30-100% 2. 50-100% 3. 70-100% 4. 90-100%.

The mean absolute volume of the various ventilation zones and the original lung volume is shown in table 1.

Table 1. Absolute lung structure volume, cc.

Structure	Volume, cc	Relative lung volume
Lungs	4306.91	
50-100%	1301.39	30.22%
60-100%	1000.46	23.23%
70-100%	706.84	16.41%
80-100%	428.07	9.94%
90-100%	172.27	4.00%

The original plan was then reoptimized with a functional ventilation zone structure for 50-100% ventilation. This zone was chosen to be the optimal impact/size ratio for plan optimization. New plans were normalised to be the same as the original PTV coverage and were approved as clinically acceptable. The example of dose distribution between the original (right) and new plan (left) are shown in figure 3.

Fig. 3. Example of dose fluence reduction over high ventilation zones (shown with arrows).

For every case we looked at the original plans functional zone mean dose values before and after optimization.

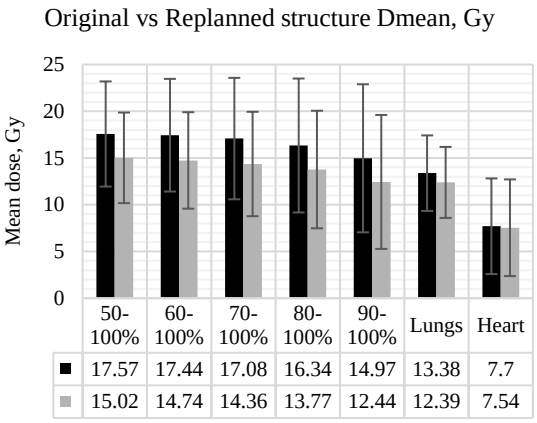

Fig. 4. Original and replanned dose statistics.

Table 2. Planning structure dose difference.

Structure	Original D_{mean}, Gy	Replanned Dmean, Gy	Percentage difference
50-100%	17.57	15.02	-14.51%*
60-100%	17.44	14.74	-15.47%*
70-100%	17.08	14.36	-15.92%*
80-100%	16.34	13.77	-16.33%*
90-100%	14.97	12.44	-16.52%*
Lungs	13.38	12.39	-7.34%*
Heart	7.7	7.54	-2.08%
			***p<0.001**

Differences in mean dose between the original and replanned cases were statistically significant ($p<0.001$) in every metric except the heart mean dose, where the difference was not statistically significant (table 2). This dose reduction was possible by redistributing the planned fluence through the less functional lung zones (Fig.3).
In terms of patient quality of life, the replanned cases also showed statistically significant ($p<0.01$) improvement in NTCP for radiation induced pneumonitis, shown in figure 5.

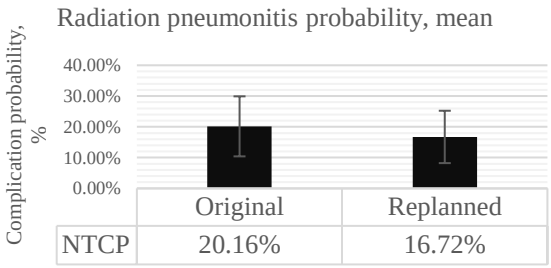

Fig. 4. NTCP between original and replanned cases.

4. Discussion

Functional ventilation planning can be used to lower the probability of radiation pneumonitis in lung cancer patients. CTVI techniques prove to be a useful tool in visualising and segmenting high functioning lung zones. With this additional information, new planning strategies can be explored to further decrease the dose to the functional lung and improve patient quality of life after treatment. However, more research is needed on the optimal planning strategy, such as which ventilation zone to focus on and how to choose the patients that would benefit from this planning approach. Furthermore, improving existing NTCP models and development of new ones based on clinical outcomes could help narrow down the direction of similar research work. Since current lung NTCP calculation models are based largely on the mean lung dose metrics and not functional lung dose, a better approach is needed to quantify the impact of such functional sparing approaches.

5. Conclusions

Our retrospective study on lung cancer patients using functional dosimetric planning showed that with additional ventilation zone sparing we were able to spare parts of the lung with more active function and ventilation by on average 15.75%. This in turn lowers the normal tissue complication probability of radiation induced pneumonitis by 3.44%. Further research is needed to improve the NTCP model with the inclusion of additional functional zone dose metrics.

References

1. Ding, Nian-Hua; Jian Li, Jian; Sun, Lun-Quan. Molecular Mechanisms and Treatment of Radiation-Induced Lung Fibrosis. *Current Drug Targets*; 2013; 14:11, 1347-1356.
2. Cella, L., D'Avino V., Palma G., et.al. Modeling the risk of radiation-induced lung fibrosis: Irradiated heart tissue is as important as irradiated lung. *Radiotherapy and Oncology*; 2015; 117:1;36-43.
3. Niezink, A.G.H., van der Schaaf, A., Wijsman, R., et al. External validation of NTCP-models for radiation pneumonitis in lung cancer patients treated with chemoradiotherapy. *Radiotherapy and Oncology*; 2023; 186.
4. Kipritidis, J., Woodruff, H.C., Hegi-Johnson, F. et.al. New pathways for end-to-end validation of CT ventilation imaging (CTVI) using deformable image registration. *IEE 13th international symposium on biomedical imaging (ISBI)*; 2016.
5. Eslick, E.M., Kipritidis, J., Gradinscak, D., Stevens, M.J., et. al. CT ventilation imaging derived from breath hold CT exhibits good regional accuracy with Galligas PET. *Radiother Oncol.*, 2018; 127:2, 267-273.

MEDICAL PHYSICS IN THE BALTIC STATES 16 (2023)

Proceedings of International Conference "Medical Physics 2023"
09-11 November 2023, Kaunas, Lithuania

GADOLINIUM IN COASTAL WATERS – TIME TRENDS AND POSSIBLE SOURCES

Sören MATTSSON[1], Kristina ERIKSSON STENSTRÖM[2], Guillaume PÉDEHONTAA-HIAA[1]
[1]Lund University, Medical Radiation Physics, ITM, Skåne Univ. Hospital, Malmö, Sweden
[2]Lund University, Department of Physics, Lund, Sweden
[1]soren.mattsson@med.lu.se; [2]kristina.stenstrom@hep.lu.se; [3]guillaume.pedehontaa-hiaa@med.lu.se

***Abstract*:** Samples of *Fucus serratus* and *Fucus vesiculosus* taken in Swedish coastal waters have been analysed for Gd by ICP-MS. The results for one site with frequent sampling show significantly increasing levels during the last 30 years, most likely a result of the increasing use of Gd-containing contrast agents for MR-imaging at hospitals and other health care institutions. Samples taken at the west-, south- and east-coast in 2020 show considerable variation in Gd-concentration from site to site with highest level in northern Kattegat

Keywords: Gadolinium, *Fucus*, Sweden, environmental monitoring

1. Introduction

Gadolinium (Gd) is a rare earth element. It is increasingly used in high-tech products, which leads to release of increasing amounts of Gd to the environment – a situation similar to many other rare earth elements. Because of its neutron capturing ability, Gd is also used to regulate neutron fluence rate in reactor cores of nuclear power plants. Addition of Gd oxide (Gd_2O_3) to uranium oxide pellets used in nuclear reactors improves the efficiency of nuclear fuel burning.

Since 1988, another very important application of Gd is its use as a contrast agent in medical magnetic resonance imaging (MRI). The properties of its trivalent cation (Gd^{3+}) make it suitable to serve as the central ion in chelates administered intravenously to patients as a contrast agent in MRI. The seven unpaired electrons account for the strong paramagnetic effect. Macro-cyclic Gd^{3+} compounds are considered less likely to release free Gd^{3+} ions in the human body than linear chelates. Such Gd-chelates have been widely used for more than thirty years.

The contrast agent is injected into the human bloodstream and excreted via the kidneys. Due to the high stability of these compounds, the anthropogenic Gd was assumed not to react in the human body (which is the prerequisite for its use as a contrast agent, because Gd^{3+} is toxic). The Gd-chelates have a half-life of about 1.5 hours in the human body if renal function is normal, and around 90% of the total administration is excreted in 12 hours. A single administration of Gd-chelate contains 1-2 g of Gd [1].

The cumulative number of administrations, and the chemical structure of the chelate given, are factors of importance for the amount of Gd that is retained in tissues. The chemical properties of Gd and its medically used chelates, as well as its toxicity and potential side effects related to injection of Gd-chelates is described by Blomkvist et al [2]

During the past decades, knowledge has increased about potential harmful effects of Gd-chelates in patients with severe renal dysfunction. In such patients, there is a risk for a potentially disabling and lethal disease, nephrogenic systemic fibrosis [2]. Restricting the use of Gd-chelates in persons with severely impaired renal function has decreased the occurrence of this toxic effect in the last decade. There has also been an increasing awareness of Gd-retention in the body, even in patients without renal dysfunction [2].

Between 1998 and 2008, the worldwide use of Gd-contrast increased almost 10-fold. The Gd compounds in the form of chelates are excreted mainly unmetabolized from the body through the urine and passes through the wastewater treatment plants almost unaffected into the aquatic environment [1,2]. In 1996, for the first time, increased Gd concentrations were reported in river waters [3]. Later studies of Gd in surface water and drinking water have indicated that Gd from contrast agents are not being removed in waste water treatment plants and not either at tap water production [4-13].

As mentioned above, the first Gd-based contrast agent became available for clinical use in 1988 and since then a number of new Gd chelates have been developed and approved [14,15]. These compounds are water soluble and are characterized by a very high stability.

Brown algae such as *Fucus* species have previously been used as sensitive bioindicators for various radionuclides in the marine environment [16] They are therefore good

candidates to investigate the content of Gd in coastal waters and biota.
The aim of the present investigation was to study the long-term variation of the Gd concentration in previously collected samples of brown algae from a sampling area on the Swedish west coast and to get a picture of today's Gd levels at other coastal areas of Sweden.

2. Materials and methods

The concentration of radionuclides and stable metals (including Gd) has been measured in *Fucus serratus* and *F. vesiculosus*, collected at various locations along the Swedish westcoast since 1976. At one location (Särdal), these brown algae have been regularly collected, most of the time every second month, since 1967 [16]. In March-May 2020, the study was expanded to also include the south and east coasts of Sweden [17,18].
The Särdal samples were based on a large number of whole plants (>25). Samples from the other sites were based on one to three plants only.
The Gd concentration in *Fucus* has been analysed by Inductively Coupled Mass Spectrometry (ICP-MS) analysis at Department of Biology (Instrumental Chemistry), Lund University and later on in a cooperation between Departments of Biology and Geology at Lund University. The stable isotope analysed was ^{157}Gd. The results reported are elemental concentrations, assuming that the Gd-isotopes keep their natural abundance in the seaweed samples.The relative standard deviation for the individual measureements was typically 2-10%.

3. Results and discussion

3.1. Temporal variations of the Gd concentration

The levels Gd in *Fucus* from Särdal in the period 2011-2021 are shown in Figure 1. For Gd there is an increase with a factor of around 3 from 2011 to 2021. This three-fold increase is consistent with measurements made in other coastal areas such as the San Frasisco bay in the United States [4].
Earlier collected samples show still lower concentrations than the 2011-results as shown in Figure 2. The increase in time is likely to be explained mainly by the increased use of Gd-containing contrast agents in MRI investigations in hospitals and other health care institutions. An interesting observation is that the highest concentrations, seven times higher than in 2011, were observed in 2018, a year with an exceptionally hot and dry summer.

3.2. Spacial variations of the Gd concentration along the Swedish coast

Fucus samples were collected at the various sites along the Swedish coast, from Strömstad (Site 1) on the northernmost west coast near the border to Norway, to Svenskärs Fiskeläge (Site 45) on the Gulf of Bothnia, with a higher number of samples collected near the nuclear power plant sites. a correlation between the Gd-levels and the ^{14}C-levels [18]. Gd

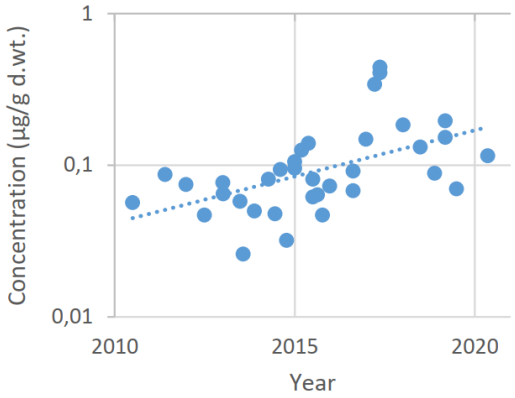

Fig. 1. Concentration of Gd in *Fucus serratus* from Särdal 2011-2021. Note that the scale is logarithmic. The dotted line indicates an exponential increase by time.

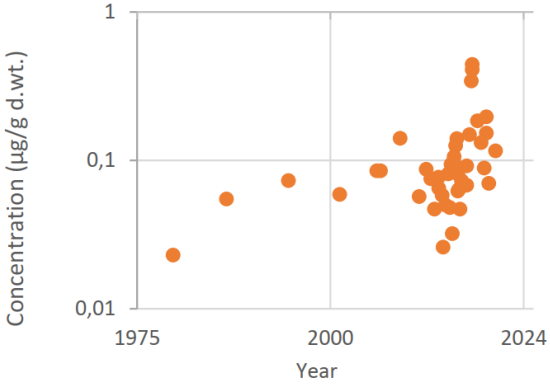

Fig. 2. Concentration of gadolinium in *Fucus serratus* from Särdal 1979-2021. Note that the scale is logarithmic.

Details about the location of the sites can be found in Stenström and Mattsson [18]. As seen in Figure 3, the highest Gd concentrations were found in Kattegat, close to Ringhals NPP and there is also is present at Ringhals NPP in fuel rods (as Gd2O3) [19]. The Gd concentration varies significantly at nearby sites in Skagerrak, Kattegat, the Baltic Sea and the Gulf of Bothnia indicating local sources either in the form of geological deposits or releases of Gd from MR contrast agents. The variation in Gd concentration between nearby sites is less pronounced in southern Kattegat and in the Öresund Strait. Sites located at the outflow of lake Vänern and of lake Vombsjön are characterized by lower salinity than the nearby sites and have higher Gd concentrations than in nearby sites. These increases in Gd concentration thus most likely stem from river runoff (e.g. from use in hospitals) [17].
It must be noted that Gd is also naturally occurring. It is released from bedrock, sediment and soil and occurs in the ion form Gd^{3+}. A large fraction of this naturally dissolved Gd is associated with colloids, and as described by Kulasis et al [20], such colloids aggregate during the mixing of freshwater and seawater in estuaries of low salinity.
Part of natural Gd is then removed with the colloids. The anthropogenic Gd is however almost unaffected. This also means that the Swedish coastal waters are influenced by anthropogenic Gd complexes from other European countries in the same way as for example ^{129}I, ^{99}Tc and ^{14}C.

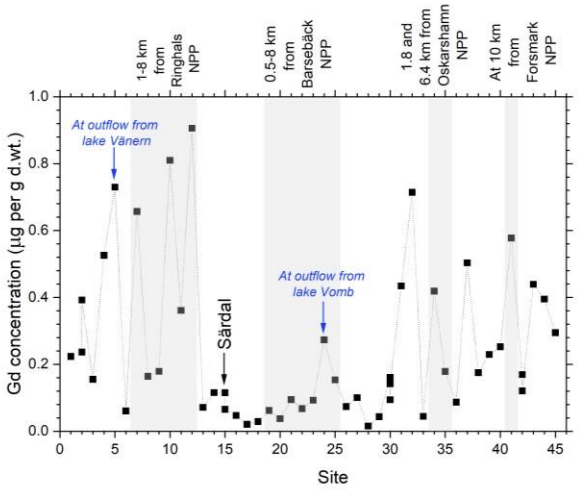

Fig. 3. Concentration of Gd in *Fucus* from the Swedish west-, south- and east-coast between 3 March and 13 May 2020.

4. Conclusions

There was an increase in the Gd concentration in brown seaweed from the Swedish west coast with a factor of around 3 from 2011 to 2021.The increase is most likely a result of the increasing use of Cd-containing contrast agents for MR-imaging in hospitals and other health care institutions. The considerable variation of the concentration along the Swedish coast motivate further studies of Gd in the marine environment in order to determine the possible origins of these contaminations.

5. Acknowledgements

Thanks are due to Tomas Naeraa, PhD, at Department of Geology, Lund University and Sofia Mebrahtu Wisén, PhD, and Jürgen Kuhn, Ph.D., at Department of Biology, Lund University for performing the Gd-analyses.

References

1. Rogowska J., Olkowska E., Ratajczyk W. and Wolska L. Gadolinium as a new emerging contaminant of aquatic environments. Env Toxicol Chem 37(6), 1523-1534, 2018. https://doi.org/10.1002/etc.4116.

2. Blomqvist L., Nordberg G.F., Nurchi, V.M and Aaseth J.O. Gadolinium in medical imaging— usefulness, toxic reactions and possible countermeasures-A review. Biomolecules 2022, 12, 742. https://doi.org/10.3390/biom12060742

3. Bau M. and Dulski P. Anthropogenic origin of positive gadolinium anomalies in river waters. Earth and Planetary Science Letters 143 (1-4), 245-255, 1996.

4. Hatje V., Bruland K.W., Flegal A.R., 2016. Increases in anthropogenic gadolinium anomalies and rare earth element concentrations in San Francisco Bay over a 20 year record. Environ. Sci. Technol. 50, 4159–4168. https://doi.org/10.1021/acs.est.5b04322

5. Knappe A., Möller P., Dulski P. and Pekdeger A., 2005. Positive gadolinium anomaly in surface water and ground water of the urban area Berlin, Germany. Chemie der Erde - Geochemistry 65, 167–189. https://doi.org/10.1016/J.CHEMER.2004.08.004.

6. Kulaksiz S., 2013. Rare earth elements as emerging contaminants in the Rhine river, Germany and its tributaries. PhD Thesis, Jacobs University Bremen, http://nbn-resolving.de/urn:nbn:de:gbv:579-opus-1002727.

7. Kulaksız S. and Bau M., 2011. Anthropogenic gadolinium as a microcontaminant in tap water used as drinking water in urban areas and megacities. Appl. Geochem. 26, 1877–1885. https://doi.org/10.1016/j.apgeochem.2011.06.011.

8. Lawrence M.G., 2010. Detection of anthropogenic gadolinium in the Brisbane river plume in Moreton bay, Queensland, Australia. Mar. Pollut. Bull. 60, 1113–1116. https://doi.org/10.1016/j.marpolbul.2010.03.027.

9. Lawrence M.G., Ort C. and Keller J., 2009. Detection of anthropogenic gadolinium in treated wastewater in South East Queensland, Australia. Water Res. 43, 3534–3540. https://doi.org/10.1016/j.watres.2009.04.033.

10. Möller P., Paces T., Dulski P. and Morteani G. Anthropogenic Gd in surface water, drainage system, and the water supply of the city of Prague, Czech Republic. Environ Sci Technol 36, 2387-2394, 2002.

11. Möller P., Knappe A. and Dulski P., 2014. Seasonal variations of rare earths and yttrium distribution in the lowland Havel river, Germany, by agricultural fertilization and effluents of sewage treatment plants. Appl. Geochem. 41, 62–72. https://doi.org/10.1016/

12. Schmidt K., Bau M., Merschel G. and Tepe N. Anthropogenic gadolinium in tap water and in tap water- based beverages from fast-food franchises in six major cities in Germany. Science of the Total Environment 687 1401–1408, 2019

13. Tepe N., Romero M. and Bau M., 2014. High- technology metals as emerging contaminants: strong increase of anthropogenic gadolinium levels in tap water of Berlin, Germany, from 2009 to 2012. Appl. Geochem. 45, 191–197. https://doi.org/10.1016/j.apgeochem.2014.04.006.1

14. Pietsch H. 25 years of contrast-enhanced MRI: Developments, current challenges and future perspectives Adv Ther 2016 Jan;33(1):1-28. doi: 10.1007/s12325-015-0275-4.

15. Gulani V., Calamante F., Shellock F.G., Kanal E., and Reeder S.B., on behalf of the International Society for Magnetic Resonance in Medicine. Gadolinium deposition in the brain: summary of evidence and recommendations. www.thelancet.com/neurology, 16, July 2017

16. Mattsson S., Eriksson Stenström K. and Pédehontaa- Hiaa G. Long-time variations of radionuclides and metals in the marine environment of the Swedish west-coast studied using brown algae. Report SSM 2022:13. Available at www.stralsakerhetsmyndigheten.se 2022

17. Eriksson Stenström K and Mattsson S. Marine 14C levels around the Swedish coast – Additional gamma spectrometry measurements and ICP-MS analysis of brown algae (Fucus spp.). Report BAR-2021/02, MA RADFYS 2021:02, Lund University 2021. Available at https://lucris.lub.lu.se/ws/portalfiles/portal/111217791/Report_SSM2019_5225_final.pdf

18. Eriksson Stenström K and Mattsson S. Spatial and temporal variations of 14C in Fucus spp. In Swedish coastal waters. Journal of Environmental Radioactivity 242 (2022) 106794

19. Insulander Björk K., Lau C.W.,Nylén H., and Sandberg U., 2013. Study of thorium-plutonium fuel for possible operating cycle extension in PWRs. Science and Technology of Nuclear Installations Article ID 867561, 8 pages http://dx.doi.org/10.1155/2013/867561

20. Kulaksız S. and Bau M., 2007. Contrasting behaviour of anthropogenic gadolinium and natural rare earth elements in estuaries and the gadolinium input into the North Sea. Earth Planet. Sci. Lett. 260, 361–371. https://doi.org/10.1016/j.epsl.2007.06.016.

MEDICAL PHYSICS IN THE BALTIC STATES 16 (2023)

Proceedings of International Conference "Medical Physics 2023"
09-11 November 2023, Kaunas, Lithuania

HOW TO DETECT RADIONUCLIDES SPECIFIC TO THE EUROPEAN SPALLATION SOURCE IN SOIL SAMPLES?

Guillaume PÉDEHONTAA-HIAA[1*], Robert FROST[2,3], Vytenis BARKAUSKAS[4], Kristina ERIKSSON STENSTRÖM[2], Mikael ELFMAN[2], Christian BERNHARDSSON[1], Christopher RÄÄF[1]

[1] Medical Radiation Physics Malmö, Department of Translational Medicine, Lund University, Sweden; [2]Division of Particle and Nuclear Physics, Department of Physics, Lund University, Sweden; [3]Division of Applied Nuclear Physics, Department of Physics & Astronomy, Uppsala University, Sweden; [4]Centre for Physical Sciences and Technology, Vilnius, Lithuania

guillaume.pedehontaa-hiaa@med.lu.se

***Abstract*:** The European Spallation Source (ESS) is a neutron research facility under construction in southern Sweden. The facility will produce a wide range of radionuclides including ^{148}Gd, ^{187}W, ^{172}Hf, ^{182}Ta and ^{178n}Hf that could be released into the environment in an accident scenario. Detection limits for these contaminants in soil were estimated to be in the mg k^{-1} range for ICP-MS and <3 Bq per 200 ml soil for gamma-ray spectroscopy.

Keywords: Environmental radiology, Metal traces analysis, Emergency preparedness, Mass spectrometry, Gamma-ray spectroscopy

1. Introduction

The European Spallation Source (ESS) is a neutron research centre under construction outside of Lund, Sweden. In the upcoming years, the facility will produce powerful neutron beams for applications in, for example, material science and biology. The neutrons will be produced via spallation, using a 2 GeV, 5 MW proton accelerator irradiating a tungsten target. Through the nuclear reactions in the target and the activation of surrounding material, a wide range of radioactive by-products will be generated. The ESS-target inventory has been calculated by different authors such as Barkauskas *et al.* [1], Kókai *et al.* [2] or Mora *et al.* [3] for the 5 MW proton beam.

If released, some of these radioactive materials may end up in the soil, water and plants and eventually reach the human food chain. Different environmental release scenarios exist for normal operation, maintenance operations and after accidents. In the case of major accident, the Swedish Radiation Safety Authority (SSM) has defined a list of the most important radionuclides regarding dose to the public for the first 7 days after the event. This list includes ^{148}Gd, ^{187}W, ^{172}Hf, ^{182}Ta and ^{178n}Hf, with the first one having the highest dosimetric impact [4].

Environmental contamination by stable W, Hf and Ta usually originate from industrial activities (mining, smelting, metallurgy, coal burning), military activities (W ammunitions), agriculture (fertilisers) and road traffic [5], [6]. Unlike Gd (and the rare earth elements in general) for which many environmental studies have been conducted, the behaviour of W, Hf and Ta in the environment is not well understood since they were not considered to be toxic. The potentiall toxicity of W has, however, drawn more attention in the recent years due to a possible connection to cases of leukaemia in the United States [7]. The information available on environmental Ta is summarised in only one review by Filella [8] and most of the literature found on Hf in the environment is linked to its separation from Zr.

Knowledge on the transfer of the elements from soil to plant relevant to the local environment of the ESS is also very limited with only one study on transfer of Hf and Ta to barley [9] and two on the transfer/toxicity of W to corn and peas [10], [11]. There is thus a need to develop analytical methods to quantify W, Hf and Ta both in soil and plants in order to build radioecological models that could be used to predict the spread of radioactive releases by the ESS in the environment.

In this study, a first step is taken toward this goal by investigating the limits of detection (LoD) that could be achieved for this list of nuclides by two commonly used analysis techniques: inductively coupled plasma mass spectrometry (ICP-MS) and gamma-ray spectroscopy.

In the case of ICP-MS (a non-radiometric technique), the LoDs are well established for traces of metals in solution. The unknown parameter is the efficiency of the methods used to extract these traces from soil samples. Soil samples were extracted from around the ESS facility using conventional methods for environmental monitoring and a method dedicated to the extraction of

W. Based on these experimental data, the LoDs expected for contaminated ESS soil samples were estimated. Regarding gamma-ray spectroscopy, the gamma-ray spectra of mixtures of ESS-specific radionuclides were simulated and then combined with experimental data from ESS soil samples. The obtained semi-synthetic spectra were then assessed in order to estimate the LoDs achievable for different source terms and levels of contamination.

2. Material and Methods

2.1. Sampling

Five samples consisting of 7 cm deep topsoil cores were selected among a bank of samples previously collected around the ESS facility [12]. The location of the sample sites is presented in Figure 1. A reference sample of contaminated industrial soil with certified values for W, Hf, Ta and Gd (LGC, NCS DC73323A) was also analysed for validation purposes.

Fig. 1. Maps of the ESS location in the southern Baltic region (top) and the soil sampling locations around the ESS (bottom) (Maps source: ©OpenStreetMap contributors)

2.2. Extraction methods

Two extraction methods for trace elements in soil (also called soil digestion methods) were tested. The methods are pseudo-total extractions that do not dissolve the silicates in the soil samples. Thus, the fraction of W, Hf and Ta contained in silicates cannot be extracted.

Aqua regia digestion is a pseudo-total extraction of the sample which is a method commonly used in environmental monitoring studies of metals in soil. Samples of 0.5 g of soil were mixed with 20 mL of aqua regia (3:1 hydrochloric acid/nitric acid), heated at 70°C for 4 h, and then evaporated to dryness and redissolved in 25 mL of 2% nitric acid. After 20 min of centrifugation, the liquid fraction was collected and 2% nitric acid was added up to a 50 mL total before storage at 5°C until analysis.

In the second method, the hydrochloric acid is replaced by phosphoric acid to enhance the extraction yield of W according to Bednar *et al.* [13]. Samples of 0.5 g of soil were mixed with 2.5 mL of concentrated nitric acid (65%), 2.5 mL of water and 1 mL of phosphoric acid and heated at 95°C for 30 min. 10 mL of concentrated nitric acid were added and the mixture was headed at 95°C for 120 min. 3 mL of hydrogen peroxide were slowly added to the sample (15 min at 95°C). 2 mL more of hydrogen peroxide were added to the sample (120 min at 95°C). Finally, the samples were evaporated close to dryness and after cooling, 25 mL of 2% nitric acid were added to the samples. After 20 min of centrifugation, the liquid fraction was collected and 2% nitric acid was added up to a 50 mL total before storage at 5°C until analysis.

2.3 ICP-MS and ICP-AES analyses

The extracted fractions were diluted 20 times in 2% nitric acid and measured by ICP-MS on a Bruker Aurora Elite instrument at the Department of Geology at Lund University, Sweden. The instrument was calibrated using diluted solutions of W, Ta and Hf (TraceCERT®, Supelco®). The following nuclides were measured: ^{177}Hf, ^{178}Hf, ^{181}Ta, ^{182}W, and ^{183}W. The concentration calculations for each element were performed assuming that their respective isotopes were present in the sample at their natural abundance.

Some samples were also analysed by inductively coupled plasma atomic emission spectroscopy (ICP-AES) on a Perkin Elmer Optima 8300 instrument at the Department of Biology at Lund University.

2.3. Semi-synthetic gamma-ray spectra

The simulation work was based on a high purity germanium (HPGe) detector (Ortec GEM 100, SN:S44-P41442A) at Medical Radiation Physics, Lund University. Gamma-ray spectra obtained with this detector from five soil samples in 200 ml plastic vials collected outside ESS in 2017 [12] where used to establish an experimental average soil profile. The spectra were pooled using the software GammaVision (Ortec) to yield a summed gamma-ray spectrum representing the typical activity concentrations of naturally occurring radionuclides from ^{238}U-series, ^{232}Th-series and ^{40}K.

The geometry of the HPGe detector was simulated using Nucleonica (Nucleonica GmbH), the setup window for which is shown in Fig. 2. Gamma-ray spectra of mixtures of ESS-specific nuclides were then obtained using the parameters of the simulated detector.

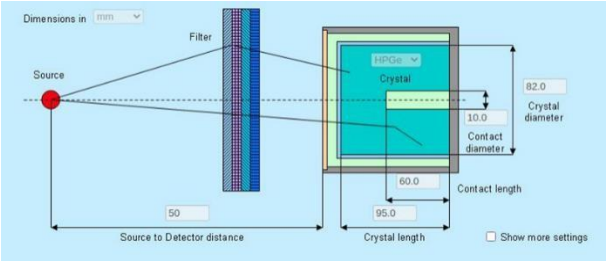

Fig. 2. Detector model from Nucleonica, using a simplified geometry of a 100% relative efficiency P-type HPGe-detector N.B: the source-endcap distance is not to scale with the detector crystal length.

3. Results

3.1. Extraction of W, Hf and Ta with phosphoric acid

The five soil samples and the reference material were extracted using the phosphoric acid procedure from Bednar *et al.* [13] and measured by ICP-MS. The obtained concentrations are reported in Table 1. By comparing the measured values to the certified concentrations of the reference material, it was possible to determine the efficiency of the extraction (see Table 2). In the hypothesis that the reference material and the ESS soil (sandy loam [5]) have the same response to the extraction procedure, the efficiencies determined in Table 2 can be used to normalise the concentrations of the three elements. These values can then be compared to their environmental levels estimated by the geological survey FOREG [14], as presented in Table 3.

Table 1. Concentration of W, Hf and Ta in five ESS soil samples and a reference material measured by ICP-MS (uncertainty: standard deviation)

Sample ID	W (mg kg^{-1} N = 4)	Hf (mg kg^{-1} N = 4)	Ta (mg kg^{-1} N = 4)
E3	0.29 ± 0.05	0.68 ± 0.14	0.03 ± 0.02
E52	0.38 ± 0.05	0.81 ± 0.19	0.04 ± 0.03
E258	0.22 ± 0.04	0.46 ± 0.14	0.04 ± 0.03
E331	0.32 ± 0.04	0.42 ± 0.07	0.03 ± 0.01
E344	0.64 ± 0.38	0.42 ± 0.11	0.03 ± 0.02
Ref	2.96 ± 0.44	0.71 ± 0.11	0.03 ± 0.02

Table 2. Efficiency of the phosphoric acid extraction on industrial soil certified reference material determined by ICP-MS (uncertainty: standard deviation)

Element	Reference value (mg kg^{-1})	Mean value measured by ICP-MS (mg kg^{-1} N = 4)	Efficiency (%)
W	7.4	2.96 ± 0.44	40.0
Hf	8.3	0.71 ± 0.11	8.6
Ta	1.6	0.03 ± 0.02	1.9

Table 3. Comparison between the calculated concentrations from the soil extractions and estimated data from geological surveys (uncertainty: standard deviation)

Element	Mean concentration* (mg kg^{-1}, N = 5)	Range concentration* (mg kg^{-1})	Estimated levels from FOREGS (mg kg^{-1})
W	0.9 ± 0.3	0.6-1.6	< 5.0
Hf	6.5 ± 1.5	4.9-9.5	8.8-11.7
Ta	1.8 ± 1.2	1.7-2.1	0.21-0.69

*normalised by the efficiency

3.2 Extraction with Aqua Regia extraction

The set of five samples and a reference soil material described in section 3.1. was extracted using aqua regia and measured by ICP-AES. No value above LoD could be measured for W, Hf or Ta. When the same elements were extracted by the phosphoric acid method measurable amount of W were detected which indicates that the extraction yields of the three elements were lower using aqua regia than phosphoric acid.
On the contrary, the concentrations of Gd, another ESS-relevant element, were in the same range regardless of the extraction method and the analytical method.

3.3. Simulation of contamination scenarios

FLUKA simulation results, from Barkauskas and Stenström [1], were used as a reference for the radionuclide inventories in the ESS target at different times. Two points in time were considered: the end of the 5-year operational period (t_0), when activity in the target is at its highest; and 350 days after the end of operation (t_{350}). Out of these two inventories only the gamma-ray emitters, or parents of gamma-ray emitters, with activities over 1 Bq were kept. Due to limitations of FLUKA, nuclides with isomeric states were not included in the inventory; the true inventory is therefore expected to be larger.
In the hypothesis that the relative amounts of the target radionuclides would be dispersed equally in the environment after a release, three concentration of target material in soil samples were defined in order to provide a wide range of contamination scenarios:

n_1: 30 mg of target material per m^2 of soil, equivalent to evenly dispersing 1% of the target over 1 km^2;
n_2: 300 µg m^{-2}, equivalent to evenly dispersing 1% of the target over 100 km^2, or 0.01% of the target over 1 km^2;
n_3: 3 µg m^{-2} of soil.

From the two time-points and the three cases of soil contamination, six hypothetical contamination scenarios can be defined. To reduce the input data required for simulating in Nucleonica, radionuclides with activities of less than 0.01 Bq in each sample composition were removed. The six samples are summarised in Table 4. For reference, the total mass of target material for n3 would correspond to a single particle approximately 4 µm in diameter.

Table 4. Summary of the ESS radionuclide contamination in each of the simulated soil samples

Sample	Total mass of target material (µg)	Total mass of radionuclides (ng)	Num. of gamma-ray emitters > 0.01 Bq	Total activity (Bq)
t0_n1	58.905	4.04	192	1.37 x 10^6
t0_n2	0.589	3.97 x 10^{-2}	176	1.37 x 10^4
t0_n3	0.006	3.96 x 10^{-4}	84	136.6
t350_n1	58.905	1.96	86	1.12 x 10^5
t350_n2	0.589	1.88 x 10^{-2}	61	1.12 x 10^3
t350_n3	0.006	1.88 x 10^{-4}	21	11.13

3.4. Semi-synthetic spectra

The semi-synthetic gamma-ray spectra generated by combining Nucleonica simulations with real background data are presented in Figure 3. These spectra are highly complex which presents challenges for peak identification. Regardless of the contamination scenario, it can be reasonably assumed that this level of complexity is representative of a potential real-world situation.
Both the number of lines, and the total activity of the samples can be seen to be higher in the t0 spectra; as would be expected from the decay of the shorter-lived radionuclides by t350. Significantly, it is the higher-energy lines in the t0 spectra which disappear preferentially. This means that for longer-lived nuclides with lines in this high energy region (> 2000 keV), the LoDs in a soil sample may decrease the further in time a measurement is made from a release.

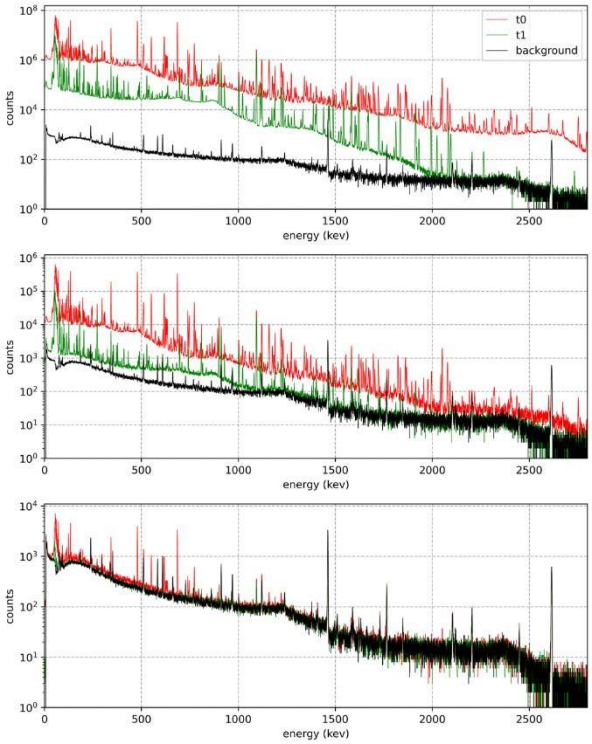

Fig. 3. Semi-synthetic gamma-ray spectra representing different fractions of target material in the simulated samples; from top to bottom: n1, n2 and n3. Spectra at two points in time were considered: the end of the 5-year operational period (t0), and 350 days after operation has ceased (t1). The background spectrum is repeated in each plot for comparison.

3.5. Estimation of gamma-ray spectroscopy LoDs

Estimates of the LoDs were manually extracted for ^{181}W, ^{187}W, ^{182}Ta and ^{175}Hf using a specific peak for each nuclide, that was observable on the spectra from Fig. 3 using the software GammaVision.
For each peak, a region of interest (ROI) in terms of energy was defined around it; and within this ROI, the peak was fitted with the sum of a linear function, to account for background, and a Gaussian function to account for the peak. From the area of the Gaussian function covering the peak of interest, the counts-above-background for this peak was obtained, with associated fit uncertainties. As the activity of each radionuclide was an input variable to the simulations used to generate the spectra, they were known for all spectra. A linear function could then be fitted to the three points of counts vs activity, resulting in a calibration that was independent of the agreement between the efficiency calibration simulated in Nucleonica and the real HPGe detector set-up used for the backgroud, for each nuclide in each set of t_0 and t_{350} spectra. The process was also repeated, for semi- synthetic spectra containing only the nuclide of interest, combined with the soil spectrum. The resulting LoDs for all nuclides studied are presented in Table 5. The values presented in Table 5 are only estimates and should be used with caution. The uncertainties stated, only take into account statistical uncertainties from the fitting algorithms used, and do not account for systematic uncertainties that could originate from the choice of ROI, the treatment of the measured soil spectra, or for the accuracy of the synthetic spectra generated in Nucleonica. The table entries which contain no data, all had uncertainties exceeding 100% of the corresponding LoD value.

Table 5. Estimates of the limits of detection (LoDs), of gamma-ray emitting radionuclides, that could be detectable in a volume of 200 ml of soil. Estimates are based on a 24h measurement by a shielded, stationary, HPGe gamma-ray spectrometer. Values for accidental release from the ESS. Uncertainties on LoDs are propagated from the fit uncertainties only.

Nuclide	T½ (days)	Fitted gamma peak	LoD (Bq) at	
			t0	t350
^{175}Hf	0.0	1221 keV	2.19±0.00	2.28±0.43
^{182}Ta	11.7	343 keV	-	-
^{181}W	21.2	65 keV	-	0.90 ± 0.0
^{187}W	1.0	479 keV	0.64±0.39	Not present

4. Discussion

4.1. Extraction of W, Hf and Ta from soil

According to the values obtained for the reference soil (Table 2), the efficiency of the phosphoric acid extraction is low for Hf and very low for Ta. The measured Ta of 0.03 ± 0.02 mg kg^{-1} also presented a large relative standard deviation. It confirms the data found in the literature [14], [15] on the difficulties to extract Ta, in particular the fact that Ta is only soluble and stable in hydrofluoric acid solutions.
The efficiency of the W extraction is better even if limited to 40%. This value is consistent with the efficiency obtained by Bednar *et al.* [13] (25% for soils with 2 mg kg^{-1} of W), for samples with low concentrations of W (25% for 2 mg kg^{-1}). According to Bednar *et al.*, this method achieves higher extraction efficiencies with samples containing metallic W or higher concentrations of W (76 to 98% for samples with more than ≈ 100 mg kg-1 of W) . This method would thus be more advantageous for the analysis of samples actually contaminated by W target materials from the ESS.
The extraction with aqua regia, the most common method for environmental monitoring, does not achieve significant extraction of W, Hf or Ta (no values above LoD measured by ICP-MS). However, it is a suitable method for other elements produced by the ESS target

such as Gd or Lu [5]. This difference of behaviour depending of the extractant could eventually be used to selectively separate and purify the elements of interest.
In the case of Ta, the alternative to pseudo-total extraction is total extraction using hydrofluoric acid that will dissolve all minerals in the soil samples and stabilise Ta in solution.

4.2 Concentrations of stable W, Hf and Ta in ESS soil samples

After normalization by the efficiencies determined in Table 2, the concentrations of W, Hf and Ta in the ESS-soil samples and their associated uncertainties can be seen in Table 3. All the concentrations of W and Hf in the soil samples are lower than, or within the expected range of, concentrations based on the FOREGS geological survey. The Ta values are above the expected values of FOREGS but the associated uncertainties are very high due to the poor extraction yield of 1.9%. The results seem homogeneous for all the locations. Thus, the analysed soil samples collected around the ESS do not seem to present existing contamination of W, Hf or Ta due to agricultural practices or road traffic.

4.3. Detection limits of W, Hf and Ta in soil by ICP-MS

According to the literature [16], the LoDs for the metals of interest measured by ICP-MS are ranging from 2 to 5 parts per trillion (ppt) in solution which means that concentrations down to the μg kg^{-1} range could be measured in soil with this analytical technique. In the case of W, the efficiency of extraction of 40% was satisfactory for the natural content of W in soils. A contamination by ESS target material would mainly be composed of stable W regardless of the target irradiation duration and the section of target affected by the accident release.
Natural variations of W concentration of ±0.3 mg kg^{-1} were observed in the soil samples. Increases of the W concentration of soil in the range of a few mg kg^{-1} could thus be attributed to a contamination by ESS materials. An increase near the local roads could however be possible due to traffic but could be confirmed or discarded by additional measurement in other locations near these roads [6]. In the case of Hf and Ta, the uncertainties on the natural concentration measured by ICP-MS reach ±1.5 and ±1.2 mg kg^{-1} respectively due their poorer extraction efficiencies (about 9% and 2% respectively). An increase of Hf or Ta concentration in soil after contamination by ESS materials would thus be harder to detect than an increase of W.
In addition, the efficiency of the extraction method for these two elements in irradiated target material or stable analogues like mixtures of metal oxides is unknown while it can reach up to 98% for W according to the litterature. In order to solve the analytical challenge posed by Hf and Ta, a total dissolution method (soil fusion or hydrofluoric acid) should be recommended to reach a LoD in the range of mg kg^{-1} measured by ICP-MS.

4.4 Semi synthetic spectra

The data extracted from the semi-synthetic spectra emphasise the challenge presented by the analysis of complex spectra which will result from the measurement of soil contaminated by target material from the ESS. The estimation of the LoD for a given ESS-specific radionuclide is also not a trivial task. In the case of ^{182}Ta, it was not possible to obtain reliable LoD estimates for any of the time points or contamination conditions examined. A ROI, ideal for a particular peak of a radionuclide, in a spectrum collected at one point in time, will not necessarily be ideal for other points in time. Great care will therefore be required when attempting to extract quantitative information in a reproducible manner from an authentic real-world-measurement. Work is currently being undertaken to systematise the process for peak LoD extraction from these spectra, using the GammaVision software package [17]. As metastable radionuclides such as ^{178n}Hf that were not included in the source term calculated with FLUKA used here, further work is required to account for them. This is particularly important for metastable nuclides such as ^{178n}Hf, that have a significant contribution to the long-term dose. Work is also being undertaken to identify a suitable key nuclide that could be used in a similar manner as ^{137}Cs is used in the long-term environmental assessment of fallout from nuclear fission releases [18].

5. Conclusions

Based on the existing source term calculations for the composition of the ESS tungsten target, the Swedish Radiation Safety Authority has established a list of radionuclides of most concern in case of environmental release including ^{148}Gd, ^{187}W, ^{172}Hf, ^{182}Ta and ^{178n}Hf. Measuring the complex mixture of ESS-specific radionuclides in the environment would present an analytical challenge.
In this article, the performance of extraction methods to quantify the existing levels of W, Hf and Ta by ICP-MS were tested. Increases in the range of mg of W per kg of soil could be detected if the samples are extracted with nitric and phosphoric acid thanks to satisfactory extraction yield of 40% of W. The extraction of Hf and Ta by phosphoric acid is more difficult with efficiencies of about 9% and 2% being achieved respectively. The quantitative extraction of these two elements would require the use of hydrofluoric acid.
Simulation of gamma-ray spectra of local soil samples contaminated by ESS-specific radionuclides have been performed. From these simulations, a LoD of <3 Bq in a 200 ml soil sample was estimated. for ^{175}Hf, ^{181}W and ^{187}W, for a 24 hour meaurment. Due to the complexity of the radionuclide mixture and its variations in time, more research is necessary to define the best nuclide candidate to monitor environmental release on the long term by gamma-ray spectroscopy, as is done with ^{137}Cs for nuclear energy related releases. This work is currently ongoing.

References

1. V. Barkauskas and K. E. Stenström Eriksson,'Prediction of the radionuclide inventory in the European Spallation Source target using FLUKA',*Nucl. Instrum. Methods Phys. Res. B*.

2. Z. Kókai *et al.*, 'Comparison of different target material options for the European Spallation Source based on certain aspects related to the final disposal', *Nuclear Instruments and Methods in Physics Research Section B: Beam Interactions with Materials and Atoms*, vol. 416, pp. 1–8, Feb. 2018, doi: 10.1016/j.nimb.2017.11.027.

3. T. Mora *et al.*, 'An evaluation of activation and radiation damage effects for the European Spallation Source Target', *Journal of Nuclear Science and Technology*, vol. 55, no. 5, pp. 548–558, May 2018, doi:10.1080/00223131.2017.1417173.

4. Strålsäkerhetsmyndigheten, 'Underlag till placering i beredskapskategori för ESS och beredskapsplaneringen kring anläggningen', SSM2018-1037–4, Apr. 2018.

5. G. Pédehontaa-Hiaa, C. Bernhardsson, V. Barkauskas, K. Eriksson Stenström, C. L. Rääf, and S. Mattsson, 'Region-specific radioecological evaluation of accidental releases of radionuclides from ESS', Strålsäkerhetsmyndigheten, SSM2019-1010

6. M. Bäckström, U. Nilsson, K. Håkansson, B. Allard, and S. Karlsson, 'Speciation of Heavy Metals in Road Runoff and Roadside Total Deposition', *Water, Air, & Soil Pollution*, vol. 147, no. 1, pp. 343–366, Jul. 2003, doi: 10.1023/A:1024545916834.

7. A. Koutsospyros, W. Braida, C. Christodoulatos, D. Dermatas, and N. Strigul, 'A review of tungsten: From environmental obscurity to scrutiny', *Journal of Hazardous Materials*, vol. 136, no. 1, pp. 1–19, Aug. 2006, doi: 10.1016/j.jhazmat.2005.11.007.

8. M. Filella, 'Tantalum in the environment', *Earth- Sci. Rev.*, vol. 173, pp. 122–140, Oct. 2017, doi: 10.1016/j.earscirev.2017.07.002.

9. I. Shtangeeva, 'Accumulation of scandium, cerium, europium, hafnium, and tantalum in oats and barley grown in soils that differ in their characteristics and level of contamination', *Environ Sci Pollut Res*, vol. 29, no. 27, pp. 40839–40853, Jun. 2022, doi: 10.1007/s11356-021-18247-y.

10. G. Petruzzelli and F. Pedron, 'Influence of Increasing Tungsten Concentrations and Soil Characteristics on Plant Uptake: Greenhouse Experiments with Zea mays', *Applied Sciences*, vol. 9, no. 19, Art. no. 19, Jan. 2019, doi: 10.3390/app9193998.

11. I.-D. S. Adamakis, E. P. Eleftheriou, and T. L. Rost, 'Effects of sodium tungstate on the ultrastructure and growth of pea (Pisum sativum) and cotton (Gossypium hirsutum) seedlings', *Environmental and Experimental Botany*, vol. 63, no. 1, pp. 416–425, May 2008, doi: 10.1016/j.envexpbot.2007.12.003.

12. C. Bernhardsson *et al.*, 'Assessment of "Zero Point" radiation around the ESS facility', Lund University, MA RADFYS 2018:01, BAR-2018/04, 2019.

13. A. J. Bednar, W. T. Jones, M. A. Chappell, D. R. Johnson, and D. B. Ringelberg, 'A modified acid digestion procedure for extraction of tungsten from soil', *Talanta*, vol. 80, no. 3, pp. 1257–1263, Jan. 2010, doi: 10.1016/j.talanta.2009.09.017.

14. 'Foregs Geochemical Atlas'. http://weppi.gtk.fi/publ/foregsatlas/index.php (accessed Oct. 30, 2020).

15. C. Reimann and P. de Caritat, 'Establishing geochemical background variation and threshold values for 59 elements in Australian surface soil', *Science of The Total Environment*, vol. 578, pp. 633–648, Feb. 2017, doi: 10.1016/j.scitotenv.2016.11.010.

16. Inorganic Ventures, 'Inorganic Ventures, Periodic Table', Oct. 19, 2022. https://www.inorganicventures.com/periodic-table

17. R. J. W. Frost *et al.*, 'A simulation-based approach to evaluating the detection limits of spallation products in environmental samples by gamma-ray spectroscopy', *manuscript in preparation*.

18. C. Rääf, R. J. W. Frost, C. Bernhardsson, and G. Pédehontaa-Hiaa, 'Projected external-doses from an accidental release of ESS spallation-target products -- Time-dependence and radionuclide contribution', *manuscript in preparation for Nordic Society of Radiation Protection conference proceedings*.

MEDICAL PHYSICS IN THE BALTIC STATES 16 (2023)

Proceedings of International Conference "Medical Physics 2023"
09-11 November 2023, Kaunas, Lithuania

ENVIRONMENTAL RADIATION BASELINE AROUND THE BELARUSIAN NUCLEAR POWER PLANT – ASSESSMENTS IN BELARUS AND LITHUANIA

Christian BERNHARDSSON[1], Valery RAMZAEV[2], Aliaksandr DVORNIK[3], Mattias JÖNSSON[1], Guillaume PÉDEHONTAA-HIAA[1], Kristina ERIKSSON-STENSTRÖM[4], Christopher RÄÄF[3], Charlotta NILSSON[4], Mattias OLSSON[5], Siarhei HAPONENKA[3], Vytenis BARKAUSKAS[6], Vladislav NEKRASOV[2], Aleksandr VODOVATOV[2], Larisa CHIPIGA[2], Andrius PUZAS[6], Ieva JOGAITE[7], Diana ADLIENĖ[7], Sören MATTSSON[1]

Author affiliations as during the time of the respective expeditions

[1]Medical Radiation Physics Malmö, Department of Translational Medicine, Lund University, Sweden; [2]St Petersburg Research Institute of Radiation Hygiene named after Professor P.V. Ramzaev, Russia; [3]Institute of Radiobiology National Academy of Sciences of Belarus, Belarus; [4]Department of Physics, Division of Particle and Nuclear Physics, Lund University, Sweden; [5]Lund University, Department of Geology, Lund, Sweden; [6]Center for Physical Sciences and Technology, Vilnius, Lithuania; [7]Kaunas University of Technology, Kaunas, Lithuania
christian.bernhardsson@med.lu.se

***Abstract*:** Prior to the operation of the first Belarussian nuclear power plant (BelNPP), the baseline of the radiation environment was determined within a radius of about 30 km from BelNPP. This independent assessment was carried out during two expeditions in 2019. In 2022, a similar survey was carried out (during the initial operation of BelNPP) on the Lithuanian side of the boarder. Here we present the overall project and some general results of the baseline assessments.

Keywords: Astravets, activity concentration, radionuclides, dose rate, baseline.

1. Introduction

At the 14th Medical Physics in the Baltic States conference (2019), we reported on the intention of performing zero-point assessments around the Belarusian nuclear power plant (BelNPP) and around the European Spallation Source (ESS) in Lund, Sweden [1]. Here we present an update of the radiation baseline assessments carried out around BelNPP (in Belarus and in Lithuania) and show some general results of the radiation levels in the area.

Before commissioning of a NPP, a pre-operational monitoring must be conducted. This baseline (zero point) is later used as a basis for the NPP´s environmental monitoring program during the operational phase, and later, at the post-operational phase. The results of the monitoring programs, reported at regular intervals, allow for direct and retrospective assessments of doses to the representative person [2]. The preoperational mapping includes contributions from past events, if any, *e.g.* radioactive contamination from the operation of the decommissioned Ignalina NPP (100 km north of BelNPP), the Chernobyl accident, and global fallout; contributions from natural and anthropogenic sources form the baseline during the pre-operational monitoring. Additional contributions to the baseline exposure (*e.g.* discharges from a NPP) may later add to the baseline and be compared to the pre-operational exposure level. Hence, the purpose of pre-operational assessments of the radiation environment are several: to establish a zero-point of the radiation exposure and its variability; to obtain background data for identification of diffuse long-term discharges; to gather data for reporting to authorities and the public; to act as the basis for measures/improvements as well as continued research and development.

The first nuclear power plant in Belarus is located in the Astravets district of the Grodno region (N54.76, E26.09), about 130 km (NW) from Minsk and about 50 km (E) from Vilnius. The area is characterized by farmlands, forests, and villages with Astravets being the main town of the region with a population of about 11 000 in 2018 [3]. The Viliya river crosses the region (and the 12.9 km observation zone) into Lithuania (Neris), after which it floats into the Baltic Sea. BelNPP is operating two 1194-MW Russian VVER-1200 reactors (water-water energetic reactors of type AES-2006 Atomstroyexport). The first reactor of BelNPP was connected to the electrical grid on May 10, 2021, and the second reactor was connected to the network in July 2023, as stated by the official news of BelNPP [4,5].

Since 2016 the governmental institution Belhydromet has been monitoring the radiation environment within and around the observation zone (12.9 km radius) [6]. Apart from environmental samplings, there are also automated radiation monitoring systems installed around BelNPP

that can be viewed online (https://rad.org.by/). The assessment program of the preoperational baseline of Belhydromet is now, during the operation phase, handled by BelNPP [7].

To our knowledge, the assessment described here forms the only independent baseline around BelNPP, covering gamma emitters, ^{3}H and ^{14}C in Belarus and in Lithuania. The present baseline provides background information on natural and anthropogenic sources of radiation in the areas monitored prior to the full operation of the BelNPP. It is based on monitoring of gamma-emitting radionuclides (*in situ*, dose rate in air, activity concentration in soil and in various foodstuffs), activity concentrations of ^{3}H (waters and various foodstuffs), and ^{14}C (grass and various foodstuffs). Here we present the general outline of the baseline assessments conducted in Belarus and in Lithuania with general preliminary results of the studies.

2. Structure of the baseline monitoring program

The independent monitoring program around BelNPP was carried out with support from the Swedish Radiation Safety Authority (SSM). The working group consisted of members from long-lasting cooperation between Lund University (LU) and Russia (Institute of Radiation Hygiene, IRH), Belarus (Institute of Radiobiology, IRB) and Lithuania (Center for Physical Sciences and Technology, FTMC; Kaunas University of Technology, KTU). The developed program was based on previous experience and recommendations of similar assessments, *e.g.* [8,9]. The aim was to get a detailed map of the radiation environment around BelNPP in Belarus and Lithuania, with reference sites that are expected to also be accessible in the future.

The general strategy of the program was to determine the radiation environment in the air, in the ground, in water, at a number of selected sites as well as samplings at these sites and in between them. The intention was also to cover as many sites as possible during the limited time of the expeditions, 2×4 days in Belarus and 3 days in Lithuania, to increase the chances of re-visiting the sites unchanged in the future. The radiation environment at each of the sites was mapped in the same way and samples were collected where it was possible and relevant. The general assessment approach for the radiation baseline assessments in the current program was as follows:

Selection of sites

The sites in Belarus were selected to be in the vicinity of the BelNPP, accessible by car, covering all wind directions (equally distributed around the NPP), preferably on flat surfaces with no obscuring nearby objects. Geographic coordinates were determined for all sites using GPS navigators. Some sites were selected together with Belhydromet to overlap with their reference sites. In total, 45 sites within about 30 km of BelNPP were covered in the program in Belarus (Fig. 3). In Lithuania, the same criteria were used when selecting the sites, with the additional condition that the sites should be distributed along the border to Belarus from Ignalina decommissioned NPP in the north to about 30 km south of Vilnius. In total, 17 sites were covered in the program in Lithuania (Fig. 4). Based on the above criteria, the best sampling locations were determined by visual inspection of the selected sites. The large number of sites investigated increases the chances of future re-assessments of several of the same sites without any physical disturbances having altered the radiation environment at the sites.

In situ measurements

At each of the selected sites, a pre-defined measurement program was conducted. Centrally in each of the flat and opened areas (about 40×40 m^2), a squared surface was defined (about 5×5 m^2) and a portable NaI(Tl) gamma spectrometer-dosimeter (63 mm (Ø) × 63 mm) MKS AT6101D (ATOMTEX, Belarus) was used for measurement of *in situ* gamma spectra and assessment of dose rate of gamma radiation (acquisition time >15 min) (Figs. 1,2). In close vicinity of the surface (in Belarus only), a stationary passive optically stimulated luminescence dosemeter (OSLD) was positioned 1 m above the ground. The light-proof and carefully protected OSLD holder contained 10 individual NaCl pellets [10], for later retrieval and readout. At three evenly distributed positions within the surface, the ambient dose equivalent rate in air was measured for about 15 min at each position, using an Automess dose rate meter with a 6150AD-b/E scintillator probe (Automess, Germany). In addition, over the extended area covering the surface, a backpack-configured (1.5″×1.5″) $LaBr_3$ detector with 1 s acquisition time, was used for mapping the variation in the gamma radiation fields over the selected areas in Belarus. On average, 600 measurement positions were acquired at each site.

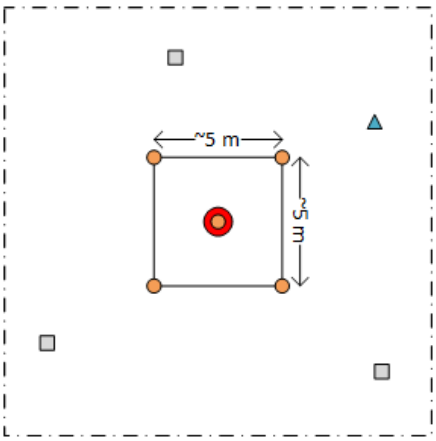

Fig. 1. A top view sketch of the assessments at the sites (about 40×40 m^2) and soil sampled surface (about 5×5 m^2). The five small circles indicate where soil cores were taken, the large circle indicates the position of the *in situ* detector, the squares illustrate where dose rate assessments were carried out and the triangle illustrates the position of the OSLD. The large area was covered by mobile (backpack) spectrometric measurements.

Collection of samples

Deep soil core samples were taken at each site. The principle of the sampling was according to the "envelope" method, with one core in each corner of the surface and one core in the center of the surface (Fig. 1). Each core had a length of >20 cm (Ø=5 cm) and was

divided into slices corresponding to: 0-2.5 cm, 2.5−5 cm, 5−7.5 cm, 7.5−10 cm, 10−15 cm, and 15−20 cm. Each soil layer from the five cores was then mixed into one sample for each depth for the individual sites in Belarus and in Lithuania. Due to logistics, about half of the soil samples collected in Belarus were analyzed at IRH, all other samples were analyzed at LU. Activity concentrations of gamma-emitting radionuclides were measured using lead-shielded semiconductor gamma spectrometers. Intercomparison measurements between IRH and LU were made previously and the results agreed within the estimated uncertainty intervals [11].

Apart from soil samples at the selected sites, other samplings were carried out in the areas between the sites in order to determine potential exposures and pathways to the people living in the area. Additional samplings in Belarus included apples, carrots, beetroot, potatoes, and grass for analysis of gamma-emitting radionuclides and samples from various waterbodies for ^{3}H analysis using liquid scintillator counting (Beckman LS 6500). Furthermore, some samples of grass, apple, potato, and beetroot were analyzed for ^{3}H, and ^{14}C concentrations using single-stage accelerator mass spectrometry (SSAMS) at Lund University. ^{14}C levels were determined in terms of the unitless quantity fraction modern, F^{14}C [12]. In Lithuania, apart from soil samples at the reference locations, apples, carrots, fern, and needles of spruce were collected for analysis of gamma-emitting radionuclides, and various environmental samples were collected for analysis of ^{3}H and ^{14}C.

Fig. 2. Photo of a site in Belarus for *in situ* gamma spectrometry, mobile mapping, soil sampling, measurement of ambient dose equivalent rate, and positioning of stationary dosemeters according to Fig. 1.

2.1. Assessments in Belarus

Pre-operational data were collected in Belarus in 2019, before the start of the first reactor. One expedition was carried out in September and one in October, with about 10 participants during each expedition, covering 45 sites (Fig. 3). The sites within ~5 km from BelNPP were distributed evenly in all directions. Further out, up to 30 km from BelNPP, the sites were fairly evenly distributed and at places accessible by car.

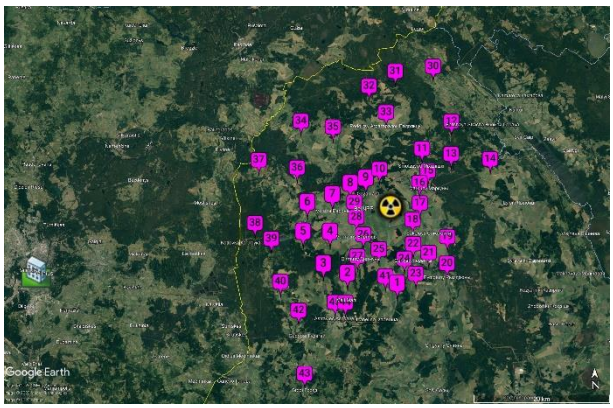

Fig. 3. Location of sampling sites in Belarus around BelNPP (marked with ☢) on a Google Earth map. Vilnius is marked with 🏛.

2.2. Assessments in Lithuania

As it was not possible to accomplish the baseline assessments in Lithuania prior to the commissioning of both reactors at BelNPP, the expedition to Lithuania took place in November 2022, just after the start of the operation of both reactors. Although this is not a zero-point baseline *per se*, it may still be used for comparison to future assessments at the reference locations, keeping in mind the short operation of BelNPP in November 2022. Seven persons from LU, FTMC and KTU participated during the expedition, covering 17 sites (Fig. 4). The sites were distributed along the border to Belarus from Ignalina NPP (decommissioned in 2009) in the north to Turgeliai in the south, the latter located about 30 km south of Vilnius. The sampling sites were selected denser close to Ignalina NPP: just outside the entrance, +200 m, +1300 m, +4300 m, +9000 m.

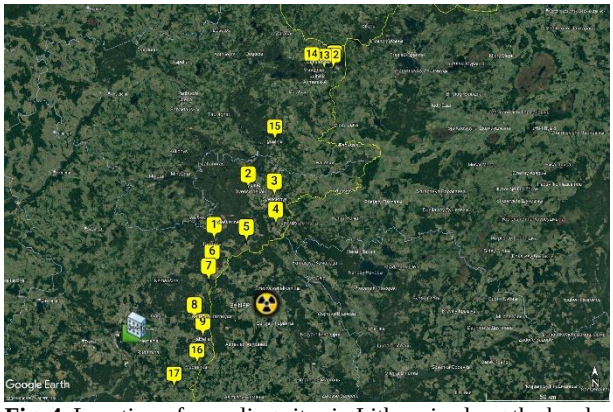

Fig. 4. Location of sampling sites in Lithuania along the border to Belarus on a Google Earth map. BelNPP is marked with ☢ and Vilnius is marked with 🏛.

3. Results

Here we present the preliminary results and general trends observed during the three expeditions. The reported activity concentrations in soil in Belarus represent about 50% of the sites that were measured at LU. The final results of the baseline assessment programs in Belarus and in Lithuania will be reported in separate publications.

3.1. Radiation baseline around BelNPP in Belarus

Ambient dose equivalent rate

In situ gamma spectrometry at the 45 different sites in Belarus showed ambient dose equivalent rates, 1 m above the ground, in the range 32 to 72 nSv/h (average = 53 nSv/h, with a coefficient of variation, C_v = 17%), completely dominated by natural gamma-emitting radionuclides. The stationary measurements using the scintillation probe showed ambient dose equivalent rates, 1 m above the ground, in the range 67 to 113 nSv/h (average = 87 nSv/h, C_v = 12%). This is in agreement with the "Pre-operational studies in the area of the Belarussian NPP (zero background)" by LLC Environmental Safety Agency [13] that indicated dose rates in the range 49 to 95 nSv/h (closer to the NPP and using a car-mounted detector system). The variability within the sites, in terms of C_v, for the mobile (backpack) assessments, was on average 13%. The corresponding number for the variability between the sites was 33%. None of the OSLD´s have yet been collected from the stationary positions at the different sites.

Concentration of gamma-emitting radionuclides in various samples

In short, *ex situ* assessments of the soil samples were performed for the activity concentration of naturally occurring radionuclides: ^{40}K, ^{214}Bi (a decay product of ^{238}U series), ^{228}Ac (decay product in the ^{232}Th series) and anthropogenic ^{137}Cs. The naturally occurring radionuclides were, as expected, found at all depth layers, with slightly varying concentrations depending on *e.g.* the composition of the soil. Only a few soil samples (n=8) had ^{137}Cs activity concentrations below the minimum detectable activity (MDA). For the aforementioned radionuclides, the average activity concentrations (on dry weight, d.w.) were, respectively:

$A_{avg}(^{238}U)$ = 17.3 Bq/kg (range: 1.1−34 Bq/kg),
$A_{avg}(^{232}Th)$ = 19.6 Bq/kg (range: 5.3−36 Bq/kg),
$A_{avg}(^{40}K)$ = 520 Bq/kg (range: 151−872 Bq/kg),
$A_{avg}(^{137}Cs)$ = 5.0 Bq/kg (range: 0.8−21 Bq/kg).

As for the other environmental samples, the studied radionuclides were below the MDA for the measurement times: $MDA_{avg}(^{238}U)$ = 47 Bq/kg, $MDA_{avg}(^{232}Th)$ = 20 Bq/kg, $MDA_{avg}(^{137}Cs)$ = 5.5 Bq/kg. The average activity concentration of ^{40}K was measured to 837 Bq/kg for the grass (n=14) and 324 Bq/kg for apples (n=7).

Activity concentrations of ^{3}H and ^{14}C in various samples

The activity concentration of ^{3}H in samples of foodstuff collected near the investigated sites (including apples, carrot, beetroot and potato; n=11) was below the MDA of 1.64 Bq/L for 6 samples and was on average 2.0±0.9 Bq/L for the 5 samples above MDA (range: 1.67−2.70 Bq/L). A total of 36 samples of water from rivers, lakes, and private and public wells were also measured. Only 8 out of 36 water samples were above the MDA of 1.64 Bq/L with an average activity concentration of 2.0±0.8 Bq/L (range: 1.65−2.69 Bq/L). The measured values in foodstuff and water were all in the expected range of activity concentrations for the environmental samples. Thus, no anthropogenic tritium contamination was detected during the assessment.

Samples of grass, apple, potato, and beetroot (n=20) were analyzed for their $F^{14}C$ values. The average $F^{14}C$ was 1.011 (range: 1.003−1.016) [12]. As reported in [12], this indicates no evidential traces of ^{14}C from the Chernobyl accident or from other present or nearby sources.

3.2. Radiation baseline around BelNPP in Lithuania

Ambient dose equivalent rate

In Lithuania, *in situ* NaI(Tl) assessments at the 17 sites showed ambient dose equivalent rates, 1 m above the ground, in the range 38 to 72 nSv/h (average = 50 nSv/h, C_v = 19%). Corresponding measurements using the scintillation probe at the same sites showed ambient dose equivalent rates, 1 m above the ground, in the range 76 to 112 nSv/h (average = 93 nSv/h, C_v = 11%).

Concentration of gamma-emitting radionuclides in various samples

The soil samples from Lithuania were analyzed with respect to the same radionuclides as the samples from Belarus. As for the soil sampled in Belarus, the soil from Lithuania showed varying concentrations of the naturally occurring radionuclides with small amounts of ^{137}Cs. Several soil samples (n=39) had ^{137}Cs activity concentrations below the MDA. For the respective radionuclides studied the average activity concentrations (d.w.) were, respectively:

$A_{avg}(^{238}U)$ = 18.9 Bq/kg (range: 8.1−81 Bq/kg),
$A_{avg}(^{232}Th)$ = 18.0 Bq/kg (range: 4.6−38 Bq/kg),
$A_{avg}(^{40}K)$ = 538 Bq/kg (range: 303−1550 Bq/kg),
$A_{avg}(^{137}Cs)$ = 4.4 Bq/kg (range: 0.8−23 Bq/kg).

As for the other environmental samples, the studied radionuclide concentrations were below the MDA for the indicated measurement time: $MDA_{avg}(^{238}U)$ = 75 Bq/kg, $MDA_{avg}(^{232}Th)$ = 33 Bq/kg, $MDA_{avg}(^{137}Cs)$ = 8.8 Bq/kg, except for ^{40}K (range: 216 Bq/kg (one sample of grass) to 1.8 kBq/kg (one sample of carrot)).

Activity concentration of ^{3}H and ^{14}C in various samples

The activity concentration of ^{3}H in water was above the MDA of 1.64 Bq/L in only one of the 6 samples measured (river or private well water) with 2±1 Bq/L measured in a river water sample. Thus, no contamination with ^{3}H was detected during the assessment in Lithuania.

None of the samples collected in Lithuania has yet been analyzed for ^{14}C.

4. Conclusions

The independent preoperational assessment programs around the BelNPP include 45 sites in Belarus and 17 sites in Lithuania (along the border to Belarus). The preliminary results show no unexpected activity concentrations (gamma emitters, ^{3}H, ^{14}C) and insignificant amounts of Chernobyl ^{137}Cs. As expected, considering the short distance between the sites, the assessments at the 17 sites in Lithuania are (on average) in good agreement with the 45 sites in Belarus, both in terms of the assessed ambient dose equivalent rates and *ex situ* measurements of soil samples.

5. Funding

This work was financially supported by the Swedish Radiation Safety Authority (SSM2019-6032).

6. Acknowledgments

The authors would like to thank the inhabitants of the visited locations for providing help and access to sites and samples. We also would like to thank the staff of BelNPP information centre in Astravets for their help with logistic and administrative support as well as the staff at Ignalina NPP for granting us access to the sampling sites.

References

1. Bernhardsson C., Eriksson Stenström K., Mattsson S., et al. Zero point assessment of the radiation environment – examples of a program applied in Sweden (ESS) and in Belarus (BelNPP). Proceedings of the 14th International conference ”Medical Physics in the Baltic States”, Kaunas, 2019, p. 85-88.
2. International Atomic Energy Agency, Environmental and source monitoring for purpose of radiation protection, IAEA safety standards No. RS-G-1.8, IAEA, Vienna (2005).
3. National statistics committee – the republic of Belarus: Population as of January 1, 2018 and the average annual population for 2017 in the republic of Belarus by regions, districts, cities, urban settlements. https://www.belstat.gov.by/ofitsialnaya-statistika/publications/izdania/public_bulletin/index_8782/ (14 September, 2023, date accessed). (In Belarusian).
4. Belarusian nuclear power plant hompage (news). *The first power unit of BelNPP is connected to the electric grid*. https://belaes.by/en/news/item/3268-pervyj-energoblok-belaes-vklyuchen-v-set.html (14 September, 2023, date accessed).
5. Belarusian nuclear power plant hompage (news). *The second power unit of BelNPP is connected to the network*. https://belaes.by/en/news/item/4055-vtoroj-energoblok-belaes-vklyuchen-v-set.html (14 September, 2023, date accessed).
6. The Ministry for Emergency Situations of the Republic of Belarus. *Overview of the state of nuclear and radiation safety in the Republic of Belarus for 2019*. https://gosatomnadzor.mchs.gov.by/upload/iblock/dcd/the_review_of_a_status_of_nrs_in_belarus_2019_ru.pdf (14 September, 2023, date accessed). (In Russian).
7. Report on radiation-and-environmental monitoring in the area of the Belarusian Nuclear Power Plant. State enterprise ”Belarusian NPP”. https://belaes.by/images/data/09-01-2023-2.pdf. (14 September, 2023, date accessed).
8. Bernharsson C., Eriksson Stenström K., Jönsson M., et al. Assment of „Zero Point“ radiation around the ESS facility. (MA RADFYS 2018:01)(BAR-2018/04). Lund University.
9. Eriksson Stenström K., Skog G., Bernhardson C., et al. Environmental levels of radiocarbon in Lund, Sweden, prior to the start of the Europena spallation source. Radiocarbon, 64(1): 51-67, 2022.
10. Waldner L. and Bernhardson C. NaCl pellets for prospective dosimetry using optically stimulated luminescece: signal integrety and long-term versus short-term exposure. Radiation and Environmental Biophysics. 59:693-702, 2020.
11. Ramzaev V.P., Bernhardsson C., Dvornik A.A., Bakarikova Zh.V., Karlberg O., Vodovatov A.V., Jönsson M., Nekrasov V.A. Results of international comparison tests on determination of ^{137}Cs activity concentration in soil samples. *Radiatsionnaya Gygiena* = Radiation Hygiene. 2020. Vol. 13, No. 4 P. 101-109.
12. Stenström Eriksson K., Barkauskas V., Bernhardsson C., et al. Preoperational assessment of ^{14}C in the vicinity of the Belarusian nuclear power plant. Proceedings of the 15th International conference ”Medical Physics in the Baltic States”, Kaunas, 2021, p. 133-137.
13. Express report: Pre-operational studies in the area of the Belarusian NPP (zero background). Ekatrinburg, 2019. https://www.belaes.by/ru/otchet-po-rezultatam-ekologicheskogo-monitoringa-v-zone-nablyudeniya-belorusskoj-aes.html. (14 September, 2023, date accessed). (In Russian).

MEDICAL PHYSICS IN THE BALTIC STATES 16 (2023)

Proceedings of International Conference "Medical Physics 2023"
09-11 November 2023, Kaunas, Lithuania

FEASABILITY OF USING A PORTABLE OSL READ-OUT UNIT FOR DOSE ASSESSMENT OF NaCl PELLETS

Maria KARAMPIPERI[1], Christopher L. RÄÄF[2], Christian BERNHARDSSON[3]
Medical Radiation Physics, Department of Translational Medicine, Lund University, Sweden
[1]maria.karampiperi@med.lu.se; [2]christopher.raaf@med.lu.se; [3] christian.bernhardsson@med.lu.se

***Abstract*:** The current study investigates the performance of a portable OSL/IRSL reader during radio-nuclear emergency situations, for *in situ* estimation of the public exposure using NaCl pellets. The dose range varied between 0.52 and 381 mGy and the response is compared with two common laboratory readers for dosimetry applications. A linear response was found for both IRSL and OSL. The minimum detectable dose for the portable reader, is about 1.7 and 52.5 μGy for OSL and IRSL read-out, respectively.

Keywords: salt pellets, prospective dosimetry, Optically Stimulated Luminescence (OSL), SUERC reader, NaCl

1. Introduction

Under the threat of a radiological or nuclear accident or a terrorist attack involving release of radionuclides, the application of retrospective and prospective dosimetry is imperative. Estimation of the public's exposure in the earliest possible stage is crucial for the determination of the appropriate measures in the exposed area and for public information on the radiological consequences.

One of the most common methods applied into retrospective and prospective radiation dosimetry is Optically Stimulated Luminescence (OSL), where the investigated sample material is stimulated by light, in the optical spectrum (blue, green or violet). When infra-red wavelength is used, the method is called IRSL (Infra-Red Stimulated Luminescence). After the material is stimulated by light, a luminescence signal is recorded, that in turn is proportional to the radiation dose of the material.

Among other investigated materials for dose assessments of the population, ordinary household salt exhibits promising OSL and IRSL properties [1-4]. Prior studies show that pellets pressed by common household salt exhibit e.g. a high luminescence signal per unit absorbed dose, low detection threshold, and high stability, properties needed for dosimetry probes for dosimetry applications [5].

However, the use of dedicated stationary readers to extract information regarding the dose exposure may implement delays. Hence, research groups have started to study the potential of using homemade/portable readers in combination with ordinary salt grains, for retrospective dosimetry [6-8].

The current study investigates the potential use of a portable OSL/IRSL read-out unit, called SUERC (SUERC, Glasgow, UK), which was initially developed for geological and/or archaeological applications [9], in combination with NaCl pellets. Dosimetric characteristics, such as dose response and detection limits, are examined with the use of SUERC, and are compared to two common laboratory-based readers, the Risø TL/OSL, DA-20 and DA-15 (DTU Physics, Denmark).

2. Materials & Methods

2.1 NaCl pellets production

A common Swedish sea salt (Falksalt® finkornigt medelhavssalt, Hanson & Möhring, Sweden) was used for producing the NaCl pellets. All pellets were produced from the same box of salt. Grains with sizes between 100 and 400 μm were selected through sieving, as the pellets produced using this size of grains exhibit optimal mechanical and luminescence properties [5].

For the production, a desktop tablet press tool (TDP 0 Desktop Tablet Press, LFA Machines Oxford, Ltd) was used. Using this press, applying approximately 0.5 tonnes pressure, it is possible to produce about 1200 pellets per hour. The NaCl pellets have a diameter of 4mm, thickness of 0.8±0.2 mm and a weight of 28±1 mg. The whole process of pellet production took place under light conditions. Therefore, potential natural signal is fully depleted prior to using the pellets. The pellets were stored before use for about three days for stabilisation of the luminescence properties, as previously suggested [10].

2.2 Irradiation & Read-out units

The pellets were irradiated in the Risø TL/OSL readers (models DA-15 and DA-20) with beta radiation sources of $^{90}Sr/^{90}Y$, with nominal dose rates of 3.81 mGy/s and

0.52 mGy/s, at the time of the measurements. Therefore, the applied dose range was between 0.52 mGy and 381 mGy. After irradiation, the samples were stored in lightproof plastic film canisters. Between irradiation and read-out, approximately two days elapsed. The aim of this storage period is to overcome the acute fading period, and thus, no fading is concerned between exposure and measurements [5].

The OSL/IRSL measurements were conducted using three different readers: two Risø TL/OSL readers (models DA-15 and DA-20) and the SUERC portable OSL reader. The main characteristics, such as the wavelength (λ), the maximum output power (P_{max}) and the applied output power (P_{used}) of the readers are presented in Table 1 [9],[11]. The applied LEDs' power of the Risø readers was tuned so that it approached the power of the SUERC LEDs (not tunable). For blue LEDs, the two Risø readers were in good agreement with the SUERC reader, while for the IR light, the discrepancy in the output power is about 20%. In both Risø units, two Hoya U-340 filters were applied (5- and 2.5-mm thickness), while in SUERC a UG11 was employed. The filter combinations remained the same for both OSL and IRSL read-outs.

Table 1. Characteristics of the three readers under investigation.

Reader	Stim. Light	λ (nm)	P_{max} (mW)	P_{used} (mW)
Risø DA-15	Blue	470	47	29
	IR	870	168	113
Risø DA-20	Blue	470	86	27
	IR	850	348	104
SUERC	Blue	470	25	25
	IR	880	90	90

2.3 Protocols

Two different read protocols were applied in the current study (Table 2). The first one was for investigating the OSL dose response, using blue light. Step 3 in Table 2 is applied in order to investigate the depletion degree during the first OSL read-out. Steps 3 and 6 have the same purpose, when combining the IRSL and OSL read-outs. Furthermore, after the IRSL measurements, OSL read-outs are included in order to investigate if the prior stimulation with IR light influences the signal of the blue stimulation. For all stimulations, the continuous wave (CW) mode was applied.

Table 2. OSL and IRSL protocols applied for the evaluation of the readers.

Step	OSL Protocol	Combination of IRSL and OSL
1	Dark counts (10 s)	Dark counts (15 s)
2	OSL (30 s)	IRSL (30 s)
3	Residual OSL (30 s)	Residual IRSL (30 s)
4	Dark counts (10 s)	Dark counts (15 s)
5		OSL (30 s)
6		Residual OSL (30 s)
7		Dark counts (15 s)

3. Results & Discussion

3.1. SUERC reader's sensitivity for NaCl pellets

Considering that the geometry of SUERC reader is designed for geological samples, where large mass is used, the small size of NaCl pellets, combined with the distance from the PMT, results in a relatively low signal, compared to the Risø readers. In addition, the dose range which is appropriate for retrospective dosimetry is lower compared to the one relevant to geological applications. Therefore, the first step was to determine the optimal number of pellets that should be placed together in the petri dish of the SUERC reader.

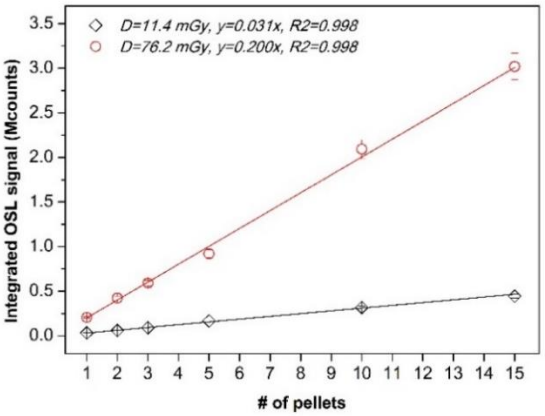

Fig. 1. OSL signal in relation to the number of pellets used with SUERC reader, for two different doses: 11.4 mGy and 76.2 mGy. The uncertainty corresponds to 5% of the value.

Figure 1 depicts the integrated OSL signal with respect to the number of pellets used, for 11.4 and 76.2 mGy. A linear expression is found between the signal and the number of pellets. If less than 5 pellets are used, the signal is very low and the OSL curves are not properly distinguishable, especially for lower doses. This issue becomes more obvious when using IRSL, since the signal is about 44 times lower than for OSL, as described further. On the other hand, a large number of pellets is impractical for realistic situations. Thus, for all further read-outs, 5 pellets are used for the measurements with the SUERC reader. For both Risø readers, one pellet was used at a time. However, for all three readers, all measurements were repeated four times, on new (sets of) pellets, for statistical purposes. For comparison with the two stationary readers, the signal of the SUERC reader is normalized to the number of pellets.

3.2. Reproducibility in SUERC

An additional reason for using more than one pellet per read-out is the reproducibility of the signal. To evaluate the reproducibility of the pellets, OSL curves were recorded for 8 individual pellets, after irradiation with 11.4 mGy. The standard deviation was about 8% of their mean signal. The reproducibility was also measured by 5 sets of 10 pellets combined, also irradiated with the same dose. In this case, the standard deviation was about 4% of their mean signal, leading to more reproducible curves. For comparison, for the same

dose, the reproducibility in the DA-20 and DA-15 was about 15% and 5%, respectively.

3.3. Background measurements

The signal of unirradiated pellets is considered as background. Table 3 illustrates the background signals as recorded for the three readers, for the OSL and IRSL signals, respectively. The background is the results of the average of the first 15 s of the curve, while the uncertainty corresponds to the standard deviation of four measurements, with different samples. Considering the SUERC reader, some modifications were necessary in order to increase the sensitivity of the reader with respect to NaCl pellets. The geometry of this reader is designed for geological applications. However, the small dimension of the salt pellets covers only a very small surface of the holder, leading to higher background reflection. Therefore, a piece of Styrofoam was placed inside of the petri dish, with a black paper cover, leading to significant background signal reduction.

Table 3. Background signal (counts/s) for the three readers.

Stimulation type	Risø DA-20	Risø DA-15	SUERC
OSL	10.4 ± 0.7	35.1 ± 2.0	15.3 ± 1.9
IRSL	1.9 ± 0.3	30.2 ± 2.1	5.4 ± 0.7

3.4. Dose response

The dose response of the NaCl pellets in the three readers is depicted in Figure 2a for the blue light stimulation and Figure 2b for the infra-red stimulation, in a logarithmic scale in order to easier visualize the entire dose range. For OSL, it is shown that both Risø readers and the SUERC reader exhibit similar response, while the signal of the SUERC reader normalized to the number of pellets is significantly lower. For the IR stimulation, the DA-20 and DA-15 exhibit similar signals, while the SUERC reader records lower signals. The trend of all dose response curves can be described with a linear regression (linear scale), or a power equation (logarithmic scale).

In both OSL and IRSL, the residual signals were recorded. For OSL, the DA-20 and DA-15 readers present residual signals of about 3% of the initial OSL signal, while for the SUERC reader the residual is about 8%, showing that the depletion degree of the NaCl pellets is less with the SUERC. Regarding IRSL, the residual signals correspond to about 20% of the initial IRSL signals for DA-20 and DA-15, while it corresponds to about 30% for SUERC. In IR stimulation, the residual signal is important and not negligible for any of the readers, with SUERC showing again the lowest degree of depletion.

The purpose of evaluating the combination of IRSL and OSL read-outs in the same protocol was to investigate the possibility of using a rapid screening of samples using IRSL followed by a more accurate dose estimation using OSL. Therefore, the OSL signal of the first protocol (direct OSL) is compared to the OSL signal after two IRSL read-outs (subsequent OSL). The results indicate that the subsequent OSL is reduced by 2% and 5% compared to the direct OSL, for the DA-15 and DA-20 respectively. On the other hand, for the SUERC, the subsequent OSL signal was found 24% lower compared to the direct signal. The latter case shows the importance of implementing a correction factor, if IRSL and OSL are applied in combination, during measurements with SUERC.

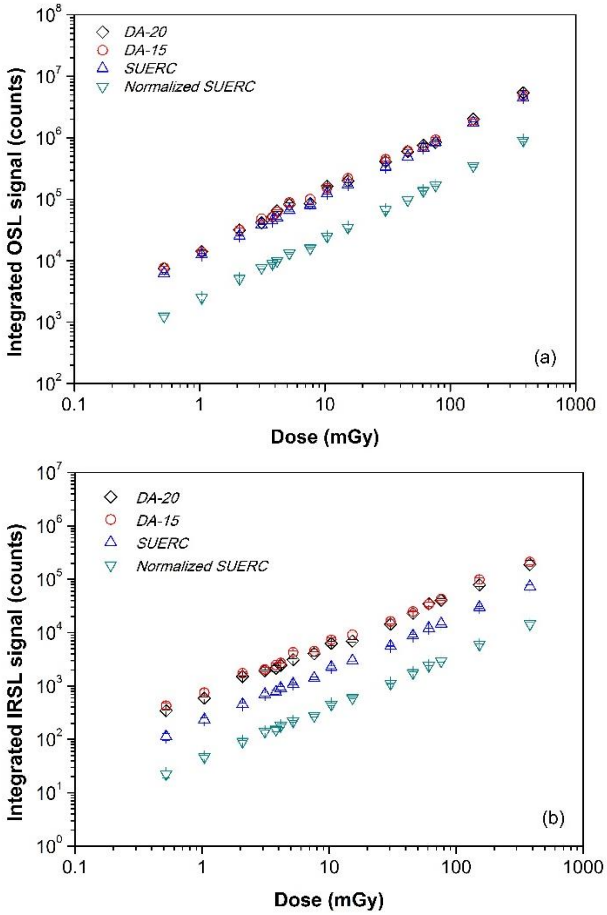

Fig. 2. OSL (a) and IRSL (b) dose response curves, in logarithmic scale, for the NaCl pellets as recorded with the 3 readers.

3.5. Multiple OSL measurements with the SUERC reader

Since it was observed that the depletion of NaCl pellets OSL signal is less with the SUERC reader, the residual OSL signal was investigated further. Thus, four consecutive OSL read-outs were applied to pellets irradiated with three doses: 7.6, 15.2 and 30.5 mGy. It was found that the OSL signal corresponds to 7%, 3% and 2% of the initial OSL, for the second, third and fourth OSL read-out, respectively and independent on the dose.

3.6. Detection limits

The minimum detectable dose (MDD) is calculated based on the standard deviation of unirradiated samples, σ_0, and the sensitivity (counts mGy^{-1}) of the studied material [12], as it is given by Equation (1):

$$MDD = \frac{3\times\sigma_0}{Sensitivity} \quad (1)$$

For all readers, the MDD is lower for the blue light stimulation compared to the IR. Specifically, the MDD for OSL is between 0.8 and 2.2 μGy, while for IRSL the relative range is 13.9-52.5 μGy. The DA-20 reader exhibits the lowest MDDs both for OSL and IRSL, while DA-15 and SUERC present relatively similar limits (using 5 pellets together for the SUERC reader). Finally, for the SUERC signal normalized to the number of pellets, the MDD is higher, for both stimulation wavelengths, compared to Risø readers.

Comparing the present results with the research of Alghamdi et al. [8], where SUERC was employed to study NaCl grains, the NaCl pellets exhibit lower MDD. In the same paper [8], 1g of salt grains was used and the results showed MDD of 6.7 and 340 μGy for OSL and IRSL, respectively, in contrast to 53 and 1.7 μGy, of the current study (using NaCl pellets).

4. Conclusions

The present work investigates the potential use of a portable OSL/IRSL reader (SUERC) with NaCl pellets, for R/N emergency preparedness applications. For this purpose, the OSL and IRSL dose response, the signal depletion and the minimum detectable dose were studied and compared to two typical laboratory readers for dosimetry applications (Risø TL/OSL readers, models DA-20 and DA-15).

It was determined that 5 NaCl pellets give a sufficient signal with the SUERC reader for the dose range of interest of the study (<<100 mGy). Using five pellets at a time, the OSL dose response curve was similar with the ones recorded by the two Risø readers, while the IRSL signal was about 3 times less for the SUERC. In addition, it was shown that the signal was not depleted completely after the 30 s of stimulation. Only 2% of the OSL signal remains after the read-outs in DA-20 and DA-15, while about 8% remains unbleached in SUERC. The residual signal after IRSL is significant for all three readers, with the larger remaining signal, 31%, corresponding to SUERC reader.

In case of an incident, the IRSL signal can be used for a rapid screening, while in long-term, more accurate dose determinations can be applied using the OSL signal, for individuals that the original dose exceeded a pre-defined threshold, for the IRSL signal. Furthermore, it is shown that the OSL signal is affected by IR stimulation prior to the OSL for the SUERC reader by approximately 24%. Consequently, if a combined protocol must be applied in an emergency preparedness situation, a correction should be implemented.

The minimum detectable dose (MDD) for NaCl pellets was calculated for each reader, showing that SUERC and DA-15 exhibit similar MDD for IRSL and OSL. The MDD for DA-20 is significantly lower.

In conclusion, the low MDD values for SUERC show that the reader is appropriate for *in situ* assessments of radiation absorbed doses with NaCl pellets in emergency situations.

Further investigation will focus on extension of the dose response curves to lower doses than 0.5 mGy, as well as investigation of salt grains directly coming from exposure sites, without any pellet pressing process. In addition, after emergency preparedness procedures are optimised for the SUERC reader, field measurements will be performed to simulate a realistic scenario.

5. Acknowledgement

This project was supported by the Swedish Radiation Safety Authority [SSM2022-1103].

References

1. Bernhardsson, Christian, et al. "Household salt as a retrospective dosemeter using optically stimulated luminescence." Radiation and environmental biophysics 48 (2009): 21-28.

2. Christiansson, Maria, et al. "Using an optimised OSL single-aliquot regenerative-dose protocol for low-dose retrospective dosimetry on household salt." Radiation protection dosimetry 144.1-4 (2011): 584-587.

3. Ekendahl, Daniela, Boris Bulánek, and Libor Judas. "A low-cost personal dosemeter based on optically stimulated luminescence (OSL) of common household salt (NaCl)." Radiation Measurements 85 (2016): 93-98.

4. Spooner, Nigel A., et al. "Luminescence from NaCl for application to retrospective dosimetry." Radiation Measurements 47.9 (2012): 883-889.

5. Waldner, Lovisa, and Christian Bernhardsson. "Physical and dosimetric properties of NaCl pellets made in-house for the use in prospective optically stimulated luminescence dosimetry applications." Radiation measurements 119 (2018): 52-57.

6. Mandowski, A., and M. Biernacka. "Anomalous regeneration of OSL in sodium chloride–Experiment and modeling." Radiation measurements 71 (2014): 265-269.

7. Majgier, Renata, Magdalena Biernacka, and Arkadiusz Mandowski. "Properties of the model for radiation induced optically stimulated luminescence (OSL) in sodium and potassium chlorides." Radiation Measurements 127 (2019): 106142.

8. Alghamdi, Hamdan, et al. "The use of portable OSL and IRSL measurements of NaCl in low dose assessments following a radiological or nuclear emergency." Frontiers in Public Health 10 (2022): 969829.

9. Sanderson, David CW, and Simon Murphy. "Using simple portable OSL measurements and laboratory characterisation to help understand complex and heterogeneous sediment sequences for luminescence dating." Quaternary Geochronology 5.2-3 (2010): 299-305.

10. Waldner, Lovisa, Christopher Rääf, and Christian Bernhardsson. "NaCl pellets for prospective dosimetry using optically stimulated luminescence: Signal integrity and long-term versus short-term exposure." Radiation and environmental biophysics 59 (2020): 693-702.

11. Risø manual found at: https://www.fysik.dtu.dk/english/research/radphys/research/radiation-instruments/tl_osl_reader/manuals

12. Piesch, E., and B. Burgkhardt. "Environmental monitoring. European interlaboratory test programme for integrating dosemeter systems." (1984).

MEDICAL PHYSICS IN THE BALTIC STATES 16 (2023)

Proceedings of International Conference "Medical Physics 2023"
09-11 November 2023, Kaunas, Lithuania

INVESTIGATION OF THE SURFACE MORPHOLOGY OF PHOTOCHEMICALLY SYNTHESISED AgNP-PVB NANOCOMPOSITE COATINGS USING ATOMIC FORCE MICROSCOPY

Mindaugas ILICKAS[1], Asta GUOBIENĖ[1], Brigita ABAKEVIČIENĖ[1,2]
[1]Institute of Materials Science of Kaunas University of Technology, Lithuania;
[2]Department of Physics, Kaunas University of Technology, Lithuania
mindaugas.ilickas@ktu.edu

***Abstract*:** In this study, polyvinyl butyral (PVB) has been proposed as a stabilizing agent, while silver nitrate ($AgNO_3$) was employed as a precursor for the UV-mediated photochemical synthesis aimed at the formation of coatings on quartz glass substrates. Within the experimental framework, the coatings underwent exposure to UV irradiation under two distinct light intensity conditions. The surface morphology of these coatings was subsequently scrutinized via atomic force microscopy.

Keywords: UV-mediated synthesis; photochemical reduction; atomic force microscopy, image segmentation

1. Introduction

Metal nanoparticles have attracted considerable scientific attention due to their antimicrobial attributes stemming from their unique optical characteristics, surface resonance scattering, electrical conductivity, elevated surface energy, and noteworthy surface-to-volume ratio. Diverse synthesis methods are employed to tailor the colloidal stability of these nanoparticles at biocompatible concentrations [1].

The utilization and medical applications of nanoparticles, characterized by their extensive effective surface area capable of modulating drug pharmacokinetics, reducing toxicity, and augmenting biological responses, have been well-established. A focal point of current research pertains to silver nanoparticles (AgNPs) spanning the range of 5-110 nm in size, which manifest both antibacterial and antiviral properties [2]. Intriguingly, the antimicrobial efficacy of these nanoparticles remains consistent across their size spectrum. Nevertheless, when these nanoparticles are incorporated into other environments, such as polymer matrices, meticulous control of particle size on coating surfaces becomes imperative to ensure sustained antiviral activity. Recent investigations have concentrated on AgNPs within the 5-20 nm size range, demonstrating favourable responses to viral pathogens [3].

Jeremiah et al. [4] posited the antiviral potential of AgNPs against SARS-CoV-2. To impede viral activity, AgNPs initially adhere to the surfaces of viral proteins containing sulfhydryl groups, thereby perturbing disulfide bonds within the protein structure, and destabilizing the viral protein, ultimately disrupting the viral protein-ACE2 receptor interaction. The nature of AgNP inhibition is contingent upon factors such as their size, shape, and concentration. In this study, spherical AgNPs with a 10 nm diameter and concentrations ranging from 1 to 10 ppm were utilized. It is noteworthy that exceeding an AgNP concentration of 20 ppm results in cytotoxicity, attributed to the generation of reactive oxygen species (ROS) through the interaction between AgNPs and living cells. Similar concentrations of AgNPs have been employed in the fabrication of protective masks [5].

It is essential to highlight that investigating the antiviral properties of AgNPs, whether administered independently or in combination with various compounds, necessitates exceedingly low concentrations of these nanoparticles, with their size contingent upon the specific type of living cell [4], [6]. Relatively few scientific publications have explored the incorporation of AgNPs into polymeric composite materials for comprehending the antiviral attributes of AgNPs [7], [8]. Furthermore, not all researchers uniformly report Ag concentrations in ppm.

In this study, $AgNO_3$ was employed as the precursor for incorporation into polymer matrices to form composites through a photochemical synthesis method. The concentration of $AgNO_3$ was systematically adjusted during synthesis. Consequently, the resulting AgNPs within the composite material were dispersed uniformly throughout the polymer matrix, with AgNP concentrations ranging from 100 to 1000 ppm. This specific concentration range of AgNPs was chosen to facilitate the creation of a stable composite coating

through photochemical synthesis, achieved by exposing the film surface to UV light. It is important to note that this coating is intended for applications where it does not come into direct contact with human open wounds or living cells. It is worth mentioning that concentrations of AgNPs typically used in medical bandage infused with silver colloidal solutions span from 50 to 700 ppm [9].

Within the scope of this investigation, the reduction of $AgNO_3$ to form AgNPs was a critical step in yielding AgNPs with antiviral attributes, falling within the size range of 10 to 20 nm [10, 11].

2. Materials and Methods

A proposed method for synthesizing AgNP-PVB nanocomposites involved UV-mediated photochemical processes to prepare coatings on quartz glass substrates. This was accomplished using a modified doctor blade coating technique. The precursor material employed in this synthesis was $AgNO_3$. Throughout the synthesis process, the $AgNO_3$ solution was introduced into a PVB solution. The experiments were conducted under ambient conditions, specifically at room temperature and atmospheric pressure. A dual-wavelength UV source (Desaga Heidelberg 220V, 75W) emitting light at wavelengths of 254 nm (with an intensity of 1.64 mW/cm^2) and 366 nm (with an intensity of 0.80 mW/cm^2) was utilized in this research. Samples were irradiated for 5, 10, 20 and 30 min.

The investigation of surface morphology and mechanical properties at the nanometric scale was conducted employing a NanoScience NanoWizard®3 scanning probe microscopy system (see Fig. 1.), equipped with requisite accessories from Bruker, Germany. These measurements were executed within an ISO class 5 clean room environment, employing both contact and tapping modes. Specifically, an I-shaped silicon ACTA - AppNano probe with a needle tip diameter of less than 10 nm, pyramid geometry, a stiffness coefficient of 40 N/m, and a resonant frequency of 300 kHz was employed for data acquisition. The resultant data were subsequently processed using the specialized image processing software, JPKSPM Data Processing.

To evaluate the morphology and size distribution of the AgNPs-PVB nanocomposite coatings acquired through atomic force microscopy (AFM), we applied the machine learning-based software program Ilastik 1.4.0. [12] and the open-source image processing tool Fiji 2.14.0 [13].

Ilastik represents a user-friendly and intuitive application that facilitates efficient optimization of training by providing prompt and precise outcomes to the user. Algorithm training is accomplished effortlessly through simple actions such as mouse-click selection or object delineation. If the initial image classification and training prove to be imprecise or unsatisfactory, the program can be retrained with supplementary object labels. Incorporating new labels while retaining previous ones enhances the amount of information accessible for algorithmic processing, yielding more comprehensive and accurate object and pixel analysis [12]

Fig. 1. AFM Scanning probe microscopy system JPK NanoWizard®3 [14]

Fiji is a derivative of ImageJ, another widely utilized software for the analysis of diverse image types [13]. Similar to Ilastik, Fiji leverages sophisticated algorithms to expedite image processing. In our study, we employed the Fiji program to assess the size and distribution of AgNPs (see Fig. 2.) subsequent to their AFM image processing with Ilastik.

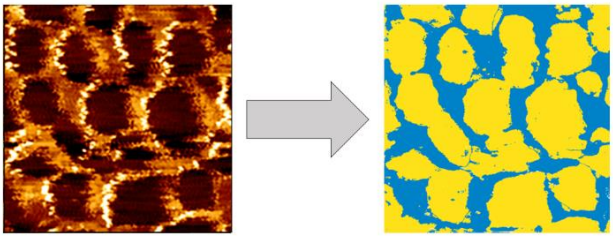

Fig. 2. Automated object detection and classification in AFM images using Ilastik software

3. Results and discussion

In this study, the assessment of surface morphology, dimensions of structural constituents, and nanomechanical characteristics of the coatings was conducted employing the scanning probe method. It was ascertained that the dimensions of AgNPs within the UV-mediated photochemical synthesis of AgNPs-PVB nanocomposite coatings exhibited a discernible reduction as a function of increasing UV irradiation duration, ranging from 5 to 30 min. Two-dimensional phase diagrams, as depicted in Fig. 3, revealed distinct regions characterized by varying shades. A phase transition exceeding 10^o within these diagrams signifies the presence of two distinct materials. The darker regions corresponded to AgNPs, while the lighter regions represented the PVB matrix. The 2D phase images provided empirical confirmation that the manipulation of UV irradiation duration yields precise control over the resultant particle sizes. Specifically, the dimensions of AgNPs exhibited a notable decrease, transitioning from an initial dimension of 100 nm (observed at a 5-min exposure time) to a mere 55 nm (observed at a 30-min exposure time), these values were estimated from the profilograms using the JPKSPM Data Processing software.

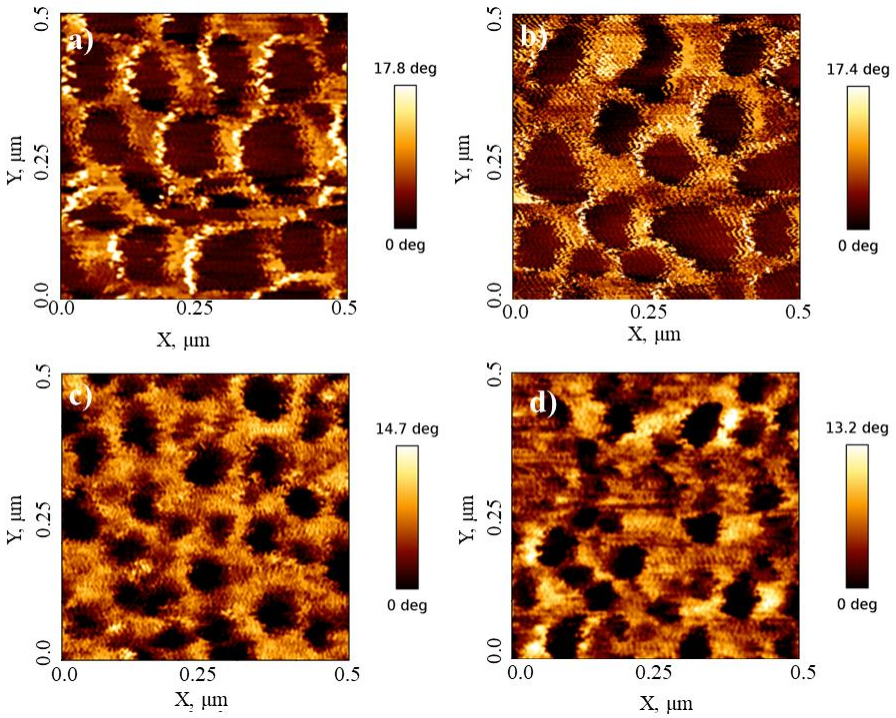

Fig. 3. AFM 2D phase images of AgNP-PVB nanocomposite: a) 5 min; b) 10 min; c) 20 min; d) 30 min

The 2D phase images underwent processing using the software tools Ilastik and Fiji to extract the size distribution and mean size of synthesized particles. The resultant particle size distributions derived from the 2D phase images are depicted in Fig. 4. Notably, across all instances, polydisperse particles were obtained, offering potential applications in combatting a variety of bacterial and viral strains. However, with the passage of time, a noticeable deviation from the initial particle reduction pattern observed in the raw images processed by the Ilastik program emerged.

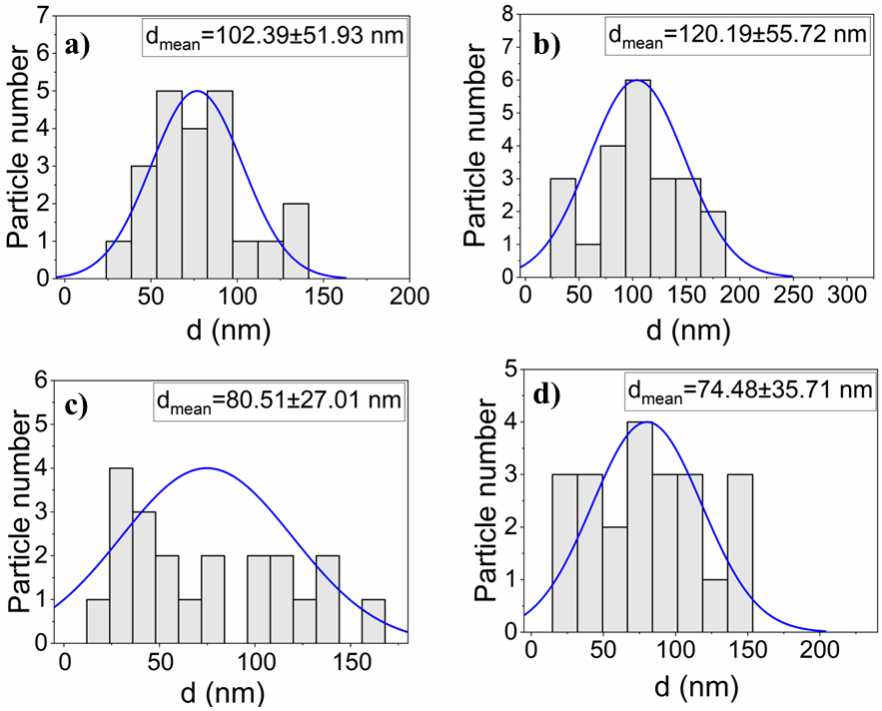

Fig. 4. Determination of AgNP size distributions in AgNP-PVB nanocomposite coatings derived from 2D phase images: a) 5 min; b) 10 min; c) 20 min; d) 30 min

This deviation may be attributed to the possibility of insufficient training in the artificial intelligence model. It is hypothesized that within regions where the PVB matrix was genuinely present, it may have provided structural support to AgNPs, potentially augmenting their exposed surface area. Consequently, this phenomenon could result in larger particle diameters, thereby influencing their overall size distributions.

Despite the potential distortion in the particle size distribution, Fig. 4. still illustrates a declining trend over time.

In forthcoming research endeavors, there exists the prospect of conducting a more profound inquiry into the structural and morphological attributes inherent to AgNPs-PVB coatings. Additionally, such investigations may encompass antiviral and antibacterial assays, aimed at elucidating the effectiveness of these coatings in combatting microbial agents.

4. Conclusions

The primary objective of this study was to assess the surface morphology characteristics of AgNP-PVB nanocomposite coatings derived from $AgNO_3$ and PVB through UV photochemical synthesis in situ. The findings of this study demonstrate the successful formation of nanocomposite coatings via photochemical synthesis, featuring a well-organized dispersion of AgNPs within the polymer matrix. AFM phase imaging enabled differentiation between distinct materials (AgNPs and PVB matrix) and facilitated the determination of particle widths (synthesized AgNPs ranged from 55 to 100 nm). Notably, the application of artificial intelligence (AI) for the determination of particle distributions exhibited limitations in accuracy. This was primarily due to the aggregation of AgNPs within the AI regions of the PVB matrix, resulting in an observed increase in particle size. Nevertheless, it is envisioned that with further refinement and training of AI algorithms, this technology holds substantial promise as a powerful tool for achieving precise and reliable particle size distributions. In prospective research endeavors, these AgNPs-PVB coatings hold potential utility in conducting investigations related to antiviral and antibacterial properties, given their controlled surface morphology and established suitability for such applications.

References

1. Nasiriboroumand M., Montazer M., and Barani H., Preparation and characterization of biocompatible silver nanoparticles using pomegranate peel extract, J Photochem Photobiol B, vol. 179, pp. 98–104, Feb. 2018.

2. Song Y., Li R., Sun Q., and Jin P., Controlled growth of Cu nanoparticles by a tubular microfluidic reactor, Chemical Engineering Journal, vol. 168, no. 1, pp. 477–484, Mar. 2011.

3. Ratan Z. A. et al., Silver Nanoparticles as Potential Antiviral Agents, Pharmaceutics, vol. 13, no. 12, p. 2034, Nov. 2021.

4. Jeremiah S. S., Miyakawa K., Morita T., Yamaoka Y., and Ryo A., Potent antiviral effect of silver nanoparticles on SARS-CoV-2, Biochem Biophys Res Commun, vol. 533, no. 1, pp. 195–200, Nov. 2020.

5. Grozdanov A. and Paunovic P., Functionalized nanoparticles in facemasks for protection of Covid 19, Material Science & Engineering International Journal, vol. 5, no. 5, pp. 142–146, Sep. 2021.

6. Akter M. et al., A systematic review on silver nanoparticles-induced cytotoxicity: Physicochemical properties and perspectives, J Adv Res, vol. 9, pp. 1–16, Jan. 2018.

7. Ibrahim H. M., Zaghloul S., Hashem M., and El-Shafei A., A green approach to improve the antibacterial properties of cellulose based fabrics using Moringa oleifera extract in presence of silver nanoparticles, Cellulose, vol. 28, no. 1, pp. 549–564, Jan. 2021.

8. Shenashen M. A., El-Safty S. A., and Elshehy E. A., Synthesis, Morphological Control, and Properties of Silver Nanoparticles in Potential Applications, Particle & Particle Systems Characterization, vol. 31, no. 3, pp. 293–316, Mar. 2014.

9. Saeb A. T. M., Al-Rubeaan K. A., Abouelhoda M., Selvaraju M., and Tayeb H. T., Genome sequencing and analysis of the first spontaneous Nanosilver resistant bacterium Proteus mirabilis strain SCDR1, Antimicrob Resist Infect Control, vol. 6, no. 1, p. 119, Dec. 2017.

10. Hamouda T., Ibrahim H. M., Kafafy H. H., Mashaly H. M., Mohamed N. H., and Aly N. M., Preparation of cellulose-based wipes treated with antimicrobial and antiviral silver nanoparticles as novel effective high-performance coronavirus fighter, Int J Biol Macromol, vol. 181, pp. 990–1002, Jun. 2021.

11. Behbudi G., Effect of silver nanoparticles disinfectant on covid-19, vol. 2, no. 2, pp. 63–67.

12. Berg S. et al., ilastik: interactive machine learning for (bio)image analysis, Nat Methods, vol. 16, no. 12, pp. 1226–1232, 2019.

13. Schindelin J. et al., Fiji: an open-source platform for biological-image analysis, Nat Methods, vol. 9, no. 7, pp. 676–682, 2012.

14. KTU MMI, AFM Scanning probe microscopy system JPK NanoWizard®3, https://apcis.ktu.edu/MMI/lt/site/katalogas?more=6742 (accessed Sep. 27, 2023)

MEDICAL PHYSICS IN THE BALTIC STATES 16 (2023)

Proceedings of International Conference “Medical Physics 2023”
09-11 November 2023, Kaunas, Lithuania

ON ISOTOPIC LABELING IN PLANT PHYSIOLOGY RESEARCH

Anka GEORGIEVA-HRISTEVA, Todorka L. DIMITROVA
University of Plovdiv "Paisii Hilendarski", 24 Tsar Assen Str., Plovdiv, Bulgaria
doradimitrova@uni-plovdiv.bg

***Abstract*:** The use of radioactive isotopes in research on plant physiology began with the early work of George de Hevesy. In 1913 he started his study of Pb salt solubility in water and in 1923 the Pb salt uptake in plants was reported. Hevesy developed a method of Pb labeling via an isotope of radium. In 1943 he was awarded the Nobel Prize in Chemistry "for his work on the use of isotopes as tracers in the study of chemical processes" (Hevesy, 1044).

Further on, Ruben and co-authors (Ruben S. et al., 1939) used ^{11}C to trace the mechanisms of photosynthesis. They explored heavy oxygen in water molecule $H_2[^{18}O]$ as a tracer and demonstrated that the release of O_2 in photosynthesis is due to water splitting, instead of CO_2 splitting, as was considered before (Ruben S. et al., 1941). Later, scientists started using ^{14}C, ^{32}P, and other radioactive isotopes included in various organic and inorganic chemical compounds in biophysics and plant physiology research.

Recently, the application of non-radioactive isotopes in scientific research has become more attractive because of safety reasons. But in many cases, it could not replace the use of radioactive isotopes.

Nowadays, advanced technology provides a large variety of analytical methods – from different types of spectroscopy and chromatography to NMR and PET (Truong et al., 2014; Masakapalli, 2014; Allen et al., 2015; Deborde at all, 2017, Coenen and al., 2021).

The aim of this work is to present a brief overview of isotopic labeling in research on plant physiology. This will help in choosing suitable isotopic labels and methods& techniques for studying the impact of different physical factors on *in vitro* plant systems.

Keywords: isotopic labeling, labeling techniques, plant metabolism, plant physiology.

1. Introduction

Plant metabolism is described by complex and intertwined processes passing through a number of intermediate products. Every single external impact such as a pathogen or environmental factor has its impact on the plant physiology. This can alter the metabolic pathways of synthesis of a given compound, and increase or decrease its amount. Isotopic labeling makes it possible to identify substances that are synthesized as a specific reaction to a given impact. Knowledge of the metabolic pathways allows for supporting the growth and development of plants in case they fall into unfavorable conditions.

2. Processes traced by labeling

One of the first processes that was explained by isotopic labeling was the mechanism of photosynthesis and the origin of oxygen (O_2) released by plants during it. In these studies, it was found that the "dark" reactions of carbon fixation do not require light to proceed (Ruben et al., 1939). The second consideration was that the release of O_2 during photosynthesis was due to water splitting, rather than CO_2 splitting as previously thought (Ruben et al., 1941).

Yano and co-authors (Yano et al., 1972) performed the biosynthesis of cyclopropane and cyclopropene fatty acids in cultures of several species of Malvaceae. Labeled cyclopropane and cyclopropene fatty acids obtained after incubation with labeled methionine confirmed that the ring methylene group was derived from the methyl group of methionine. The intermediate products through which the synthesis passes have been identified.

A major process that is being followed in plants is disease resistance. Salicylic acid is the primary inducer. There are different pathways for the synthesis of salicylic acid (SA) in plants (Chen et al., 2009).

In studies conducted with Primula acaulis and Gaultheria procumbens, labeling of leaf segments with ^{14}C-phenylalanine and ^{14}C-cinnamate indicated a pathway of SA synthesis via o-coumarate. When the same plants were labeled with ^{14}C benzoate, labeled SA was detected again, indicating the use of two pathways for the synthesis of the desired acid (El-Basyouni et al., 1964).

In studies carried out with tomato plants inoculated with Agrobacterium tumefaciens and labeled with [3-^{14}C] cinnamic or [carboxyl-^{14}C] benzoic acid, a qualitative and quantitative change in the patterns of incorporation of related phenolic acids between infected and control

plants was found. According to the authors, the results indicate pathogen interference in the β-oxidation of at least two phenylpropanoid acids from the lignification pathway. (Chadha et al., 1974).

In a study conducted with tobacco inoculated with tobacco mosaic virus, a hypersensitive response was observed, which was expressed in a drastic increase in SA levels. In infected plants, SA accumulation was accompanied by an increase in benzoic acid levels. Studies with ^{14}C labeling indicated that the label is transferred from transcinnamic acid to SA via benzoic acid and implicated this pathway as essential for SA synthesis in tobacco (Yalpani et al., 1993).

Silverman and co-authors (Silverman et al., 1995) confirmed that SA synthesis pathways in tobacco were applicable to rice as well.

In cucumber, uninfected tissues from an infected plant were examined for the amount of SA. Acquired systemic resistance expressed by increased SA synthesis compared to controls was established. Radiolabeling showed that SA was synthesized from phenylalanine and benzoic acid. (Meuwly et al., 1995).

In potato studies, radiolabeling of untreated leaves showed that SA is synthesized from phenylalanine and that cinnamic and benzoic acids are intermediates in SA synthesis (Coquoz et al., 1998).

Skirycz and co-authors (Skirycz et al. 2011) investigated the response of Arabidopsis thaliana to mild and prolonged osmotic stress. Analysis of protein changes showed that plastid ATPase, Calvin cycle, and photorespiration were down-regulated, but Mitochondrial ATP synthesis was up-regulated. This demonstrates the importance of mitochondria in maintaining plastid functions during water stress. In addition, these studies allow the identification of candidate genes for improving plant development under water limitation.

Truong and co-authors (Truong et al., 2014) have proposed experimental measurement methods for flow analysis. These methods allowed the determination of biomass composition (lipids, proteins, soluble sugars, and starch). As a model plant system, researchers used soybean embryo culture.

Grusak and co-authors (Grusak et al., 1994) developed a methodology for the complete labeling of soybean plants, which could subsequently be used to study the metabolism of animals and even humans.

3. Isotopes used to label plants

The most commonly used radioisotope for marking of plants is ^{14}C. It is used both as CO_2 (Kuzyakov et al., 2006) and incorporated into the molecules of various organic compounds.

Another isotope of carbon - ^{11}C is also used in research, but its application is not so widely advocated due to the need for a cyclotron for its preparation, as well as the much shorter half-life compared to that of ^{14}C (^{11}C - T1/2=21.5 min, 14C – T1/2 = 5730 years). Other radioactive isotopes are also used in practice – ^{35}S, ^{32}P, ^{33}P.

In many cases, the use of radioactive isotopes cannot be replaced. Recently, the application of non-radioactive isotopes in scientific research has become more attractive because of safety reasons.

Another isotope finding application in the study of plant metabolism is ^{18}O re-incorporated into the CO_2 molecule (Cournac et al., 1993).

The main non-radioactive isotopes are: ^{13}C (Masakapalli et al., 2014) and ^{15}N (Skirycz et al., 2011). The authors emphasize that labeling with stable isotopes does not affect the growth and physiology of higher plants. (Arsova et al., 2012).

4. Plant Labeling Techniques

Before starting to label plants, it is necessary to select a suitable substance involved in the metabolic process that will be studied. The labeling technique depends on the aggregate state of the substance used for labeling. When using labeled CO_2, the main method used is labeling in a chamber with an air fan for intensive internal air circulation.

The label as a solution of sodium carbonate is placed in a vial connected by tubing to the labeling chamber. The addition of 5M sulfuric acid to the sodium carbonate solution in the vial via a Teflon tube allows the complete release of $^{14}CO_2$ in the chamber. Assimilation occurs within 2 hours after the pulse is applied. Any unassimilated $^{14}CO_2$ is then removed by pumping the air from the chamber through 1M sodium hydroxide solution for 1 hour.

^{14}C collected in 1M sodium hydroxide solution was measured using scintillation cocktail after chemiluminescence decay. Absolute ^{14}C activity was standardized by the SPQ(E) method to an external standard using the LKB Wallac standard library. Shoots and roots were dried at 600 C^o, then mixed and pulverized in a ball mill before analysis for radioactivity. The activity was measured after burning a 1g sample in an oxidizer with a liquid scintillation cocktail Permafluor E+ using a liquid scintillation counter. (Kuzyakov et al., 2006).

When using organic compounds containing radionuclides, ^{14}C is most often used, but there is a large variety of organic compounds that can be used. When using organic compounds, the most common technique is to add them to the plant's nutrient medium. Another technique used is to spray plant leaves with a solution of the compound containing the marker.

Regardless of the way the label is applied, the compounds that are labeled are isolated and subjected to radiometry.

In the case of plants labeled with ^{15}N, inorganic compounds are most often used. The most commonly used compound is NH_3NO_4, which could be added to the medium in which plants are grown (Arsova et al., 2012).

Two-dimensional [^1H, ^{13}C] heteronuclear single quantum correlation (HSQC) and nuclear magnetic resonance (NMR) spectroscopy are comprehensive tools in metabolic flux analysis using ^{13}C experiments. NMR is particularly suitable when extensive measurements of isotopomers are required. HSQC analysis can distinguish quantitative differences. This specifies important

information about compartments of radionuclides in the plant system. Fluxes are obtained from the numerical solution of these balances and a stoichiometric model which includes data on biomass composition as well as rates of consumption of carbohydrate and nitrogen sources. (Truong et al., 2014).

5. Conclusions

Studying the metabolism of plants remains challenging despite intensive research in this area. Isotopic labeling enables the investigation of metabolic operations and network fluxes. Basic aspects of lipid metabolism in plants are defined by isotopic labeling. The most recent methods such as MS and NMR allow the use of non-radioactive isotopes.

We intend to use isotopic labeling to study the impact of different physical factors on *in vitro* plant systems. The choice of the substance with which we will label the plants, as well as the isotope used, will be consistent with the capabilities of our laboratory as well as with the isotopes allowed for use under the laboratory's license. However, the literature study on isotopic labeling, methods, and techniques will be of help to create the best possible conditions for our experiments. We consider that it can be useful for other authors as well.

References

1. De Hevesy, G. E. O. R. G. E. (1944). Some applications of isotopic indicators. *Nobel Lecture*, *12*.
2. Ruben, S., Hassid, W. Z., & Kamen, M. D. (1939). Radioactive carbon in the study of photosynthesis. *Journal of the American Chemical Society*, *61*(3), 661-663.
3. Ruben, S., Randall, M., Kamen, M., & Hyde, J. L. (1941). Heavy oxygen (O18) as a tracer in the study of photosynthesis. *Journal of the American Chemical Society*, *63*(3), 877-879.
4. Truong, Q. X., Yoon, J. M., & Shanks, J. V. (2014). Isotopomer measurement techniques in metabolic flux analysis I: nuclear magnetic resonance. *Plant Metabolism: Methods and Protocols*, 65-83.
5. Masakapalli, S. K., Ratcliffe, R. G., & Williams, T. C. (2014). Quantification of 13 C enrichments and isotopomer abundances for metabolic flux analysis using 1D NMR spectroscopy. *Plant Metabolic Flux Analysis: Methods and Protocols*, 73-86.
6. Allen, D. K., Bates, P. D., & Tjellström, H. (2015). Tracking the metabolic pulse of plant lipid production with isotopic labeling and flux analyses: past, present and future. *Progress in Lipid Research*, *58*, 97-120.
7. Deborde, C., Moing, A., Roch, L., Jacob, D., Rolin, D., & Giraudeau, P. (2017). Plant metabolism as studied by NMR spectroscopy. *Progress in Nuclear Magnetic Resonance Spectroscopy*, *102*, 61-97.
8. Coenen, H. H., & Ermert, J. (2021). Expanding PET-applications in life sciences with positron-emitters beyond fluorine-18. *Nuclear medicine and biology*, *92*, 241-269.
9. Yano, I., Morris, L. J., & Nichols, B. W. (1972). The biosynthesis of cyclopropane and cyclopropene fatty acids in higher plants (Malvaceae). *Lipids*, *7*, 35-45.
10. Chen, Z., Zheng, Z., Huang, J., Lai, Z., & Fan, B. (2009). Biosynthesis of salicylic acid in plants. *Plant signaling & behavior*, *4*(6), 493-496.
11. El-Basyouni, S. Z., Chen, D., Ibrahim, R. K., Neish, A. C., & Towers, G. H. N. (1964). The biosynthesis of hydroxybenzoic acids in higher plants. *Phytochemistry*, *3*(4), 485-492.
12. Chadha, K. C., & Brown, S. A. (1974). Biosynthesis of phenolic acids in tomato plants infected with Agrobacterium tumefaciens. *Canadian Journal of Botany*, *52*(9), 2041-2047.
13. Yalpani, N., León, J., Lawton, M. A., & Raskin, I. (1993). Pathway of salicylic acid biosynthesis in healthy and virus-inoculated tobacco. *Plant physiology*, *103*(2), 315-321.)
14. Silverman, P., Seskar, M., Kanter, D., Schweizer, P., Métraux, J. P., & Raskin, I. (1995). Salicylic acid in rice (biosynthesis, conjugation, and possible role). *Plant physiology*, *108*(2), 633-639.
15. Meuwly, P., Molders, W., Buchala, A., & Metraux, J. P. (1995). Local and systemic biosynthesis of salicylic acid in infected cucumber plants. *Plant Physiology*, *109*(3), 1107-1114.
16. Coquoz, J. L., Buchala, A., & Métraux, J. P. (1998). The biosynthesis of salicylic acid in potato plants. *Plant physiology*, *117*(3), 1095-1101.
17. Skirycz, A., Memmi, S., De Bodt, S., Maleux, K., Obata, T., Fernie, A. R., ... & Inze, D. (2011). A reciprocal 15N-labeling proteomic analysis of expanding Arabidopsis leaves subjected to osmotic stress indicates importance of mitochondria in preserving plastid functions. *Journal of Proteome Research*, *10*(3), 1018-1029.
18. Grusak, M. A., & Pezeshgi, S. (1994). Uniformly 15N-labeled soybean seeds produced for use in human and animal nutrition studies: Description of a recirculating hydroponic growth system and whole plant nutrient and environmental requirements. *Journal of the Science of Food and Agriculture*, *64*(2), 223-230.
19. Kuzyakov, Y., Shevtzova, E., & Pustovoytov, K. (2006). Carbonate re-crystallization in soil revealed by 14C labeling: experiment, model and significance for paleo-environmental reconstructions. *Geoderma*, *131*(1-2), 45-58.)
20. Cournac, L., Dimon, B., & Peltier, G. (1993). Evidence for 18 O labeling of photorespiratory CO 2 in photoautotrophic cell cultures of higher plants illuminated in the presence of 18 O 2. *Planta*, *190*, 407-414.
21. Arsova, B., Kierszniowska, S., & Schulze, W. X. (2012). The use of heavy nitrogen in quantitative proteomics experiments in plants. *Trends in plant science*, *17*(2), 102-112.)

MEDICAL PHYSICS IN THE BALTIC STATES 16 (2023)

Proceedings of International Conference "Medical Physics 2023"
09-11 November 2023, Kaunas, Lithuania

RE-CALCULATION AND EVALUATION OF COMPENSATIVE BIOLOGICAL EFFECTIVE DOSE FOR UNSCHEDULED INTERRUPTION IN HEAD AND NECK CANCER RADIOTHERAPY

Ieva JOGAITĖ[1], Reda ČERAPAITĖ-TRUŠINSKIENĖ[2], Artūras ANDREJAITIS[3], Jurgita LAURIKAITIENĖ[4]
[1,4]Kaunas University of Technology; [2]Lithuanian University of Health Sciences; [3]Hospital of Oncology LSMU
[1]vjogaite@gmail.com; [2]reda.cerapaite-trusinskiene@lsmuni.lt; [3]arturas.andrejaitis@kaunoklinikos.lt,
[4]jurgita.laurikaitiene@ktu.lt

***Abstract*:** Head and neck cancers progress at a rapid pace and it is highly influenced by the timing of treatment sessions. Based on the linear quadratic model and treatment guidelines, the newly calculated/ re-calculated dose (Gy) was compared to the allowed tolerance limits from radiotherapy treatment plans. Obtained results showed that this methodology, replanning treatment may be useful for clinical applications, guaranteeing the quality of the radiation treatment from a radiobiological point of view.

Keywords: interruption, biological effective dose, head and neck, compensation, radiotherapy.

1. Introduction

The biological effects of radiation therapy have been extensively studied over the past three decades. The development of the linear quadratic (LQ) model has provided the most medical insights into cell survival and radiobiological effects of ionizing radiation. This model incorporates the α/β ratio, based on two parameters which are adjusted to represent individual biological characteristics, and therefore contributes to the establishment of personalized radiation therapy [1].
Head and neck cancer is classified as a rapidly proliferating tumour [2]. Therefore, a one-day gap in treatment delivery can reduce local control approximately by 1.4%, while a week-long break results in 10-12% deterioration. It is known that within four weeks, the cancer can grow significantly and invade nearby tissues [3]. For this reason, any interruptions in radiation therapy are undesirable and should be prevented. In 2019, during the global pandemic caused by the COVID-19, many patients experienced disruptions that lasted from several days to weeks [4]. The aim of the research was to develop an acceptable compensative model for unplanned radiotherapy interruptions for head and neck cancer. This was to be done in accordance with the recommendations first proposed by the Royal College of Radiologists in 1996 [5], with the latest guidelines following in 2019 [6].

2. Materials and methods

This scientific project was completed at the Kaunas University of Technology in cooperation with the Lithuanian University of Health Sciences Hospital (LSMUH), Kaunas Clinics, Oncology Hospital as part of a master's thesis. The aim of the research was to develop an acceptable compensative model for unplanned radiotherapy interruptions for head and neck cancer. The mathematical model was implemented using Microsoft Excel. Applying the previously developed LQ model in order to perform BED calculations (for the tumor and organs at risk), new values for dose per fraction were obtained in a set of test cases. The determined values were evaluated using the treatment planning system "Eclipse" and the novel radiotherapy planning technique – volumetric arc therapy (VMAT) (Fig. 1). Its accuracy is ensured by regular testing of the gamma index, which has a clinical reference of 2 mm/ 2% or 3 mm/ 3%.

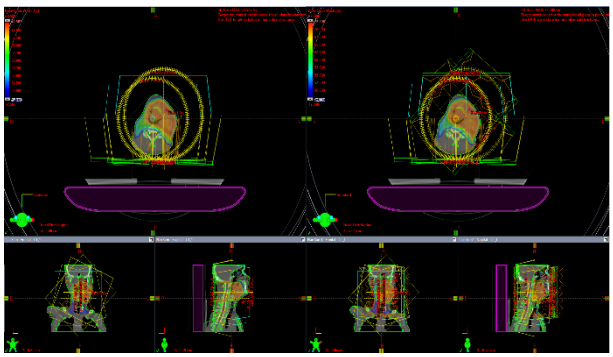

Fig. 1. View of the VMAT radiotherapy re-planning system graphical user interface (GUI)

After re-calculating the modified fractional dose, the amount of irradiation to critical organs also changed. Plans that exceeded the tolerable doses for delineated

critical organs were re-planned trying to achieve the tolerable level.

In total 14 patients of the LSMUH - Kaunas Clinics, Oncology Hospital were evaluated. The study group was selected by random sampling. Each patient was estimated in three stages:

– 1 stage: PTV50 – 50 Gy;
– 2 stage: PTV60 – 10 Gy;
– 3 stage: 10 Gy.

These cases were chosen according to the following criteria: gap duration, radiotherapy regime, as well as location of the malignancy. This study focused on patients with certain type of tumours who missed part of their treatment and, therefore, required a recalculated treatment plan. Furthermore, the analysis only assessed depersonalized information, such as cancer site and gap length. For this reason, ethics board approval was not required.

2.1. Re-evaluation of biological effective dose

The development of the compensation model was implemented based on calculations of cell survival and the actual dose that falls within the planning target. With regard to the linear quadratic (LQ) model and biological effective dose (BED), the equations were combined to measure the consequences of missed treatment courses, and to simultaneously recover the assigned dose to the tumour while avoiding excess radiation to healthy tissues.

For an early responding tissues and tumours, BED_{10} was calculated by subtracting the potentially repopulated cells. Therefore, final calculation of the BED_{10} [7]:

$$BED_{10} = n(applied) * d * \left(1 + \frac{d}{\alpha/\beta}\right) + n(residual) * x * \left(1 + \frac{x}{\alpha/\beta}\right) - (T - T_k) * K, \quad (1)$$

where *n (applied)* is the number of completed fractions, *n (residual)* the number of planned fractions, *d* is the dose per fraction in Gy, *x* the new dose per fraction, *T* is the entire duration of the treatment, the *Tk* is estimated as the start ("kick off") of a cell proliferation in days. For rapidly multiplying (especially lung, head and neck) cancer, it varies from 21 – 32 days. The *K* coefficient describes the amount of radiation necessary to sterilise repopulated cells. Its unit is Gy/day. In some studies, the *K* value may vary from 0.8 to 2.2 Gy/day according to the individual case. However, most of the clinical calculations were performed using an average value of 0.9 for the *K* factor [8].

3. Results

Interruption of radiation therapy is common in everyday practice. According to the national audit performed in Great Britain: 63% of the population has missed a part of treatment at least once [9]. However, national hospitals do not have such regulations. Adopting a structured plan into the treatment process is a necessary next step.

3.1. Interruption simulation in clinical practice

An analysis of different interruption scenarios presented mixed results (Table 1). The radiobiological data calculations were chosen instead of those from other compensatory methods (bi-fractionation or application of radiotherapy on weekends and public holidays). This method was selected expressly to estimate the average dose and overall duration, when other strategies cannot ensure adequate recovery of lost radiation courses. The main variable was the interruption interval, which ranged from 7 to 14 days. An additional factor, late tissue and organ complications, was evaluated after the introduction of the new fractional dose.

Table 1. Results of the different interruption scenarios and BED_3 for late normal tissue complications following the compensative strategy

Situations	Gap (days)	T modified	n applied	n residual	x (Gy)	BED3 modified (Gy)	Difference in BED_3 (%)
1.	14	53	20	10	3.2	132.8	13.8
2.	14	60	20	15	2.6	139.5	19.5
3.	12	53	20	10	3.2	132.8	13.8
4.	10	53	20	12	2.8	131.6	12.8
5.	10	58	20	15	2.5	135.4	16.1
6.	8	53	20	14	2.43	128.2	9.9
7.	8	56	20	15	2.42	132.2	13.4
8.	7	53	20	15	2.29	127.2	9.1

The first situation was evaluated further. Discontinuation occurred at the end of the course of the radiotherapy. The final plan exceeded only one week (from 46 to 53 days). However, there was not enough time to complete the entire course. Therefore, five fractions were lost and compensated with an increased dose of 3.2 Gy. However, it should be considered that the dose for late complications exceeded the initial value by 13.8%, as any increases in dose are unfavourable. Nevertheless, an actual impact on critical organs can be seen applying the new dose in the radiotherapy re-planning program.

3.2. Measurements of late complications using a radiotherapy planning system

For our studied set of cases, organs such as the spinal cord and parotid glands on both sides were selected. The modified dose was subsequently tested using the computerized radiotherapy planning program "Eclipse". The main criterion was compliance with the limits of organs at risk. Restrictions were designed following the Quantitative Analyses of Normal Tissue Effect in the Clinic (QUANTEC) protocol [10].

Assessment of effects on healthy tissues included theoretical knowledge and practical examination. Therefore, the evaluation process incorporated not only consideration of dose volume histograms (DVH), which define the exposure of surrounding healthy organs, but also spatial properties of radiation allocation, and other comorbidities related to the patient.

Cancer of the root of the tongue was chosen for the evaluation of late-responding organ exposure after

radiotherapy re-planning. Kilo-voltage cone beam computed tomography (kV-CBCT) imaging was performed during the planning process. Dose volume histogram (DVH) and volume (cm^3), maximal and mean doses (Gy) data were compared with compensated plan values (Fig. 2).

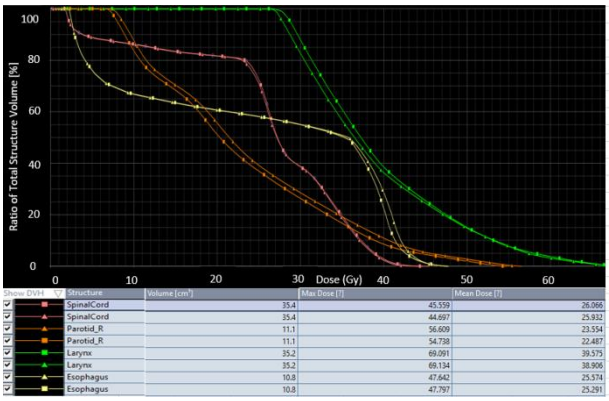

Fig. 2. Comparison of original and modified radiation therapy plan using dose volume histogram (DVH) with additional explanation of variables: structure, volume (cm3), max and mean doses (Gy)

In order to avoid late complications, the dose to the spinal cord should not exceed 50 Gy. When the dose to the spine reaches 59 Gy, the probability of developing myelopathy (adverse effect) increases from 0.2 to 5%. Another common late complication of head and neck cancer due to excessive irradiation of the parotid glands is xerostomia. For this reason, less than 25 Gy should be applied to both parotids [11].

Based on the collected values from the radiotherapy planning system, the doses to the spinal cord (Fig. 3) ranged from 30.56 to 49.63 Gy after the initial treatment modification. In comparison, the original plans without any alteration in radiation doses and fractionation, received consistently lower irradiation than compensated plans after the break.

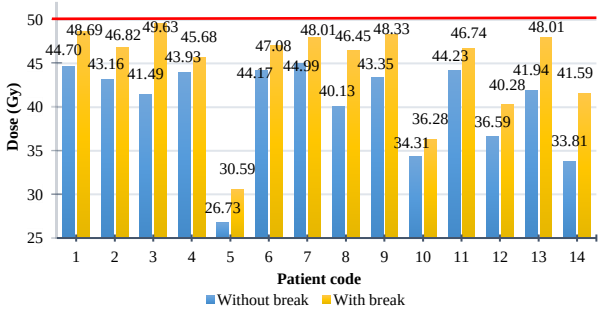

Fig. 3. Comparison of dose (Gy) to the spinal cord before and after compensation

A similar method was used to adjust for the right parotid gland. In this scenario four participants, 1, 4, 7 and 8, exceeded the dose constrains (Fig. 4).

However, suitable doses to the right parotid were only achieved when a lower fractional dose than 3.2 Gy was operated on the selected cases (Fig. 5). Therefore, the dose was reduced from 25.10 to 23.81 Gy for the first, from 25.35 to 21.86 Gy for the fourth, from 25.61 to 23.93 Gy for the seventh, and finally from 26.27 to 24.97 Gy for the eighth patient.

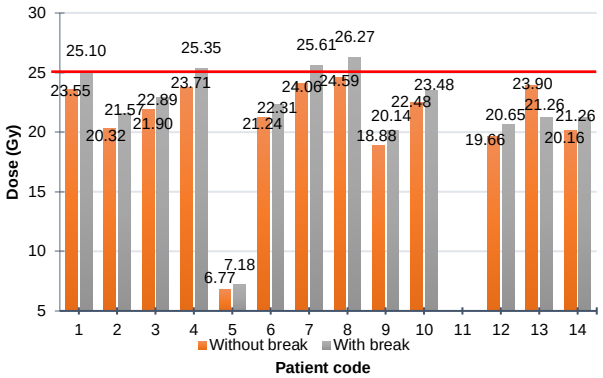

Fig. 4. Comparison of dose (Gy) to the right parotid gland before and after compensation (before optimisation)

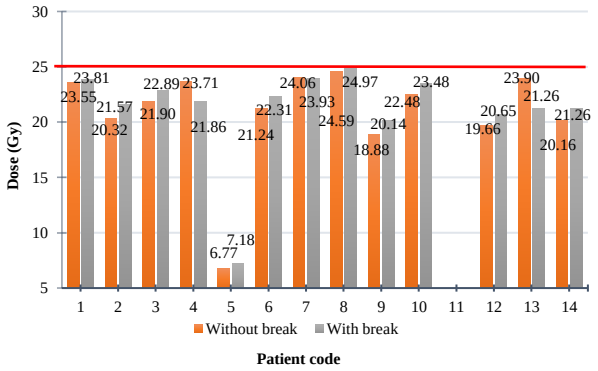

Fig. 5. Comparison of dose (Gy) to the left parotid gland before and after compensation (after optimisation)

Some medical cases were re-evaluated due to dose escalation after a break. As a result, after the optimisation none of the 14 patients evaluated in the first situation exceeded the spinal cord and parotid gland dose limits. Nevertheless, calculation of the biological dose for the missed treatment should not be considered beneficial in every clinical situation and only a qualified specialist can give a final decision on the treatment modification. Late tissue complications remain the most significant detail from the recalculation results.

3.3. Compensative radiotherapy implementation

Implementation of the compensation strategy for missed radiotherapy courses is a complex mechanism and requires a multidisciplinary team. As suggested by G. Pozo et al. [12] there are well-defined steps in the direction of safer radiation therapy re-planning:

1. First of all, an appropriate study of any available literature related to the compensative methods for the unplanned gap;
2. Introduction to the medical personnel about the obtained information from the research justifying advantages and disadvantages in any treatment alterations;
3. Finally, designation of the health care specialist committee for the final evaluation and protocol establishment.

The strategy of missed treatment correction includes the selection of the appropriate compensative method together with well-developed communication between hospitals and also importantly, increase in investment to

allow for additional treatment delivery windows (Fig. 6). The ASARA ("As short as reasonably achievable") principle should be applied to minimise any interference where possible. Although some components of radiotherapy compensation are unquestionably better than others, practical considerations (the available equipment and hospital funding) seem to have an impact on the choice of missed treatment control strategy. In order to find a consensus plan that assists the patient and the medical staff, it is important to consider more than one of the potential solutions.

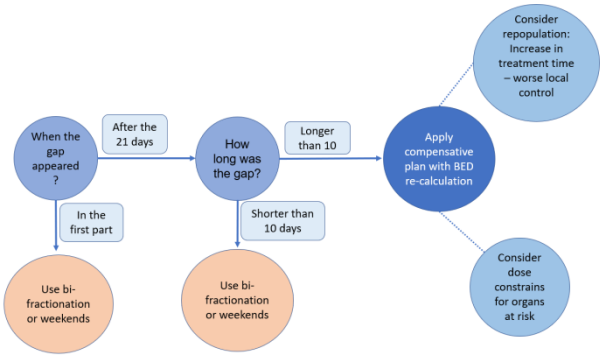

Fig. 6. An algorithm designed for undesirable interruptions in radiation therapy management

The physician must accept the final decision, regarding what kind of alteration in treatment will be adopted (fractionation, timing, dose). Changes in radiation dose in order to control tumour growth should not exceed the normal tissue control. Depending on the circumstances, a radiologist might keep the same treatment plan.

4. Conclusions

Simulating different interruption cases for head and neck patients showed that 14 days interruption still can be compensated using radiobiological model and it can be considered as a possible alternative after a missed radiotherapy treatment. The most extreme of the simulated cases was analysed based on 3D treatment planning system. Results of analysis showed that the re-calculated dose per fraction increased from 2 Gy/fr. to 3.2 Gy/fr. applied for 14 head and neck cancer patients exceeded the radiation dose limit (> 25 Gy) to the right parotid gland only four of them. However, satisfactory results were obtained after reducing the dose to remaining fractions of the specific plans.

The compensation "model" was implemented according to the international guidelines. In the first part of radiotherapy, the gap can be managed by using the bi-fractionation method and including weekends in the therapy. However, after approximately 21 days of treatment, the radiobiological effect should be recalculated according to the biologically effective dose. Concordantly, we recommend that healthcare centres should maintain databases in which patient treatment is tracked and implement protocols for missed radiotherapy courses.

References

1. Dale RG., Jones B. et al. Radiotherapy treatment interruptions during the Covid-19 pandemic: The UK experience and implications for radiobiology training. Radiation Physics and Chemistry, England, 2022.;200.
2. Xu C., Yang K. B. et al. Radiotherapy interruption due to holidays adversely affects the survival of patients with nasopharyngeal carcinoma: a joint analysis based on large-scale retrospective data and clinical trials. Radiation Oncology. 2022;17(1):1-11.
3. Caudell J.J., Tores-Roca J.F., Gillies R.J. et al. The future of personalised radiotherapy for head and neck cancer. Lancet Oncology. 2017;18(5):e266-e273.
4. Jones B., Dale R. et al. Clinical and practical considerations in the design of appropriate compensation schedules following treatment interruptions. BJR Open. 2020;2(1):20200041.
5. Royal College of Radiologists. Guidelines for the management of the unscheduled interruption or prolongation of a radical course of radiotherapy, London: Board of Faculty of Clinical Oncology, Royal College of Radiologists, 1996.
6. Higgins G. et al. The Timely Delivery of Radical Radiotherapy: Guidelines for the Management of Unscheduled Treatment Interruptions Fourth Edition. 2019.
7. Fowler J.F. Practical Time–Dose Evaluations, or How to Stop Worrying and Learn to Love Linear Quadratics. 2011:3-50.
8. Jones B., Dale R.G., Hopewell J. Additional guidance on management of unscheduled radiotherapy treatment interruptions in patients during the COVID-19 pandemic. [viewed 6 March 2023]. Access via: www.rcr.ac.uk/cancer-treatment-documents
9. James N.J., Robertson G., Squire C.J., et al. A national audit of radiotherapy in head and neck cancer. *Clinal Oncology*. 2003;15(2):41-46.
10. Noël G., Antoni D. Organs at risk radiation dose constraints. *Cancer Radiother*. 2022;26(1-2):59-75.
11. Schultheiss T.E., Kun L.E., Stephens L.C. Radiation response of the central nervous system. *Int J Radiat Oncol Biol Phys*. 1995;31(5):1093-1112.
12. Pozo G., Pérez-escutia M.A., Ruíz A., et al. Management of interruptions in radiotherapy treatments: Adaptive implementation in high workload sites. *Rep Pract Oncol Radiother*. 2019;24(2):239-244.

MEDICAL PHYSICS IN THE BALTIC STATES 16 (2023)

Proceedings of International Conference "Medical Physics 2023"
09-11 November 2023, Kaunas, Lithuania

DEVELOPMENT OF 3D PRINTING COMPOSITES FOR PATIENT-TAILORED APPLICATIONS IN RADIOTHERAPY

Antonio JREIJE[1], Neringa KERŠIENĖ[2], Paulius GRIŠKEVIČIUS[2], Diana ADLIENĖ[1]
[1]Kaunas University of Technology, Department of Physics, Studentų Str. 50, Kaunas, Lithuania;
[2]Kaunas University of Technology, Department of Mechanical Engineering, Studentų Str. 56, Kaunas, Lithuania
antonio.jreije@ktu.edu; neringa.kersiene@ktu.lt; paulius.griskevicius@ktu.lt; diana.adliene@ktu.lt

***Abstract*:** Additive manufacturing (AM), a powerful tool for the creation of complex items for different applications at a relatively low cost, a shorter production time, and a lower amount of waste, has found various patient-tailored medical applications. This work aims to investigate the use of a new 3D printing composite for manufacturing complex patient head & neck fixation masks. 3D composite filaments were extruded in-house from ABS with various concentrations of Bi_2O_3 metal additives. Evaluation of the new 3D printed materials indicated good stiffness and robustness (UTS between 20.9-25 MPa and YM between 1887 and 2504 MPa) and no sign of deterioration after exposure to ionizing radiation up to 70 Gy.

Keywords: 3D printing, Fused deposition modelling, radiotherapy, immobilization devices

1. Introduction

Radiotherapy is one of the most common treatments of cancer that delivers high doses of ionizing radiation to a specific area of the patient. High-energy radiation beams are used to stop the proliferation of tumor cells by damaging their genetic components (i.e. DNA). During radiotherapy, targeting accuracy is vital in order to minimize unwanted irradiation of surrounding healthy tissue [1]. Therefore, patient movements must be minimized in order to ensure precise radiation dose delivery predominantly to the tumor site while limiting exposure of healthy cells [1]. This can be achieved by using immobilization devices that fixate the patient in the desired position over the treatment course while allowing reproducibility of the treatment setup over as many as 40 sessions [1]. The most widely used fixation devices are non-invasive types which consist of securely fixating the treated body area to the treatment table by means of a custom-fitted mask from a thermoplastic sheet. Prior to treatment planning, the custom mask is molded directly on the patient's region of interest with a thickness in the range of 1.5–3 mm [2]. However, the accuracy of the mask fitting depends largely on the operator's experience with molding thermoplastic with a high degree of accuracy. Poorly made masks as well as changes in geometry of the irradiated anatomy region over the course of the treatment due to weight loss or shrinkage of superficial tumor can also be an issue allowing some degree of patient motion during treatment [2].

Fused deposition modeling (FDM) also known as fused filament fabrication (FFF) is one of the most widely available 3D printing technology based on layer-by-layer material extrusion. The process involves feeding a thermoplastic or composite filament into an extruder nozzle where it is melted and then deposited in a predetermined path [3]. Since FDM first development by Stratasys Inc. in the late 1980s, this technology has shifted from a predominantly rapid prototyping technology used for design verification to an end-use manufacturing enabling the production of complex, customizable parts [3].

In the field of radiation oncology, 3D printing has nascent potential applications including manufacturing patient-tailored devices such as quality assurance phantoms, brachytherapy applicators, and bolus [4]. Such patient-specific models may be hard to fabricate using traditional material fabrication techniques such as casting or molding, may have a high cost of production, or may be labor intensive thus making it not readily available for routine use [4]. With 3D printing technology, patient data acquired from any imaging modality in the common DICOM format (Digital Imaging and Communications in Medicine) can be used to generate a virtual 3D model of the anatomical region of interest [5]. After additional image post-processing, the generated source file can be used for 3D printing. A variety of imaging modalities available in the clinical setting can be used to generate patient models including computed tomography (CT), magnetic resonance imaging (MRI), or even a simple 3D surface scanner [5].

The main objective of this work was to develop material for the patient-specific fixation mask using 3D printing technology. To achieve this primary purpose, the work was divided into four phases: (1) fabricate new Bi_2O_3

enriched commercial acrylonitrile butadiene styrene (ABS) filaments; (2) investigate the interaction of radiation with the 3D-printed samples; (3) evaluate the stiffness and robustness of the customized immobilization device through mechanical testing of different 3D samples (4) assess the effect of exposure to ionizing radiation on the properties of the newly developed 3D materials.

2. Materials & Methods

2.1. Fabrication of composite filaments

ABS pellets were purchased from 3Devo Filament Maker, Netherlands. The chosen additive, Bismuth oxide Bi2O3 (300 mesh, 99.99%), was purchased from Sigma Aldrich. For the production of 3D printable filament, ABS pellets were dry mixed with different amounts of Bi2O3 additives (1%, 3%, 5% wt). Filaments of 1.75 mm diameters were extruded in 100 g batches using a screw extruder (Precision 350, 3Devo Filament Maker, Netherlands) (Fig. 1-A). Standard 3Devo material preset for ABS was selected for extrusion while taking into account that the extrusion device had four heating zones: preheating (240°C), melting (230°C), shear (220°) and extrusion (215°C). The transition temperature of ABS from solid to liquid was 215 °C. Spooling was only initiated after the extruded filament reached a stable diameter.

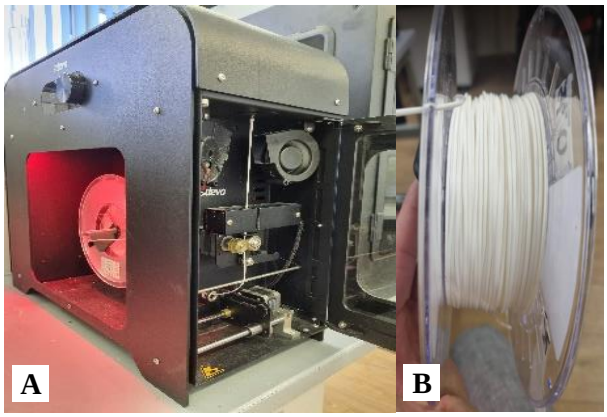

Fig. 1. Extrusion with 3Devo Filament Maker [A] of 3D filaments of 1.75 mm diameter [B].

2.2. 3D sample preparation and irradiation

Three types of samples were printed from the produced filaments for the investigation of the mechanical properties, surface morphology, and radiation attenuation properties of the samples.

For radiodensity and surface morphology analysis, cube samples were printed with dimensions of 50x50x5 mm and 5x5x1 mm respectively.

For mechanical evaluation of the new composite materials, tensile specimens were 3D printed according to ISO527-2 standard (type 1A specimens) (Fig. 2-B).

3D printing was done using the commercially available desktop 3D printer Zortrax M300 (Olsztyn, Poland) in all cases. The printing temperature was set to 260-280°C depending on the amount of additive. Additional printing parameters were set as follows: 100% solid infill, 0.29 mm layer thickness, and 80°C build plate temperature.

Irradiation was performed with Clinac DMX linear accelerator (Varian, US) at the Oncology Hospital of Kaunas University of Health Sciences. Irradiation was carried out in air at room temperature (25 °C) with 6MeV photons. Samples were exposed to 4 different doses (2, 6, 30, and 70 Gy) while keeping one sample of each material for the control. Applied doses represented prescribed dose/fraction and total irradiation dose during 3D conformal (2 and 30Gy) and more complex Intensity-modulated radiation therapy (IMRT) treatment(6 and 70 Gy) respectively.

2.3. Radiation attenuation properties

The radiodensity of 3D filaments in terms of HU and filament homogeneity was evaluated using a computed tomography scanner (CT). The printed sample plates were scanned in a GE Revolution HD CT scanner (GE, USA) with 64 detector rows using 120 kVp, 200 mA, axial acquisition with a slice thickness of 1.25 mm. For each plate, Image J (NIH, Bethesda, MD) was used to measure the mean HU and standard deviation SD in a 20 mm^2 square region-of-interest (ROI) for five consecutive slices along the plate.

2.4. Mechanical testing

Tensile tests of the 3D printed samples were performed using mechanical testing machine: ElectroPuls® Linear-Torsion (Instron, Norwood, MA, US) (Figure 2), which includes Instron® advanced digital control electronics, a bi-axial Dynacell™ load cell, console software, electrically operated crosshead lifts, a T-slot table for flexible test setups and very advanced, hassle-free tuning based on specimen stiffness. Sample specimens were fixed in self-tightening clamps and extended along the sample's major longitudinal axis at a constant test speed of 1.00000 mm/min until the specimen fractured. The gauge length was L_0 = 25 mm. The load sustained by the specimen and the elongation were measured.

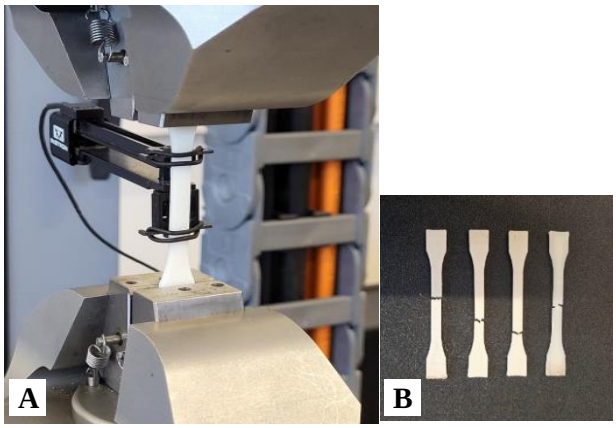

Fig. 2. [A] Mechanical testing with ElectroPuls® Linear-Torsion; [B] specimens after the tensile test.

2.5. Surface morphology

Differences in surface morphology and topography between irradiated and non-irradiated samples were investigated using atomic force microscope (AFM). AFM experiments were carried out at room temperature

using a NanoWizard III AFM (JPK Instruments, Bruker Nano GmbH, Berlin, Germany). AFM images were collected using a V-shaped silicon cantilever (spring constant of 3 N/m, pyramidal tip shape, tip curvature radius (ROC) of 10.0 nm and cone angle of 20◦) operating in contact quantitative imaging mode. AFM data was processed by SurfaceExplorer software (Microtestmachines Co., Belorussia).

3. Results

The optimal immobilization method ensures a balance between patient comfort and maintaining effective immobilization without compromising the quality of the radiation beam. In radiotherapy, ongoing progress involves the integration of innovative technologies borrowed from other fields of science, including additive manufacturing. Recent developments in 3D technology have opened up new possibilities for utilizing a variety of new composite materials. The present work intended to investigate the usability of newly developed 3D composite filament for head and neck fixation masks.

The effect of different wt % of BiO2 on the radiodensity of 3D printed samples was evaluated in the first step. Achievable HU values of ABS/Bi2O3 filaments ranged from -133 to 1020 HU, corresponding to bismuth oxide percentages by weight of 0 to 5%. Moreover, there was a strong linear correlation between metal filler percentage and radiopacity (R^2 = 0.9926). It should be noted that all the sample plates were printed as solid (at 100% infill density). This infill percentage was selected to maximize the x-ray attenuation of the materials, to investigate the homogeneity of the extruded filaments, and to evaluate the quality of the printed samples (i.e. presence of printing failures and air gaps).

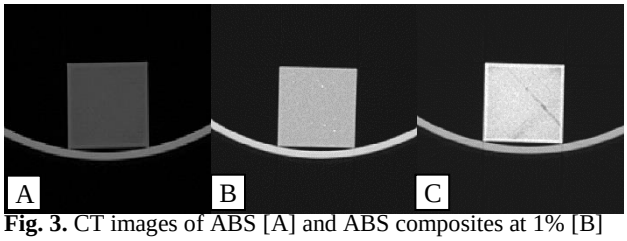

Fig. 3. CT images of ABS [A] and ABS composites at 1% [B] and 5% wt.[C] of Bi_2O_3 metals filler.

CT images of the interior of the plate test specimens with varying concentrations of Bi2O3 are shown in Figure 2. CT images revealed an overall homogeneous distribution of the filler agent within the samples for all concentrations (0.5 - 5% wt.). The images showed that at Bi_2O_3 concentrations of 3% and 5% wt, only few bright grainy spots were visible throughout the solid regions, indicating to the existence of particle clusters. No printing failures or other artifacts of the FDM printing process were observed except for ABS with 5% Bi_2O_3 where an air gap of width ranging from 0.35 to 0.6mm was observed.

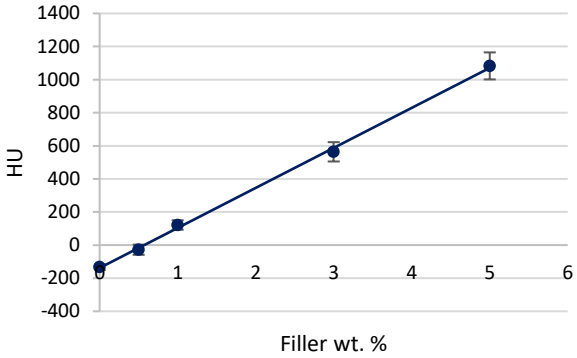

Fig. 4. Radiopacity of ABS samples containing different concentrations of Bi_2O_3 metal fillers.

Immobilization devices should have optimal mechanical properties, including a high ultimate tensile strength (UTS) and Young's modulus (YM), in order to withstand the forces exerted on the devices by patients throughout the treatment course. Additionally, these devices should maintain minimal deformation even when patients cough, sneeze, swallow, or try to change their body orientation during treatment. An extensive comparison of the tensile strength and Young's modulus versus the filler percentage of ABS/Bi_2O_3 composites was performed and results are presented in Fig. 4-A and in Table 1. It was found that the tensile strength of ABS/Bi_2O_3 composites decreased from 25 MPa at 0% wt. to 20.9 MPa at 5% wt. while the Young's Modulus decreased from 2504 MPa to 1887 MPa with the addition of 5% Bi_2O_3.

Metal particle clumping within the polymer matrix and interaction of the particles with the polymer matrix is the cause for variations in mechanical properties as a function of metal percentages. Samples with lower % w.t of fillers show better dispersion than the 5% where more agglomerated particles are present. Therefore, at higher filler concentrations, the interaction between the polymer and the particles must have an adverse effect on the strength of the material matrix.

It should be noted that 3D printed material investigated in this study indicated significantly improved UTS and YM

Table 1. Mechanical properties of non-irradiated and irradiated 3D printed composite samples.

Dose, Gy	Specimen	Maximum Load, N	Tensile Stress at Maximum Load (UTS), MPa	Young's Modulus, MPa
0	ABS 0% Bi_2O_3	250.77	25.08	2504
	ABS 1% Bi_2O_3	232.23	23.22	2019
	ABS 3% Bi_2O_3	248.28	24.83	2350
	ABS 5% Bi_2O_3	209.12	20.91	1887
70	ABS 0% Bi_2O_3	272.33	27.2	2217
	ABS 1% Bi_2O_3	216.82	21.68	1831
	ABS 3% Bi_2O_3	255.98	25.59	1775
	ABS 5% Bi_2O_3	218.31	21.83	1914

when compared to the most widely used thermoplastic materials in the clinical setting, polyester-based materials, predominantly polycaprolactone (PCL). Polycaprolactone has a tensile strength in bulk ranging from 10.5 to 16.1 MPa and Young Modulus ranging from 343.9 to 364.3 MPa [6].

The effect of irradiation with 6 MeV up to 70 Gy on the properties of the 3D printed samples was also investigated in this study (Fig. 4 and Table 1). Materials used for fixation devices should be resistant to ionizing radiation and maintain their mechanical and attenuation properties for the duration of the treatment cycle. Tensile strength results showed no slight change in the UTS after irradiation (between 3% - 8%). Moreover, the addition of 5% Bi_2O_3 had a beneficial effect on the elasticity of the thermoplastic polymer after irradiation with 70 Gy (YM increased by 14%). On the other hand, the YM of pure ABS decreased by 11% after irradiation with 70 Gy.

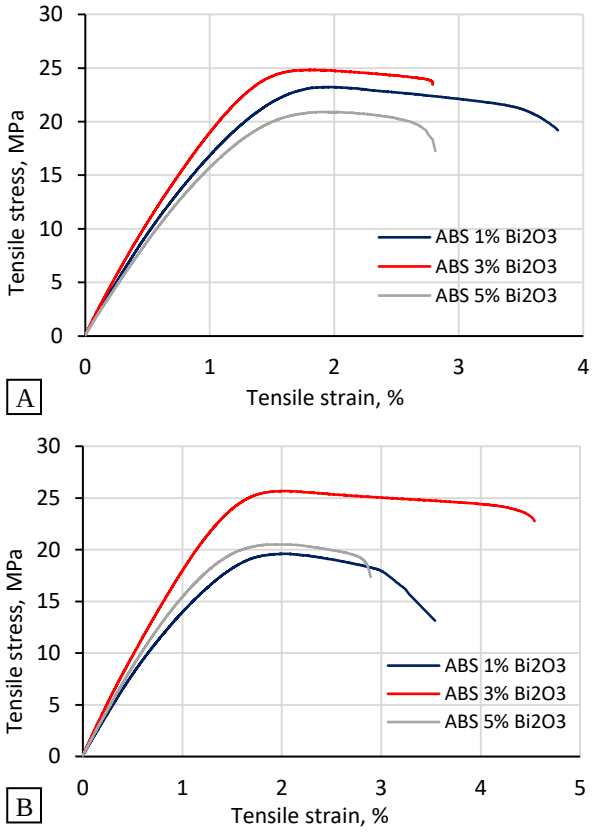

Fig. 4. Tensile stress and strain diagram of non-irradiated and irradiated 3D printed composite samples.

In addition, the fixation mask should have a smooth surface for optimal patient comfort. The effect of ionizing radiation on the surface morphology of 3D samples was evaluated with atomic force microscopy. AFM images of ABS and ABS/Bi_2O_3 5% samples before and after irradiation with low doses of ionizing radiation revealed that the surface roughness of irradiated ABS samples was slightly increasing reaching the highest roughness at 70Gy. Opposite trends can be observed for ABS/ Bi_2O_3 where the surface roughness decreased steadily with increasing irradiation dose.

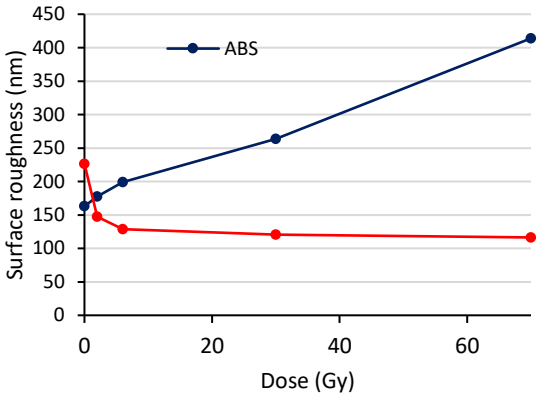

Fig. 5. Variation in surface morphology of ABS and ABS/ Bi_2O_3 with different irradiation dose.

4. Conclusions

This study presents new knowledge about the use of 3D printing composite for patient tailored applications in radiotherapy. The newly developed 3D printing composite are stronger than thermoplastics used commonly for fixation devices. Moreover, ABS/Bi_2O_3 composites are durable and resistant to the damaging effect of ionizing radiation. The results showed that at the highest concentration of Bi_2O_3 in samples an increase in elasticity and decrease in surface roughness after exposure to irradiation doses are typically encountered during a full treatment cycle; although these changes were not significant. 3D printing in healthcare is projected to grow exponentially in the upcoming years, and therefore the 3D printing materials for patient specific applications must be extensively studied in order to maintain optimal patient treatment outcome

References

1. Lee HT, Kim SI, Park JM, Kim HJ, Song DS, Kim HI, et al. Shape memory alloy (SMA)-based head and neck immobilizer for radiotherapy. J Comput Des Eng. 2015, 2, 176–82.
2. Dieterich S, Ford E, Pavord D, Zeng J. Chapter 6 - Immobilization Techniques in Radiotherapy. Elsevier, 2016. p. 87–94.
3. Gibson I, Rosen DW, Stucker B. Additive manufacturing technologies. Springer, 2010.
4. Barton MB, Jacob S, Shafiq J, Wong K, Thompson SR, Hanna TP, et al. Estimating the demand for radiotherapy from the evidence: a review of changes from 2003 to 2012. Radiother Oncol. 2014, 112, 140–4.
5. Jreije A, Keshelava L, Ilickas M, Laurikaitiene J, Urbonavicius BG, Adliene D. Development of Patient Specific Conformal 3D-Printed Devices for Dose Verification in Radiotherapy. Appl Scienc. 2021, 11(18), 8657.
6. Eshraghi, S, Das S. Mechanical and microstructural properties of polycaprolactone scaffolds with one-dimensional, two-dimensional, and three-dimensional orthogonally oriented porous architectures produced by selective laser sintering. Acta biomaterialia, 2014, 6(7), 2467–2476.

MEDICAL PHYSICS IN THE BALTIC STATES 16 (2023)

Proceedings of International Conference "Medical Physics 2023"
09-11 November 2023, Kaunas, Lithuania

COMPARISON OF THE PHANTOM BASED OUT-OF-FIELD DOSE MEASUREMENTS IN INTENSITY-MODULATED RADIOTHERAPY AND VOLUMETRIC-MODULATED ARC THERAPY

Vilius MILAŠIUS[1], Jurgita LAURIKAITIENE[1], Todorka L. DIMITROVA[2], Sofia MILENKOVA[2], Militsa MILUSHEVA[2], Diana ADLIENE[1]
1Department of Physics, Kaunas University of Technology, Studentu str. 50, Kaunas, Lithuania. 2Department of Physics, Faculty of Physics and Technology, University of Plovdiv "Paisii Hilendarski", 24 Tsar Asen St., 4000 Plovdiv, Bulgaria

***Abstract*:** In the external beam radiotherapy, advanced techniques such as Intensity-Modulated Radiotherapy (IMRT) and Volumetric-Modulated Arc Therapy (VMAT) have gained prominence for their precise dose delivery within the treatment field. However, concerns about the dose levels in the out-of-field regions persist, particularly in the context of potential risks to healthy tissues. Consequently, this study presents a comprehensive comparison of out-of-field dose measurements in IMRT and VMAT using phantom-based methods, calculating plans, using different algorithms (Analytical Anisotropic Algorithm (AAA) and Acuros). The findings revealed important insights into the differences between IMRT and VMAT in terms of out-of-field doses, shedding light on the respective advantages and limitations of these two contemporary radiotherapy modalities. These insights are valuable for the treatment planning and decision-making to optimise patient outcomes, trying to minimise radiation exposure to non-targeted tissues.

Keywords: out-of-field doses; anthropomorphic phantom; intensity modulated radiotherapy; volumetric arc therapy

1. Introduction

The primary goal of external beam radiotherapy (EBRT) is to deliver a high dose of radiation to the tumour while minimising radiation exposure to surrounding healthy tissues. Enhanced irradiation techniques and therapeutic strategies means an increased effectiveness of cancer treatment. Due to this reason patients' survival and life expectancy increase. However, even innovative radiotherapy techniques are used where normal/healthy tissues are inevitably irradiated, from daily imaging (Image-Guided Radiotherapy), and are influenced by out-of-field doses. It is determined that out-of-field doses during radiotherapy could lead to potential late effects and secondary malignancies, especially after irradiation with low doses [1-2]. It was observed that the new treatment planning systems can assure an accurate dose delivery to the target, but some of them for the locations outside the treatment fields underestimate the irradiation doses [3-4]. Even the numerous measurements with anthropomorphic phantoms were done, therefore, there is still a lack of data for the out-of-field doses measurements. Due to this reason *the aim of this experimental study* was to compare and analyse phantom based out-of-field doses registration, using two different treatment planning techniques (Intensity Modulated Radiotherapy and Volumetric Arc Therapy) and dose calculation algorithms (AAA and Acuros).

2. Materials and methods

2.1. Treatment planning

The anthropomorphic male pelvis region phantom (Sun Nuclear, CIRS model no. 801-P-A) (Fig. 1) [5] was used for the treatment planning and the main results analysis. The phantom was scanned with 0.625 mm slice thickness using the GE Bright Speed Computed Tomography (CT) scanner at the Hospital of Lithuanian University of Health Sciences Kaunas Clinics, Oncology Hospital, Department of Radiotherapy.

Using treatment planning system Eclipse™ (Varian Medical System) the selected prostate cancer patient CT images and all contoured structures with deformable registration were registered on the anthropomorphic phantom CT images.

So, for the selected prostate cancer patient four treatment plans (2 VMAT with 3 full arcs (179°-181°)) (AAA and Acuros) and 2 IMRT with 8 fields geometry (every 45°) (AAA and Acuros)) on the anthropomorphic phantom CT images were planned (Fig. 2) and optimised regarding the clinical constraints and QUANTEC recommendations (Table 1).

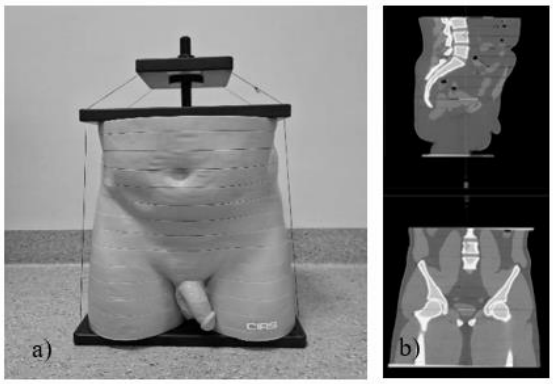

Fig. 1. Anthropomorphic phantom CIRS Model 801-P-A and CT scanned images

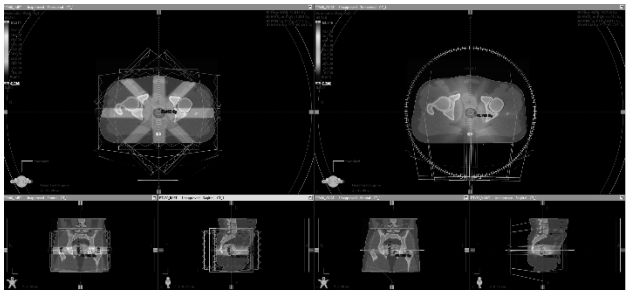

Fig. 2. Evaluation of VMAT and IMRT treatment plans

Table 1. QUANTEC recommendations [6-7]

Organs at risk	Dose (Gy) or dose/volume parameters
Rectum	V_{50}<50%
	V_{65}<25%
	V_{70}<20%
Bladder	V_{55}<50%
	V_{65} < 50 %
	V_{70} < 35 %
Penile bulb	$D_{60-70\%}$ < 70 Gy
	$D_{95\%}$ < 50 Gy
Femoral heads	V_{50} < 5 %
Small intestine	$D_{max} \leq$ 52 Gy
	V (≥50 Gy) < 5 %
Colon	$D_{max} \leq$ 55 Gy
	V_{50} < 10 %
Pelvic bone	V (≥30 Gy) <30%, Dmean <20 Gy

VMAT and IMRT plans were calculated using the AAA and Acuros algorithms, keeping the same MU per beam. All the plans were calculated for the maximum 6 MeV flattening filter-free (FFF) energy beams. The maximum prescribed dose per plan for the planning tumour volume (PTV) was equal to 60 Gy/20 fractions.

2.2. Out-of-field doses evaluation

Out-of-field doses evaluation for this study was done using 3 different dose profiles.
Irradiation doses provided outside the treatment field edge (less than 5 % of the prescribed dosage [3]).

3. Results and discussion

Dose profiles were analysed for two different inverse treatment planning techniques (IMRT and VMAT) and were calculated with two calculation algorithms (AAA and Acuros) (Fig. 2).

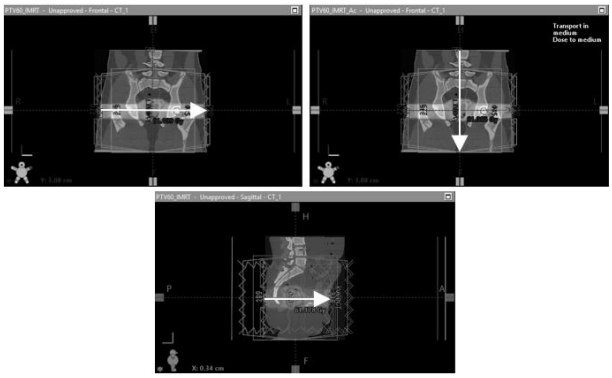

Fig. 3. 2 frontal views (marked by an arrow) and 1 sagittal view of IMRT treatment plan, planned with Acuros algorithm

As it could be observed and expected from the obtained results (Fig. 4 (for the sagittal views) and Fig. 5 (frontal view)), in the high dose region (PTV) – treatment region, the four treatment plans delivered similar dose levels, and the difference was not significant. The same tendency of the results was observed and for the frontal views.

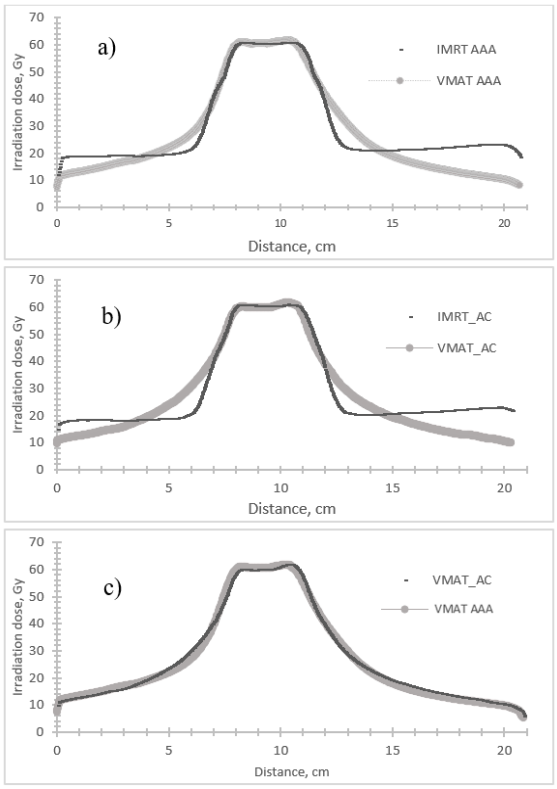

Fig. 4. Comparison of 1 sagittal view for different techniques IMRT and VMAT treatment plans, planned with AAA and Acuros algorithms

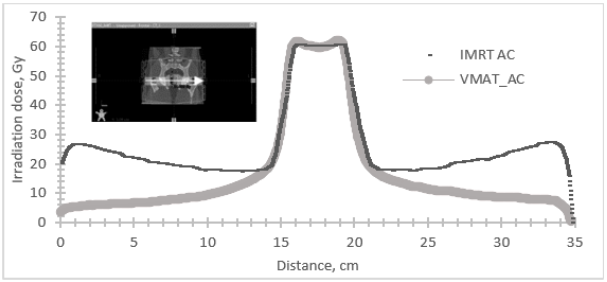

Fig. 5. The frontal view of IMRT and VMAT treatment plans, planned with Acuros algorithm

As it could be seen in a distance from the PTV the irradiation doses decrease and the disagreements between treatment planning techniques (IMRT and VMAT) increase (Fig. 4 and Fig. 5), but if technique was the same, registered difference was not so significant (Fig. 4 c)).

The obtained results showed that even dose constraints regarding the QUANTEC (Table 1) were fulfilled for all planned, but it was observed that dependant on organ. It was found that in the most cases of this study IMRT in comparison to VMAT plans spare of normal tissues had a better outcome (average radiation doses reconstructed in 3D outside the treatment fields), even in greater distance (5 cm) from the treatment field edge for the IMRT plans were registered higher doses (Table 2).

Table 2. Irradiation dose differences compared between IMRT and VMAT for the mostly influenced OARs

Tech-nique	Calcula-tion algorithm	Organ at risk (OAR)	Distance from the treatment field edge, cm	Dose, Gy
IMRT	AAA	Bladder	1.5	27.6
			3.0	20.7
			5.0	**20.9**
		Mean dose (whole organ), Gy		**29.5**
		Rectum	1.5	27.3
			3.0	**19.5**
		Mean dose (whole organ), Gy		**23.9**
	Acuros	Bladder	1.5	29.2
			3.0	20.2
			5.0	**20.4**
		Mean dose (whole organ), Gy		**28.7**
		Rectum	1.5	26.5
			3.0	**18.9**
		Mean dose (whole organ), Gy		**23.0**
VMAT	AAA	Bladder	1.5	37.0
			3.0	23.7
			5.0	**15.4**
		Mean dose (whole organ), Gy		**32.1**
		Rectum	1.5	30.2
			3.0	**21.3**
		Mean dose, Gy		**23.6**
	Acuros	Bladder	1.5	32.3
			3.0	23.8
			5.0	**17.1**
		Mean dose, Gy		**31.7**
		Rectum	1.5	33.9
			3.0	**23.4**
		Mean dose, Gy		**23.5**

Even it is known that calculation algorithm Acuros in a distance (10 cm) from the field edge calculates a slower slope in comparison with 3D CRT [3], thus in this study comparing VMAT and IMRT techniques such a difference was not observed. Since it is known that [6-9] the use of TPS is not suitable for predicting administered doses for distant organs, and despite the fact that Acuros calculates doses at a greater distance from the PTV compared to AAA, it tends to underestimate, for example, head and neck doses up to 50 % [3]. Therefore, this inaccuracy can lead to significant discrepancies in the Dose-Volume Histogram (DVH) for organs that are partially within the treatment beams, such as the spinal cord, for example [3]. In particular Howell et al. [10] reported underestimations exceeding 40% using AAA when the distance from the field edge ranged from 3 cm to 11 cm in 3D CRT. Additionally, Taddei et al. [11] found mean discrepancies of 14% with AAA in 3D CRT when the distance from the beams varied from 1 cm to 8 cm. Due to this reason the next step of this study will be to compare the results determined by the treatment planning system Eclipse™ with the measurements registered using 2D gafchromic films dosimetry.

4. Conclusions

Even irradiation treatment planning techniques like VMAT and IMRT ensures more efficient irradiation of the target, minimising possible side-effects, but still it remains a risk of secondary cancer malignancies related to out-of-field doses. Analysing obtained results, it was found that chosen treatment planning technique and even calculation algorithm of the doses could have a significant impact on the average radiation doses reconstructed in 3D outside the treatment fields, especially evaluating out-of-field doses. Due to this reason, it is recommended to do additional dosimetry measurements, for example, using 2D gafchromic films.

References

1. Knežević Ž., Stolarczyk L., Bessieres I., Bordy M. J., Miljanić S., Olko P. Photon dosimetry methods outside the target volume in radiation therapy: Optically stimulated luminescence (OSL), thermoluminescence (TL) and radiophotoluminescence (RPL) dosimetry. Radiation Measurements, Vol. 57, 2013, p. 9-18, ISSN 1350-4487.
2. Miljanić S., Bordy M. J., d'Errico F., Harrison R., Olko P. Out-of-field dose measurements in radiotherapy – An overview of activity of EURADOS Working Group 9: Radiation protection in medicine. Radiation Measurements, Vol. 71, 2014, p. 270-275, ISSN 1350-4487.
3. Julie Colnot, Sofia Zefkili, Régine Gschwind, and Christelle Huet, Out-of-field doses from radiotherapy using photon beams: A comparative study for a pediatric renal treatment. J Appl Clin Med Phys. 2021 Mar; 22(3): 94–106.
4. Kry F. S., Bednarz B., Howell M. R., Dauer L., Followill D., Klein E., Paganetti H., Wang B., Wuu S. C., Xu G. X. AAPM TG 158: Measurement and calculation of doses outside the treated volume from external-beam radiation therapy. Med. Phys, 44 (10), 2017, p. e391- e429.
5. Sun nuclear. N.d. Virtual human male pelvis phantom model 801-P. [online]. [viewed 18 April, 2023]. https://www.cirsinc.com/products/radiation therapy/virtual-human-male-pelvis-phantom/
6. Li G., Li Y., Wang J., Gao X., Zhong Q., He L., Li C., Liu M., Liu Y., Ma M., Wang H., Wang X., Zhu H. Guidelines for radiotherapy of prostate cancer (2020 edition). Prec Radiat Oncol, Vol. 5, 2021, p. 160–182
7. Sardaro A., Turi B., Bardoscia L., Ferrari C., Rubini G., Calabrese A., Ammirati F., Grillo A., Leo A., Lorusso F., Santorsola A., Stabile Ianora A. A. and Scardapane A. The Role of Multiparametric Magnetic Resonance in Volumetric Modulated Arc Radiation Therapy Planning for Prostate Cancer Recurrence After Radical Prostatectomy: A Pilot Study Front. Oncol., 2021, 10:603994.
8. Miljanić S., Bessieres I., Bordy I. M., d'Errico F., Di Fulvio A., Kabat D., Knežević Ž., Olko P., Stolarczyk L., Tana L., Harrison R. Clinical simulations of prostate radiotherapy using BOMAB-like phantoms: Results for photons. Radiation Measurements, Vol 57, 2013, p. 35-47, ISSN 1350-4487.
9. Zhang P., Happersett L., Hunt M., Jackson A., Zelefsky M., Mageras G. Volumetric modulated arc therapy: planning and evaluation for prostate cancer cases. Int. J. Radiat. Oncol. Biol. Phys, Vol. 76, 2010, p. 1456e-1462.

10. Howell RM, Scarboro SB, Taddei PJ, Krishnan S, Kry SF, Newhauser WD. Methodology for determining doses to in-field, out-of-field and partially in-field organs for late effects studies in photon radiotherapy. Phys Med Biol. 2010;55:7009–7023.

11. Taddei PJ, Jalbout W, Howell RM, et al. Analytical model for out-of-field dose in photon craniospinal irradiation. Phys Med Biol. 2013;58:7463–7479.

MEDICAL PHYSICS IN THE BALTIC STATES 16 (2023)

Proceedings of International Conference "Medical Physics 2023"
09-11 November 2023, Kaunas, Lithuania

IRRADIATION OF PHSIOLOGICAL SOLUTION WITH HIGH ENERGY ELECTRONS – A WAY TO INCREASE CYTOTOXIC/CYTOSTATIC EFFECT

Liudmyla ASLAMOVA[1], Mykhaylo ZABOLOTNYY[2], Galina DOVBESHKO[3], Galina SOLYANIK[4], Olena GNATYUK[5], Magda TSAPKO[6]
[1,2,6]Taras Shevchenko National University of Kyiv, Ukraine; [3,5]Institute of Physics of NASU, Kyiv, Ukraine; [4]R.E. Kavetsky Institute of Experimental Pathology, Oncology and Radiobiology of NASU, Kyiv, Ukraine
[1]aslamova258@gmail.com; [2]fedcba137@ukr.net; [3]matinelli@gmail.com; [4]gsolyanik@gmail.com, [5]hrysantemka@gmail.com, [6]nmrlab2007@ukr.net

***Abstract*:** The processes determining the ability of physiological saline (SP) to realize cytotoxic/cytostatic effects on some tumor cells are being investigated. The SP was irradiated with electrons with an energy of 1 MeV, the absorbed dose was in the range of [2 – 80] kGy. Lewis lung carcinoma (LLC) cell line was used for characterization studies. It has been proven that the amount of the absorbed dose affects the optical absorption spectra of the samples and leads to the occurrence of a cytotoxic/cytostatic effect.

***Keywords**:* doxorubicin, saline, irradiation, carcinoma, cytotoxicity.

1. Introduction

The problem of resistance to antimicrobial drugs is a global threat to human health and development. Its solution requires urgent efforts of science and technology. In 2020 the World Health Organization called this problem one of the ten global threats to public health facing humanity.

Among the new directions of technological progress in medicine, primary attention is paid to the treatment of oncological patients with the help of drug therapy [1, 2]. Experience shows that the appointment of antitumor chemopreparations is associated with a number of significant problems. These include the non-specific effect and high toxicity of antitumor drugs for organs and tissues not affected by the tumor. A serious obstacle to the therapeutic effect of drug therapy is the resistance of malignant neoplasms to cytostatics.

Thus, it is important to identify new biologically active materials, to study their physical-chemical and therapeutic properties. Creating effective and low-toxic anticancer drugs based on them is an urgent task of modern pharmacology and practical oncology. An essential component of this task is establishing the relationship between the physical and medical-biological properties of anticancer drugs. It is important to modify the pharmacological properties of already known anticancer drugs to increase their effectiveness and reduce toxicity.

Modern methods of physics, nanophysics and radiation medicine allow us to approach the solution of this problem. An extremely important issue is the choice of the optimal modifying admixture. Modification of drug molecules with surface-active nanoparticles has important theoretical and practical significance.

This is the way to obtain therapeutic drugs with molecules of optimal size. Thus, it is possible to achieve biological compatibility with healthy body cells and specific interaction with tumor cells.

One of the most promising new ways of modifying anticancer drugs has proven itself to be the development based on the use of preliminary irradiation with high-energy electrons of the solvent of the therapeutic drug.

The aim of the work is to study the effect of high-energy electron irradiation of physiological saline on its optical properties and its cytotoxicity towards malignant cells of Lewis lung carcinoma (LLC) in order to evaluate the possibilities of the basic foundations of the technology of modification of existing anticancer agents.

2. Samples and methods of experiment

SP (0.9% NaCl solution, Novopharm-Biosintez, Ukraine) was used in the course of the studies in sealed polyethylene vials of 200 ml. Doxorubicin solutions were prepared from doxorubicin powder (Sigma, USA) and FR, bringing the concentration of the active drug to 5 mg/ml.

High-energy irradiation was carried out with electrons with an energy of 1 MeV at the Argus resonant linear electron accelerator. The value of the absorbed dose of radioactive irradiation ranged from 2 to 80 kGy. Absorption spectra of doxorubicin solution in FR were recorded using an IR-Fourier spectrometer (Bruker IFS 66, Germany) and a Shimadzu UV-260 diffuse reflectance spectrophotometer. The accuracy of

determining the wave number was 0.2 cm^{-1}, and the accuracy of determining the transmittance was 0.1 %. IR spectra were processed using the OPUS 5.5 program. Measurements were carried out no later than 14 days after exposure to physiological saline. The temperature of the sample was within 20–25°C.

To study the pharmacological activity of the antitumor drug doxorubicin, the cell line of Lewis lung carcinoma (LLC) from the National Bank of Cell Lines and Tumor Strains of IEPOR was used R.E. Kavetsky National Academy of Sciences of Ukraine.

Cells were maintained in nutrient medium RPMI 1640 (Sigma, USA) with the addition of 10% ETS (Sigma, USA), 2 mM L-glutamine and 40 μg/ml gentamicin at a temperature of 37°C.

3. The results of experiments and their discussion

Preliminary measurements of the dependence of sample absorption on the time interval between irradiation and determination of spectra showed that radiation-induced changes in spectra disappear in 2-6 months. Therefore, the time between the irradiation of the samples and the registration of their optical spectra did not exceed 14-23 days.

The influence of irradiation on the properties of the physiological saline is illustrated in Fig. 1, where the spectral dependences of the extinction E(I) of the physiological saline in the visible and UV ranges on the value of I are shown.

Considering that the difference between the extinction spectra of irradiated and non-irradiated samples is being studied, the object of study should be Δ(I)=E(I) – E(0), which is shown in Fig.2.

For further analysis of the spectral dependence Δ(I) without taking into account the contribution of scattering processes, we change the base lines of the plots in Figs. 2, taking into account that the spectra of light scattering on spherical particles are proportional to $1/\lambda^{\alpha}$. Here, the parameter α = 4 when the particle size is less than λ (Rayleigh scattering), and α< 4 when the particle size is ~ λ (Mie scattering).

As their value, we will use the interpolation curves of the corresponding graphs in Fig. 2, an example of which is illustrated in Fig. 3.

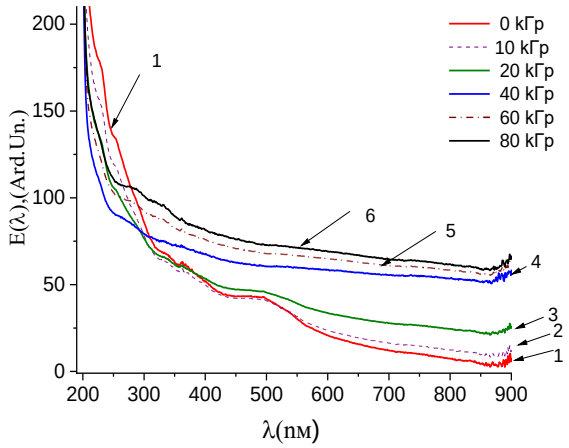

Fig. 1. Dependencies of RF extinction (E) on wavelength (λ) in the UV and visible range at different values of I. Curve 1 obtained without irradiation, 2 – at an absorbed dose of 10 kGy, 3 – 20 kGy, 4 – 40 kGy, 5 – 60 kGy, 6 – 80 kGy

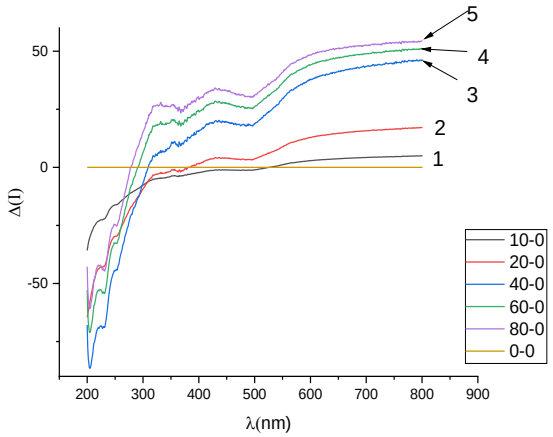

Fig. 2. The difference between the A(I) extinction spectra of irradiated and non-irradiated samples is presented. (1) represents A(10), (2) represents A(20), (3) represents A(40), (4) represents A(60), (5) represents A(80)

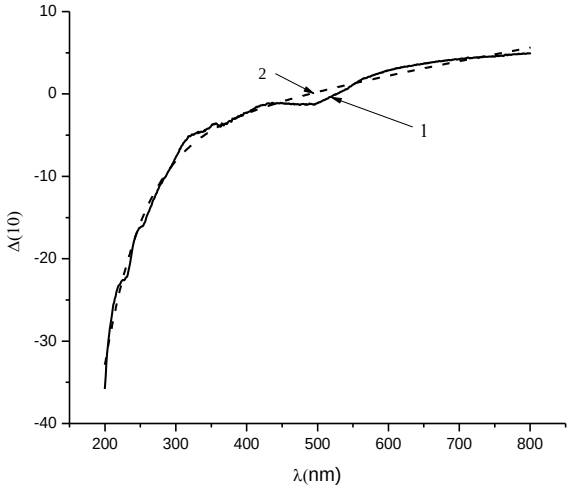

Fig. 3. Graph of the line Δ(10) and its monotonic interpolation curve (2)

Subtracting the monotonic line (2) from the line (1) of Fig. 3, let's obtain the graph of the function A (10), which characterizes the change in the absorption of the SP after its irradiation.

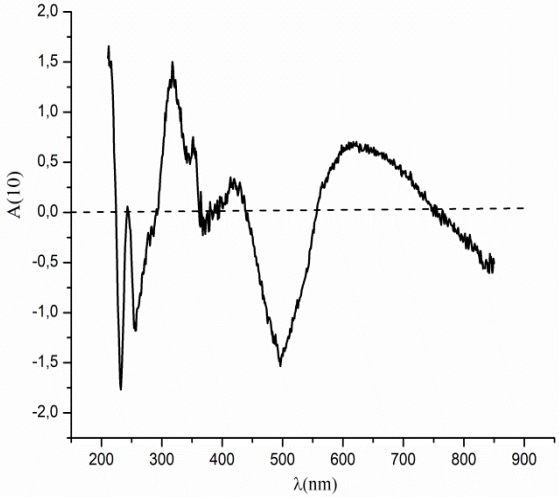

Fig. 4. Change in the absorption spectrum of SP at I = 10 kGy

In a similar way, the changes in the absorption spectra of SP at I=< 20, 40, 60, 80 kGy, which are shown in Fig. 5, are analysed.

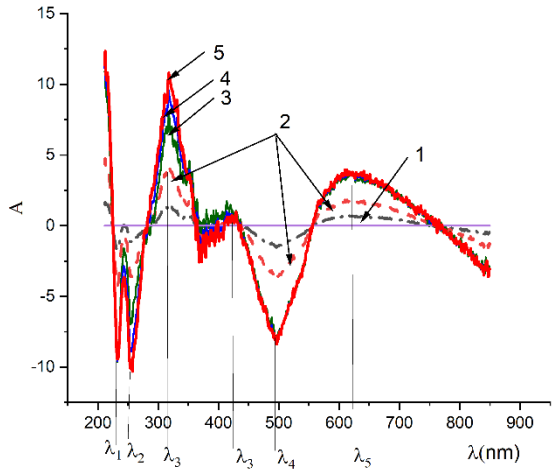

Fig. 5. Change in the absorption spectrum of SP at I = 10 (1), 20 (2), 40 (3), 60 (4), 80 (5) kGy; λ_1 = 231 nm, λ_2 = 253 nm, λ_3 = 419 nm, λ_4 = 495 nm, λ_5 = 621 nm

It follows from the information in Fig.5 that, up to experimental accuracy, the Δ (I, λ) function has extrema at the λ_1, λ_2, λ_3, λ_4, λ_5, points for all I from the range 10 - 80 kGy. The values of the function Δ (I, λ) at the points λ_1, λ_2, λ_4 are of the same sign, and at the points λ_3, λ_5, of the opposite sign for all values of I.

From this it follows that the function can be represented as a product of functions of one variable I and λ Note that at a fixed value λ < 400 nm, the modulus of the function Δ (I, λ) increases as I increases from 40 to 80 kGy. For a fixed λ> 400 nm, the modulus of the function Δ (I, λ) does not change.

A similar investigation was carried out in the case of a different classification of doxorubicin, classified in the approved and not approved RF.

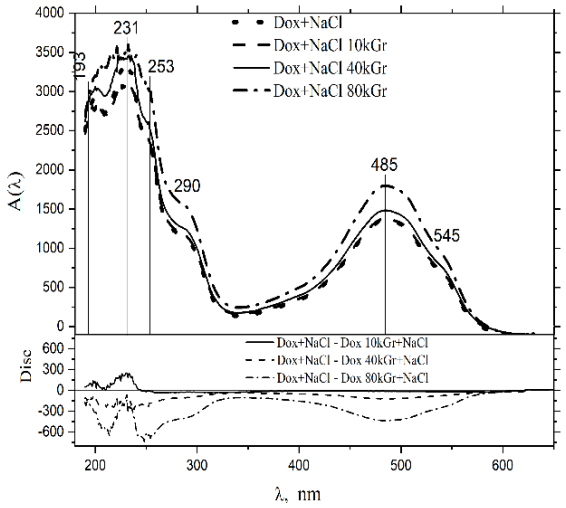

Fig. 6. Spectra of doxorubicin dissolved in untrained and irradiated saline in the UV, visible region of the spectrum

Fig. 6 shows a comparison of the optical spectra for solutions of doxorubicin in non-irradiated and irradiated saline. The absorbed radiation dose was 10, 40, 80 kGy. Note that a doxorubicin solution in a physiological solvent (Fig. 6) has characteristic features of the absorption spectra of a physiological solution without doxorubicin impurities (Fig. 5).

Such coincidences are - 1) the coordinates of the extrema of the function A (I, λ) as a function of λ in the range 200≤λ≤850 nm does not depend on the value of I, 2) in the UV range is the coincidence of the absorption lines: 231 and 253 nm, 3) Lines 495 nm (Fig. 5) and 500 nm (Fig. 6) can be considered conditionally coinciding of reasons. It is known from the literature that the specific nature of conjugated aromatic rings as closed systems creates opportunities for additional channels of structural rearrangements. Elucidation of the causes of coincidences and differences in the spectra. Fig. 5 and Fig. 6 should make it possible to elucidate the patterns of interaction between the molecular groups of doxorubicin and carcinoma molecules in the presence of a physiological solution. Such correlations in the spectra can be caused by a number electronic transition. In particular, when the number of closed systems increases, the excitation energy of molecules decreases and the absorption bands shift to the long-wave region of the spectrum.

The same independence from the value of the absorbed radiation dose is shown by the coordinates of the absorption spectra of doxorubicin solution in the IR range of the spectrum (Fig.7).

In the region of absorption of valence vibrations of OH-NH-CH molecular groups at 3800-2400^{-1} cm, we can see a significant increase in the intensity of this band in all samples with irradiated solvent without exception, as well as in the case of irradiated doxorubicin. In addition, a high-frequency shift of the maximum of this band is observed, compared to the control sample (doxorubicin dissolved in unirradiated SP).

The dependence of band intensities on the solvent irradiation dose is not directly proportional to the dose. The strongest effect of absorption enhancement in the region of hydrogen bonds is observed for a dose of 10 Gy, which was minimal in this experiment. Such an effect suggests that it is small doses that are more effective in this case. However, with a further increase in the radiation dose, processes of formation of free radicals may occur as a result of the radiolysis of water, which in turn may enter into redox reactions with doxorubicin. On the other hand, the presence of Na and Cl ions in the solution can be a protector of such reactions.

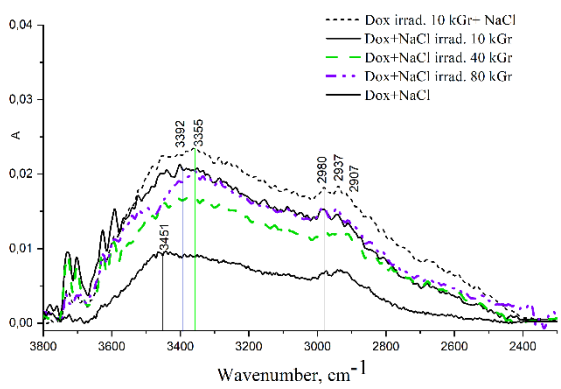

Fig. 7. Spectra of doxorubicin dissolved in untrained and irradiated saline in the IR region of the spectrum

The biomedical part of the research was carried out according to the standardized methodology - studies were conducted to determine the effect of prior irradiation of SP on its cytotoxic/cytostatic properties [2, 3].
Research on the effect of irradiation with high-energy electrons of sodium chloride as a solvent on the cytotoxic/cytostatic activity of doxorubicin dissolved in it showed an increase in the pharmacological activity of the anticancer drug (Fig. 8).

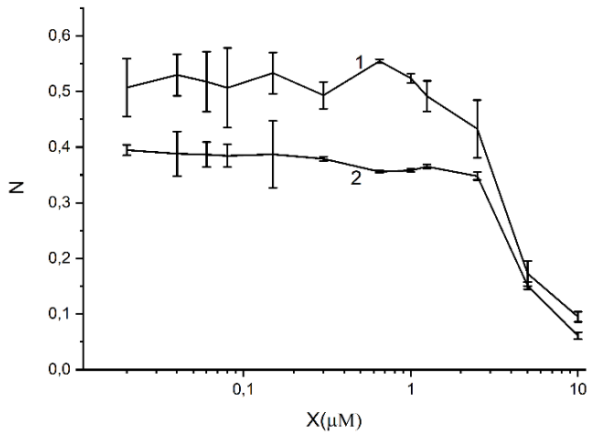

Fig. 8. Number (N) of living LLC cells (in parts of the same species in control wells) after 24 years of doxorubicin incubation (for different concentrations of X), varying between non-irradiated (1) and irradiated (2) SP

The most pronounced modification of the cytotoxic effect of doxorubicin is recorded in the range of low concentrations of the drug (<2.5 μM), the decrease in the percentage of living cells in which almost completely coincides with the cytotoxicity of irradiated sodium chloride without doxorubicin. At higher concentrations of doxorubicin (>2.5 μM), the dynamics of changes in the number of living cells with and without sodium chloride irradiation are practically the same. Thus, the obtained results confirm the possibility of enhancing the cytotoxic effect of antitumor drugs, which usually correlates with the enhancement of their antitumor activity, by irradiating the solvent, in this case SP, with high-energy electrons.

4. Conclusions

The effect of modifying the cytotoxic/cytostatic activity of SP was investigated when using the pre-irradiation of physiological solution with electrons with an energy of 1 MeV and an absorbed radiation dose ranging from 4 to 80 kGy for 2 to 6 months, depending on the amount of the absorbed dose. This effect is explained within the framework of the model babstones.
Independence of the directions of changes in the absorption spectra SP and doxorubicin solution was proven when the absorbed radiation dose changes at a constant value of the wavelength λ.
Independence of the coordinate of the extrema of the absorption change function from the presence of the absorbed radiation dose was established**.**

References

1. Bukowski K., Kciuk M., Kontek R. Mechanisms of Multidrug Resistance in Cancer Chemotherapy, Int. J. Mol. Sci., 2020, 21, p. 3233-3257; doi:10.3390/ijms21093233.
2. Aslamova L., Zabolotnyy M., Dovbeshko G., Solyanik G. Increasing the antitumor efficacy of doxorubicin by high – energy irradiation of saline. Proceedings of the 15th International Conference “Medical Physics in the Baltic States”, Kaunas, 2021. p. 70-73; https://doi.org/10.15407/jnpae2022.02.131.
3. Zabolotnyy M. A., Barabash M. Yu., Boboshko Ye. M., Grynko D. O., Kolesnichenko A. A., Lytvyn R. V., Sezonenko A. Yu., Loskutova T. V., Aslamova L.I., Minitska N. V. Photoconductive Materials for Ordered Nanoobjects Based on Template. Nanosystems, Nanomaterials, Nanotechnologies, 2023. v. 21, № 1, p. 57–71.

MEDICAL PHYSICS IN THE BALTIC STATES 16 (2023)

Proceedings of International Conference "Medical Physics 2023"
09-11 November 2023, Kaunas, Lithuania

THE EFFECT OF DIFFERENT ACTIVITIES OF ALPHA PARTICLES ON GLIOBLASTOMA 3D CELL CULTURE

Džiugilė VALIUKEVIČIŪTĖ[1,2], Greta BUTKIENĖ[2], Mindaugas DŽIUGELIS[3], Sigitas TIŠKEVIČIUS[4], Mantas GRIGALAVIČIUS[5], Jonas VENIUS[2,3]
[1]Department of Physics, Kaunas University of Technology; [2]National Cancer Institute, Biomedical Physics laboratory, Vilnius, Lithuania. [3]National Cancer Institute, Medical Physics Department, Vilnius, Lithuania, [4]National Cancer Institute, Nuclear Medicine Department, Vilnius, Lithuania, [5]Dept. Of Radiation Biology, Institute for Cancer Research, The Norwegian Radium Hospital, Oslo University Hospital. Oslo, Norway,
dziugile.valiukeviciute@ktu.edu; greta.butkiene@nvi.lt; mindaugas.dziugelis@nvi.lt; sigitas.tiskevicius@nvi.lt; mangri@rr-research.no; jonas.venius@nvi.lt

***Abstract*:** Targeted radionuclide therapy demonstrates promising outcomes when treating healthy tissues with better accuracy while at the same time causing fewer side effects. Owing to their high linear energy transfer (LET), alpha particles possess a significant potential to induce double-strand breaks in cellular DNA. 3D cell cultures stand out as an optimal method for analyzing the *in vitro* effects of alpha particles on malignant cells. The impact of various ^{223}Ra solution activities on 3D cell cultures (spheroids) was investigated.

Keywords: alpha particles, glioblastoma, ^{223}Ra, 3D cell cultures

1. Introduction

Cancer is one of the most lethal diseases globally [1]. In 2018, one in six deaths was attributed to this disease [2]. Modern radiation treatment techniques can often effectively shrink or eliminate tumor cells. In certain cases, there is a need to deliver larger doses to eradicate malignant cells but it is often restricted due to concerns for patient safety [3]. While more than half of all patients benefit from at least one radiotherapy session during their treatment, the procedure also poses risks. One significant concern is the side effects stemming from overexposure of healthy tissues adjacent to the tumor [4]. For the treatment to be effective, the radiotherapy dose must be potent enough to induce double-strand breaks in the DNA of malignant cells. Although ionizing radiation can cause various types of DNA damage, double-strand breaks (DSB) stand out as the primary lesions, resulting in the loss of reproductive integrity, which is crucial to radiotherapy's effectiveness [5].

The ability of ionizing radiation to cause DSB strongly correlates with the LET thus meaning that ionizing radiation with a higher LET can inflict greater DNA damage at lower doses to surrounding structures [5, 6]. Alpha particles, being large and heavy, have limited penetration capabilities. The biological damage potential of alpha particles is approximately 20 times larger compared to gamma or beta radiation [4, 6]. In the hypoxic environment, high LET radiation is able to effectively eliminate malignant cells and it is less affected by the cell's growth cycle [4]. This means that alpha particles are particularly suitable for targeted treatment due to their short traveling distance and high LET values that ensure the damaging effect at the binding site, affecting only targeted cells [7].

Cell culture is a popular tool for conducting *in vitro* experiments with biological tissue. It allows researchers to examine how the cells respond to various treatments and determine changes in microenvironmental conditions. Monolayer cell culture (two-dimensional (2D) cell culture) does not adequately replicate the *in vitro* tumor architecture and microenvironment [8]. At natural conditions, all cells in the human body are interconnected, forming a three-dimensional (3D) environment [9]. Such conditions can be replicated by 3D cell cultures, characterized by similar dispersion of nutrients and medications, and the presence of hypoxic zones in the center of a spheroid. Therefore 3D cell cultures are close to the natural structure of tumors and as a result, they are regarded as an *in vitro*-like platform for cancer research [2].

Glioblastomas are among the most aggressive malignant tumors. They tend to form metastases, exhibit rapid angiogenesis, and possess hypoxic areas [10]. There also exists a subpopulation of malignant cells that are resistant to ionizing radiation treatment and are tumorigenic. For a successful treatment that prevents future tumor recurrence, it is crucial to eliminate all malignant cells, especially the tumorigenic ones. Due to their resistance,

a higher dose of ionizing radiation or a combination of multiple cancer treatment techniques must be applied [7]. Given the characteristics mentioned above, glioblastomas are good candidates for alpha therapy treatment. The primary aim of this research was to quantitatively evaluate the effect of different alpha particle doses on the growth of the tumorous cells in a 3D model. Different activities of ^{223}Ra and different sizes of spheroids were used in this investigation. The exact evaluation of the radiation dose needed to reduce spheroid growth to a certain amount would help to determine the optimal ^{223}Ra activity for a combined treatment experiment, ensuring cancer destruction with minimal damage to healthy tissues.

2. Materials and Methods

2.1. Cell lines and 3D cell culture formation

The Glioblastoma cancer cell line was used in experiments.

3D cell cultures (spheroids) were prepared using the agarose method. For this purpose, flat-bottomed 96-well plates (TPP) were coated with 1.5% wt/vol agarose gel to prevent cell adhesion. 1.5% wt/vol agarose gel was made from agarose powder (Sigma-Aldrich) and DPBS (Dulbecco′s Phosphate Buffered Saline, Sigma-Aldrich). The cells were pelleted at the bottom of the agarose gel by centrifuging the plates at 500g for 20 minutes using a swinging bucket centrifuge (*Laboratory Centrifuge LMC-3000, Biosan*). Following centrifugation, the plates were incubated under standard cell culture conditions for 7 days at 37°C and 5% CO_2 in a humidified incubator. Figure 1 shows how the sample looks just after centrifugation, and Figure 2 shows how the sample looks 7 days after formation.

The primary size of the spheroids is dependent on the number of cells used for their formation. To ensure consistency in cell number, the cells were counted using a Malassez counting chamber. During the experiments, spheroids were formed from 500, 1000, and 2000 cells.

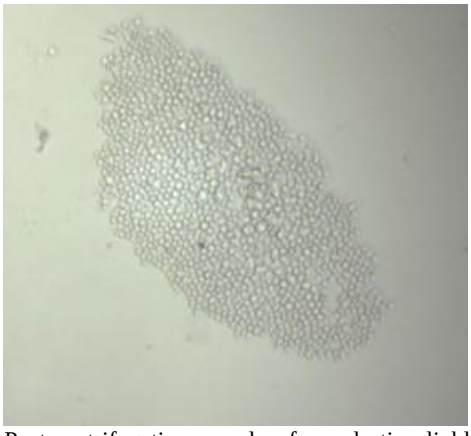

Fig. 1 Post-centrifugation sample of neoplastic glioblastoma cells.

2.2. 3D cell culture treatment with ^{223}Ra solution

Fully formed spheroids (7 days after seeding) were treated with ^{223}Ra solution (*Xofigo*®, Bayer, Germany) at activities 0.1; 0.15; 0.375; 0.6; 0.75; 1; 1.125; 1.25; 1.5 and 1.75 kBq/100 μL. 50 μL of the ^{223}Ra solution was added to each well containing a spheroid and then incubated under standard culture conditions for 24 hours. After 24 hours, the spheroids were washed three times with RPMI 1640 medium to remove any residual ^{223}Ra.

2.3. Activity evaluation

To ensure precise solution activity measurements, custom-made measurement equipment was constructed. The equipment comprises of NUVIA INSTRUMENTS COMO 170 activity meter and a 1.5 mL test tube holder that was specifically designed for this purpose. The metrological characteristics of the activity meter were validated on 2022-11-22 by the Ignalina Nuclear Power Plant's validation and calibration laboratory, which is accredited by the Lithuania National Accreditation Bureau.

A set of samples of known activities were prepared and measured using the activity measuring equipment, and a calibration curve was established and this calibration was used to monitor the activity of prepared treatments.

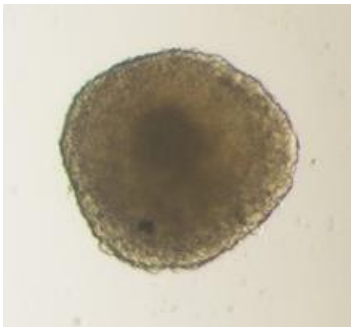

Fig. 2 A spheroid sample of neoplastic glioblastoma cells, 7 days after formation.

2.4. ^{223}Ra effect on 3D cell culture evaluation: microscopy and colorimetric assay

The size of the spheroids was assessed using an optical microscope (*Nikon Eclipse TE2000-U*) at three experiment phases: before treatment, 7 days after treatment, and 14 days after treatment. The size changes were quantified using the ImageJ program. Viability tests were conducted 14 days post-treatment. The XTT viability assay was utilized to evaluate cell viability and proliferation. To carry out this test, the culture medium was replaced with a solution containing XTT (*2,3-bis-(2-methoxy-4-nitro-5-sulfophenyl)-2H-tetrazolium-5-carboxanilide*) salt, PMS (*phenazine methosulfate*) reagent, and RPMI 1640 medium. 100 μL of the XTT solution was added to each well. The plate was then incubated under standard culture conditions for 2 hours. Following incubation, absorbance at wavelengths of 490 nm and 630 nm was measured using a microplate reader (microplate reader *800^{TS}, BioTek*). The mean absorbance values were subsequently compared to those of the control group.

3. Results

To evaluate how different activities affect cells in a 3D cell culture, glioblastoma cells were cultured as spheroids. The effect on cell viability was assessed by measuring spheroid size changes. The size of spheroids

is highly dependent on environmental conditions and the treatment activity, which was the only variable in environmental conditions. Changes in the spheroid size indicated "spheroid health" — under harsh conditions, cell proliferation slows down and spheroids stop growing. Figure 3 illustrates the impact of different treatment activities on spheroid size (spheroids were formed from 1000 cells) 7 days and 14 days post-treatment compared to their size before treatment.

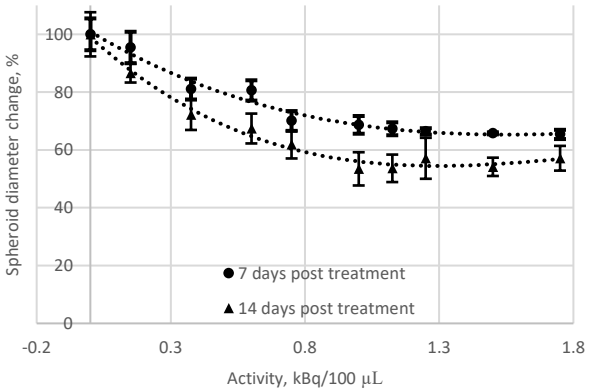

Fig. 3 Glioblastoma spheroids' diameter changes 7 days post-treatment and 14 days post-treatment in comparison with the control group when spheroids were formed from 1000 cells.

The control group (cells without ^{223}Ra solution) was constantly growing, and the size changes between day 0 and 7th; the 14th day is depicted as 100% change. Spheroids treated with ^{223}Ra activities between 0.15 kBq/100 µL - 0.375 kBq/100 µL also exhibited growth at both 7th and 14th days, but at slower rates. This indicates, that the destruction of cells with ionizing radiation started to appear and it resulted in an average of 9%, 22%, and 24% reduced spheroid size after 7 days, indicating size changes of treated spheroids compared to untreated ones. On the 14th day, an average of 13%, 18%, and 32% size reduction was observed for activities 0.15 kBq/100 µL - 0.375 kBq/100 µL. Treated with 0.6 kBq/100 µL spheroids exhibited growth on the 7th day, but on the 14th day, their shrinkage was observed. This resulted in an average spheroid size reduction of 30% after 7 days and 38% after 14 days. Spheroids treated with activities higher than 0.75 kBq/100 µL did not show size increment even on the 7th day after treatment. For all activities higher than 1 kBq/100 µL, spheroids were decreased by more than 35% after 7 days and more than 45% after 14 days. Figure 4 shows the spheroid formed from 1000 cells on the 14th day after treatment with the activity of 1.0 kBq/100 µL.

In order to evaluate the impact of alpha particles on differently-sized cell cultures, spheroids derived from glioblastoma cells were formed from 500 and 2000 cells. The effect on cell viability was evaluated by measuring the size of spheroids before and after 14 days of treatment. Figure 5 illustrates the responses of different size glioblastoma spheroids.

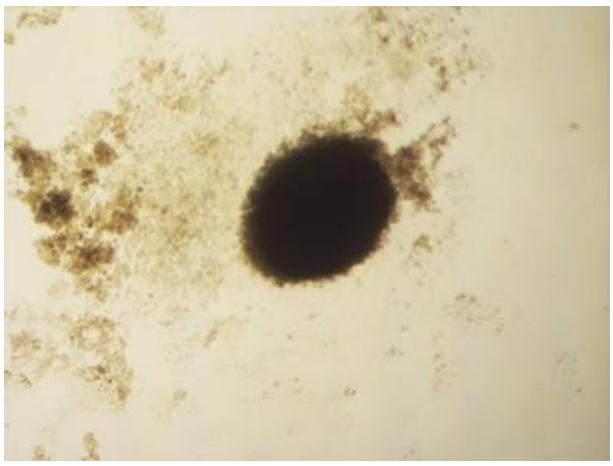

Fig. 4 Glioblastoma spheroid (formed from 1000 cells), on the 14th day post-treatment (treatment activity: 1.0 kBq/100 µL).

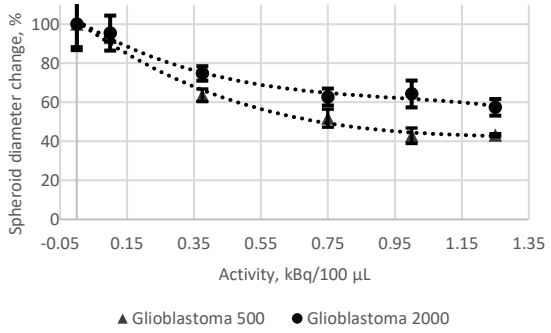

Fig. 5. Diameter changes of Glioblastoma spheroids, which were formed from 500 or 2000 cells, 14 days post-treatment in comparison with the control group.

The initial size of the spheroid is directly dependent on the number of cells used to form it. Specifically, spheroids derived from 500 cells are smaller compared to those derived from 2000 cells (the average diameter of a spheroid formed from 500 cells is 469 µm; the average diameter of a spheroid formed from 2000 cells is 660 µm).

As it was expected, treatment with ^{223}Ra resulted in decreased spheroids size, meaning that the cells' viability also decreased. Treatment with 0.1 kBq/100 µL activity resulted in 5% size reduction of 2000 cells spheroid and in 7% size reduction of 500 cells spheroid on the 14th day. An average reduction of 25% for 2000 cells spheroid and 37% reduction for 500 cells spheroid was observed after its treatment with 0.375 kBq/100 µL activity. The highest used activity of 1.25 kBq/100 µL resulted in an average size reduction of 43% for 2000 cells spheroid and 57% reduction for 500 cells spheroid.

These results indicate, that smaller spheroids exhibit more significant diameter changes after the treatment with ^{223}Ra, leading to the conclusion that, due to high linear energy transfer and short penetration depth of alpha particles, the destruction effect of ionizing particles is more significant on smaller spheroids.

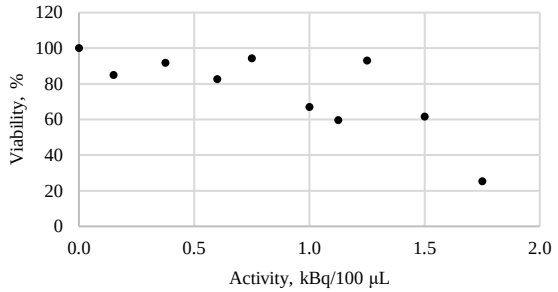

Fig. 6 XTT viability test results from glioblastoma spheroids 14 days after treatment with different activities of ^{223}Ra solution

The viability test using the XTT kit yielded information about cell viability within spheroids. Figure 6 displays XTT test results for glioblastoma cancer spheroids after 14 days post-treatment, highlighting the mean values of cell viability, revealing the tendency of decreased cell viability with increased activity. Changing the activities from 0.15 kBq/100 µL to 0.75 kBq/100 µL cell viability decreases to ~80-90%; at the activities between 1.0kBq/100µL to 1.5 kBq/100µL cell viability decreases to ~ 60% and at the activity of 1.75 kBq/100µL cell viability drops drastically, to almost 20%.

4. Conclusions

The obtained results help to clarify how alpha particles affect 3D cell cultures. It is known, that different cancer cells possess different sensitivity to the treatment applied, therefore our research helps to draw guidelines for the glioblastoma cell line viability evaluation using alfa particles as a treatment agent. It was demonstrated, that treatment activity and spheroid size are among the variables that determine the overall outcome. The size of the spheroid plays a pivotal role in evaluating responses. Due to the short range of alpha particles, spheroids with smaller diameters frequently show an enhanced response to the treatment. Tumors often have different treatment resistance levels due to the inhomogeneity of cells and their properties. The application of multiple treatments must be considered seeking the best outcomes. It is typical to search for treatment conditions that can slow tumor development by 20% to discover the best combination of treatments. However, due to the variety of influencing factors, it is challenging to determine a treatment scheme that will reduce tumor growth by 20%. Studies involving cell cultures need a lot of skills and hours of practice to get consistent results with small variations. Moreover, measurements of size do not directly take into account the impact of alfa particles on the inside cells, therefore viability tests are of the highest priority for assessing treatment efficacy. XTT results inferred, that 20% reduction of the glioblastoma spheroids can be achieved with treatment activities ranging from 0.15 kBq/100 µL to 0.75 kBq/100 µL. Spheroid size measurements have shown, that decrease in cell viability by 20% was obtained with activities less than 0.75 kBq/100 µL (on the 7th day of evaluation) and ~ 0.375 kBq/100 µL (on the 14th day of evaluation).

It was found that XTT tests can identify the relationship between diameter changes and spheroid viability, and this relationship may speed up the evaluation of spheroid viability in the future. A more precise correlation between size changes and cell viability obtained from biochemical viability tests could be established after additional investigations. Insights from former experiments provide valuable instructions for the future work.

5. Acknowledgement

This project has received funding from the Research Council of Lithuania (LMTLT), agreement No [P-SV-23-353].

References

1. Bray, F., Laversanne, M., Weiderpass, E. and Soerjomataram, I. The ever-increasing importance of cancer as a leading cause of premature death worldwide. *Cancer*. Online. 15 August 2021. Vol. 127, no. 16, p. 3029–3030.

2. Chaicharoenaudomrung, N. Kunhorm, Ph. and Noisa, P. Three-dimensional cell culture systems as an in vitro platform for cancer and stem cell modeling. *World Journal of Stem Cells*. Online. 12 December 2019. Vol. 11, no. 12, p. 1065. doi 10.4252/wjsc.v11.i12.1065.

3. Corroyer-Dulmont, A., Valable, S., Falzone, N. Frelin-Labalme, A. M., Tietz, O., Toutain, J., Soto, M.S., Divoux, D., Chazalviel, L., Pérès, E.A., Sibson, N.R., Vallis, K.A. and Bernaudin, M. VCAM-1 targeted alpha-particle therapy for early brain metastases. *Neuro-Oncology*. 2020. Vol. 22, no. 3. doi 10.1093/neuonc/noz169.

4. Riquier, H., Wera, A.C., Heuskin, A.C., Feron, O., Lucas, S. and Michiels, C. Comparison of X-ray and alpha particle effects on human cancer and endothelial cells: Survival curves and gene expression profiles. *Radiotherapy and Oncology*. 1 March 2013. Vol. 106, no. 3, p. 397–403. doi 10.1016/j.radonc.2013.02.017.

5. Franken, N.A.P., Ten Cate, R., Krawczyk, P.M., Stap, J., Haveman, J., Aten, J. and Barendsen, G.W. Comparison of RBE values of high- LET α-particles for the induction of DNA-DSBs, chromosome aberrations and cell reproductive death. *Radiation Oncology*. 8 June 2011. Vol. 6, no. 1, p. 1–8. doi 10.1186/1748-717x-6-64/figures/2.

6. LIU, L. J. Model of cell response to alpha-particle radiation. *arXiv*. 4 July 2012. P. arXiv:1207.1001. Available from: https://ui.adsabs.harvard.edu/abs/2012arXiv1207.1001L/abstract.

7. Ceder, J. and Elgqvist, J. Targeting prostate cancer stem cells with alpha-particle therapy. *Frontiers in Oncology*. 2017. Vol. 6, no. JAN. doi 10.3389/fonc.2016.00273.

8. Fontana, F., Raimondi, M., Marzagalli, M., Sommariva, M., Gagliano, N. and Limonta, P. Three-Dimensional Cell Cultures as an In Vitro Tool for Prostate Cancer Modeling and Drug Discovery. *International Journal of Molecular Sciences 2020, Vol. 21, Page 6806*. 16 September 2020. Vol. 21, no. 18, p. 6806. doi 10.3390/ijms21186806.

9. Białkowska, K., Komorowski, P., Bryszewska, M. and Miłowska, K. Spheroids as a Type of Three-Dimensional Cell Cultures—Examples of Methods of Preparation and the Most Important Application. *International Journal of Molecular Sciences 2020, Vol. 21, Page 6225*. 28 August 2020. Vol. 21, no. 17, p. 6225. doi 10.3390/ijms21176225.

10. Sattiraju, A., Solingapuram S., Kiran K., Xuan, A., Pandya, D.N., Almaguel, F.G., Wadas, T.J., Herpai, D.M., Debinski, W. and Mintz, A. IL13RA2 targeted alpha particle therapy against glioblastomas. *Oncotarget*. 2017. Vol. 8, no. 26. doi 10.18632/oncotarget.17792.

MEDICAL PHYSICS IN THE BALTIC STATES 16 (2023)

Proceedings of International Conference "Medical Physics 2023"
09-11 November 2023, Kaunas, Lithuania

EVALUATION OF THE PERFORMANCE OF THREE OCCUPATIONAL RADIATION DOSIMETRY EQUIPMENT IN DIFFERENT SETTINGS

Antonio JREIJE[1,2], Leonid KRYNKE[1], Kirill SKOVORODKO[1], Birutė GRICIENĖ[1,3]
[1]Vilnius University Hospital Santaros Klinikos, Vilnius, Lithuania; [2]Department of physics, Kaunas University of Technology, Kaunas, Lithuania; [3]Department of Radiology, Nuclear medicine and Medical physics, Faculty of Medicine, Vilnius University, Vilnius, Lithuania.
antonio.jreije@ktu.edu; leonid.krynke@santa.lt; kirill.skov@gmail.com; birute.griciene@santa.lt

***Abstract*:** Active personal dosimeters (APDs) have proven to be highly effective monitoring and optimization tool for occupational radiation exposure across various ionizing radiation applications. In order to be used in conventional and interventional radiology, these dosimeters must be sensitive to low energy photon beams and short pulsed radiation in addition to being able to record a wide range of doses. The aim of this work is to verify the performance and reliability of six dosimeters. Experiment were performed using frequently used radiology and fluoroscopy protocols. The dose equivalent registered by three APDs and three professional dose rate meters (DRM) were comparable. At low exposure time, the accuracy of APDs slightly decreased. However, the dose equivalent rates of tested ADPs were found to be unreliable when compared with DRMs.

Keywords: Radiation protection, Occupational exposure, Electronic dosimeter, Real time dosimetry

1. Introduction

Active dosimeters offer distinct advantages compared to passive detectors. They allow real-time measurements and enable the setting of a dose rate alarm for exceeding specific thresholds. Previous studies have emphasized the utility of active personal dosimeters in enhancing radiation protection of workers and raising awareness of unforeseen exposures [1,2].

Over the past decade, active dosimeters have undergone significant advancements, enhancing not only the dosimetric capabilities of first devices but also their mechanical characteristics and resistance to environmental factors. New active personal dosimeters (APDs) now feature automated data management systems and robust data transfer to centralized units [2].

Worldwide the medical field, particularly medical diagnostics, employs the largest number of workers exposed to ionizing radiation. Among them, interventional radiology operators, nurses and surgeons are most likely to receive high doses while standing close to the primary radiation field [3]. Therefore, this workers group would benefit the most from a real-time and precise assessment of their radiation exposure during X-ray procedures, as well as immediate warnings of unexpected high doses [3].

Fluoroscopy-guided procedures use pulsed ionizing radiation fields with multiple pulses per second (ranging from 2 to 30) and a pulse width of 5 to 80 milliseconds [4]. The photon energy typically falls within the range of 20 to 150 kV, and the instant dose rate can reach up to 10 Sv/h, depending on the medical staff's position [4].

The employment of ADP in pulsed radiation fields remains very limited due to reported problems in these types of radiation fields. Moreover, there is a notable absence of international standards that address the performance of active dosimeters in pulsed radiation fields. As a result, there is a pressing need to address this challenge and improve the performance of APDs in pulsed radiation environments. This has sparked considerable interest in evaluating APD performance under these conditions, revising existing standards, and developing new calibration facilities that can accurately assess the response of APDs to pulsed radiation.

The aim of this paper is to presents the initial results obtained during the evaluation of the response of three ADPs for occupational dosimetry in real time, used in conventional and interventional radiology and compare them to the performance of three professional dose rate meters (DRM).

2. Materials and Method

Six commercial active dosimeters and dose rate meters were tested in this study: Thermo EPD TruDose, Mirion DMC 3000, Polymaster PM1610B, Atomtex AT1123, RTI Piranha R100B and RTI scatter probe (Fig. 1). The main features of the tested dosimeters such as type of the

Table 1. Main characteristics of tested active dosimeters as provided by the manufacturers

	Energy range		Dose equivalent rate range		Dose equivalent range		Detector type
	Min	Max	Min	Max	Min	Max	
RTI Piranha R100B	-	150 KeV	2 nSv/h	152 mSv/h	0.2 nSv	3 kSv	Solid-state
Atomtex AT1123	15 KeV	10 MeV	50 nSv/h	10 Sv/h	0.1 nSv	100 Sv	Scintillation
RTI scatter probe	10 KeV	150 KeV	0 mSv/h	200 mSv/h	2 nSv	999 Sv	Solid-state
Mirion DMC 3000	15 KeV	7 MeV	0.1 µSv/h	20 Sv/h	0.1 µSv	10 Sv	Silicon diode
Thermo EPD TruDose	16 KeV	1.5 MeV	0.05 µSv/h	10 Sv/h	0.1 µSv	10 Sv	Silicon diode
Polymaster PM1610B	20 KeV	10 MeV	0.01 µSv/h	12 Sv/h	0.05 µSv	20 Sv	Geiger-Mueller tube

sensor, energy range and dose rate range, as indicated by manufacturers, are summarized in Table 1. Apart from the type of detector being different (semiconductor, scintillator and Geiger-Mueller tube), the other differences among the selected dosimeters include the energy range, dose and dose rate ranges. The RTI Scatter probe cover only a restricted energy range up to 150 keV which is enough for fields of radiology. The RTI scatter probe is a semiconductor detector with two separate detector areas of 10 cm^2 and 100 cm^2 that connects via USB cable to the Ocean Next™ 3.0 software (RTI Group, Mölndal, Sweden) for real time reading and reporting. Moreover, air kerma was measured with RTI Piranha R100B and was converted to dose equivalent using conversion coefficient provided by ICRU report 57 [4].

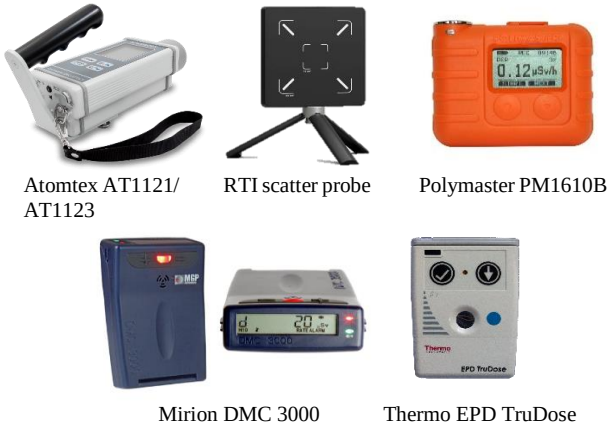

Fig. 1. Active dosimeters tested in this study.

Experimental measurements were performed at Vilnius University Hospital Santaros Klinikos with Siemens Luminos dRF MAX, a 2-in-1 fluoroscopy and radiography system. It should be noted that the x-ray equipment received regular periodical quality control and assurance testing in accordance with the radiation protection act of the Republic of Lithuania [5].

Table 2. Parameters for the clinical set-up used in this study.

	kV	mA	mAs	Filtration (mm Cu)	Pulses/s
X-ray	40-120	20-100	2-10	0	-
Fluoro	73	25-30	-	0.2	3 - 30
Fluoro cine	113	-	0.9	0	2-4

The field of view (FOV) at the flat detector set during the experiment was collimated to 30x30 cm for all measurements. Both radiology and fluoroscopy protocols which require different exposure parameters and duration of pulses, were selected to test the different dosimeters. Table 2 summarizes the parameters used for each clinical set-up.

The experimental setup aimed to simulate clinical practice is shown in Fig. 1. In order to simulate the radiation scattered by the patient's body, a 25x25x20 cm^3 PMMA (polymethyl methacrylate) slab phantom was placed on the X-ray table. The dosimeters were placed at a distance 1.5 m from the PMMA phantom. The dosimeters were positioned in level with the center of the phantom thus modeling the position of the radiologist/nurse/caregiver.

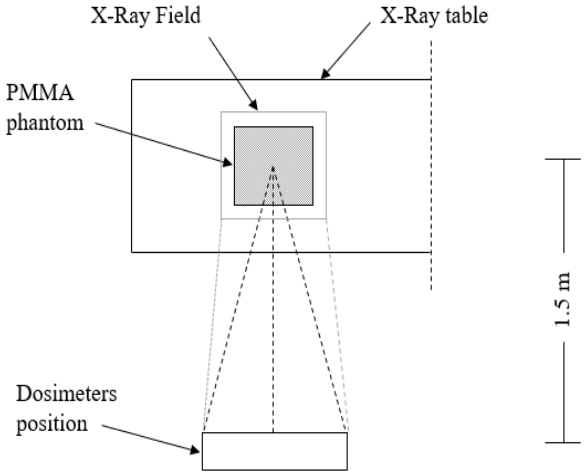

Fig. 2. Top view of the configuration used for the experimental setup.

The main objective was to evaluate the functional operation of these devices in realistic conditions with the possibility to select specific field parameters. Tests were performed to determine the response of the selected dosimeters in terms of dose equivalent and dose equivalent rate.

The repeatability of each dosimeter system was tested by repeating the exposure three times in each type of irradiation for the same unit. The dosimeter reading variability and the relative measuring uncertainty was estimated.

For conventional radiology, the influence of several parameters including tube voltage (kV), exposure time (ms) and current tube product (mAs) on the response of the dosimeter in pulsed mode was studied. For interventional radiology, the response of the dosimeters in different pulsed mode was studied.

3. Results and discussion

The performance of different dosimeters in term of dose equivalent and dose equivalent rate in conventional radiology using 80 kV, 10 mAs and 100 ms is summarized in Table 3. For dose equivalent response, all dosimeters had a very comparable reading. Atomtex AT1123, RTI scatter probe and Polymaster PM1610B displayed ~0.65 µSv while thermo EPD Trudose, RTI Piranha R100B and Mirion DMC 3000 showed 0.73, 0.77 and 0.79 µSv respectively. The largest difference reported between the different dosimeter was 19%. The repeatability test indicated that all the dosimeters have reliable reading except for Mirion DMC 300 where the reading varied between 0.63 and 0.88 (Coefficient of variation = 0.178).

However, the dose equivalent rate response was less accurate. Only RTI Piranha R100B and Atomtex AT1123 had high measurement repeatability since they are dedicated dose rate meters with large detectors and detectable dose rate equivalent as low as 0.1 and 2 nSv for Atomtex AT1123 and RTI Piranha R100B respectively. Moreover, RTI Piranha R100B displayed dose equivalent rate 16-19% higher than Atomtex AT1123 and RTI scatter probe. On the other hand, Mirion DMC 3000 and Polymaster PM1610 recorded very low doses equivalent rates while failing to measure anything in one of the exposures.

Dosimeters response was measured for the same kV and mAs but with lower exposure time (20 ms). It should be noted that the minimal exposure time under which the APDs can operate was not provided by the manufacturers. The minimum detectable duration of continuous short-term radiation as specified by the manufacturer is 0.03 s and 0 s for Atomtex AT1123 and RTI Piranha R100B respectively. In theory, while using these exposure parameters, the recorded dose equivalent should not change. That is the case for all dosimeters except RTI scatter probe. RTI scatter probe has three measuring modes (normal mode, free run and timed mode). When the irradiation rate is expected to be higher than 5 µSv/h during the entire measurement, normal mode should be used. In this case the scatter probe will auto-trig when the irradiation rate is above the trig level. However, when the irradiation rate is below 5 µSv/h, free-run or timed mode is recommended. In such case, the scatter probe will then be manually trigged. In this study, normal mode was used for all measurements. Moreover, the repeatability of the results was low except for RTI Piranha R100B. Regarding dose equivalent rates reading, all of the APDs and DRMs underestimated the dose rate by more than twice except for RTI Piranha R100B that provided accurate measurements.

The response of dosimeters at different tube voltage ranging from 40 to 120 kV was also investigated. The measured dose equivalent increased exponentially with increasing kV for all dosimeters. Overall, as can be seen in Fig. 3-A, reading of different dosimeters are similar while the calculated percentage difference decreased at higher kV.

Table 3. Dose equivalent response (µSv) of dosimeters in conventional radiology protocol (81 kV; 100 mA; 100 ms; 10 mAs)

81 kV 100 mA 100 ms	Piranha R100B	AT1123	RTI scatter probe	DMC 3000	PM1610B	EPD TruDose
1.	0.78	0.64	0.65	0.87	0.63	0.7
2.	0.77	0.64	0.64	0.63	0.59	0.7
3.	0.77	0.65	0.70	0.88	0.7	0.8
Mean	**0.77**	**0.64**	**0.66**	**0.79**	**0.64**	**0.73**
Coefficient of variation	**0.007**	**0.009**	**0.05**	**0.178**	**0.087**	**0.079**

Table 4. Dose equivalent rate response (mSv/h) of dosimeters in conventional radiology protocol (81 kV; 100 mA; 100 ms; 10 mAs); *n/m: nothing registered

81 kV 100 mA 100 ms	Piranha R100B	AT1123	RTI scatter probe	DMC 3000	PM1610
1.	28.53	23.7	22.23	0.514	n/m
2.	28.14	22	22.36	0.565	0.160
3.	28.12	23.4	26.43	n/m*	0.014
Mean	**28.26**	**23.03**	**23.67**	-	-
Coefficient of variation	**0.008**	**0.039**	**0.100**	-	-

Table 5. response of dosimeters in conventional radiology protocol (81 kV; 500 mA; 20 ms; 10 mAs)

81 kV 500 mA 20 ms	Piranha R100B		AT1123		RTI scatter probe		DMC 3000	PM1610B	EPD TruDose
	Dose equivalent (µSv)	Dose equivalent rate (mSv/h)	Dose equivalent (µSv)	Dose equivalent rate (mSv/h)	Dose equivalent (µSv)	Dose equivalent rate (mSv/h)	Dose equivalent (µSv)	Dose equivalent (µSv)	Dose equivalent (µSv)
1.	0.78	140.13	0.69	36	0.39	66.35	0.69	0.62	0.8
2.	0.78	139.85	0.69	39	0.34	65.77	0.79	0.54	0.6
3.	0.70	144.16	0.67	40	0.36	69.05	0.64	0.91	0.8
Mean	**0.75**	**141.38**	**0.68**	**38.33**	**0.36**	**67.06**	**0.71**	**0.69**	**0.73**
Coefficient of variation	**0.063**	**0.017**	**0.017**	**0.054**	**0.069**	**0.026**	**0.108**	**0.282**	**0.157**

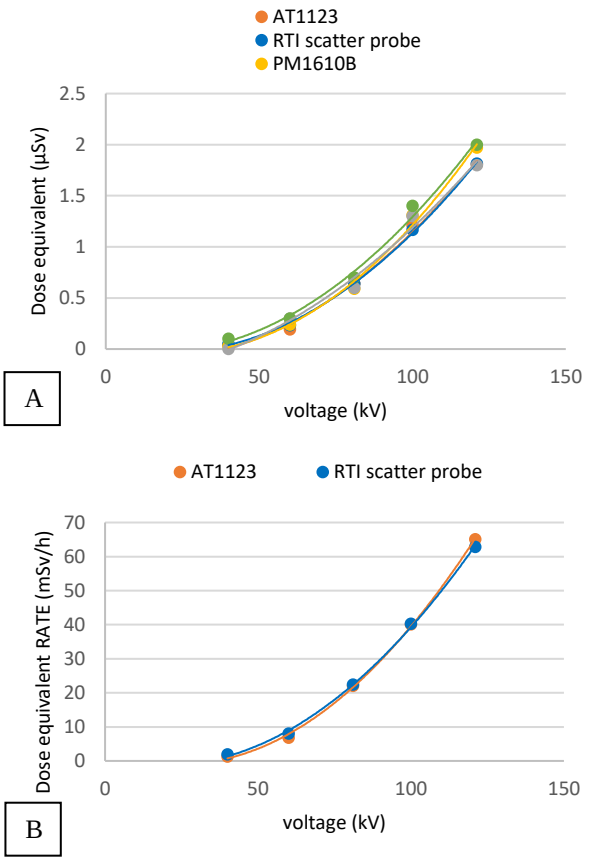

Fig. 3. Dose equivalent [A] and dose equivalent rate [B] response of dosimeters in conventional radiology at different kV (100 mA; 100 mAs).

At 40 kV, a very low equivalent dose was measured for RTI scatter probe, Atomtex AT1123, and Polymaster PM1610 (0.05, 0.04, 0.03 µSv respectively). On the other hand, Mirion DMC 3000 did not register any dose equivalent and Thermo EPD TruDose displayed an inaccurate dose (0.1 µSv) since both of these APDs cannot register a dose equivalent less than 0.1µGy. At 60 kV, the largest percentage difference of 35% for dose equivalent response was found between Atomtex AT1123 (0.19 µSv) and Mirion DMC 3000/Thermo EPD TruDose (0.30 µSv) while the other dosimeters displayed 0.23, 0.26, 0.24 µSv for RTI scatter probe, Atomtex 1121 and Polymaster PM1610B respectively. However, at higher kV, the percentage difference decreased significantly between dosimeter and reached 15.7%, 16.7% and 10% at 80, 100 and 120 kV respectively. At these tube voltages, Thermo EPD TruDose displayed the highest dose equivalent. The dose equivalent rate results for Atomtex AT1123 and RTI scatter probe for the same kV range are presented in Fig. 3-B. The correlation between dose rate and kV was exponential for all three dosimeters with the two curves almost merging together. For Mirion DMC 3000, Thermo EPD TruDose and Polymaster PM1610B, the dose equivalent rate results were not included because these dosimeters had significantly low dose rate with no clear correlation.

Similar trends can be observed for dose equivalent and dose rates measured in fluoroscopy mode. In the exception of Thermo EPD TruDose and Polymaster PM1610B, all dosimeters displayed comparable dose equivalent for all pulse/s. Regarding dose equivalent rates, reading from Mirion and Polymaster were not reliable especially at low pulse rates.

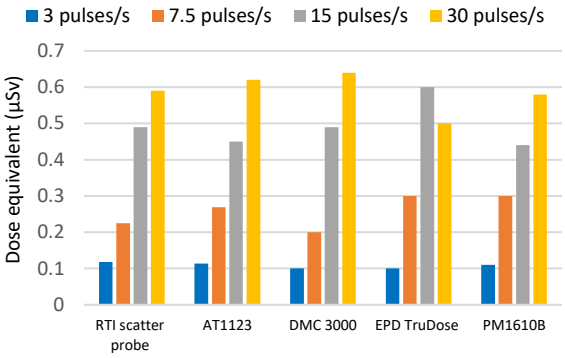

Fig. 4. Dose equivalent response of dosimeters in fluoroscopy using normal mode.

4. Conclusion

In summary the repeatability of dose equivalent reading was good for almost all dosimeters. Below certain exposure dose or time, the accuracy all dosimeter decreases. Moreover, the results indicate that dose equivalent reading are more reliable than dose equivalent rate reading especially at low exposure time and short pulsed radiation and therefore should be used instead in regular dosimetry measurement. Similar results were observed for evaluation performed in fluoroscopy mode where dose equivalents were more accurate especially at lower pulses/s.

References

1. Ginjaume M. Performance and approval procedures for active personal dosemeters. Radiat. Prot. Dosimetry. 2011, 144 (1-4), 144–149.
2. Bolognese-Milsztajn T., Ginjaume M., Luszik-Bhadra M., Vanhavere F., Wahl W., Weeks A. Active personal dosemeters for individual monitoring and other new developments. Radiat. Prot. Dosimetry. 2004, 112 (1), 141-168.
3. Martin CJ. Personal dosimetry for interventional operators: when and how should monitoring be done?. *Br J Radiol*. 2011;84(1003):639-648.
4. ICRP Publication 139. Occupational radiological protection in interventional procedures ICRP Publication 139. Ann ICRP. 2018;47(2):1–112.
5. Hygiene Standard HN 78:2009 “Quality control requirements and evaluation criteria in medical X - ray diagnostics” adopted by the Order No. V-922 by the Minister of Health Care. 2009.

MEDICAL PHYSICS IN THE BALTIC STATES 16 (2023)

Proceedings of International Conference "Medical Physics 2023"
09-11 November 2023, Kaunas, Lithuania

ANALYSIS OF DOSE PLANNING RISK FOR CENTRAL NERVOUS SYSTEM CANCER PATIENTS ASSOCIATED WITH PATIENT SETUP ERRORS

Julija JOKŠAITĖ[1,2], Evelina JASELSKĖ[1,2], Diana ADLIENĖ[2]
[1]Oncology Institute, Lithuanian University of Health Sciences, LT-50161 Kaunas, Lithuania; [2]Department of Physics, Kaunas University of Technology, Studentu str. 50, Kaunas, Lithuania;
julijajoksaite@gmail.com; evelina.jaselske@kaunoklinikos.lt; diana.adliene@ktu.lt

***Abstract*:** Accuracy is one of the most important requirements for radiation therapy treatment delivery. Therefore, this work was aimed to evaluate dose planning risk associated with set-up errors arising during patient positioning. To evaluate the risks, the planning organ at the risk margins (PRV) was calculated and implemented. Results have shown that the use of PRV margin, on average, reduces doses delivered to the organs at risk by 1.69 - 3.08 Gy. Additionally, no significant decrease in plan quality was observed.

Keywords: central nervous system, organs at risk, planning target volume, dose planning risk.

1. Introduction

Although nowadays radiotherapy is performed employing advanced radiotherapy delivery techniques such as volumetric modulated arc therapy (VMAT), intensity-modulated radiation therapy (IMRT), stereotactic radiosurgery (SRS) or proton therapy, the accuracy of treatment still is affected by uncertainties that arise during treatment preparation and execution [1]. The impact of errors on the target coverage is controlled with the use of planning target volume (PTV) margin. Implementation of safety margins to monitor doses received by organs at risk (OARs) known as planning organ at the risk (PRV) margin has been recommended in ICRU report 83 [2] as exceeding tolerance doses for OARs, such as the brainstem, chiasma and optical nerves can cause various long-term complications for the patients who underwent the treatment [3].
However, in clinical practice, the use of PRV is still not widely implemented. Moreover, studies analysing the PRV effect on the dose planning risks for central nervous system (CNS) cancer patients are also very limited. Therefore, it is necessary to perform more research and analyse the effect of PRV implementation on the dose planning risks for CNS cancer patients.

2. Materials and methods

2.1. Patient selection

35 adult CNS cancer patients treated using VMAT (6 MeV) treatment delivery technique were randomly selected for the research. The majority of patients were prescribed to standard treatment of 60 Gy total dose delivered in 30 fractions (2 Gy per fraction).

2.2. Calculation of Set-up Errors and Planning Organ at Risk Volume

Position verification was performed using the onboard imager (OBI) system integrated into the linear accelerator as a part of the IGRT daily position verification protocol.
The positioning data of each patient was extracted from the offline review. In total 992 CBCT scans were analysed.
Systematic and random set-up errors were evaluated based on the methodology proposed by van Herk [4], while PRV margins were calculated according to the formula derived by McKenzie et al [5]:

$$PRV\ margin = 1.3\Sigma + 0.5\sigma \quad (1)$$

2.3. Re-planning

Volumes of the brainstem, optic nerves and chiasma were expanded by the calculated PRV margin in 27 plans in which the total prescribed dose was 60 Gy. Selected treatment plans were re-planned using the Varian Eclipse 16.1 AAA algorithm. The geometry of the original treatment plans was maintained in the new plans. Additionally, a new clinical goals protocol incorporating dose constraints for OARs already implemented in the clinic and dose constraints for PRVs recommended by DAHANCA [6] was developed (Table 1.).

Table 1. Clinical goals protocol

No.	Structure	Objective	Variation
Most important			
1	PTV	V 95 % ≥ 95 %	
Very important			
2	CNS-PTV	V 60 Gy ≤ 3.00 cm^3	
3	Brainstem	V 59 Gy < 10 cm^3	
4	Brainstem surface	D_{max} ≤ 60 Gy	
5	Brainstem interior	D_{max} ≤ 54 Gy	
6	Chiasma	D_{max} ≤ 55 Gy	
7	Optic nerves	D_{max} ≤ 55 Gy	
8	PRV brainstem	D_{max} ≤ 60 Gy	
9	PRV chiasma	D_{max} ≤ 60 Gy	
10	PRV optic nerves	D_{max} ≤ 60 Gy	
Important			
11	Eye lenses	D_{max} ≤ 10 Gy	
12	Pituitary	D_{mean} ≤ 20 Gy	≤ 40 Gy
13	Hippocampus	D 40 % ≤ 7.30 Gy	
14	Cochlea	D_{mean} ≤ 32 Gy	≤ 45 Gy

2.4. Generation of Uncertainty plans

After adding PRV margins and re-planning, original plans that exceeded dose constraints were analysed further by generating patient set-up errors. It was achieved by shifting the isocenter of each plan by ± 3 mm in longitudinal, lateral and vertical directions. Generation of the uncertainty plans allowed us to evaluate whether treatment plans with added PRV margins are less susceptible to dose planning risks caused by the patient set-up errors.

3. Results and discussion

3.1. Patient set-up errors

Mean patient set-up errors with calculated values of systematic and random errors are presented in Table 2. Values of systematic and random errors in different directions varied between 1.43 – 1.56 mm and 1.10 – 1.30 mm, respectively. Mean errors varied more significantly, between -1.88 mm and 0.51 mm.

Table 2. Calculated values of systematic, random and mean patient set-up uncertainties

Patient set-up error	Vertical, mm	Longitudinal, mm	Lateral, mm
Systematic Σ	1.43	1.50	1.56
Random σ	1.30	1.15	1.10
Mean	-1.88	0.51	0.27

Q-Q plots (Fig.1) and the Wilko-Shapiro normality test revealed that the distributions of the patient set-up errors do not follow a normal distribution (p-values were 9.939×10^{-14}, 1.416×10^{-8} and 7.197×10^{-5} in vertical, longitudinal, and lateral directions, respectively).

3.2. Planning organ at risk margins

Calculated values for PRV margins were 2.51 mm, 2.53 mm, and 2.58 mm in vertical, longitudinal and lateral directions. Different studies investigating safety margins for organs at risk have reported PRV margins in a range between 0.08 - 3.8 mm (Table 3). Therefore, values of PRV margins obtained from measurements in the clinic are in accordance with results obtained in other radiotherapy clinics.

Due to the limitations of the treatment planning system, the calculated PRV margins were rounded up to 3 mm.

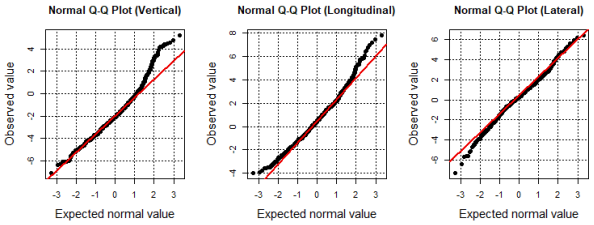

Fig. 1. Q-Q plots of patient set-up errors along vertical, longitudinal and lateral directions

Table 3. Comparison of PRV margins obtained in our clinic and margins reported by other studies.

Source	Structures	Vrt, mm	Lng, mm	Lat, mm
Calculated (TrueBeam)	Brainstem Optic nerves Chiasm	2.51	2.53	2.58
Piotrowski et al. [7]	Lens	1.8	1.3	1.9
Breen et al. [8]	Spinal Cord	5.4		
Li et al. [9]	Brainstem Spinal Cord Chiasm Eyes Lens Optic Nerves Inner Ears	0.3 1.34 0.1 0.87 1.85 1.14 0.8	0.05 0.59 0.24 0.29 0.35 0.5 0.15	0.08 0.91 0.43 0.4 1.54 0.89 0.24
Fourati et al. [10]	Brainstem	2.0		
Zhang et al. [11]	-	1.7	1.7	1.5
Mongioj et al.[12]	Brainstem Spinal Cord	2.1 3.8	3.5 3.2	2.3 2.0

3.3. Evaluation of Planning Organ at Risk Volume Doses

Doses received by the structures after adding a 3 mm margin were evaluated based on the dose constraints provided by the DAHANCA (Fig.2). The evaluation revealed that the brainstem is at greatest risk of receiving higher than allowed dose, with PRV dose constraint being exceeded in 55.56 % of the plans. Studies have shown that exceeding 60 Gy dose for 1 cm^3 of the brainstem is associated with a 15.7 % risk of necrosis [13].

For other structures, PRV dose constraints were met more successfully, nevertheless, chiasma, left and right optic nerves received more than 60 Gy in 22.22% 7.41 % and 11.11 % of the plans, respectively. Higher than tolerance doses (55-60 Gy) received by these structures are linked with 3 % to 7 % risks of toxicity, while doses greater than 60 Gy are associated with 7 % to 20 % toxicity risks [14].

3.4. Re-planning and Dose Risk Evaluation

Re-planning resulted in the reduction of the maximum dose in the majority of the plans. Furthermore, dose constraints to all the plans were met (Fig. 3 - 6).

The maximum dose to the brainstem was reduced in 21 out of 27 plans. While the mean maximum dose received

by the structure decreased from 43.79 Gy down to 40.71 Gy in the re-planned plans (Fig. 3).

For chiasma, after the re-planning maximum dose was reduced in 22 plans, the mean maximum dose across all plans decreased from 30.91 Gy down to 28.27 Gy (Fig. 4).

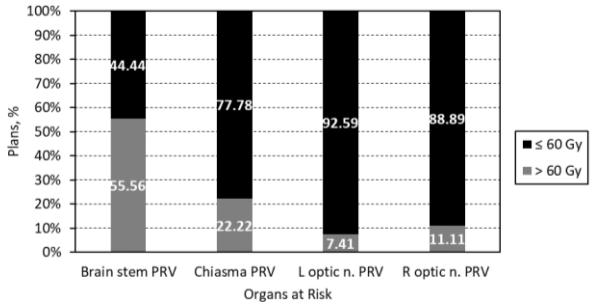

Fig. 2. Percentage of plans for which PRV dose constraints were exceeded (red) or met (black) after expanding the structures with a 3 mm margin

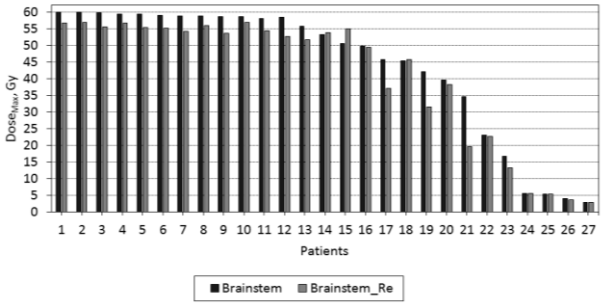

Fig. 3. Maximum doses delivered to the brainstem in the original (black) and re-planned (red) plans

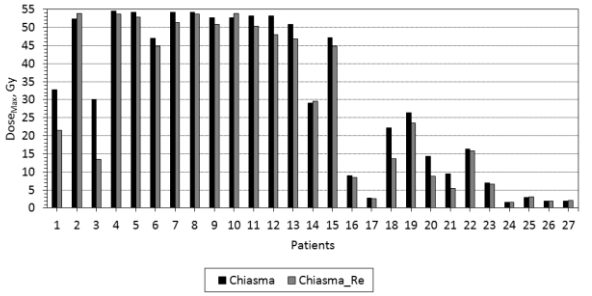

Fig. 4. Maximum doses delivered to the chiasma in the original (black) and re-planned (red) plans

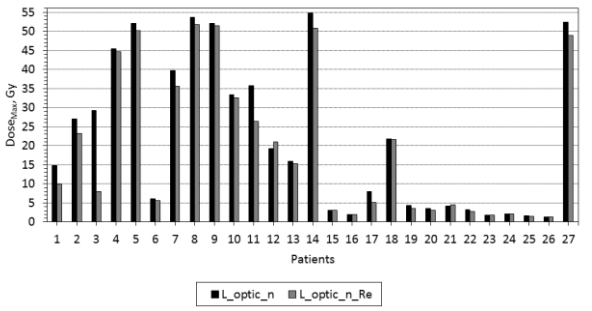

Fig. 5. Maximum doses delivered to the left optic nerve in the original (black) and re-planned (red) plans

The mean maximum dose for the left optic nerve was reduced by 2.27 Gy from 21.83 Gy down to 19.56 Gy. In total, maximum dose reduction was achieved in 23 plans (Fig. 5).

For the right optic nerve, the maximum dose on average was reduced by 1.69 Gy, from 19.54 Gy down to 17.85 Gy. The maximum dose was reduced in 19 plans (Fig. 6).

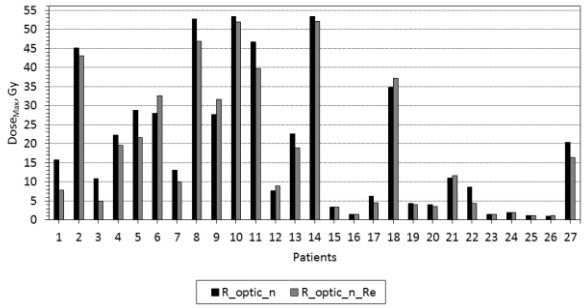

Fig. 6. Maximum doses delivered to the right optic nerve in the original (black) and re-planned (red) plans

An increase in the maximum dose observed in a few plans resulted from the effort to reduce the dose received by different organs at risk while still trying to maintain adequate PTV coverage. Therefore, in order not to compromise target coverage, the dose to some structures was reduced at the expense of the dose to other structures. PTV coverage in all re-planned plans was successfully maintained to be at least 95 % of the 95 % isodose (Fig. 7). Overall target coverage increased in 13 plans by 0.06 % to 3.68 %.

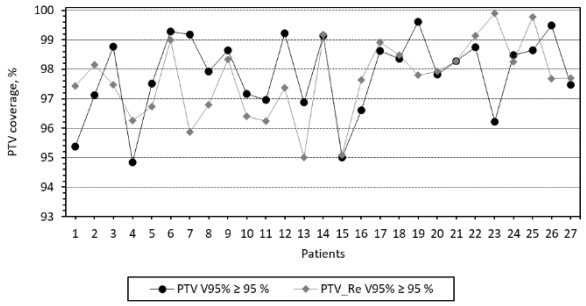

Fig. 7. PTV coverage with 95 % isodose in the original (black) and the re-planned (red) plans

While overall PTV coverage was improved, the mean minimum dose to the target was lower by 2.27 Gy in comparison with the original plans. A decrease in the minimum dose was observed in 19 out of 27 plans. The most significant plan deterioration was noticed in plans where the target was in close proximity to several organs at risk from different directions. Plan quality in such situations could be improved by implementing more sophisticated optimization algorithms and by selecting optimal priority values for the target and organs at risk.

3.4. Evaluation of uncertainty plans

In total, 15 plans were additionally analysed by generating uncertainty plans. 6 out of 15 of the re-planned plans passed all the dose constraints to the organs at risk even with ± 3 mm shifts, while for the rest 9 re-planned plans clinical goals were met only partially.

Directional isocenter shifts and the number of plans that exceeded dose constraints for different structures are presented in Fig. 8.

60 Gy dose constraint for the brainstem was met in all 90 uncertainty plans. Dose constraints for the right and left optic nerves were exceeded in 4 and in 8 uncertainty plans, respectively. Chiasma received higher than allowed doses in 24 plans. Such a high number of plans failing to meet dose constraints for chiasma in comparison with other organs at risk can be attributed to the location and tolerance dose. The location of the chiasma is closer to the base of the brain, therefore, there is a higher chance for a tumour to be located close to the chiasma than, for example, the optic nerves. Also, since the total prescribed dose is 60 Gy, the chances for the 55 Gy constraint to be exceeded are higher.

It was observed that shifting the isocenter along the z-direction leads to a significantly greater number of organs at risk of receiving higher than tolerance doses (Fig. 8). Positioning errors along the z-direction have such a pronounced impact because the dose intended for the tumour crosses the planes where the organs at risk are located.

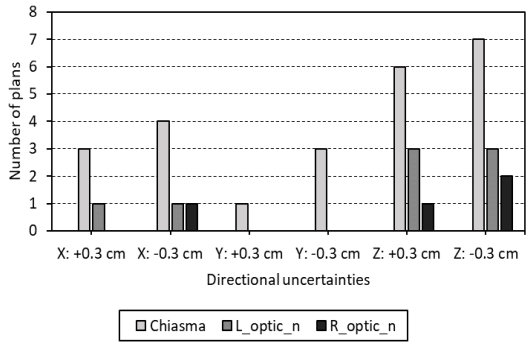

Fig. 8. Number of uncertainty plans that did not pass dose constraints for the chiasma, and optic nerves with respect to positional isocenter shifts

5. Conclusions

Implementation of PRV margins is a useful tool to evaluate dose planning risks and assure that tolerance doses to organs at risk are not exceeded. However, this approach might not be suitable for complicated cases where a large tumour is closely surrounded by several organs at risk.

References

1. Van der Merwe D., et al. Accuracy requirements and uncertainties in radiotherapy: a report of the International Atomic Energy Agency. Acta oncologica. 2017, 56(1), p. 1–6.
2. Azzam P., et al. Radiation-induced neuropathies in head and neck cancer: prevention and treatment modalities. Ecancermedicalscience. 2020, 14, p. 1133.
3. International Commission on Radiation Units and Measurements. ICRU Report 83, Prescribing, Recording, and Reporting Intensity-Modulated Photon-Beam Therapy (IMRT). Journal of the ICRU. 2010, 14(1).
4. Van Herk M. Errors and margins in radiotherapy. Seminars in radiation oncology. 2004, 14(1), p. 52–64.
5. Mckenzie A. M. Van Herk and Mijnheer B. Margins for geometric uncertainty around organs at risk in radiotherapy. Radiotherapy and oncology: journal of the European Society for Therapeutic Radiology and Oncology. 2002, 62(3), p. 299–307.
6. Jensen K., et al. The Danish Head and Neck Cancer Group (DAHANCA) 2020 radiotherapy guidelines. Radiotherapy and oncology: journal of the European Society for Therapeutic Radiology and Oncology. 2020, 151, p.149–151.
7. Piotrowski T., et al. Estimation of the planning organ at risk volume for the lenses during radiation therapy for nasal cavity and paranasal sinus cancer. Journal of medical imaging and radiation oncology. 2015, 59(6), p.743–750.
8. Breen S. L., et al. Spinal cord planning risk volumes for intensity-modulated radiation therapy of head-and-neck cancer. International journal of radiation oncology, biology, physics. 2006, 64(1), p. 321–325.
9. Li J., et al. Geometric Changes to the Central Nervous System Organs at Risk During Chemoradiotherapy for Locally Advanced Nasopharyngeal Carcinoma. Journal of Surgery and Research. 2022, 5(August), p. 477-485.
10. Fourati N., et al. PRV brainstem during the nasopharyngeal IMRT: margin calculation and dosimetric implications. Radiotherapy and Oncology. 2019, 133, S1020.
11. Zhang S., et al. Analysis of setup error based on CTVision for nasopharyngeal carcinoma during IGRT. Journal of applied clinical medical physics. 2016, 17(4), p. 15–24.
12. Mongioj V., et al. Set-up errors analyses in IMRT treatments for nasopharyngeal carcinoma to evaluate time trends, PTV and PRV margins. Acta Oncologica. 2011, 50(1), p. 61-71.
13. Fan X., et al. Dosimetric analysis of radiation-induced brainstem necrosis for nasopharyngeal carcinoma treated with IMRT. BMC Cancer. 2022, 22(178).
14. Marks L. B., et al. Use of normal tissue complication probability models in the clinic. International journal of radiation oncology, biology, physics. 2010, 76(3 Suppl), S10–S19

MEDICAL PHYSICS IN THE BALTIC STATES 16 (2023)

Proceedings of International Conference "Medical Physics 2023"
9 – 11 November 2023, Kaunas, Lithuania

DIGITAL TECHNOLOGIES FOR COMBATING CORRUPTION IN MEDICINE

Rūta NEDZINSKIENĖ[1], Egidijus NEDZINSKAS[2]
Kaunas University of Technology[1]; Lithuania Business College[2]
ruta.nedzinskiene@ktu.lt[1]; egidijus.nedzinskas@ltvk.lt[2]

***Abstract*:** Digital technologies such as artificial intelligence, big data analytics mobile technology, and the Internet of Things, generate positive improvements in the whole society and industry. Digitalization is increasing global competitiveness, impacting public sector and private lives. On the other hand, corruption threatens the legal, political, social, and economic system of a country. Corruption is a particularly serious problem in medicine. The fight against corruption is one of the main goals of each state, thus the question is how digital technologies can help combat corruption in medicine. The article aims to reveal the legal framework of corruption prevention in medicine and to investigate the role of digital technologies in combating corruption. The results of this article are based on the analysis of the scientific literature and legal documentation.

***Keywords*:** Digital Technologies, Corruption, Corruption Prevention, Corruption in Medicine

1. Introduction

Digitalization is the most important factor of competitiveness and economic growth in the world. Digital Europe Programme for the period 2021-2027 [1] with a total budget of €7.59 billion (in current prices) seeks to boost investments in supercomputing, artificial intelligence, cybersecurity, advanced digital skills, and ensuring a wide use of digital technologies across the economy and society. Digital technologies can also serve as a powerful tool to fight against corruption in medicine. Corruption is a significant challenge to the future of human development, economic progress, and population health. According to the Corruption Perceptions Index published by Transparency International in 2022 [2], Denmark is considered the most transparent country in the world, while Lithuania ranks 62 out of 180 in terms of transparency.

The concept of corruption encompasses all spheres of social activity - private, and public, as well as the persons performing private and public functions if they gain the benefits of performing those functions [3]. Scientists also point to various forms of corruption in medicine. Corruption is defined as bribery of patients in order to obtain quality personal health care services and bribery in order to receive certain procedures, and non-sequential treatment [4]. People who use healthcare services are afraid of risking their health and they seek the best possible healthcare services, making corruption in medicine difficult to avoid and bribing the doctor as a matter of course to receive better and faster services [5]. Health systems are vulnerable to corruption due to the substantial resources and multitude of governmental and private industry actors that play a role in health services. Opportunities for corruption exist in governance, financing, human resources, medicines and technology, and other health system building blocks. Corruption negatively impacts access to quality health care and diminishes the public's confidence in the system [6].

Corruption is a particularly serious problem in the Lithuanian healthcare system. The increase in corruption in medicine is caused by such factors as low salaries of employees, worsening demographics of the Lithuanian population, and emigration of young prospective specialists [7]. Thus, the active involvement of government and society in anticorruption activities is needed here. One of the priorities of the Strategic Activity Plan of the Special Research Service of the Republic of Lithuania for 2021-2023 [8] is to identify and take measures to reduce the risk of corruption in health care.

Globally, health policymakers, planners, and donors are increasingly interested in how corruption affects access to and outcomes of healthcare and what can be done to fight corruption in the health sector [9]. With the digital revolution, the use of digital technologies can increase the efficiency, speediness, and transparency of governments and, on the other hand, can promote the dissemination of information and knowledge [10]. Thus, digital technologies are seen as a tool to promote openness and transparency and to reduce corruption in medicine. However, the participation of the government and the legal regulators of the country is of major importance here.

The goal of this article is to reveal the legal framework of corruption prevention in medicine and to investigate the role of digital technologies in combating corruption. Objectives of the research: 1) To reveal the legal

regulation of corruption prevention in Lithuania; 2) To carry out the analysis of digital technologies' role in combating corruption. Systematic and comparative analysis, synthesis, induction, deduction, abstraction, and analogy were used for the scientific literature as well as for legal document analysis.

2. The legal framework in Lithuania

The goal of corruption prevention is to strengthen national security, create social welfare, and increase the quality of administrative and public sector services so that corruption does not hinder the development of democracy and the economy of a country.

Anti-corruption system exists in every country in the world. However, in different countries its structure, influence of power, methods of work, and responsibility for corruption offenses are different. It depends on the level and perception of corruption in the country, the will of the top leadership of the state, and the degree of public involvement in the work of anti-corruption bodies [11].

In Lithuania, the main role in the fight against corruption is played by the President of the Republic of Lithuania, the Seimas of the Republic of Lithuania, the Government of the Republic of Lithuania, the Supreme Professional Ethics Commission, and the main institution – the Special Investigation Service. The purpose of the activities of the Special Investigation Service is to reduce corruption, which threatens human rights and freedoms, and the principles of the rule of law of a country. In order to achieve the transparency of legal regulation and administrative procedures in the country, the Special Investigation Service evaluates various legal acts or their proposals from an anti-corruption point of view, conducts corruption risk analyses in a certain area or process of state or municipal activity, coordinates the activities of creating a corruption-resistant environment in the public and private sectors and provides methodological assistance [12]. One of the Special Investigation Service priorities is corruption control in health care.

In Lithuania, the prevention of corruption in the field of medicine is carried out directly by an institution subordinate to the Government of the Republic of Lithuania – the Ministry of Health of the Republic of Lithuania. The Ministry of Health pays special attention to the prevention of corruption – not only population surveys are evaluated, but also corruption risk analyses are carried out by law enforcement agencies [13]. The Ministry of Health seeks to ensure high-quality and transparent health care for patients, to ensure that health care services are provided to all patients, without distinguishing between their legal, social status, disability, gender, beliefs, age, or other characteristics.

The activities of the Ministry of Health and the formulation of health care policy, as well as the organization of the prevention of corruption in the health system, are influenced by the political processes and decisions taken in the country, as well as by the guidelines on priority areas implemented by the EU.

One of the most important documents in the fight against corruption is the United Nations Convention against Corruption of 31/10/2003 [14]. The Convention entered into force in Lithuania on 20/01/2007. Lithuania provides for many of the provisions of the Convention. Lithuania has transposed many of the anti-corruption measures provided in the Convention into its national legislation.

2013-05-21 Lithuania entered the International Anti-Corruption Academy. The aim of the Academy is to promote the effective and effective prevention and fight against corruption [15]. To achieve this goal, anti-corruption education is organized, research is supported, and technical assistance in the field of corruption is provided.

On 29/06/2021, the Seimas of the Republic of Lithuania adopted a new version of the Law on the Prevention of Corruption of the Republic of Lithuania No IX-904 [16], which states that the prevention of corruption is a systematic activity aimed at increasing the resilience of public and private sector entities to corruption, which includes the identification, assessment, elimination and /or reduction of corruption risk factors by creating and implementing a system of measures for developing a corruption-resistant environment.

On 28/06/2022, the Seimas of the Republic of Lithuania approved the national agenda for the prevention of corruption for 2022–2033. It is a very important strategic planning document at the national level in the field of corruption prevention in Lithuania [17]. It states that the purpose of preventing corruption is to strengthen national security, create social welfare, improve the quality of the provision of administrative, and other public sector services, and protect the freedom of fair competition, to ensure the development of democracy and the economy. The main tasks of corruption prevention are: raising anti-corruption awareness, systematically and in a coordinated manner eliminating corruption risk factors, reducing the risk of corruption, creating the conditions for the harmonious and effective functioning of the system for the prevention of corruption, reducing economic incentives for corruption, ensuring the active involvement of private sector entities and society in the prevention of corruption, and promoting the transparent, fair and open provision of administrative, public and other services.

12/07/2019 by order of the Minister of Health of the Republic of Lithuania, a new version of the rules of conduct for employees of healthcare institutions who have encountered possible corruption crimes was approved [18]. The rules regulate how the employees of the institutions of the national health system of Lithuania must behave when faced with a possible criminal act of a corrupt nature in the activities of the institution o or after receiving information about it. In the rules, criminal acts of a corrupt nature and bribery are understood as they are defined in the Criminal Code of the Republic of Lithuania.

Thus, it can be stated that Lithuania has a sufficiently extensive regulation of international and national legislation in the fight against corruption. Nevertheless, there are major challenges faced when implementing an anti-corruption policy in Lithuania.

The Special Investigation Service of the Republic of Lithuania emphasizes the risk factors of corruption due to the lack of effective supervision and control of subordinate healthcare institutions: 1) The institutions do not connect to the Electronic Health Services and

Cooperation Infrastructure Information System and/or do not enter all the possible registration times for the patients to it; 2) The institutions use their own patient registration systems, which do not always ensure the transparency of registration procedures; 3) The institutions do not carry out controls on the workload of doctors when they work in several institutions; 4) It is not clear how the ratio of services compensated from the budget of the Compulsory Health Insurance Fund to paid services is determined; 5) The possibilities of additional visits (receptions) of patients are not sufficiently regulated [19]. The reasons mentioned do not ensure healthcare institutions' transparency and confidence in them.

Thus, regardless of the legal regulation and the actions taken, corruption in health care still remains a serious problem. There is a need for the appropriate tools to cope with this.

3. Digital technologies for combating corruption

There are many suggestions for strategies to confront corruption, including the following: enhancing financial management, managing conflicts of interest, improving policies and processes for investigations and the penalization of corrupt acts, community involvement (power of the people), using technology platforms for active surveillance, crowdsourcing information, the use of big data, and use of data mining and pattern recognition to identify fraud or abuse profiles [20].

Thus, one critical tool to leverage in the fight against corruption in medicine is the use of innovative technologies. In the field of anti-corruption, digital technologies have been widely perceived for the prevention, detection, and prosecution of corruption. As numerous studies assert, digital technologies can promote transparency, accountability, and citizen participation [10, 21-23]. The most widely praised tools include digital public services, whistleblowing tools, transparency portals websites, and mobile phone applications as well as big data analysis and artificial intelligence [2]. These tools serve the fight against corruption by enhancing access to public information, monitoring officials' activities, digitalizing public services, and enabling corruption reporting [24-25, 26-27]. Among the digital means of combating corruption, the following ones can be distinguished: 1) creation of an e-government system; 2) provision of digital public services with the use of information and communication technologies; 3) creation of tools to detect manifestations of corruption, including electronic bidding for public procurement, electronic reporting; 4) use of social networks to detect cases of corruption in the public sector; 5) use of the Internet for free access to public information and the opportunity to obtain the necessary information on the activities of public bodies, through open access, e-mail, etc. [11].

E-government is the most discussed tool for combating corruption in public services, also in medicine. E-government refers to the development and use of information and communication technologies (ICTs) with the aim of streamlining the delivery of public services to citizens, businesses, and public agencies [23]. E-Government can improve public services quality, transparency, and accountability, and so reduce corruption, but it needs the involvement of citizens [10]. Thus, the relationship between the Transparency International Corruption Perception Index and the e-government index as digital interaction between citizens and the public sector is highlighted [22]. E-government, in particular, has been used in many prominent, comprehensive transparency efforts in a number of nations. ICTs can reduce corruption by promoting good governance, strengthening reform-oriented initiatives, reducing the potential for corrupt behaviors, enhancing relationships between government employees and citizens, allowing for citizen tracking of activities, and monitoring and controlling behaviors of government employees [28].

However, the importance of e-government in reducing corruption needs to be recognized by policymakers. Despite the positive global trends towards higher levels of e-government, some countries need to reinforce it by investing in online services, and telecommunication infrastructures, but also in developing human capital in the public sector [10].

The other tool suggested for combating corruption in medicine is blockchain technology. Applications in the field of medicine could include electronic health records, health insurance, biomedical research, drug supply and procurement processes, and medical education. The utilization of blockchain currently is immature and lacks public or even expert knowledge, nevertheless, health professionals and decision-makers should be aware of the transformative potential that blockchain technology offers for healthcare organizations and medical practice [29].

The internet and social media can also be a source for disclosing cases of corruption. The Internet can reduce corruption since it provides a speedy means of sharing information at low costs and increases the risk of detection for political actors or civil servants [10].

Digitalization is expected to affect corruption significantly. A higher level of digitalization would result in a less corrupt government. However, the introduction of digital tools does not automatically translate into anti-corruption outcomes; rather, the impact hinges on the matching between digital tools and the local context, including support for and skills in using technology [30]. Digitalization could be useful for combating corruption in the context of the citizen's access, skills, and willingness to use technology. Digital technologies could be used to reduce corruption in medicine, but they need the involvement of citizens and government.

5. Conclusions

Corruption threatens the legal, political, social, and economic system. Scientists describe corruption as one of the oldest forms of crime acts. It causes a serious threat to the rule of law, democracy, and human rights, undermines the principles of social justice and competition, inhibits economic growth, and reduces people's confidence in the state. Medicine is distinguished as one of the most vulnerable to corruption areas.

Lithuania has a separate institution to fight against corruption - the Special Investigation Service. One of Special Investigation Service priorities is corruption control in health care. The prevention of corruption in the field of medicine is carried out directly by the Ministry of Health of the Republic of Lithuania. Lithuania has also a sufficiently extensive regulation of international and national legislation in the fight against corruption. Nevertheless, there are major challenges faced when implementing an anti-corruption policy in Lithuania.

The main digital tools for combating corruption in medicine are e-government systems; digital public services; tools to detect manifestations of corruption; social network websites, mobile phone applications, big data analysis, and artificial intelligence. The use of digital technologies is a significant and effective mean of countering corruption manifestations as it promotes transparency, accountability, and citizen participation. However, the introduction of digital anti-corruption tools is impossible without the openness of governments, free access to networks and information from state institutions.

6. References

1. Digital Europe Programme. European Commission. https://commission.europa.eu/funding-tenders/find-funding/eu-funding-programmes/digital-europe-programme_en [Retrieved on 2023-09-02].
2. Corruption Perceptions Index 2022. Transparency International. https://www.transparency.org/cpi2022 [Retrieved on 2023-09-18].
3. Hellman D. Defining corruption and constitutionalizing democracy. Michigan Law Review, Vol. 111, No 8, 2013. p. 1385-1422.
4. Ensor T., Duran A. Corruption as challenge to the effective regulation of the health sector. In ed. Saltman R., Busse R., Mossialos E, Open University Press. Regulating entrepreneurial behaviour in European health care system, 2002. p. 106-124.
5. Palidauskaitė J. Korupcija viešuosiuose pirkimuose: nuo teorinės apibrėžties iki atvejo studijos (I dalis). Viešoji politika ir administravimas, Nr. 32, 2010. p. 74-84.
6. Taryn Vian, Erika L. Crable. Corruption and the consequences for public health. Reference Module in Biomedical Sciences, Elsevier, 2023, ISBN 9780128012383, https://doi.org/10.1016/B978-0-323-99967-0.00031-4.
7. Nedzinskas, E., Nedzinskienė, R. Corruption Prevention in Medicine: Legal Aspects. Medical Physics in the Baltic States 2019. Proceedings of the 14th International Conference on Medical Physics. ISSN 1822-5721.
8. 2021–2023-ųjų metų strateginis veiklos planas. Special Investigation Service of the Republic of Lithuania. www.stt.lt/data/public/uploads/2021/02/2021-2023-uju-stt-strateginis-veiklos-planas-atnaujintas.pdf [Retrieved on 2023-09-10].
9. Taryn Vian, Review of corruption in the health sector: theory, methods and interventions. Health Policy and Planning, Volume 23, Issue 2, March 2008, p. 83–94, https://doi.org/10.1093/heapol/czm048.
10. Castro C, Lopes I.C. E-Government as a Tool in Controlling Corruption. International Journal of Public Administration, 2022. DOI: 10.1080/01900692.2022.2076695.
11. Halai, A., Halai, V., Hrechaniuk, R., Datsko, K. Digital Anti-Corruption Tools and Their Implementation in Various Legal Systems Around the World. In SHS Web of Conferences (Vol. 100, p. 03005). EDP Sciences, 2021. DOI: 10.1051/shsconf/202110003005 ISCSAI 2021.
12. Lietuvos Respublikos specialiųjų tyrimų tarnybos įstatymas, 2000 m. gegužės 2 d. Nr. VIII-1649, Vilnius. Seimas of the Republic of Lithuania. https://e-seimas.lrs.lt/portal/legalAct/lt/TAD/TAIS.100816/asr [Retrieved on 2023-08-19].
13. Korupcijos prevencija. Ministry of Health of The Republic of Lithuania. https://sam.lrv.lt/lt/korupcijos-prevencija [Retrieved on 2023-09-19].
14. Jungtinių Tautų Konvencija prieš korupciją, 2003-10-31. Valstybės žinios, 2006-12-14, No. 136-5145.
15. Susitarimas dėl tarptautinės organizacijos – antikorupcijos akademijos – įsteigimo. Valstybės žinios, 2013, No. 19-928.
16. Lietuvos Respublikos korupcijos prevencijos įstatymo Nr. IX-904 pakeitimo įstatymas, 2021-07-14d. Nr. XIV-471, Vilnius. Seimas of the Republic of Lithuania. https://e-seimas.lrs.lt/portal/legalAct/lt/TAD/TAIS.168154/asr [Retrieved on 2023-09-20].
17. Nutarimas dėl 2022–2033 metų nacionalinės darbotvarkės korupcijos prevencijos klausimais patvirtinimo. 2022 m. birželio 28 d. Nr. XIV-1178, Vilnius. Seimas of the Republic of Lithuania. https://e-seimas.lrs.lt/portal/legalAct/lt/TAD/bff1c501fdba11ecbfe9c72e552dd5bd?jfwid=-6arlcu7wo [Retrieved on 2023-0919].
18. Lietuvos Respublikos sveikatos apsaugos ministro įsakymas. Dėl asmens sveikatos priežiūros įstaigų darbuotojų, susidūrusių su galima korupcinio pobūdžio nusikalstama veika, elgesio taisyklių patvirtinimo, 2014 m. liepos 7 d., Nr. V-773, Vilnius. Nauja redakcija nuo 2019-07-12 d. Nr. V-801, 2019-07-10. Ministry of Health of The Republic of Lithuania, TAR 2019-07-11. https://e-seimas.lrs.lt/portal/legalAct/lt/TAD/8c119670093f11e497f0ec0f2b563356 [Retrieved on 2023-09-20].
19. Lietuvos Respublikos specialiųjų tyrimų tarnybos direktoriaus įsakymas. Dėl Lietuvos Respublikos specialiųjų tyrimų tarnybos direktoriaus 2021 m. lapkričio 30 d. įsakymo Nr. 2-246 „Dėl Korupcijos pasireiškimo tikimybės nustatymo ir jo atlikimo tvarkos rekomendacijų patvirtinimo" pakeitimo, 2022 m. rugsėjo 30 d. Nr. 2-214, Vilnius. Special Investigation Service of the Republic of Lithuania, TAR 2022-09-30. https://www.e-tar.lt/portal/lt/legalAct/f9e6bea0409f11edbc04912defe897d1 [Retrieved on 2023-09-20].
20. Patricia J García. Corruption in global health: the open secret. The Lancet, Volume 394, Issue 10214, 2019, Pages 2119-2124, ISSN 0140-6736, https://doi.org/10.1016/S0140-6736(19)32527-9.
21. Adam, I., Fazekas, M. Are emerging technologies helping win the fight against corruption? A review of the state of evidence. Information Economics and Policy, 57, 2021, 100950. DOI: 10.1016/j.infoecopol.2021.100950.
22. Campra M., Esposito P., Brescia V. Corporate social responsibility and technological perspectives in healthcare: An exploratory analysis of the evolution of the anti-corruption system through multiple case studies. Corporate Social Responsibility and Environmental Management, Early View, First Published: 17 May 2023.
23. Khan A., Krishnan S., Dhir A. Electronic government and corruption: Systematic literature review, framework, and agenda for future research. Technological Forecasting and Social Change, Volume 167, 2021, 120737, ISSN 0040-1625, https://doi.org/10.1016/j.techfore.2021.120737.
24. Bertot, J. C., Jaeger, P. T., Grimes, J. M. Using ICTs to create a culture of transparency: E-government and social media as openness and anti-corruption tools for societies. Government information quarterly, 27(3), 2010, 264-271. DOI: 10.1016/j.giq.2010.03.001
25. Davies, T., Fumega, S. Mixed incentives: Adopting ICT innovations for transparency, accountability, and anti-corruption. Anti-Corruption Research Centre, U4 Issue, No 4, 2014.

26. Kuriyan, R., Bailur, S., Gigler, S., Park, K. R. Technologies for Transparency and Accountability: Implications for ICT policy and Implementation. Open Development Technology Alliance, World Bank, Washington, DC, 2011 DOI: 10.13140/RG.2.2.19320.24320
27. Subhajyoti, R. Reinforcing accountability in public services: An ICT enabled framework. Transforming Government: People, Process and Policy, 6 (2), 2012, 135–148.
28. John C. Bertot, Paul T. Jaeger, Justin M. Grimes. Using ICTs to create a culture of transparency: E-government and social media as openness and anti-corruption tools for societies. Government Information Quarterly, Volume 27, Issue 3, 2010, Pages 264-271, ISSN 0740-624X, https://doi.org/10.1016/j.giq.2010.03.001.
29. Radanović, I., Likić, R. Opportunities for Use of Blockchain Technology in Medicine. Appl Health Econ Health Policy 16, 2018, 583–590. https://doi.org/10.1007/s40258-018-0412-8.
30. Adam I., Fazekas M. Are emerging technologies helping win the fight against corruption? A review of the state of evidence. Information Economics and Policy, Volume 57, 2021, 100950, ISSN 0167-6245, https://doi.org/10.1016/j.infoecopol.2021.100950.

MEDICAL PHYSICS IN THE BALTIC STATES 16 (2023)

Proceedings of International Conference "Medical Physics 2023"
09-11 November 2023, Kaunas, Lithuania

AUTOMATION FROM START TO FINISH: TRANSFORM YOUR DEPARTMENT WITH INCREASED PLAN QUALITY, SAFETY, AND EFFICIENCY WITH RADFORMATION SOLUTIONS

Radformation, Inc
info@radformation.com

***Abstract*:** Manual workflows tend to be time-consuming and prone to human error. By leveraging intelligent automation tools, clinics can efficiently reduce error rates, experience quantifiable time savings, and improve accuracy.
Radformation is dedicated to streamlining radiation oncology practises and elevating patient care standards through intelligent automation. Developed by a team of former clinicians, these solutions offer a holistic approach to optimising the entire treatment planning workflow. This manuscript explores Radformation's range of software tools designed to enhance the quality, safety, and efficiency of patient treatments.

Keywords: Automation, AI Contouring, Treatment Planning, Quality Improvement, Patient Care

1. Who Is Radformation?

Fig. 1. Radformation's software enables cancer clinics to do more in less time.

Radformation's team brings together individuals with dynamic backgrounds to develop software solutions that make a real difference in improving efficiencies in the clinic and advancing patient care. Through intelligent automation, we're empowering the hardest-working cancer clinics to ensure their patients receive the safest, highest quality, and most efficient treatment possible.

2. For Clinicians, By Clinicians

We are dedicated to raising the standard of patient care in radiation oncology. As former clinicians, we have the hands-on experience where it matters and unique insights to solve the challenges of our time. Our clinical background provides a critical context for creating high-impact software tools that are used daily by over 1,500 centres across the globe.

Fig. 2. Radformation's experienced team shares 500+ years of combined clinical experience to deliver the most useful and relevant solutions in the industry.

2. AutoContour*: Automated AI Contouring

Fig. 3. Automated AI contouring with AutoContour. *AutoContour is not available in all markets.

AutoContour delivers fast, AI deep-learning CT and MR contours adhering to widely accepted guidelines for organs at risk, lymph nodes, and more in any clinical workflow. AutoContour also automates planning structure generation based on your specific templates for margins, rings, crops, etc.
AutoContour works seamlessly with most treatment planning and imaging systems, and provides a unique integration with Eclipse™ and ClearCheck for streamlined contouring. The software features 200 structure models, including 15+ MR models.
With AutoContour you will find:

- Vendor-neutral solution
- Upgraded registration workspace
- Drastically reduced contouring times
- Intuitive review and editing tools

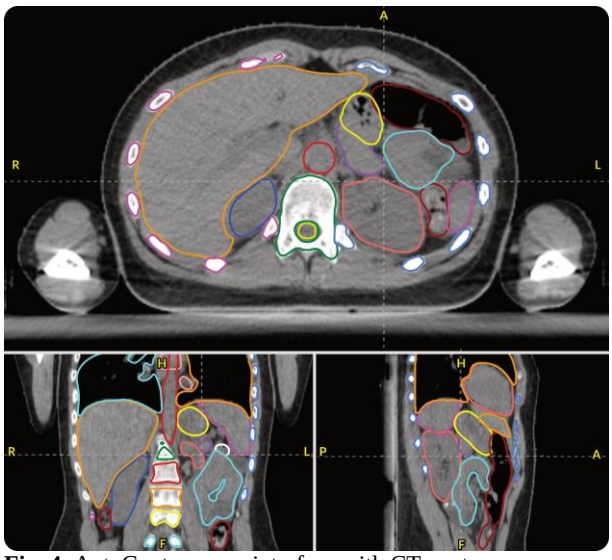

Fig. 4. AutoContour user interface with CT contours.

When Advanced Radiation Centers of New York (ARC) searched for a solution to better manage their high patient census, they found it in AutoContour. After trialing multiple AI-based auto-segmentation tools, they found AutoContour to be the best fit for their workflow. In addition to the accurate contours that served their needs for various body sites, they realised considerable time savings of 60% compared to their previous manual contouring methods.

Table 1. Some of AutoContours structure models include:

Bowel Loops	Hypothalamus
Brachial Plexus	LAD Artery
Breast Lymph Nodes	Oral Cavity
Cerebellum	Pancreas
Chestwall	Pelvic Lymph Nodes
Duodenum	Pharyngeal Constrictors
Female Pelvic Anatomy	Ribs
H&N Lymph Nodes	Vertebrae

3. EZFluence: Automated Forward Planning

EZFluence

Fig. 5. Automated forward planning with EZFluence.

EZFluence automates forward planning for any beam arrangement and any treatment site from head to toe. It standardises e-comp and field-in-field planning regardless of user while maintaining or improving plan quality compared to manual techniques.
Utilise EZFluence to:

- Automate forward planning, from head to toe
- Treat any site with any beam arrangement
- Support mixed energies
- Simplify 3&4-field breast planning

The University of Zurich investigated EZFluence in an effort to streamline 3D planning in their department. The study found worthwhile improvements in time savings, plan coverage, and reductions in hot spot volumes, including cutting the time needed for electronic compensator plans nearly in half.

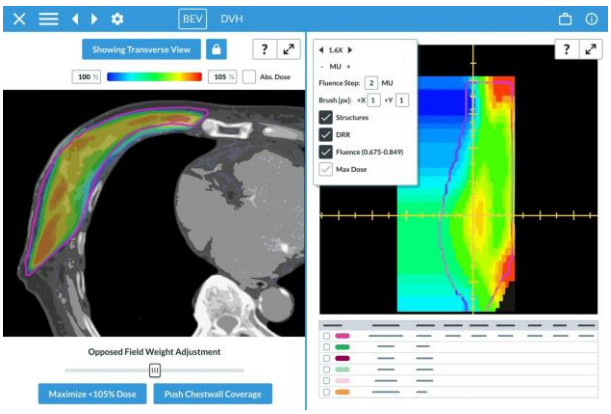

Fig. 6. EZFluence user interface for a breast plan.

By automating your forward planning, EZFluence streamlines treatment planning while ensuring the highest safety and quality standards of patient care.

4. ClearCheck: Automated Plan Evaluation

ClearCheck

Fig. 7. Automate your plan checks with ClearCheck.

ClearCheck is an automated plan check and documentation software that ensures the highest quality treatment plans and helps clinics save time with in-depth plan checks, quick plan comparison, and instant documentation. Working with virtually any TPS, ClearCheck automates various plan checks and leverages robust features, including:

- Dose Constraints
- BED/EQD2 Analysis
- Plan Checks
- Treatment Plan Checks
- Collision Checks
- Structure Checks
- Portal Dosimetry Analysis
- One-Click Reporting

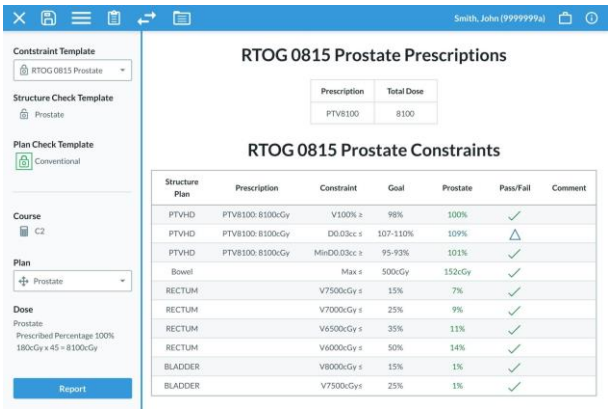

Fig. 8. ClearCheck user interface for plan checks. Standardise and simplify your plan evaluation process with ClearCheck.

5. ClearCalc: Independent Calculation Software

Fig. 9. Automate your independent calculator with ClearCalc.

An independent calculation software platform for all your second check needs. ClearCalc supports a full complement of clinical techniques, treatment planning systems, and offers a variety of algorithms from FSPB to MonteCarlo to efficiently validate plan accuracy.
ClearCalc offers:

- Fast and accurate independent secondary calculations
- A vendor-neutral solution that works with most TPS and machines
- Automatic point selector tool that suggests optimal points
- Per-structure gamma analysis

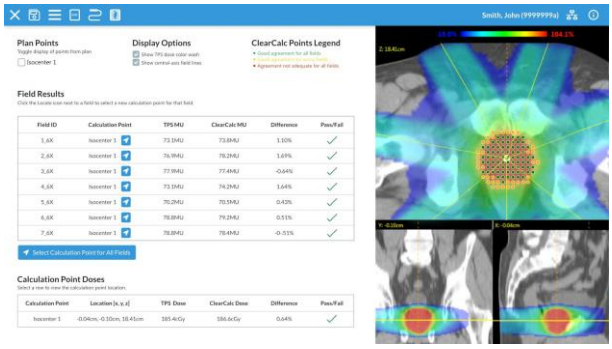

Fig. 10. ClearCalc user interface for secondary independent calculations.

By consolidating all safety and independent calculation checks to one platform, ClearCalc gives clinicians confidence in their treatment plan while saving time.

6. RadMonteCarlo: Independent Monte Carlo

Fig. 11. RadMonteCarlo offers efficient independent calculation as an optional add-on to ClearCalc. RadMonteCarlo is not available in all markets.

Harness the power of our new Monte Carlo algorithm, RadMonteCarlo, that integrates seamlessly within the existing ClearCalc interface for gold-standard plan verification. RadMonteCarlo supports a variety of clinical techniques and treatment planning systems to ensure the accuracy of your plans in minutes.
RadMonteCarlo can be used for photons, protons, and electrons, and features:

- 3D Gamma Analysis for plans and individual structures
- Calculates in under two minutes
- Fully recalculated DVH
- Interactive results

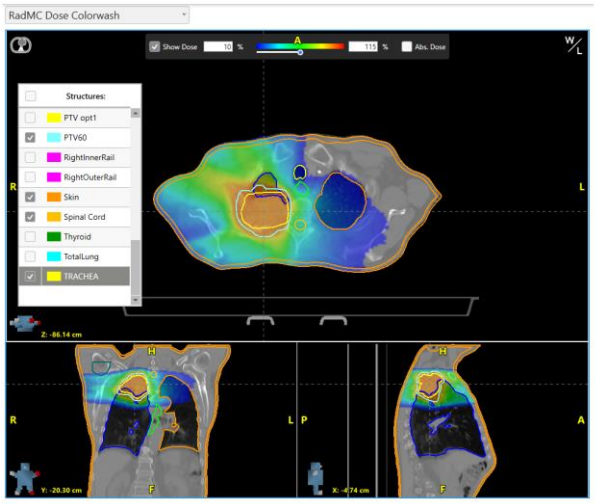

Fig. 12. RadMonteCarlo user interface featuring dose colorwash.

An independent Monte Carlo calculation, RadMonteCarlo is a single solution for multiple machines and techniques in your department.

7. ChartCheck: Automated Treatment Evaluation

Fig. 13. Automate your weekly checks with ChartCheck. ChartCheck is not available in all markets.

ChartCheck actively monitors patient data in real-time to ensure safety for ongoing treatments. With automatic notifications for failing checks, plan errors can be resolved immediately, resulting in higher-quality patient care and significant time savings.
Utilise ChartCheck for:

- Instant alerts and notifications
- Treatment review for every fraction
- Integrated offline image review
- TG-275 compliance

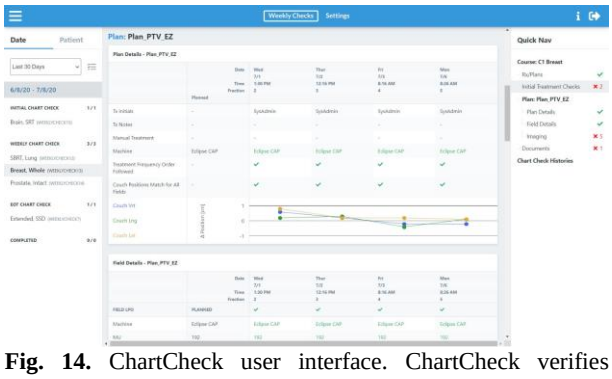

Fig. 14. ChartCheck user interface. ChartCheck verifies ongoing treatment data after each and every fraction.

By consolidating all safety and on-treatment quality checks to one platform, ChartCheck makes routine physics checks proactive and simple, saves time, and gives physicists confidence in their treatment evaluation.

8. RadMachine: Automated Machine QA

Fig. 15. RadMachine is a comprehensive QA platform to meet all your QA needs in a simple, centralised hub.

Access all your Machine QA data on a streamlined, cloud-based platform to perform, review, and track multiple QA data streams all at once. Automatically upload your data for any Machine QA test or frequency from Machine Performance Check, DailyQA3, File Directory, and ARIA® right in your browser with RadMachine.

Fig. 16. RadMachine consolidates and organises data for any test and frequency in a single location that can be accessed securely from anywhere.

Gone are the days of scattered spreadsheets and siloed data. RadMachine features:

- 70+ pre-built test packs
- Analyse routine image datasets
- Track machine faults, maintenance, and more
- Optimised for Diagnostic departments

No more spreadsheets. No more relying on multiple QA tools for different tasks. RadMachine meets all your QA needs in one platform while allowing for complete customisation to fit the unique needs of your department.

9. Time Savings Where It Matters

Radformation products are designed with time savings and convenience in mind. From start to finish, our lineup of automation tools provides efficiency along every step over the course of patient treatment. With fewer bottlenecks, clinics are able to do more in less time and focus on what matters most.

For more information or to schedule a demonstration, visit radformation.com.

iDOSE is a dose management system that automatically monitors, analyzes and reports the radiation dose received by patients.

- Display summary exposure data, with filtering and searching
- Access data from every kind of x-ray device and from every manufacturer in real time
- Get notified in case of exceeding the permitted dose levels
- Browse dose history in terms of: patients, anatomical regions, types of X-ray examinations and more
- SSDE (Size-Specific Dose Estimate)

Intrested? Contact us!

idose.eu
info@idose.eu

idose

idose

THE SMARTEST WAY TO ANALYZE RADIATION DOSE

idose.eu

CONTENT

AUTHOR INDEX

ISSN 1822–5721